

**Photovoltaics**  
from  
**Discotic Liquid Crystalline HBCs**  
&  
**Poly(2,7-Carbazole)s**

Dissertation zur Erlangung des Grades  
'Doktor der Naturwissenschaften'

am Fachbereich Chemie und Pharmazie  
der Johannes Gutenberg-Universität in Mainz

**Jiaoli Li**

Geboren in Shaanxi Province / China

Mainz 2006



*Dedicated to my family*





# CONTENTS

---

<b>Chapter 1 INTRODUCTION</b>	<b>1</b>
1.1 The Development of Organic Solar Cells.....	2
1.2 Discotic Liquid Crystals as Active Semiconductors in Electronic and Optoelectronic Devices.....	3
1.3 Conjugated Polymers as Active Components in Organic Solar Cells.....	8
1.4 Motivation.....	13
1.5 Contents of the Thesis.....	14
<b>Chapter 2 ORGANIC SOLAR CELLS</b>	<b>15</b>
2.1 The Organic Bulk Heterojunction Concept.....	15
2.2 Fundamental Processes.....	16
2.2.1 <i>The Absorption of Photons and the AM1.5 G Solar Light</i> .....	17
2.2.2 <i>Exciton Diffusion and Charge Separation at the D/A Interface</i> .....	18
2.2.3 <i>Charge Transport</i> .....	22
2.2.4 <i>Charge Recombination</i> .....	24
2.2.5 <i>The Organic Semiconductor/Metal Contact</i> .....	25
2.3 Film Morphology.....	26
<b>Chapter 3 EXPERIMENTAL METHODS</b>	<b>29</b>
3.1 Spectroscopy.....	29
3.1.1 <i>Absorption Spectra</i> .....	29

3.1.2 Photoluminescence Measurements.....	30
3.2 Cyclic Voltammetry.....	30
3.3 Microscopic Techniques.....	32
3.3.1 Atomic Force Microscopy.....	32
3.3.2 Scanning Electronic Microscopy.....	34
3.4 X-ray.....	34
3.5 Differential Scanning Calorimetry.....	35
3.6 Fabrication and Characterization of Solar Cells.....	36
3.6.1 Device Fabrication.....	36
3.6.2 Device Testing.....	38
3.6.3 Photovoltaic Parameters.....	40
3.6.3.1 I- $\lambda$ Curve (EQE- $\lambda$ Curve).....	40
3.6.3.2 I-V Curve.....	41

## **Chapter 4 APPLICATION OF HEXABENZOCORONENE (HBC) IN SOLAR CELLS 43**

4.1 Introduction.....	44
4.2 Photodiodes Based on HBC-PhC <sub>12</sub> .....	46
4.2.1 Film Forming.....	47
4.2.2 Morphology Studies on PDI Crystals.....	49
4.2.3 Device.....	54
4.2.3.1 Thermal Treatment.....	54
4.2.3.2 HBC-PMI.....	56
4.2.4 Summary.....	61
4.3 Photodiodes Based on Branched-alkyl Substituted HBCs.....	62
4.3.1 Introduction.....	62
4.3.2 Optical Properties.....	65
4.3.3 Characterization of Energy Levels.....	67

4.3.4 Photovoltaic Device.....	69
4.3.5 Morphology Investigation.....	72
4.3.6 Summary.....	78
4.4 HBC-C <sub>3</sub> OC <sub>10,6</sub> – A New Discotic Material for Solar Cells.....	78

## **Chapter 5 POLY(2,7-CARBAZOLE)S AS DONOR MATERIALS IN PHOTOVOLTAICS 84**

5.1 Introduction.....	84
5.1.1 Synthesis of Poly(2,7-carbazole) (PCz).....	84
5.1.2 Optical Properties.....	85
5.1.3 Characterization of Energy Levels.....	86
5.1.4 Comparison of PCz and PF in Solar Cell.....	87
5.2 Photodiodes based on PCz.....	89
5.2.1 Pairing PCz with PDI or PCBM.....	89
5.2.1.1 Optical Properties of the Blends.....	90
5.2.1.2 Matching Energy Levels of D/A.....	91
5.2.1.3 Charge Transfer from the Donor to the Acceptor.....	91
5.2.1.4 Photovoltaic Device.....	93
5.2.2 Optimization of Device PCz/PDI.....	94
5.2.2.1 D/A Ratio.....	94
5.2.2.2 Thermal Treatment.....	102
5.2.3 Summary.....	105
5.3 Photodiodes based on Ladder Type Poly(2,7-Carbazole)s.....	105
5.3.1 Optical Properties.....	107
5.3.2 Characterization of Energy Levels.....	109
5.3.3 Self-organization Properties.....	110
5.3.4 Photovoltaic Device.....	117
5.3.4.1 PCBM based Device.....	117

5.3.4.2 PDI based Device.....	123
5.3.5 Summary.....	132
5.4 Low Band-gap Materials containing 2,7-linked Carbazole.....	133
5.4.1 Copolymer of PCz and PDI.....	134
5.4.2 Conjugated Copolymers of 2,7-linked Carbazole and Ladderized Pentaphenylene with Diketone Bridge (LPPK).....	139
5.4.3 Small Molecule based on Carbazole and Diketone.....	142
<b>Chapter 6 GUIDELINES FOR SOLAR CELL DESIGN</b>	<b>146</b>
6.1 Absorption of Solar Light.....	146
6.2 Relative Energy Levels.....	150
6.3 Charge Transport and D/A Interfacial Area.....	152
6.4 Film Forming.....	157
<b>CONCLUSIONS AND OUTLOOK</b>	<b>161</b>
<b>REFERENCES</b>	<b>164</b>
<b>ACKNOWLEDGEMENT</b>	<b>178</b>
<b>LIST OF PUBLICATIONS</b>	<b>180</b>
<b>CURRICULUM VITAE</b>	<b>182</b>

## Index of Abbreviations

AFM	atomic force microscopy
DSC	differential scanning calorimetry
FET	field effect transistor
g	gram
HBC	hexa-peri-hexabenzocoronene
h	hour
LED	light emitting diode
min	minute
m.p.	melting point
MALDI-TOF	matrix-assisted laser desorption ionization-time of flight
NIR	near infrared
NMR	nuclear magnetic resonance
PAH	polycyclic aromatic hydrocarbons
POM	polarized optical microscopy
PR-TRMC	pulse radiolysis time-resolved microwave conductivity
RT	room temperature
STM	scanning tunneling microscopy
THF	tetrahydrofuran
UV-vis	ultraviolet/visible



## Chapter 1 Introduction

During and immediately after the oil crisis in the early 1970s, a tremendous effort was devoted to the development of photovoltaic (PV) or solar cells, in order to utilize the cleanest and most abundant of all possible renewable energy sources on the planet, viz. sunlight. Nowadays solar cells based on crystalline and amorphous silicon dominate the market. World solar PV energy production grew from 740 MW in 2003 to 1,150 MW in 2004.<sup>1</sup> While there is high demand, these inorganic semiconductors are characterized by high production costs, due to the high temperatures and vacuum steps necessary for their processing. In comparison, solution processable organic semiconducting materials represent a promising alternative and a rather new approach. They provide many desirable properties such as low price, lightweight, flexibility and semi-transparency. These features have captured the interest of scientists and engineers both in academy and industry. Aside from possible economic advantages, organic materials also possess low specific weight and are mechanically flexible – properties that are desirable for a solar cell to guarantee easy integration of the modules on any surface, from glass windows to textiles and clothes. Several geometries for organic photovoltaic devices have been investigated to date.

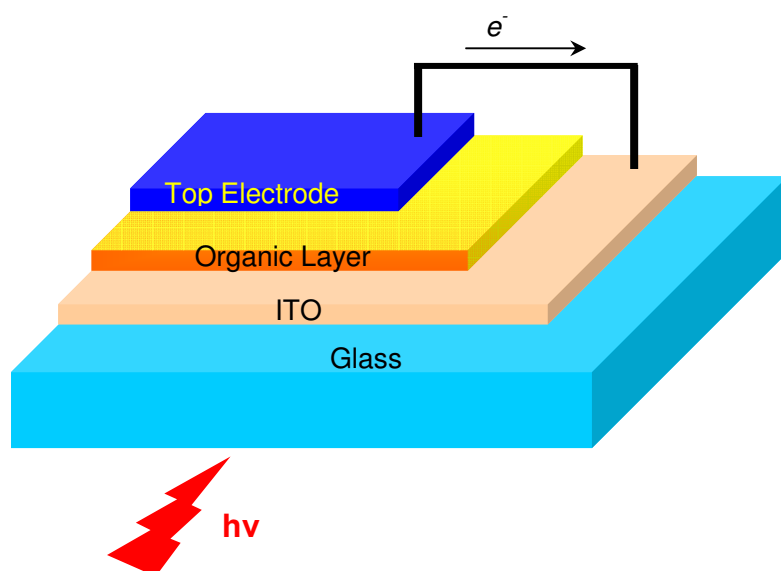


**Figure 1.1** The typical structure of organic solar cell.

Organic solar cells absorb solar light to form excitons, which dissociate into positive and negative charges. The separated charges then move to the electrodes so as to form current in the external circuit. The most frequently applied device structure is shown in Figure 1.1, where the active layer consisting of either small organic molecules or polymers is sandwiched between a transparent electrode like indium-doped tin oxide (ITO) and another counter electrode (for example, Ag or Al). The details on how a solar cell works will be discussed in chapter 2.

## 1.1 The Development of Organic Solar Cells

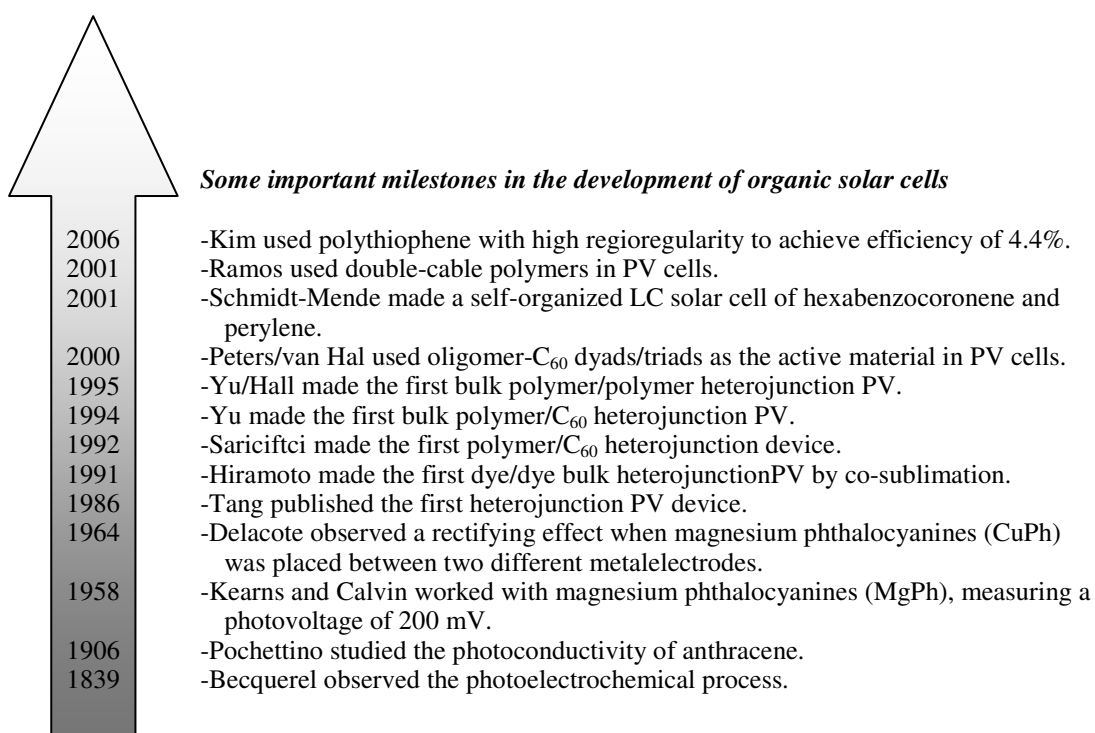


**Figure 1.2** *Some milestones in the development of organic solar cells*

The discovery of the PV effect dates back to 1839, when Becquerel observed photocurrents upon illuminating platinum electrodes covered with silver bromide or silver chloride in aqueous solution. But this remained a curiosity of science for the next three-quarters of a century. Major steps toward commercializing devices based on the PV effect



were taken in the 1940s and early 1950s when processing of highly pure crystalline silicon was developed. In 1954, scientists at Bell Labs developed the first crystalline silicon solar cell with an efficiency of 4%. In the meantime, the potential use of organic semiconductors as photoreceptors in optoelectronic systems was recognized. This class of materials has been used in efficient light-emitting diodes (LEDs)<sup>2-6</sup> and field effect transistors (FETs),<sup>7-15</sup> and so there has been considerable interest in developing efficient organic photovoltaic devices.<sup>16-25</sup>

The first generation of organic photovoltaic devices was based on a single active layer sandwiched between two metal electrodes with different work functions. The efficiencies were generally poor, in the range of  $10^{-3}$  to  $10^{-2}\%$ .<sup>16,26</sup> In 1986, Tang first introduced the concept of heterojunction with a bilayer solar cell and achieved an efficiency of 1%.<sup>27</sup> In this case, two organic layers (a phthalocyanine derivative as *p*-type semiconductor and a perylene derivative as *n*-type semiconductor) were sandwiched between two electrodes. This result was for many years the record efficiency for an organic solar cell. The next encouraging breakthrough was achieved with Sariciftci's report on the photophysics of mixtures (bulk heterojunction) of conjugated polymers with fullerene in 1992.<sup>28</sup> It was clearly shown that the forward electron transfer from excited conjugated polymers to fullerene was faster than 50 fs, while the back electron transfer rate is on the order of 1  $\mu$ s at room temperature.<sup>29</sup> Later work based on this bulk heterojunction concept developed greatly the efficiency values of organic solar cells<sup>30-37</sup>, approaching 5% for devices containing polythiophene and fullerene.<sup>38,39</sup> In addition to polymers, discotic liquid crystals are another promising class of *p*-type materials because of their capacity to self-organize into columnar stacks.<sup>40-42</sup> A major advancement was made by Schmidt-Mende et al in 2001, who reported a 34% external quantum efficiency near 490 nm.<sup>43</sup>

## 1.2 Discotic Liquid Crystals as Active Semiconductors in Electronic and Optoelectronic Devices

The term discotic liquid crystal refers to a kind of liquid crystalline molecules with a discotic core, discovered by Chandrasekhar et al. in 1977.<sup>44-47</sup> The molecules consist of a flat and rigid aromatic core with alkyl side chains on the periphery. Today the aromatic core size varies from a single benzene ring<sup>48</sup> to large extended cores consisting of more

than 132 carbon atoms<sup>49</sup> belonging to the general class of polycyclic aromatic hydrocarbons (PAHs).

Mesophases formed by these molecules can be divided into columnar, discotic-nematic, columnar-nematic and lamellar (smectic-like), among which the first organization type is the most common one (see fig. 1.3). The nematic phases reveal an ordered arrangement of the discs, but with no long-range translational order. In the columnar phase the discotic molecules stack one on top of each other into columns (labeled by the symbol D), which in turn arrange laterally into a two-dimensional unit cell. Hence, different intercolumnar arrangements of the discs are possible.

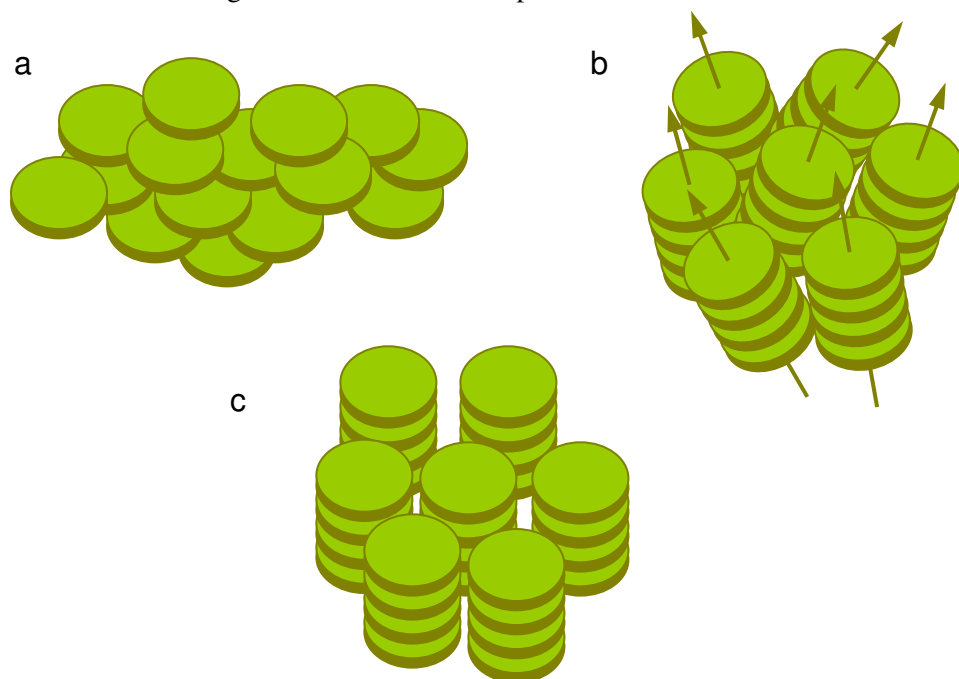


**Figure 1.3** Illustration of the different mesophases of discotic liquid crystals with a) discotic-nematic, b) columnar-nematic and c) columnar arrangement.

Normally three different 2D lattices are possible in a mesophase: hexagonal ( $\text{Col}_h$ ), rectangular ( $\text{Col}_r$ ) or oblique ( $\text{Col}_{ob}$ ) as shown in Figure 1.4. The discs are either perpendicular or slightly tilted with respect to the columnar axis.<sup>50</sup> The main driving force for the columnar self-assembly is the  $\pi$ - $\pi$  interaction between the aromatic cores. When

specific side groups are introduced into the side chains, hydrogen bonding interactions can also dominate.<sup>51-53</sup> In some cases these two forces interact synergistically leading to the formation of more stabilized columnar superstructures.<sup>54-57</sup>

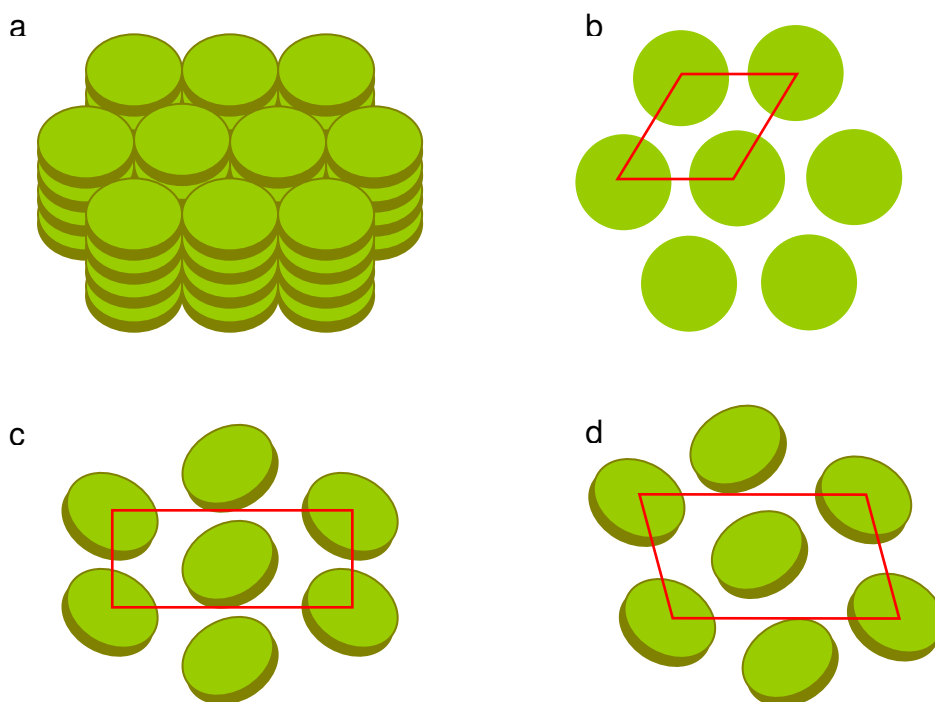


**Figure 1.4** a) columnar arrangement and top view of two-dimensional lattices of columnar phases: b) hexagonal, c) rectangular, and d) oblique.

The tendency to form one-dimensional columnar superstructures, which allow free electric charges to migrate<sup>40-42</sup>, means discotic liquid crystals are promising organic charge transport materials in a variety of devices such as LEDs,<sup>58</sup> photovoltaic devices,<sup>43,59</sup> and FETs<sup>15,60-62</sup>. Both *p*-type discotic liquid crystals such as triphenylene, phthalocyanine (Pc) and hexabenzocoronene (HBC), and *n*-type discotic liquid crystals such as perylene and anthraquinone are known (Figure 1.5).

The HBC based discotic liquid crystals have the highest hole mobility ever reported for a liquid crystal,<sup>63</sup> which reveals their great potential for use in solar cells. The

intermolecular attractive forces due to the large  $\pi$ -areas induce a pronounced propensity to self-assemble into highly organized super-structures. Modulation of the interactions has been accomplished synthetically by the introduction of different side-chains, which allow the control of its thermal behavior, the solubility and thus the processability.<sup>64-66</sup> A major breakthrough came from Schmidt-Mende et al in 2001 who, as mentioned above, showed that a mixture of the liquid crystalline HBC-PhC<sub>12</sub> and crystalline perylene diimide (PDI) when spin-coated onto an ITO substrate produced photodiodes, which exhibited extremely high external quantum efficiency (EQE) of 34% at 490 nm, corresponding to an overall efficiency of 1.95%.<sup>43</sup> The facile phase separation between the LCs and crystalline materials, the large overlap of the donor and acceptor on the interface, the high charge carrier mobility along these discotic materials and the good molecular energy level gradient between HBC and PDI are the crucial factors. Such simple but highly efficient systems hold great promise for commercial applications.

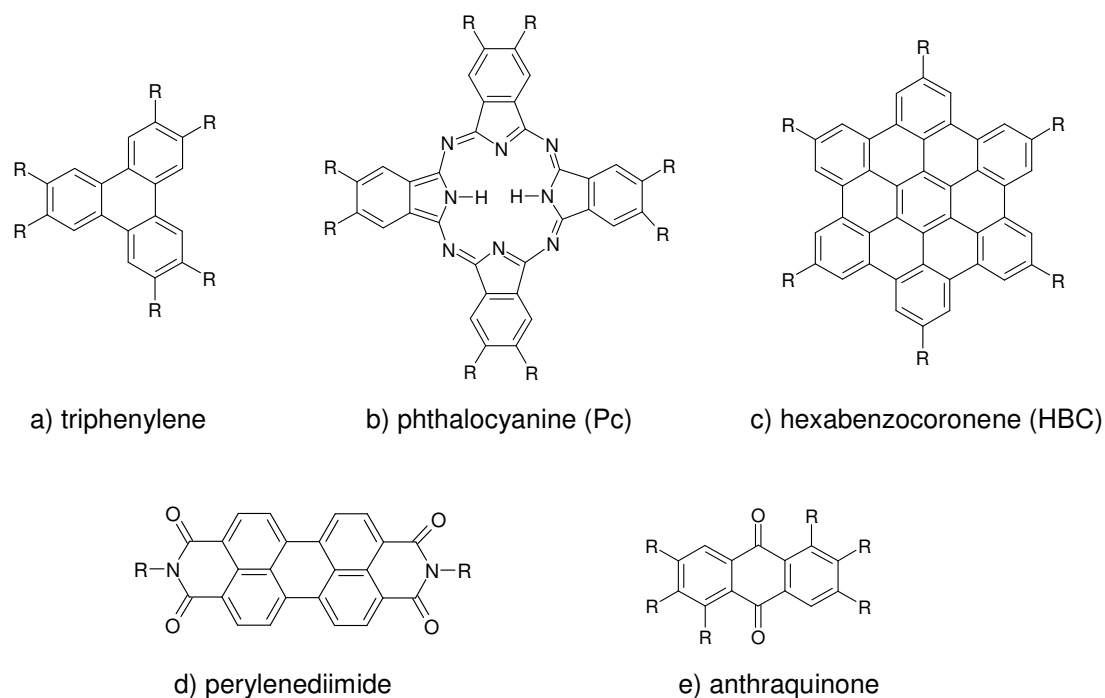


**Figure 1.5** Chemical structures of a few *p*-type (a-c) and *n*-type (d-e) discotics.

Van de Craats et al. obtained successful FET devices based on highly oriented HBC discotics, showing mobilities of the order of  $10^{-3} \text{ cm}^2\text{V}^{-1}\text{s}^{-1}$  and on/off ratios of  $\sim 10^4$ .<sup>63</sup> They found that direct processing of HBC based discotic materials on oriented films such as rubbed polytetrafluoroethane (PTFE) substrate resulted in highly ordered thin films with the columnar axis of discs parallel to the orientation axis (see schematic on Figure 1.6).

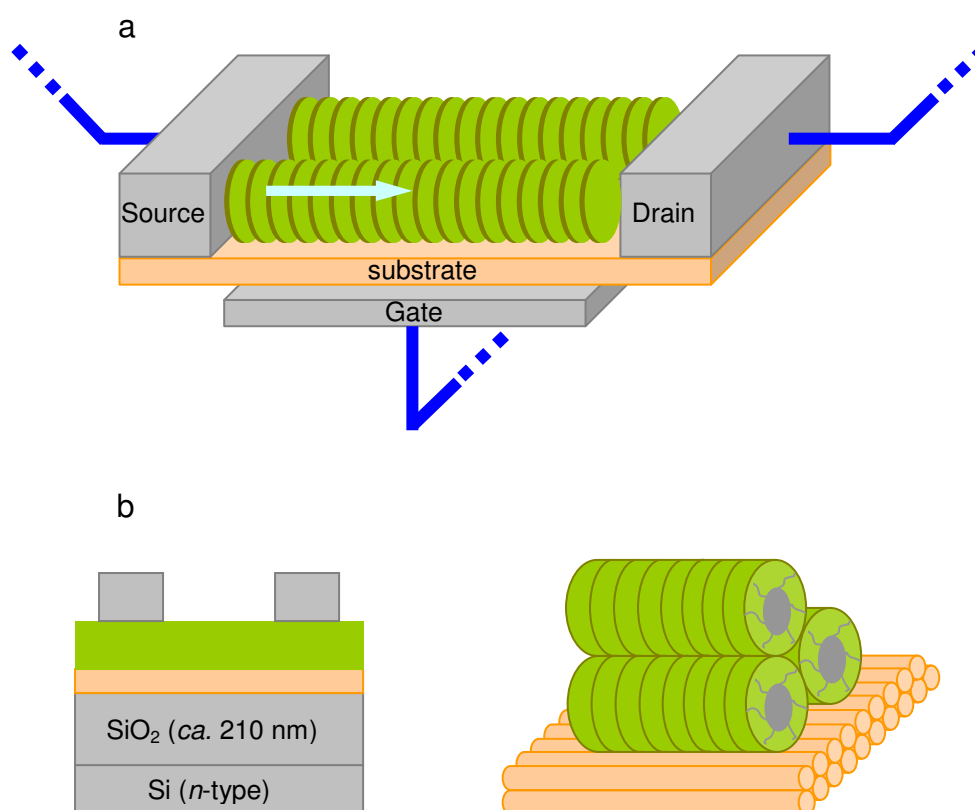


**Figure 1.6** a) Schematic representation of discotic LC materials in FETs and b) a practical FET device based on oriented HBC on rubbed PTFE layer.

A zone-casting technique developed by Tracz et al. can achieve uniaxial alignment of HBC materials onto an untreated substrate.<sup>64</sup> The principle is presented in Figure 1.7. A solution is spread out by means of a nozzle onto a moving support such as glass or silicon.

During the solvent evaporation, the material begins to precipitate or to nucleate from the solution and then crystallizes directionally onto the moving support forming in this way the aligned thin layer. Exceptionally long columns (200 ~ 500 nm) in large domains are formed as a result of zone crystallization during the solvent evaporation. FET devices with mobility as high as  $10^{-2} \text{ cm}^2 \text{ V}^{-1} \text{ s}^{-1}$  is recently achieved by Pisula et al. using this zone-casting technique.<sup>65</sup>

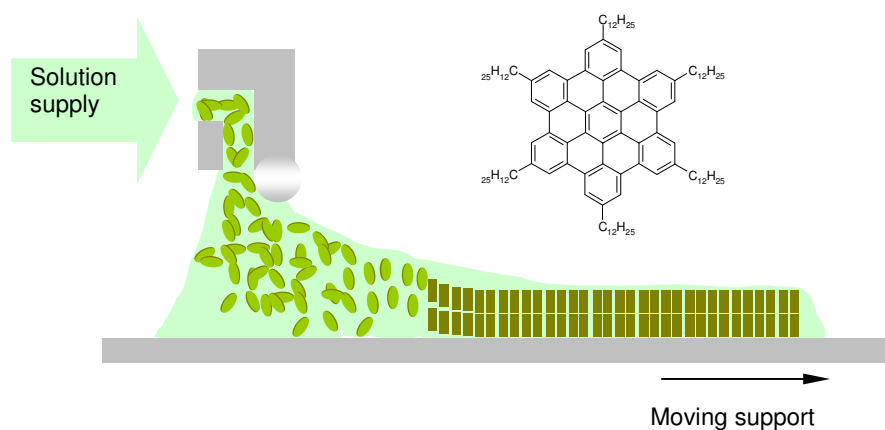


**Figure 1.7** Control of alignment of discotic materials by zone-casting

### 1.3 Conjugated Polymers as Active Components in Organic Solar Cells

Construction of an organic PV device requires the use of two types of materials viz. a donor (p-type) material and an acceptor material (n-type). Many conjugated polymers in their undoped, semiconducting state are electron donors upon photo-excitation (electrons promoted to the anti-bonding  $\pi^*$  band). A substituted fullerene, such as [6,6]-phenyl-C<sub>61</sub>-butyric acid-methylester (PCBM), is most commonly used as an acceptor.<sup>37,67,68</sup> Most of the work into such devices has used soluble polythiophenes<sup>35,69</sup> or derivatives of

poly(phenylene vinylene) (PPV)<sup>70-71</sup> as the donor material. The chemical structures of some of the widely used polymers as well as acceptor type molecules are shown in Figure 1.8.

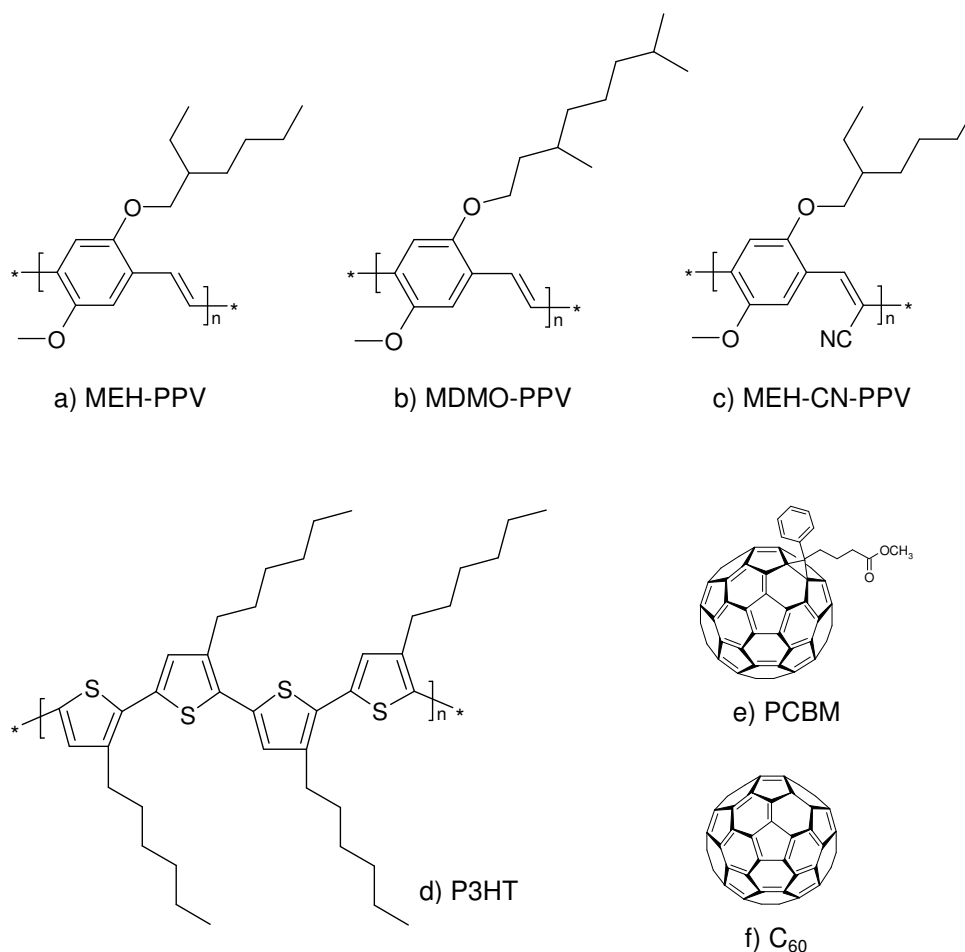


**Figure 1.8** Chemical structures of some *p*- and *n*-type materials used in solar cells: a) poly(2-methoxy-5-(2'-ethylhexyloxy)-1,4-phenylene vinylene) (MEH-PPV), b) poly(2-methoxy-5-(3,7-dimethyloctyloxy)-1,4-phenylene vinylene) (MDMO-PPV), c) poly(2-methoxy-5-(2'-ethylhexyloxy)-1,4-(1-cyanovinylene)-phenylene) (MEH-CN-PPV), d) poly(3-hexylthiophene) (P3HT), e) [6,6]-phenyl-C<sub>61</sub>-butyric acid-methyl ester (PCBM), f) C<sub>60</sub>

The first heterojunction photovoltaic devices based on these conjugated polymers adopted a bilayer structure (Figure 1.9a). The efficiency of this kind of devices was low

because of the small charge generating interface. The superior solubility of functionalized fullerenes compared to  $C_{60}$  made it possible to produce high fullerene-content composite films. With the introduction of the concept of ‘bulk-heterojunction’ (Figure 1.9b) into photovoltaic devices, significant improvements in the efficiency have been achieved using phase separated composite materials, processed through a control of the morphology of the phase separation into an interpenetrating network (‘bulk heterojunction’). The power efficiency of solar cells made from MEH-PPV/fullerene composites has increased dramatically.<sup>18</sup> In parallel, the groups of Heeger in Santa Barbara<sup>72</sup> and Friend in Cambridge<sup>17</sup> developed an approach using acceptor-type conjugated polymers (for example, CN-PPV) in an interpenetrating polymer-polymer composite with MEH-PPV, yielding polymeric PV devices with efficiencies comparable to fullerene mixed devices.

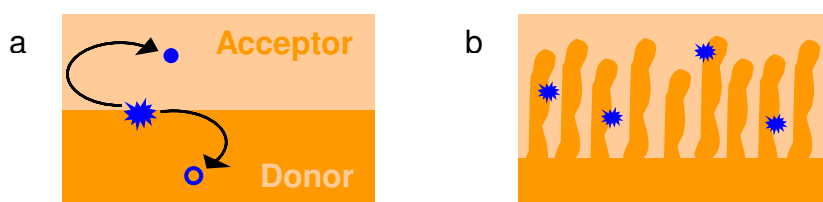


**Figure 1.9** Charge generation at D/A interface of a) bilayer and b) bulk heterojunction.

It was recently reported that organic solar cells based on polythiophene and PCBM demonstrated an overall efficiency of 5% under AM 1.5 illumination.<sup>38</sup> The improved performance was attributed to the improved nanoscale morphology, the increased crystallinity of the semiconducting polymer and improved contact to the electron-collecting electrode by thermal annealing.<sup>39</sup> The degree of regioregularity (RR) of the polymer was proved to correlate to good optical absorption and charge transport resulting from the organization of P3HT chains and domains, thus showing a strong influence on device performance.<sup>38</sup> Further progress can be achieved by stacking two cells in series<sup>73,74</sup>.

Although P3HT:PCBM solar cells are among the most efficient reported so far, they only absorb a part of the solar spectrum. So the molecular design and synthesis of low band gap materials, which have an increased absorption in the red region of the optical spectrum, gained much attention as another way to improve the performance of organic solar cells. It is promising to pair a low band gap material with PCBM, where a very fast electron transfer from the conjugated polymer to fullerene has been observed by Sariciftci.<sup>6</sup> One approach that has proven successful in achieving low band gap conjugated polymers



is the incorporation of alternating electron donating and electron accepting moieties along the polymer backbone.<sup>75</sup> The low band gaps in these materials derive from a partial charge transfer in the polymer main chain, induced by the donor-acceptor systems. Some examples of low band gap materials are shown in Figure 1.10. The typical bandgap is below 2 eV, with some even approaching 1 eV. The photovoltaic devices based on these polymers in blends with PCBM showed an efficiency of 1~2%.<sup>36,76-81</sup>

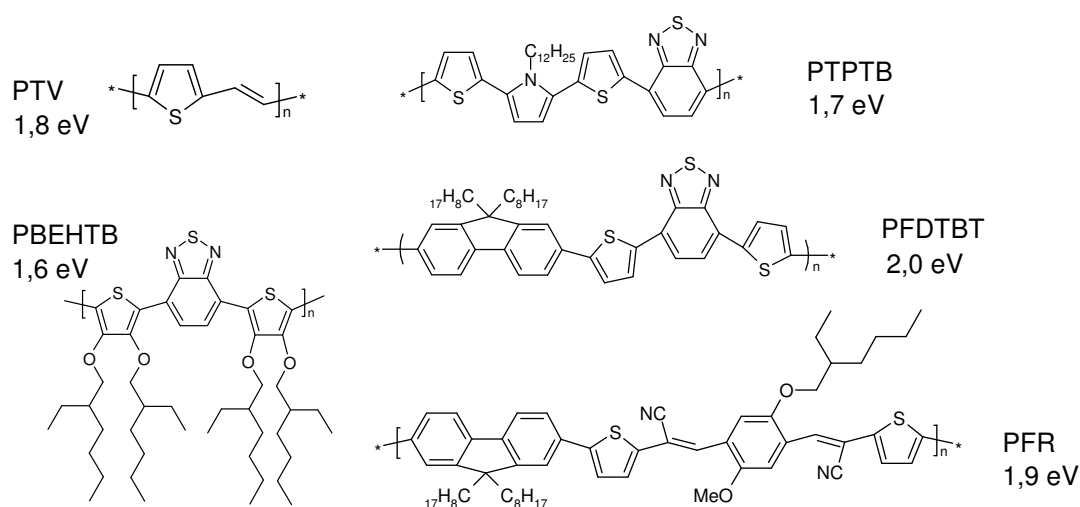


**Figure 1.10** Examples of low band gap materials. The numbers indicate the bandgap of the material.

However, for most of the reported low band gap polymers, the reduction in bandgap was realized largely by increasing the HOMO level, which makes the materials highly susceptible to aerial oxidation. A class of polymers that has to date received little attention as p-type materials for use in solar cells are the polycarbazoles. Carbazole is a well-known electron-donating material. The HOMO energy level of the carbazole based polymers (-5.6 eV) is lower than that of polythiophene (eg. -5.2 eV for P3HT<sup>82</sup>) and PPV-based materials (eg. -5.3 eV for MDMO-PPV<sup>83</sup>) mentioned above, and so they are less easily oxidized.

Poly(*N*-vinylcarbazole) (PVK, Figure 1.11c) is the most widely investigated and applied semiconductor in the carbazole family due to its photoconductive properties and ability to form charge-transfer complexes arising from the electron donating character of the carbazole moiety.<sup>84</sup> One could expect an improvement of the mobility of the charge carriers if carbazole groups are covalently incorporated in the main chain to form

conjugated backbones. There are two ways to connect carbazole units, the first is to link the repeat units at the 3- and 6- positions to yield poly(3,6-carbazole)s (Figure 1.11a), and the second to connect via the 2- and 7- positions to provide poly(2,7-carbazole)s (Figure 1.11b). Oligomers of 3,6-carbazole were first synthesized in 1967 by Ambrose.<sup>85</sup> Siove et al. succeeded in synthesizing a high molecular weight polymer by way of oxidative polymerization in 2004.<sup>86</sup> A FET based on poly(N-butyl-3,6-carbazole) showed a good charge carrier mobility of  $10^{-3} \text{ cm}^2\text{V}^{-1}\text{s}^{-1}$ .<sup>87</sup> Poly(3,6-carbazole)s have also been used as blue emitters in LED, showing a much higher stability than the more widely studied polyfluorene.<sup>86,88</sup>

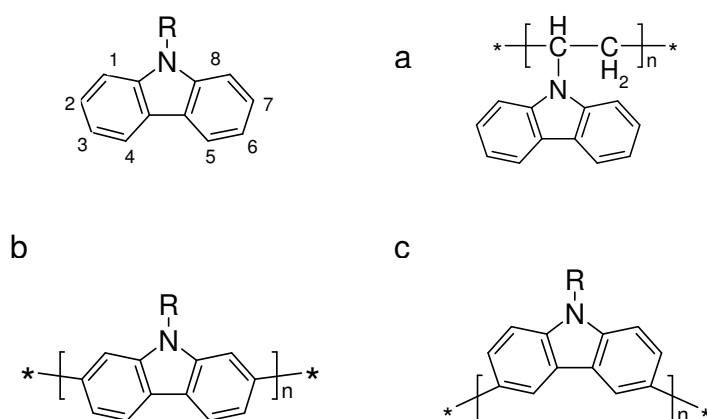


**Figure 1.11** Chemical structures for a) PVK, b) poly(2,7-carbazole), and c) poly(3,6-carbazole)

Compared to poly(3,6-carbazole)s, poly(2,7-carbazole)s have been less investigated. Nevertheless, this isomer could be very interesting for electro-active and photoactive devices, since carbazole units linked at the 2- and 7-positions should lead to materials having a longer conjugation length when compared to the 3,6- isomer.<sup>89-91</sup> But both the 2- and 7- positions are *meta* to the *ortho-para* directing amino group of the carbazole unit, rendering the synthesis of 2,7-linked carbazole-based materials not as straightforward as that of 3,6-carbazole-based materials. The 2,7-homo-polymers of carbazole previously reported had low molecular weights due to their poor solubility, limiting their use in thin-film devices. Our group has developed an efficient way to synthesize useful 2,7-dibromocarbazole derivatives in only three steps from commercially available reagents

with an overall yield of approximately 50%.<sup>92</sup> This new approach represents a real improvement, compared with the previously published synthesis of 2,7-dibromocarbazole,<sup>93</sup> and made it possible to use soluble high molecular weight poly(2,7-carbazole)s in photo-electronic devices. LEDs based on poly(2,7-carbazole)s have proved to be among the best blue light emitters, with luminance values as high as 800  $\text{cdm}^{-2}$  at about 10 V.<sup>94</sup> However, the use of polycarbazoles as donor materials in solar cells has remained till now an unexplored area of research, which is now examined in this thesis.

## 1.4 Motivation

The successful application of discotic liquid crystalline materials based on HBC molecules in electronic devices such as FETs and solar cells holds great commercial significance. However, a lot of fundamental research still needs to be done in identifying new systems as well as in improving and optimizing known structures. The present work aims at a systematic study into the relationship between molecular structure and device performance. It is imperative to thoroughly understand the various factors that determine the efficiency of a solar cell so that fully optimized devices can be generated and screened at a faster pace.

In the present investigation, HBC derivatives varying only in the length of the attached alkyl side chains (from 2-ethyl-hexyl, through 2-hexyl-decyl, to 2-decyl-tetradecyl) are used as donor materials in bulk heterojunction photovoltaic devices. These HBCs differ from the formerly reported HBC-PhC<sub>12</sub> in that the alkyl groups are directly attached to the HBC core. Therefore, the supramolecular organization of the investigated HBCs was expected to vary from that of HBC-PhC<sub>12</sub>, which was expected to affect the performance of the devices. Further, the substituted alkyl chains with different chain length can impact on the supramolecular organization of these molecules. In order to fully understand this phenomenon, the thermal properties (LC phase) needed to be investigated by DSC and WAXS. Also, to better correlate the effect of morphology on the device performance, a systematic investigation of the pure material and that of the blends by microscopy techniques (AFM and SEM) were proposed. Efforts have to be made to correlate the optical properties and redox behavior of the HBCs with the photovoltaic behavior. This study is expected to generate deeper insights into the structure-performance relations applicable not only to discotic materials but also to other classes of organic semiconductors.

The second focus of this thesis is to explore the use of 2,7-linked carbazole based conjugated polymers in PV devices. For the first time the application of this class of materials in solar cells is described. Both poly(3,6-carbazole)s and PVK based materials have been successfully applied in electronic devices, and poly(2,7-carbazole)s are even more promising materials since they have a longer conjugation length, which is beneficial for charge migration along the chains. However, the incorporation of a long branched alkyl chain in poly(2,7-carbazole) on the one hand increases the solubility of polycarbazole but on the other hand reduces the amount of light absorbing chromophores in the active layer. The large density of alkyl chains also increases the insulating effects, which prevents the intermolecular contact of semiconducting material and hampers the facile photoinduced electron transfer from donor to acceptor material as well as charge transport. One way to optimize the molecular structure is the use of ladder-type polymers, which can absorb in the parts of visible region where solar spectrum is most prominent due to their more extended conjugation. A series of ladder-type carbazole-based polymers are tested in solar cells in this work, to provide yet more information on correlating device performance to the molecular structures.

## 1.5 Contents of the Thesis

In this thesis, the application of HBC based liquid crystalline materials and 2,7-linked carbazole based conjugated polymers in organic photovoltaic devices will be described. After the introduction in this chapter on organic solar cells and the development of semiconducting materials, Chapter 2 will focus on the basic theory behind the operation of a solar cell. The chapter 3 describes the experimental methods for the characterization of the materials, and the fabrication and testing of devices. The parameters for solar cells are also introduced. Following these introductory chapters, the results are discussed in Chapter 4 for HBC based materials and in Chapter 5 for poly(2,7-carbazole)s. The performance of the devices will be discussed with an emphasis on the effects of varying the molecular structure. A series of compounds varying only in alkyl substituents are studied from a view to correlate physical properties and morphology of the films on the device performance. After the discussion on defined materials, guidelines on molecular design of materials for photovoltaic devices are presented in Chapter 6. The materials are analyzed from a chemical structure viewpoint as well as their physical properties. The possibility of using other materials is discussed based on D/A matching. The thesis will finish with a conclusion and an outlook for further work within this area in Chapter 7.

## Chapter 2 Organic Photovoltaics

In this chapter, the concept and working principle of an organic photovoltaic device are introduced. The influence of morphology of the active thin film is also discussed as an important factor determining the performance of solar cells.

### 2.1 The Organic Bulk Heterojunction Concept

The concept of bulk heterojunction in organic solar cells first emerged as a means of improving on the photocurrent from a bilayer solar cell. Despite the high quantum efficiency of photo-induced charge separation (near unity) close to the interface, the overall photocurrent of bilayer devices is very low. This can be explained by the small charge-generating regions around the interface (Figure 2.1a). Consequently, interpenetrating phase-separated *p*-type/*n*-type (D/A) network composites, i.e., bulk heterojunction, appear to be ideal photovoltaic composites (Figure 2.1b). A bulk heterojunction is by definition a blend of a *p*-type and an *n*-type semi-conductors (donor/acceptor). The blend usually comprises any of conjugated polymers, fullerene derivatives, or other photoactive small molecules (including liquid crystals).

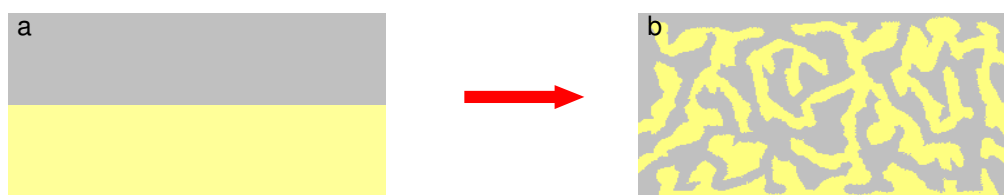


**Figure 2.1** *D/A interface from a) bilayer structure to b) bulk heterojunction system.*

By controlling the morphology of the phase separation so as to form an interpenetrating network, one can achieve a high interfacial area within a bulk material. Since any point in the composite is within a few nanometers of a D/A interface, such a

composite is effectively a bulk D/A heterojunction material. If the network in a device is bi-continuous, it will benefit the charge transport in the two separated D- or A- paths. The morphology thus greatly influences the performance of the photovoltaic devices, which would be further discussed in chapter 2.3.

## 2.2 Fundamental Processes

The fundamental processes in an organic solar cell are:

- Absorption of photons to form excitons.
- Exciton diffusion and charge separation at the D/A interface.
- Charge transport through the percolation pathways formed by Donor and Acceptor, competing with charge recombination at the trap sites.
- Charge injection from active layer into the electrodes.

Each process relies on the properties of the materials themselves or on the interface effect at either the D/A or organic/metal interface.

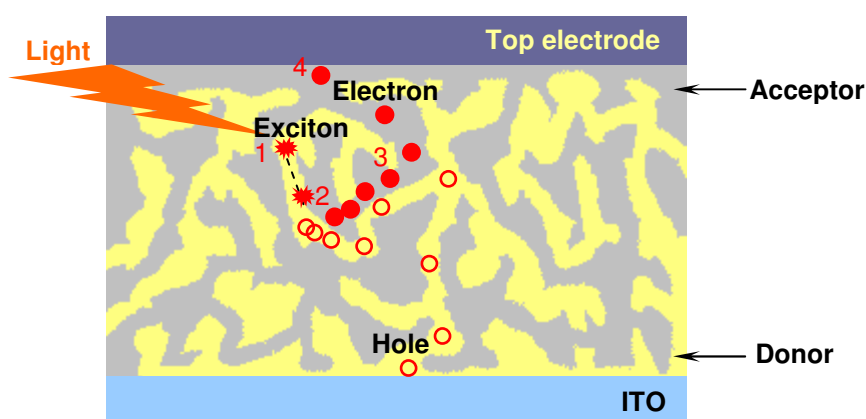


**Figure 2.2** *Fundamental processes in an organic solar cell*

### 2.2.1 The Absorption of Photons and the AM1.5 G Solar Light

The optical property of the active layer containing the donor and acceptor is of prime importance in determining the efficiency of a solar cell. A good material should have a large spectral overlap with solar irradiation. Since solar radiation reaching the earth's surface varies significantly with location, atmospheric conditions including cloud cover, aerosol content, ozone layer condition, time of day, earth/sun distance, solar rotation and activity, a standard spectrum has to be decided to provide a basis for theoretical evaluation of the effects of solar radiation and as a basis for simulator design. These standard spectra start from a simplified (i.e. lower resolution) version of the measured extraterrestrial spectra, and use sophisticated models for the effects of the atmosphere to calculate terrestrial spectra. The most widely used standard spectra are those published by the Committee International d'Eclairage (CIE), the world authority on radiometric and photometric nomenclature and standards. The conditions for the AM 1.5 spectra were chosen as the standard, as illustrated in Figure 2.3.

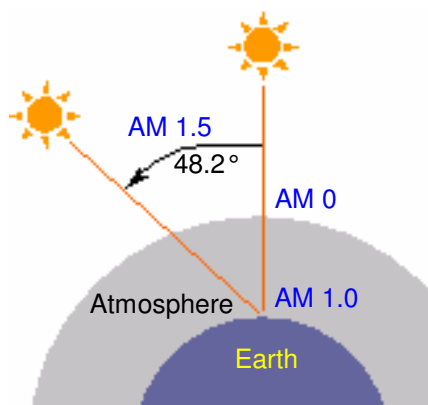


**Figure 2.3** The illustration of AM 1.5 Global solar light.

As shown in Figure 2.4, the maximum solar irradiation is at 480 nm and 70% of photons are located in the range of 400-1000 nm. For organic materials with absorption up to 600 nm, only 30% of photons could be absorbed at the most. For those with an expanded absorption spectrum to 800 nm, the percentage is doubled to about 55%. The spectra of a few of the widely used donor and acceptor materials are shown for comparison.

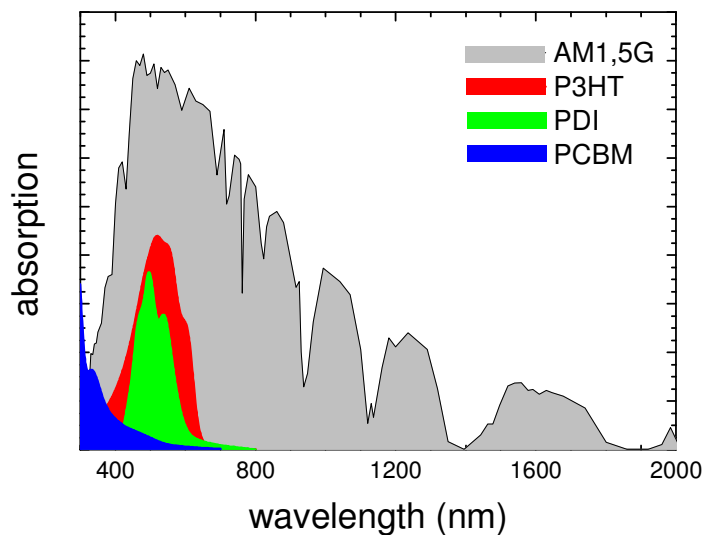
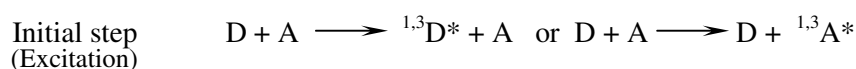


**Figure 2.4** Absorption spectra of some common materials in comparison with the standard AM 1.5G solar light.

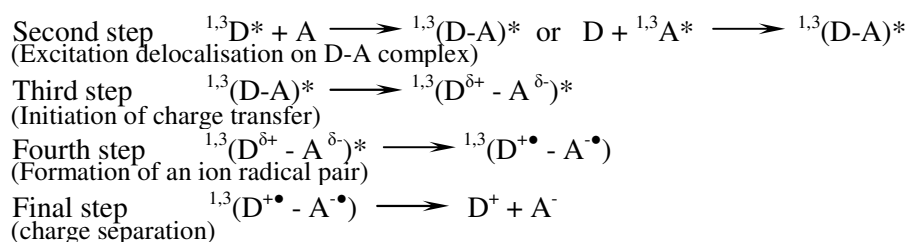
To put it simply, the idea is to match the UV absorption of the material with the solar irradiation as well as possible. The larger the overlap with the strongest emission parts of the solar spectrum, the greater the number of photons that can contribute to the photocurrent.

### 2.2.2 Exciton Diffusion and Charge Separation at the D/A Interface

Light absorption in organic materials results primarily in the production of excitons rather than free electron-hole pairs because of the low dielectric constant of the organic phase and the weak Van der Waals forces between organic molecules.<sup>95,96</sup> The different processes occurring in the intra- or intermolecular photoinduced electron transfer in a donor-acceptor composite can be divided into several steps as outlined below for a clearer understanding.<sup>97</sup> Here <sup>1</sup> and <sup>3</sup> indicate that the excited state is respectively a singlet or triplet.







At each intermediate step, the process can relax back to the ground state by releasing energy in the form of emitted radiation or heat. Subsequent to the formation of excitons, they have to migrate to the D/A interface for charge separation before decaying radiatively or nonradiatively. This requires an intimate contact between the donor and acceptor on a scale determined by the diffusion length of the excitons. The optimal distance has been widely investigated by studying the spectral response from structured devices and from measurements of absolute photoluminescence efficiency of the blends. It was reported that in both polymer (PPV/PCBM) and discotic LC-based (Porphyrin/metal) systems the exciton diffusion length was in the range of 10 nm.<sup>98,99</sup> This value can be improved by a well-ordered arrangement of the organic moieties in the conducting materials.<sup>43,100</sup> It has been demonstrated that increased ordering of perylenediimide molecules leads to higher exciton diffusion lengths ( $\sim 2.5 \mu\text{m}$ ).<sup>101-103</sup> In the efficient D/A pair of pentacene/C<sub>60</sub>, a large exciton diffusion length (65 nm for pentacene and 40 nm for C<sub>60</sub>) was observed by means of depositing the organic material onto ITO in vacuum.<sup>104</sup> Nevertheless, this rather small value requires phase separation of the D/A to be on the nano-scale, and so a bulk heterojunction is preferable to a bilayer. Each type of charge carriers is transported in a separate phase - electrons in the acceptor (e.g. PCBM) and holes in the donor (e.g. PPV). So the phase separation, which is reflected in the observable morphology of the thin film, is decisive for establishing the charge transport paths, as will be discussed further in section 2.3.

In step 3, the symbol  $\delta$  denotes the fraction of charge transferred, continuously in the range between  $0 < \delta \leq 1$ , where  $\delta = 1$  is the state where the whole electron has been transferred. For the formation of the ion radical pair in step 4, certain conditions must be fulfilled:

$$I_{\text{D}^*} - A_{\text{A}} - U_{\text{C}} < 0$$

These conditions concern the ionization potential  $I_{D^*}$  of the excited state of the donor, the electron affinity  $A_A$  of the acceptor, and the attractive Coulomb force of the separated radicals  $U_C$ , including polarization effects. In the case of charge transfer from a donor polymer to a neighboring acceptor molecule, a stabilization of the photoinduced charge separation is possible through carrier delocalisation on the cation radicals  $D^{+\bullet}$  (polarons) along the polymer chain and a structure relaxation of the anion radicals  $A^{\bullet-}$ . Except for energetic requirements, the transport properties of the excitons have to be considered for successful charge separation, which will be discussed further in section 2.2.3. The process described here is summarized in a schematic drawing of the energy levels in a D/A couple (Figure 2.5).

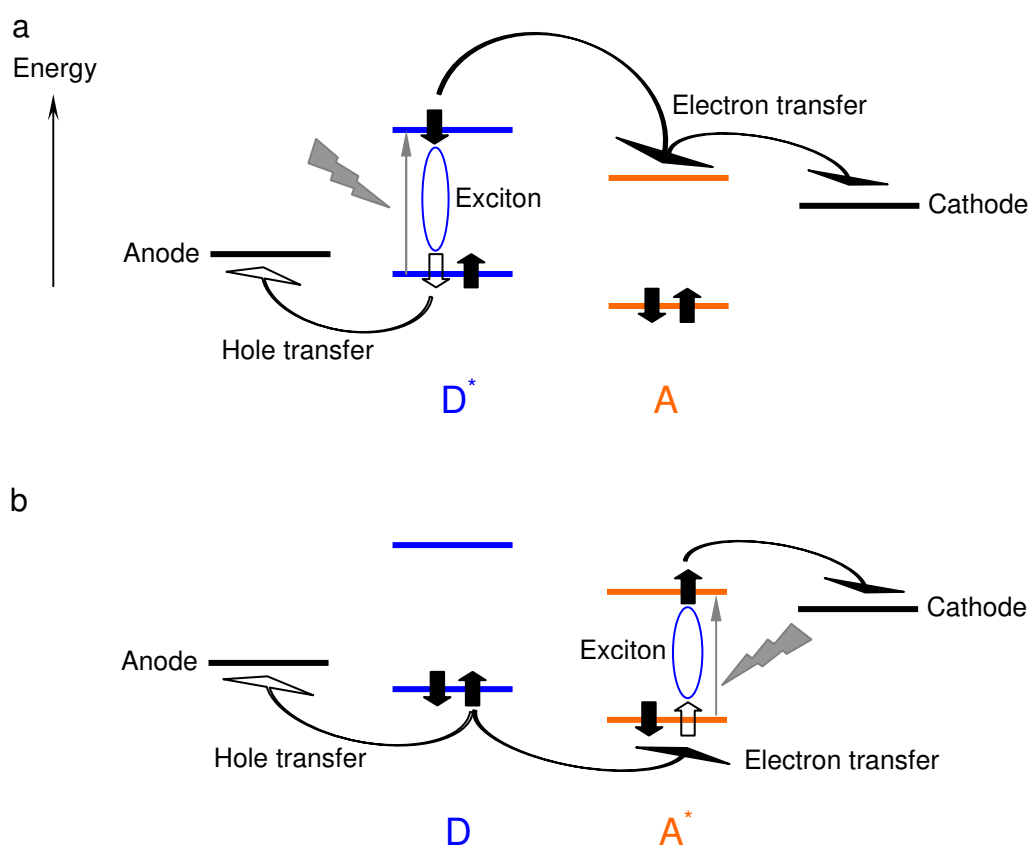


**Figure 2.5** Illustration of charge generation and transfer at the D/A interface: a)  $D^* + A$ , and b)  $D + A^*$

The rate of the charge transfer in the first case ( $D^* + A$ ) depends on the potential difference between the LUMOs of the donor and acceptor ( $\Delta L$ ) as expressed by Marcus theory.

$$k_{CT} = A \exp [-(\lambda_c + \Delta L)^2 / 4\lambda k_b T]$$

where  $\lambda_c$  is the coupling (or reorganization) energy, which can be seen as the energy required to reorganize the system and the solvent prior to charge transfer  $k_b$  is the Boltzman constant and  $T$  the temperature. This relation links the rate constant to a thermodynamical value of  $\Delta L$  (Figure 2.6).

$\Delta\phi$  is the potential difference between the HOMO of the donor and the LUMO of the acceptor. It has been reported that the open circuit voltage  $V_{oc}$  is a function of acceptor strength in conjugated polymer/fullerene system using a series of highly soluble fullerene derivatives with a variation of almost 200 mV in their first reduction potential.<sup>105,106</sup> The values of  $V_{oc}$  increase from 0.55 V up to 0.82 V for the device having the largest  $\Delta\phi$ . This indicates a large potential difference ( $HOMO_D-LUMO_A$ ) is needed for achieving high  $V_{oc}$ . This can be realized by increasing the LUMO of the acceptor or decreasing the HOMO of the donor. However, this has to be carefully modulated since the former will affect  $k_{ET}$  and the latter will reduce light absorption by increasing the bandgap.

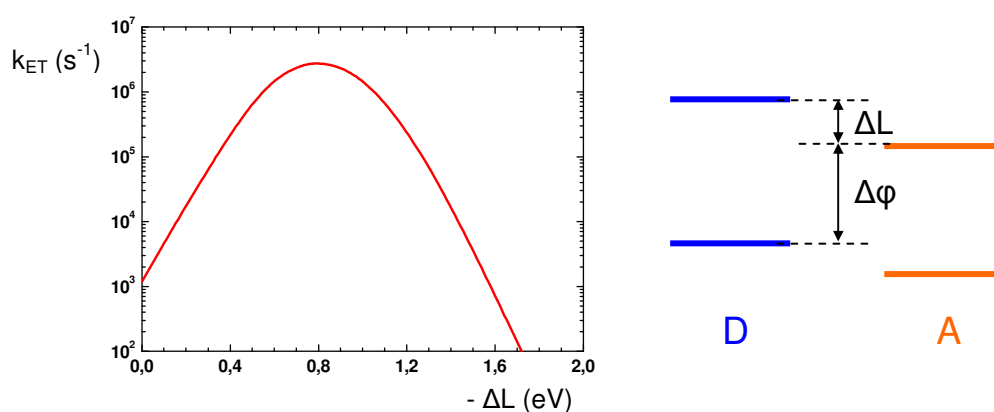


**Figure 2.6** Marcus curve and the potential diagram of a D/A pair

The exciton splitting results in a charge transfer from an excited donor to an acceptor with an energetically favorable LUMO level, or an electron transfer from the donor to the HOMO of an excited acceptor. Hence, the hole remains on the donor and free charges are created. In a donor-acceptor system formed by a conjugated polymer acting as electron donor and buckminster fullerene as the electron acceptor, a charge transfer time below 100 fs has been measured.<sup>29</sup> While in such composites the forward electron transfer time is remarkably fast, back transfer is seriously hindered, resulting in metastable charge separated states with lifetimes on the order of microseconds and an internal quantum efficiency close to 100%.

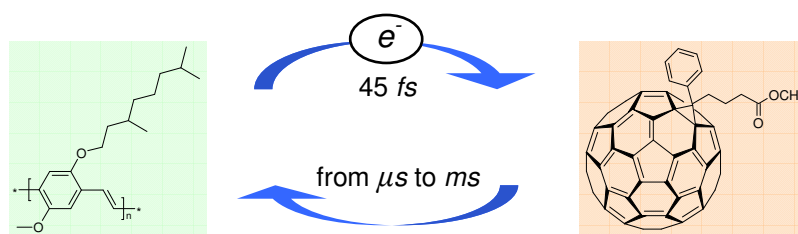


**Figure 2.7** An example of charge transfer in MDMO-PPV/PCBM system

### 2.2.3 Charge Transport

Charge transport in organic solar cells is one major factor limiting their efficiency because of the relatively low charge carrier mobility comparing with inorganic materials. Therefore, the thickness of the active layer has to be sufficiently small in order to allow an efficient charge transport to the electrodes.<sup>107</sup> As a result, the incident light cannot be absorbed completely by the thin layer and the material with strong absorptivity is required for fabricating devices, which is supplemented to the section 2.2.1.

The charge carrier mobility  $\mu$  is used to describe the charge transport ability in the two different phases. By using pulse radiolysis time-resolved microwave conductivity (PR-TRMC) method it is possible to determine the charge carrier mobility on a nanometer length scale (interface effects caused by electrodes are avoided and electric field effects are minimized, so traps caused by structural defects and impurities are far less disruptive). It is very important to emphasize that the charge carrier mobility determined by this technique provides different information from techniques such as time-of-flight (TOF) or field-effect

transistor (FET) experiments. The PR-TRMC technique reveals only the intrinsic or local mobility of charge carriers which migrate only between several molecules, whereas the mobility in the bulk, which are obtained by the TOF and FET experiments, is usually lower due to a higher degree of disorder and possible trapping sites at grain boundaries. These latter values are strongly dependent also on the long-range order of the sample, which can be affected by different processing techniques. The charge carrier mobility revealed by the PR-TRMC technique can be considered as the maximum possible values.

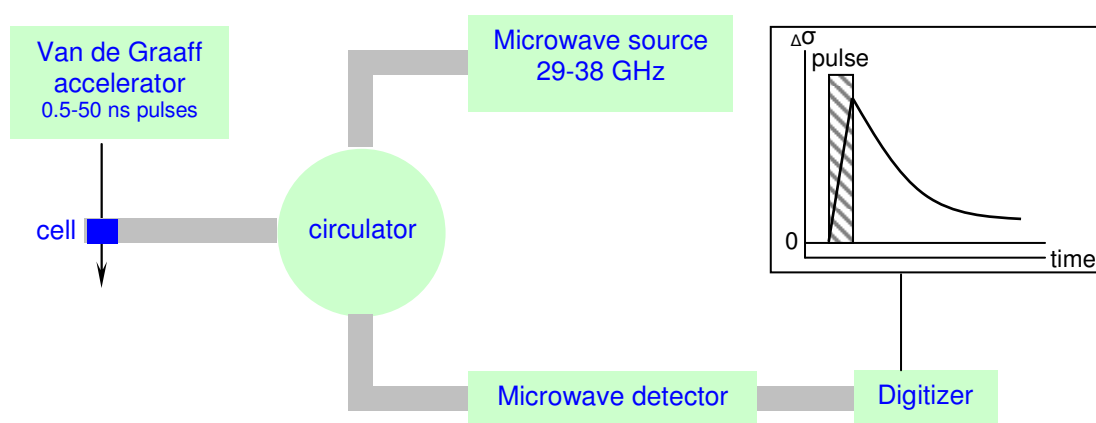


**Figure 2.8** A simplified schematic of the PR-TRMC equipment.

**Table 2.1** The electron/hole mobilities of some of the most widely used materials in PV devices

Material	Electron/Hole Mobility ( $\text{cm}^2/\text{V.s}$ )			
	FET	Lit.	TR-PRMC	Lit.
$\text{C}_{60}$	$8 \times 10^{-2} - 3 \times 10^{-1}$	108		
Perylene			0.2 (Cryst.)	
Poly (3-hexylthiophene)	$10^{-1}$	12		
Triphenylene			0.01-0.2	110
Porphyrin			0.2-0.4	111
Phthalocyanine	$2 \times 10^{-2}$	109	0.1-0.6	110-112
HBC	$10^{-2}$	66	0.2-1.0	110, 113, 114

For PR-TRMC measurements the sample is ionized by a nanosecond pulse (0.2- 50 ns) of high-energy electrons (3 MeV) to generate nearly uniform (known concentration) charge carriers throughout the sample. If the charge carriers formed are mobile, this results in an increase in the conductivity of the sample which is monitored with nanosecond time-resolution as a transient decrease in the power of microwaves which propagate through the irradiated medium. The magnitude at the end of the pulse indicates the concentration of carriers formed and their mobility. Some mobility values of the widely applied material are listed in Table 2.1.

#### **2.2.4 Charge Recombination**

The large interfacial area between the donor and acceptor phase in a bulk heterojunction solar cell allows for very efficient charge separation. However, in this morphology one can also expect high recombination losses in the bulk. Those electrons and holes, which have been generated and which do not flow out of the active layer to contribute to an electrical current, must eventually recombine. The recombination can be either radiative or non-radiative. In a radiative recombination process, a photon is emitted to carry the energy, which cannot be prevented without suppressing the ability to absorb light.

In non-radiative recombination, the energy of a recombining electron-hole pair ends up in increased vibrations of the constituent atoms. These vibrations, called phonons, are quantized and have energies in the order of 10 meV. This is much smaller than the energies of electron-hole pairs, which are typically in the range of 1-3 eV. Many phonons must, therefore, be generated simultaneously to take up the energy of the electron-hole pair. The generation of phonons often requires energy states within the energy gap, which cannot be avoided at the metal/organic interface in an organic solar cell. Metals have a continuum of states below and above the Fermi energy, which aligns with the Fermi energy of the adjacent semiconductor. These thus lie within the energy gap and recombination probabilities at the interface with the contacts are very large as a consequence. A strategy for avoiding excessive interface recombination at the contacts is to retain one type of photogenerated carrier, either electrons or holes, at a distance from the contact interface. To realize this, a thin layer of an additional semiconductor – poly(3,4-ethylenedioxythiophene) complexed with poly(4-styrenesulfonate) (PEDOT:PSS) - can be used between the anode and the organic layer to prevent direct contact of electrons and the

anode. The presence of impurities and lattice defects, which give rise to states in the energy gap, should also be avoided to prevent charge recombination.

The charge recombination within the organic film is limited by the diffusion of positive polarons towards negatively charged acceptor, as studied by Nelson in the PPV/PCBM system.<sup>115</sup> Polaron transport can be described as diffusion which is mediated by trapping and release from a limited number of deep traps. Polarons are thermally activated and move into the next available neighboring site over a barrier set at the HOMO level. Assuming a constant density of traps that are always filled with one type of charge carriers, the recombination rate will be proportional to the density of free charge carriers of the opposite charge. For a device with a P3HT/PCBM blend, the short circuit current showed a relatively linear dependence for light intensities up to 100 mW/cm<sup>2</sup>. This proves that trap-mediated recombination is the dominant recombination path in such devices.<sup>116,117</sup>

### 2.2.5 The Organic Semiconductor/Metal Contact

The contact properties determine the efficiency of charge injection and collection at the electrodes, and hence influence the performance of PV devices. However, understanding and describing the influence of electrodes with different work functions on the performance of organic semiconductor devices is still a challenging exercise.

The organic/metal contact can be understood as a mismatch between strong metallic bonds in the electrodes and weak Van der Waals forces in organic semiconductors. Schottky Contact has been introduced as a model to describe the semiconductor/metal contact.<sup>118</sup> According to quantum mechanics, carriers can tunnel through a barrier under high electric fields. In the case of an *n*-type semiconductor contacted with a metal (Figure 2.9a), whose Fermi-level is close to the LUMO level of the semiconductor, hole injection from the semiconductor to the metal is energetically favorable. Similarly, electron injection from the *p*-type semiconductor to the metal, whose Fermi-level is close to the HOMO level of the semiconductor, is preferred (Figure 2.9b).

The Schottky contact is characterized by a bending of the semiconductor energy levels due to an alignment of the Fermi energies of the two components. The bending will occur only within a few nanometers distance from the interface.<sup>119</sup> The bands inside the bulk show a linear behavior except for the strong band bending near the interface.

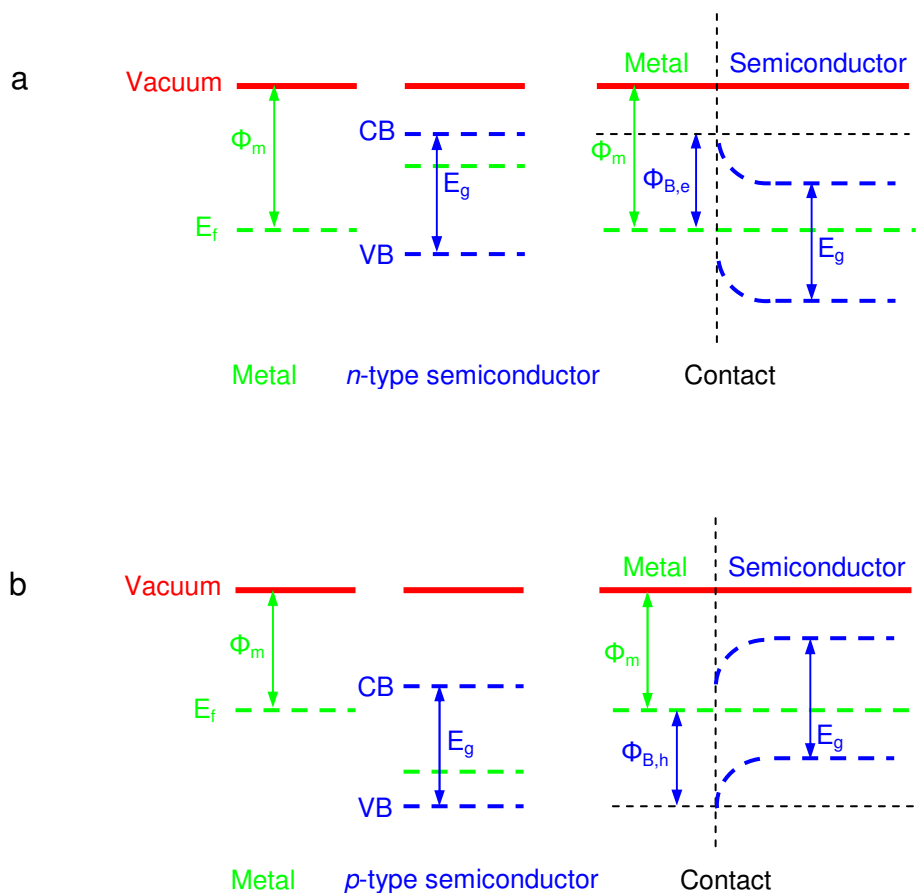


**Figure 2.9** Schottky contact at the a) *n*-type semiconductor/metal interface and b) *p*-type semiconductor/metal interface.

## 2.3 Film Morphology

As discussed before, when the bulk heterojunction concept is applied to organic solar cells, problems arise from charge separation at the D/A interface and charge transport along separate percolation pathways. The morphology of such ‘blend’ films thus becomes important since it directly describes the phase separation of the two components. It is clear that when two different materials are blended together, phase separation is likely to occur. The driving force is thermodynamical, namely when the materials are mixed, they do not gain enough entropy to yield a negative free energy of mixing, and thus mixing does not happen spontaneously. Given enough time to reach equilibrium, the blend demixes and



forms separate coexisting phases, with different compositions, consisting dominantly of one of the blend components. However, when the blend is not given enough time to complete the phase separation, for example in the most widely used film forming method – spin-coating (within seconds), an intermediate state of mixing is frozen into the solid state, giving rise to the typical morphology of a blend.

There are two main ways to effect phase separation in a blend: temperature quenching and solvent quenching. In solvent quenching, the materials are dissolved in a common solvent and form a homogeneous solution, which phase separates when the solvent evaporates from the solution. This often happens during the preparation of thin films by spin coating, drop casting, etc. This was observed by Shaheen and co-workers when fabricating devices based on MDMO-PPV/PCBM (1/4).<sup>30</sup> They used either toluene or chlorobenzene (CB) as solvent to form solutions for spin coating. The film prepared from toluene (RMS roughness ~ 10 nm) is much rougher than that from CB (RMS roughness < 1 nm), and a red-shift was further found in the MDMO-PPV absorption of the CB-cast film. Although the devices prepared from different solvents showed a similar open circuit voltage of ~0.82 V, larger short circuit current and fill factor was found in devices using CB-cast films, leading to an overall efficiency of 2.5% for CB-device and 0.9% for devices prepared using toluene-cast films. The internal morphology of the film was investigated by using scanning electron microscopy (SEM) and atomic force microscopy (AFM). Martens compared films cast from CB solution and toluene solution at different ratios of MDMO-PPV/PCBM (1:1, 1:2, and 1:4)<sup>120-122</sup> and found films from toluene solutions formed a uniform matrix at 1:1 ratio, while phase separation was observed for 1:2 and 1:4 ratios. Films from CB solution were also found to be homogeneous at 1:1 and 1:2, but phase separation was observed at the 1:4 ratio. It was concluded that the composition of the matrix depends on the solvent since CB permitted the incorporation of more PCBM in the matrix. The higher amount of acceptor in the matrix could explain why devices using films cast from CB are generally more efficient than devices cast from toluene. This work thus indicates that a homogeneous film with a large D/A interface is preferable in polymer/PCBM systems.

Temperature quenching means that a homogeneous blend is driven into the two-phase region of the phase diagram by variation of the temperature, corresponding to temperatures above the glass transition temperature,  $T_g$ , or the phase transition temperature. This would lead to phase separation closer to the equilibrium state, and develop self-organization or crystallization in separate domains. This was observed in P3HT/PCBM (1:1) film after annealing for 5 min at 80 °C.<sup>123,124</sup> The crystalline fibrils of P3HT were

formed due to a more ordered packing of the polymer chains, showing an enhancement of the hole mobility from  $0.0056 \text{ cm}^2\text{V}^{-1}\text{s}^{-1}$  (before annealing) to  $0.044 \text{ cm}^2\text{V}^{-1}\text{s}^{-1}$  (after annealing). The best efficiency of 4.4% was achieved by optimizing the annealing procedure at  $140 \text{ }^\circ\text{C}$  for 2 h.<sup>38</sup> A similar phenomenon was observed for a film of PPV/PCBM, where PCBM crystals grow with depletion of PCBM from surrounding areas during annealing.<sup>125</sup> Schmidtke combined a kind of soft lithography technique using elastomeric polydimethylsiloxane (PDMS) stamp with annealing to control the morphology of HBC/PDI film.<sup>126</sup> The PDMS stamp adheres to the film, forming a flat, top-surface, which is utilized during annealing and then easily removed. An improved performance was achieved resulting from large crystalline domains following annealing, and also from the low surface roughness and greater vertical stratification of the components in the bulk.

Except for the temperature quenching and the solvent quenching discussed above, a novel method to control the phase separation in polyfluorene photovoltaic devices was recently reported by Scherf using miniemulsion process.<sup>127</sup> This opened new ways to study the influence of the layer composition on the solar cell performance.

It has been shown that the control of film morphology is crucial in enhancing device performance. Investigation of thin films of active materials/blends thus provides insights into how to optimize photovoltaic devices using them.

## Chapter 3 Experimental Methods

The experimental methods, which are used in this work to investigate the properties of the organic material in solution and/or in solid state, are described below. The fabrication and characterization of photovoltaic devices are introduced at the end of this chapter.

### 3.1 Spectroscopy

#### 3.1.1 Absorption Spectra

The Ultraviolet-visible absorption spectroscopy is used for the detection and quantitative measurement of chromophores that undergo electronic transitions between different vibrational levels of the ground and excited states. The absorption obeys Beer's law:

$$A = \varepsilon l c$$

$A$  is absorbance,  $\varepsilon$  is the molar absorptivity with units of  $\text{Lmol}^{-1}\text{cm}^{-1}$ ,  $l$  is the path length of the sample, and  $c$  is the concentration of the compound in solution. The factor  $\varepsilon$  is an absolute value relative to wavelength, so is used to compare the ability of light absorption for materials used in photovoltaic devices. Since the strongest emission part of the solar light lies at 450-1100 nm, a high value of  $\varepsilon$  in this range is desired.

For measurements, a Perkin Elmer, Lambda 900 spectrometer was used. The sample was prepared in solution using chloroform as solvent, from which the absorptivity  $\varepsilon$  was calculated, or as thin film spin-coated from a concentrated solution with a thickness of about 100 nm.

### 3.1.2 Photoluminescence Measurements

The quenching of photoluminescence (PL) (usually from the donor material) in a thin film of the dono-acceptor blend is used to evaluate the efficiency of charge transfer from donor to the acceptor. Since charge separation prevents radiative decay, a high quenching efficiency is thus indicative of efficient charge separation which is needed for an efficient solar cell. This method thus gives an indication whether two materials can potentially be paired as a donor and an acceptor.

The sample was spin coated on quartz substrates and tested using PL system J&M TIDAS. A tungsten-halogen lamp was used as the light source, with a laser prism to split the light into a coaxial laser reference beam and a servo quadrature beam.

## 3.2 Cyclic Voltammetry

Cyclic voltammetry is a dynamic electrochemical method in which the potential applied to an electrochemical cell is scanned and any resulting changes in the cell current are monitored to yield a cyclic current response indicative of the redox (reduction and oxidation) properties of the material under study. This technique is used to determine the HOMO and LUMO levels of organic thin films, which are calculated from the onset values of the oxidation peak in the positive scan and the reduction peak in the negative scan.

$$\text{HOMO} = (E_{FOC} - E_{\text{ons}}^{\text{ox}} + E_{FOC}^{\text{measure}}) \text{ eV}$$

$$\text{LUMO} = (E_{FOC} - E_{\text{ons}}^{\text{red}} + E_{FOC}^{\text{measure}}) \text{ eV}$$

$$E_g = |\text{HOMO} - \text{LUMO}| \text{ eV}$$

Here,  $E_{FOC}$  is the standard potential energy level of Fc/Fc<sup>+</sup> redox couple with a value of -4.8 eV with respect to the vacuum level, which has been defined as zero.<sup>128,129</sup>  $E_{\text{ons}}^{\text{ox}}$  and  $E_{\text{ons}}^{\text{red}}$  are the onset values extracted from the CV data as shown in Figure 3.1.  $E_{FOC}^{\text{measure}}$  is the potential value measured under the same conditions, as the calibration standard for the system.

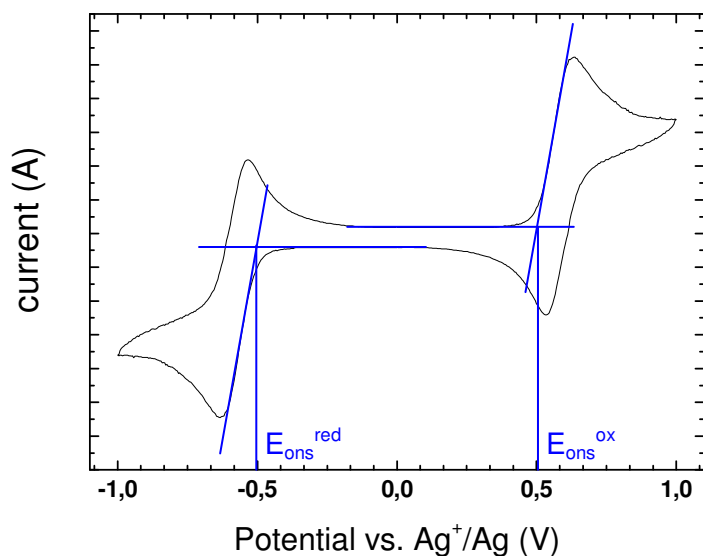


**Figure 3.1** A typical CV curve with the onset values.

If the reduction peak or the oxidation peak is missing, the band gap can be estimated from the onset of absorption in the solid state UV-Vis spectrum. It should be noted that this optical bandgap may not equal the electrochemically measured bandgap.

$$E = hv \text{ and } v = c/\lambda, \text{ so } E_g = hc/\lambda$$

Since,  $h = 6.626 \times 10^{-34}$  J.s,  $c = 3 \times 10^8$  m/s, and  $1 \text{ eV} = 1.602 \times 10^{-19}$  J,

So,  $E_g = (1241/\lambda) \text{ eV}$ , where  $\lambda$  has a unit of nm.

The measurements were performed on a Voltametric Analyzer (AutoLab PGSTAT-30, Potentiostat/Galvanostat) in a three-electrode cell with a working electrode of indium-tin-oxide (ITO) glass (sheet resistance of  $20 \Omega/\text{square}$ ), a silver quasi-reference electrode (AgQRE, calibrated with the Fc/Fc<sup>+</sup> redox couple  $E^\circ = -4.8 \text{ eV}$ ) and a Pt counter electrode. Films were spin-coated on the pre-treated ITO glass. Tetrabutylammonium perchlorate (TBAClO<sub>4</sub>, 0.1 M), and acetonitrile were used as the electrolyte and solvent, respectively.

### 3.3 Microscopic Techniques

#### 3.3.1 Atomic Force Microscopy

Atomic force microscopy (AFM) is also known as scanning force microscopy (SFM), which is a type of scanning probe microscopy with a very fine-tipped probe for scanning the surface. The essential feature of AFM is shown below.

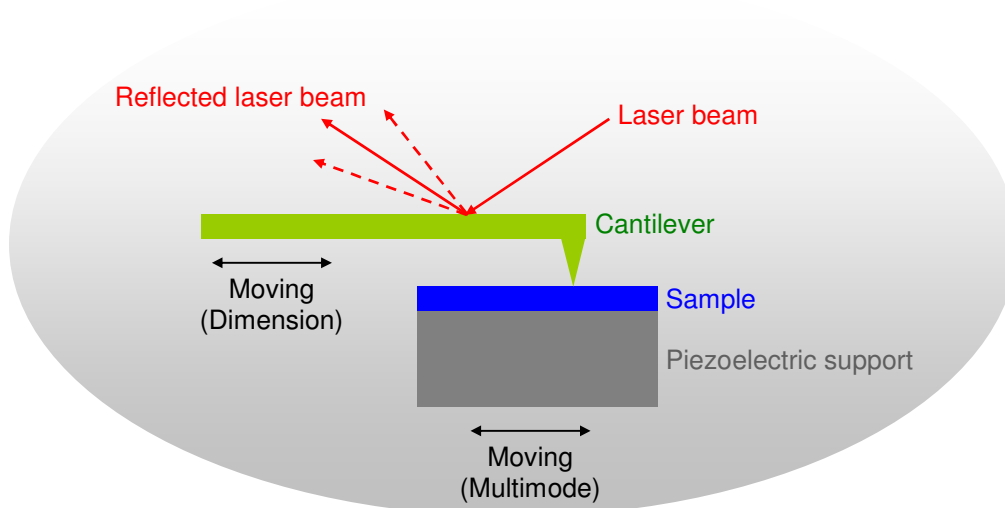


**Figure 3.2** Schematic diagram of an atomic force microscopy.

The tip of the probe, which is commonly made of silicon nitride, is attached to a cantilever bearing a reflective surface upon which a laser beam is directed. The sample is mounted on a piezoelectric support, which moves in response to surface variations sensed by the probe. As the tip is scanned over the surface, topological variations cause deflections in the cantilever that are monitored by recording the path of the reflected laser beam. A computer interprets the deflections as a three-dimensional profile of the polymer surface with resolution in the angstrom range, which is several orders of magnitude better than that obtained by scanning electronic microscopy (SEM).

There are three basic modes for AFM: contact mode, non-contact mode, and tapping mode. The contact mode microscopy gives an accurate image even at high speed scans since the tip has direct contact with the sample surface, but it also tends to destroy the sample. In non-contact mode, the probe operates in the attractive force region and tip-sample interaction is minimized. The tip does not contact the surface, so soft samples and even a liquid drop on some substrate can be observed by this mode without influencing the shape of the drop. In addition, this mode is the only AFM-mode that enables true atomic resolution.

The tapping mode is also known as intermittent contact mode. The cantilever oscillates close to or at the resonant frequency with an amplitude between 20 nm and 100 nm. The tip taps on the sample surface slightly during scanning, and only contacts it at the bottom of each swing. This technique is especially useful for imaging delicate and fragile samples, so that it is widely used in the investigation of the morphology of organic thin films.

In this work, tapping mode AFM (Multimode and Dimension 3100, Veeco) was used. The dimension 3100 microscope combines AFM and scanning tunneling microscopy (STM), which differs from AFM in that it measures the tunneling current between the tip and the surface. In dimension series microscopes, the samples remain stationary while the probe scans back and forth above them. Without limitation of the piezoelectric support, the dimensions of the sample can vary from millimeters to centimeters. The tapping mode cantilever is produced by Olympus, with type number OMCLAC 160 TS-W2 silicon. The observed samples were spin-coated on silica or ITO glass.

**Table 3.1** *Cantilever OMCLAC 160 TS-W2 silicon*

Resonance frequency (kHz)	300 (200-400)
Spring constant (N/m)	42 (12-103)
Tip Height ( $\mu\text{m}$ )	11 (7-15)
Tip radius (nm)	< 10
Tip thickness ( $\mu\text{m}$ )	4.6
Tip width ( $\mu\text{m}$ )	50
Tip length ( $\mu\text{m}$ )	160

### 3.3.2 Scanning Electron Microscopy

In scanning electron microscopy, an electron gun in a high vacuum emits a beam of high-energy electrons, which travels downward through a series of magnetic lenses designed to focus the electrons to a very fine spot. As the electron beam hits each spot on the sample, secondary electrons are knocked loose from its surface and detected to form an image with great depth of field and an almost three-dimensional appearance.

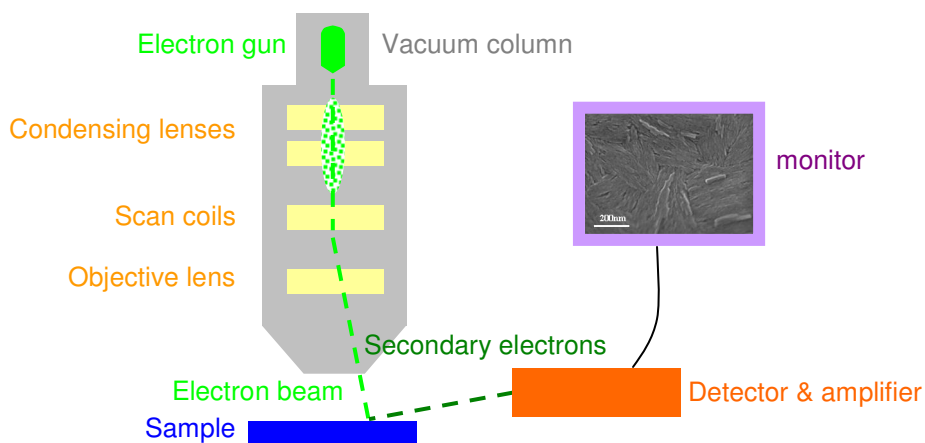


**Figure 3.3** Schematic diagram of scanning electronic microscopy.

In this study, SEM (LEO 1530 Gemini) was performed to observe both the surface and the internal morphology of thin films. The films were spin-coated onto silica wafers, so that it was easy to break them in half to observe the cross-section view of the sample. In case some of the materials had a phase transition near room temperature, the film was first immersed into liquid nitrogen, and then taken out and quickly broken in half. The fresh fractured side was subsequently observed by SEM.

### 3.4 X-ray



X-rays are generated in cathode-ray tubes when high-energy electrons impinge on metal targets. When X-rays are focused on a polymer sample (in pellet or cylinder form), two types of scattering occur. If a sample is crystalline, the X-rays are scattered coherently, that is, there is no change in wavelength or phase between the incident and scattered rays. Coherent scattering is commonly referred to as X-ray diffraction. If the sample has a non-homogeneous morphology, the scattering is incoherent and there is a change in both wavelength and phase. Incoherent scattering is referred to as diffuse diffraction or simply as scattering. Coherent scattering is determined by wide-angle measurements (WAXS) and incoherent scattering by small-angle measurements (SAXS).

The WAXS is usually applied to investigate the self-organization of organic materials. This diffraction pattern consists of a series of concentric cones arising from scattering by the crystal planes; it is recorded as concentric rings on the X-ray plate superimposed on a diffuse background of incoherent scatter. As the degree of crystallinity increases, the rings become more sharply defined, and if the crystallites are oriented (e.g. by drawing), the circles give way to a pattern of arcs and spots more nearly resembling diffraction patterns of low-molecular-weight crystalline compounds. Information on crystal dimensions, degree of crystallinity, and so on, can be gained from the diffraction patterns.

Powder X-ray diffraction experiments were performed using a Siemens D 500K Kristalloflex with a graphite-monochromized Cu K $\alpha$  X-ray beam, emitted from a rotating Rigaku RV-300 anode. 2-D WAXS measurements of oriented fibers were conducted using a rotating anode (Rigaku, 18kw) X-ray beam (CuK $\alpha$ , pinhole collimation, double graphite monochromator) with the beam perpendicular to the fiber axis and a CCD camera.

### **3.5 Differential Scanning Calorimetry**

Differential scanning calorimetry is used for quantitative studies of thermal transitions in polymers, in which a polymer sample and an inert reference are heated, usually in a nitrogen atmosphere, and thermal transitions in the sample are detected and measured. The sample holder most commonly used is a very small aluminum cup (gold or graphite is used for analysis above 800 °C), and the reference is either an empty cup or a

cup containing an inert material, such as anhydrous alumina. Sample sizes vary from 0.5 to about 10 mg.

The powder sample was measured by Mettler DSC 30 with heating rate 10 K/min in the range from -150 °C to 300 °C. This method combined with polarized optical microscopy (POM, Zeiss Axiophot optical microscope with a nitrogen flushed Linkam THM 600 hot stage) and X-ray is used to determine the phase changes within the material.

## 3.6 Fabrication and Characterization of Solar Cells

### 3.6.1 Device Fabrication

The fabrication of the device includes several steps:

- Etching of the ITO glass
- Cleaning of the substrate
- Spin-coating of the organic layer
- Evaporation of the top electrode

**Etching of the ITO glass.** Indium tin oxide (ITO, or tin-doped indium oxide) is a mixture of indium oxide  $\text{In}_2\text{O}_3$  and tin oxide  $\text{SnO}_2$ , typically 90%  $\text{In}_2\text{O}_3$  and 10%  $\text{SnO}_2$  by weight. It is transparent in thin layers and highly conductive, with an area resistance value below 20  $\Omega/\text{sq}$  at a thickness of 100 nm. The combination of transparency and conductivity makes ITO the most widely used electrode in photovoltaics.

To fabricate a solar cell, a defined working area, and thus patterned ITO, is required. The normal way to pattern ITO is to etch off the oxide using hydrochloric acid. The procedure is described in Figure 3.4.

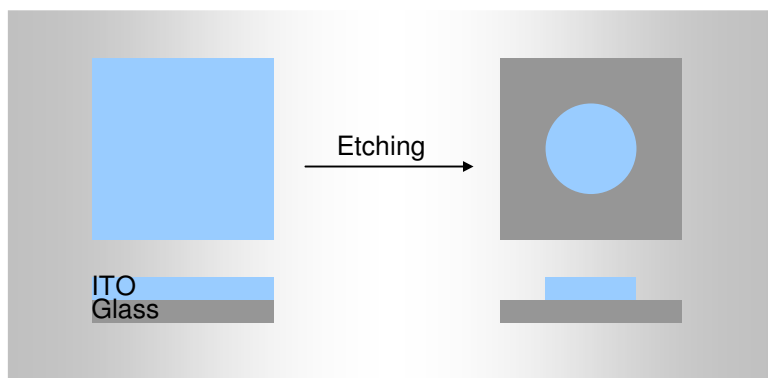


**Figure 3.4** *Patterning of ITO glass, the central part is protected and other parts are etched off.*

1. Ultrasonicate the partly protected ITO glass in a water bath with zinc powder (Aldrich, CAS 7440-66-6, 99.998%) for ~5-10 min.
2. Pour the water out, add HCl (2M), and ultrasonicate in a bath for 2 min.
3. Wash with water to dissolve the salts produced.

**Cleaning of the substrate** was done by successive washing twice with acetone, and then with isopropanol in an ultrasonic bath for 10 min each. The substrate was further cleaned in oxygen plasma for 10 min just before the spin-coating procedure.

**Spin coating of the organic layer** was done in a glove box to protect the organic material from all kinds of oxidation or degradation upon contact with water or oxygen. The solutions were prepared at a concentration of 5-20 mg/ml in chloroform, toluene, or chlorobenzene according to the solubility of the material and the thickness required. To prevent any dust or impurities, the solutions were filtered through a 0.45  $\mu\text{m}$  hydrophobic filter (Fisher, Millex 4 mm, PTFE) before spin-coating.

**Evaporation of the top electrode** was accomplished by evaporating silver or aluminium on top of the organic layer through a mask. The effective area of the device was approximately 6 mm<sup>2</sup> defined by overlap of etched ITO and the top electrode, which was accurately measured by an optical microscope for subsequent calculations. The evaporation was performed in an Edwards FL400 electron-beam evaporator (Boc. Edwards, Sussex, UK) at an evaporation rate of 5 nm/s.

The structure of the fabricated device is shown in Figure 3.5.

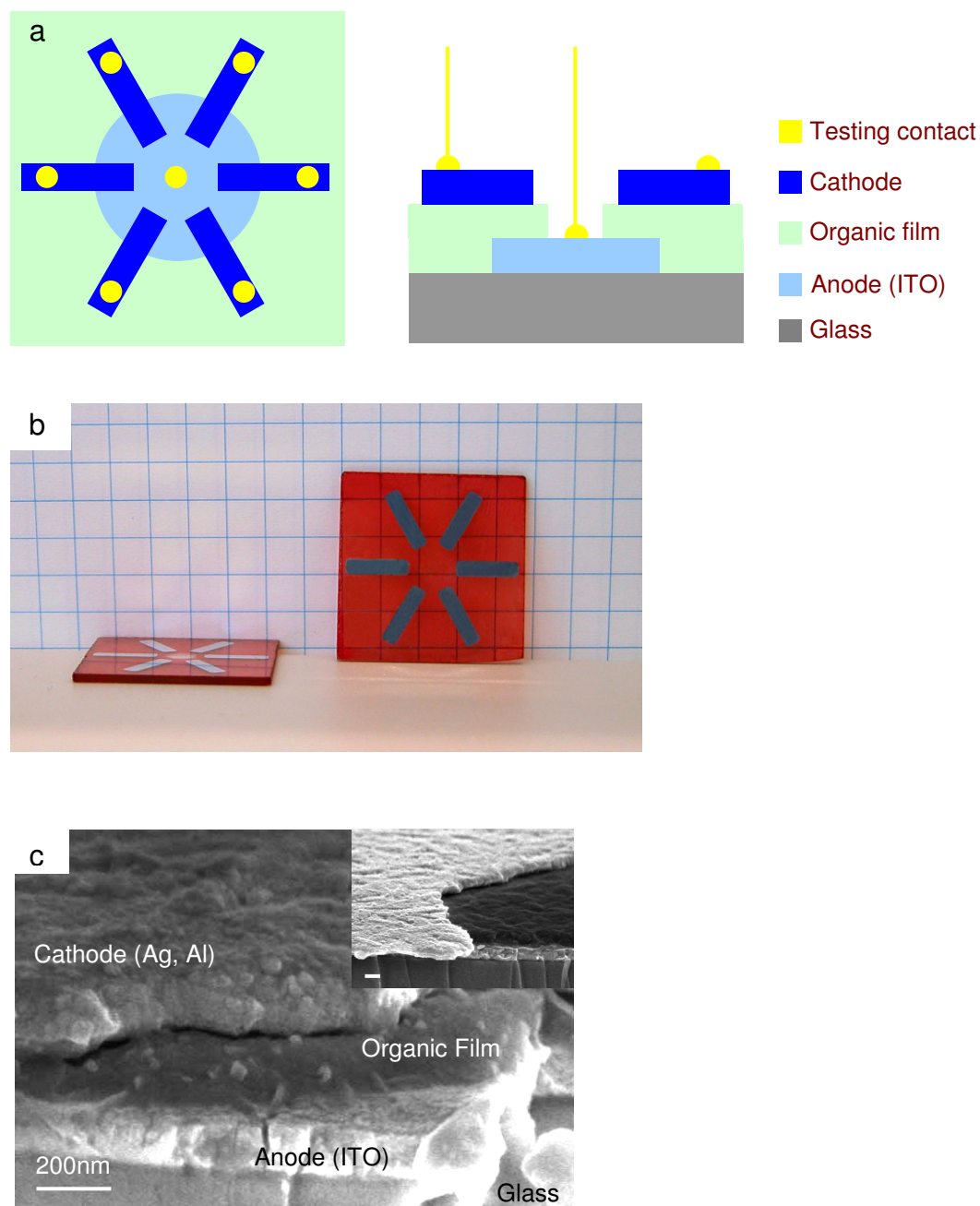


**Figure 3.5** a) Illustration of the device and the measuring strategy. b) A photograph of the fabricated device. c) The SEM image, which reveals the internal structure of the device.

### 3.6.2 Device Testing

The devices were tested in an ambient atmosphere of nitrogen. Two incident light sources were used in the testing, one is a halogen lamp source (A lampenhaus of model LSH-T100 housing a halogen lamp of 12 V, 100 W) with monochromator (Jobin Yvon GmbH, Triax 180) wavelength varying from 300 nm to 800 nm with maximum light intensity of  $6 \text{ W/m}^2$  at *ca.* 600 nm; and the other was a simulated solar light (Lichttechnik, Germany) using a 575 W metal halide lamp, in combination with an ODF filter, to produce a spectral distribution close to the global radiation AM 1.5G. The light intensity of the simulated solar light was set to 100-160  $\text{W/m}^2$ . The testing system is illustrated in Figure 3.6.

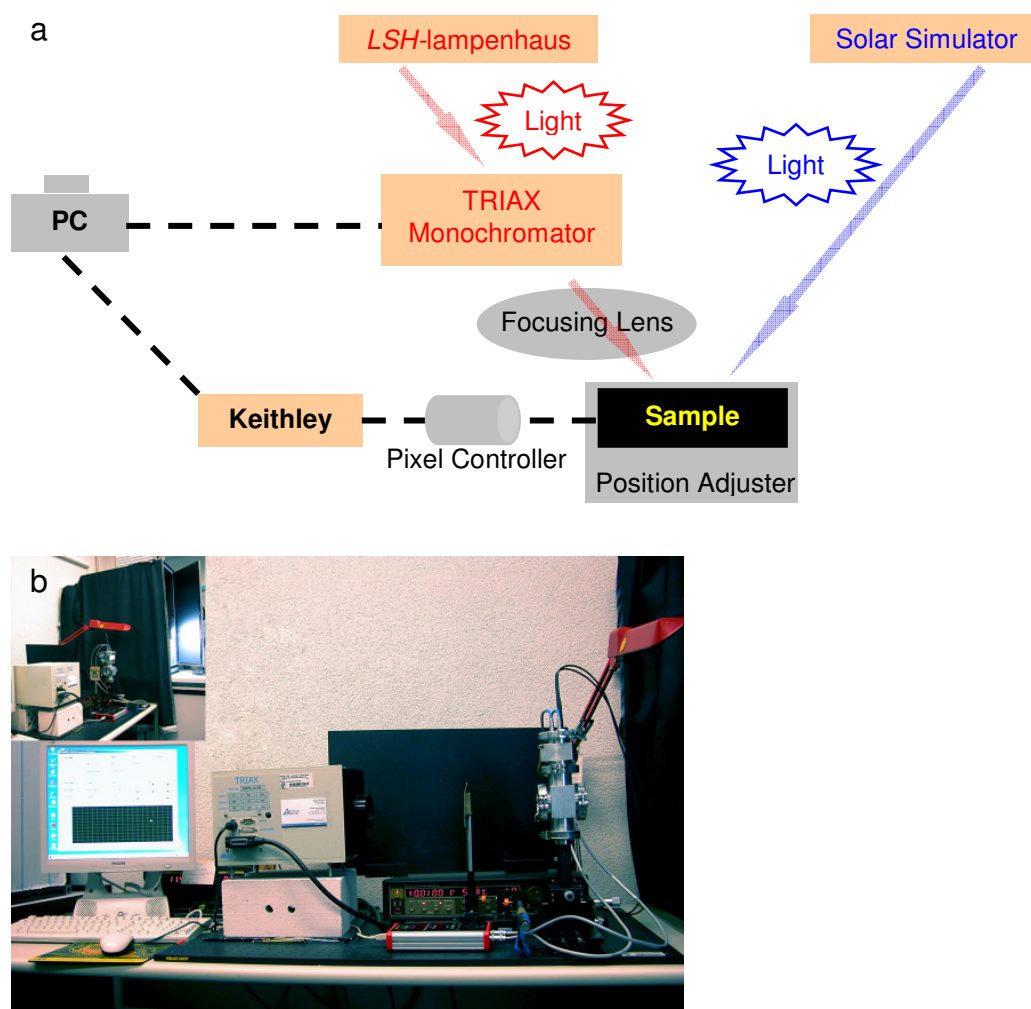


**Figure 3.6** a) The outline and b) a photograph of photovoltaic testing system used in this study.

Incident light was focused on the effective area of each device through a lens. Current-wavelength ( $I-\lambda$ ) curve and current-voltage (I-V) curve are recorded with a Keithley 236 Source-Measure Unit (Keithley Instruments Inc., USA). Two standard silicon diodes with known current-light intensity relationship were used to calibrate the incident light intensity: one for the calibration of the monochromatic light within the spectrum range from 300 nm to 800 nm; the other for the calibration of the simulated solar light with measuring range of 50~1000 W/m<sup>2</sup>. There are several universal parameters to describe the  $I-\lambda$  curve and the I-V curve, as describing in the following section.

### 3.6.3 Photovoltaic Parameters

#### 3.6.3.1 I- $\lambda$ Curve (EQE- $\lambda$ Curve)

The photocurrent- $\lambda$  curve was measured by recording the photocurrent response while continuously varying the wavelength of the incident light. An external quantum efficiency (EQE) was then calculated from the photocurrent to determine the efficiency of conversion of photons to electrons. EQE is defined as the number of collected electrons under short-circuit conditions, divided by the number of incident photons:

$$EQE = \frac{\text{Number of electrons}}{\text{Number of photons}} = 1240 \times \frac{I \text{ (mA/cm}^2\text{)}}{I_{inc} \text{ (mW/cm}^2\text{)} \times \lambda \text{ (nm)}} \quad (\%)$$

$$E_{electron} = -1.602 \times 10^{-19} \text{ (c)}$$

$$\# \text{ Electron} = Q / E_{electron} = I \text{ (A)} \times t \text{ (s)} / 1.602 \times 10^{-19} \text{ (c)}$$

$$E_{photon} = hc / \lambda = 6.626 \times 10^{-34} \text{ (J.s)} \times 3 \times 10^8 \text{ (m/s)} / 10^{-9} \text{ (m/nm)} \times \lambda \text{ (nm)}$$

$$= 1.9878 \times 10^{-17} / \lambda \text{ (J)}$$

$$\# \text{ Photon} = I_{inc} \text{ (W)} \times t \text{ (s)} \times \lambda / 1.9878 \times 10^{-17}$$

So,

$$EQE = \# \text{ Electron} / \# \text{ Photon} = 1240 \times I \text{ (A)} / I_{inc} \text{ (W)} \times \lambda$$

$$= 1240 \times I \text{ (mA/cm}^2\text{)} / I_{inc} \text{ (mW/cm}^2\text{)} \times \lambda$$

$I$  is the photocurrent and  $I_{inc}$  is the incident light intensity varied with the wavelength.  $I_{inc}$  is calibrated by measuring the photo response of a standard silicon diode with known  $I_{inc}$ - $I$  (incident light intensity - photocurrent) relationship.

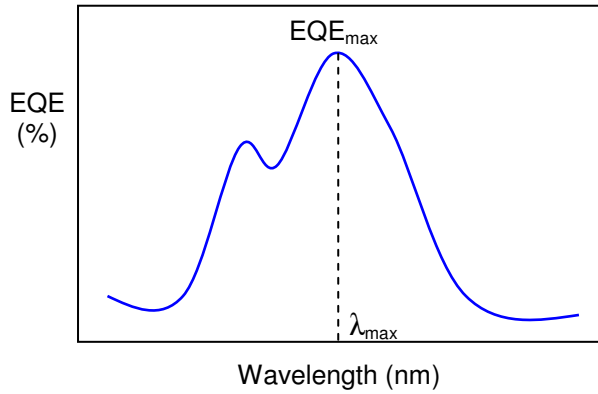


**Figure 3.7** *EQE-  $\lambda$  curve measured at monochromatic incident light.*

The maximum EQE is named as  $EQE_{max}$  (Figure 3.7), which is a key parameter for describing the device. The higher the  $EQE_{max}$ , the more efficient is the device.

### 3.6.3.2 I-V Curve

The I-V curve can be measured either at  $\lambda_{max}$  or under simulated solar light. The conditions for solar light used in this work are summarized in Table 3.2.

**Table 3.2** *Applied conditions for solar light as reference spectrum.*

Criterion	Value
Light intensity	100~160 W/m <sup>2</sup>
Sun spectrum	AM 1.5 G
Sample temperature	25°C

A typical I-V curve is shown in Figure 3.8.

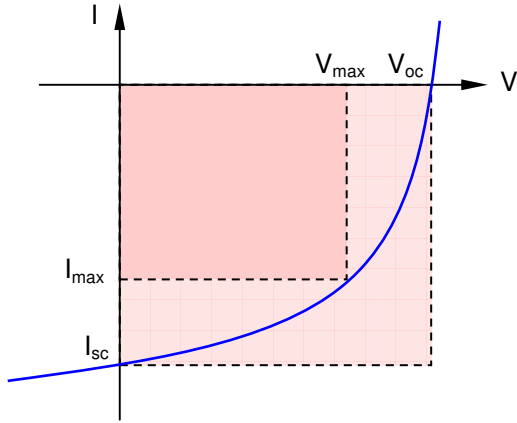


**Figure 3.8** A typical I-V curve.

Here,  $V_{oc}$  is the open-circuit voltage,  $I_{sc}$  is the short-circuit current, and  $V_{max}/I_{max}$  is defined by the maximum rectangular area under the I-V curve. The overall efficiency  $\eta$  of the device can be calculated as:

$$\eta = \frac{I_{out}}{I_{inc}} = \frac{I_{sc} \text{ (mA/cm}^2\text{)} \times V_{oc} \text{ (V)} \times FF}{I_{inc} \text{ (mW/cm}^2\text{)}}$$

The parameter FF is known as the fill factor, which is defined as:

$$FF = \frac{I_{max} \text{ (mA/cm}^2\text{)} \times V_{max} \text{ (V)}}{I_{sc} \text{ (mA/cm}^2\text{)} \times V_{oc} \text{ (V)}}$$

The maximum rectangular area under the I-V curve corresponds to the maximal output power of the device. An ideal device would have a rectangular shaped I-V curve and therefore a fill factor  $FF = 1$ . Usually the fill factor of organic photodiodes is over 0.25.

The overall efficiency is an important parameter to evaluate the performance of the device, and is the default efficiency value mentioned in the literature.



## Chapter 4 Application of Hexabenzocoronene (HBC) in Solar Cells

Discotic molecules have extensive molecular  $\pi$ -orbitals in which the electrons are delocalized. Due to the interaction between the  $\pi$ -orbitals of adjacent cores a one-dimensional pathway for charge migration along the columnar structures is possible. The peripheral substitution of the aromatic cores with long aliphatic hydrocarbon chains provides an insulation of the conducting core. In such cases one can regard these supramolecular structures as ‘nanowires’. The charge transfer takes place via hopping between localized states of neighboring aromatic molecules with assumed jump-time between 75 to 750 fs for HBCs in the mesophase.<sup>130</sup> The localization of the states in organic semiconductors, which leads to lower mobilities, has origins such as weak interactions between the single building blocks and disorder.<sup>131</sup> It was found that the charge carrier mobility in the hexagonal liquid crystalline phase is more dependent on the size of the aromatic core than on the cofacial distance between neighboring cores within the columnar stack. The mobility increases from 0.1 cm<sup>2</sup>/Vs for triphenylenes<sup>42,132,133</sup> over 0.7 cm<sup>2</sup>/Vs for phthalocyanines<sup>134-136</sup> up to 1.0 cm<sup>2</sup>/Vs for HBCs<sup>114</sup>, whereby the influence of the chain length on the charge carrier mobility becomes negligible for discotic compounds with larger aromatic cores. This relationship is explained by the increased  $\pi$ - $\pi$  interaction in the case of the larger aromatic cores leading to a more stable columnar structure thus increasing the intracolumnar charge transport. HBCs thus constitute one of the most promising donors among all reported discotic liquid crystalline materials.<sup>66,137</sup>

In this chapter, the morphology of the HBC-PhC<sub>12</sub>/PDI blend in the most successful previously reported device is investigated with an emphasis on the development of crystals of the N,N'-Bis(1-ethylpropyl)-3,4,9,10-perylenetetracarboxydiimide (PDI) acceptor with and without HBC. This is instructive for optimising the devices using PDI as acceptor. In order to determine a structure-performance relationship, a series of HBC derivatives, with different substituted alkyl/aryl chains, have been analyzed in the bulk phase with respect to optical absorption, redox behavior and supramolecular organization. The morphology of the donors and of the blends with the acceptor component have been investigated by

atomic force microscopy (AFM) and scanning electron microscopy (SEM), and the blends tested as active layers in solar cells. At the end of the chapter, a new HBC characterized by face-on arrangement is introduced as a potential active component in photovoltaic devices. This chapter thus expands the application of HBCs in photovoltaics with not only an introduction on new molecules but systematic investigations on morphology as well.

## 4.1 Introduction

Up to now, several HBC molecules (shown in Figure 4.1) have been reported for their applications in solar cells.<sup>43,62,127,138</sup> PDI has been used as acceptor material for the HBC molecules.

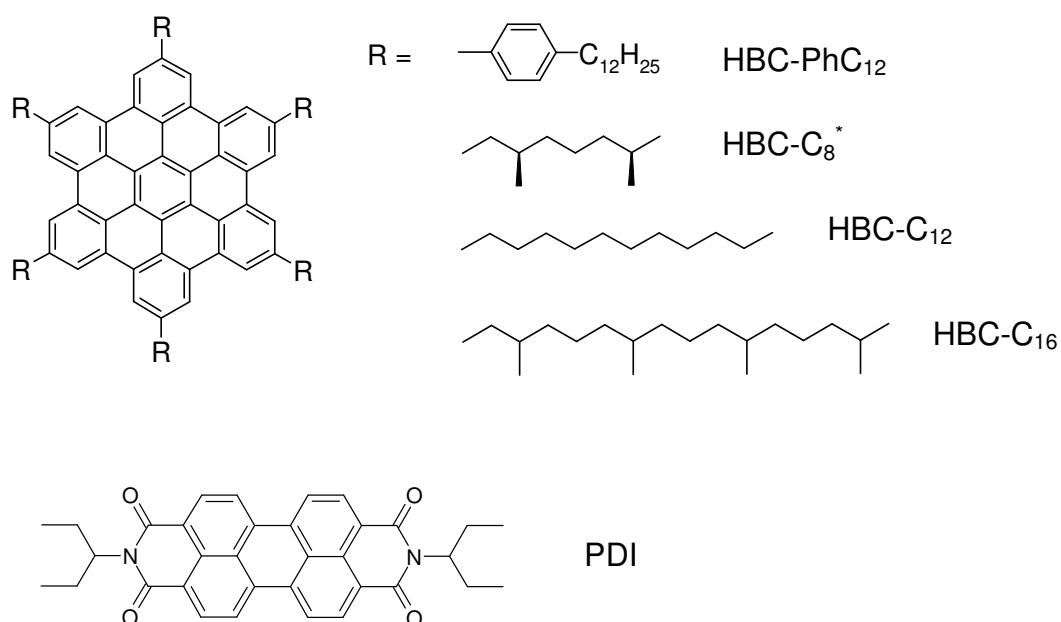


**Figure 4.1** Chemical structures of HBC molecules previously used in solar cells. PDI is adopted as acceptor material for HBCs.

Both HBC-PhC<sub>12</sub> and HBC-C<sub>16</sub> exist in columnar liquid crystalline phases at room temperature, while HBC-C<sub>8</sub>\* and HBC-C<sub>12</sub> with shorter alkyl chains are crystalline. The charge carrier mobility determined by PR-TRMC shows a higher value for HBC-C<sub>12</sub> (0.90 cm<sup>2</sup>/Vs) than for HBC-PhC<sub>12</sub> (0.22 cm<sup>2</sup>/Vs) since the former is in a more ordered phase at room temperature.<sup>42,139</sup> However, a liquid crystalline phase at room temperature supports better film formation. Therefore, a compromise between the chain-length, the intercolumnar distance, and the separation distance between donor and acceptor is required for the optimal performance of the device, that is, the larger the side chains the lower the phase transitions (i.e. LC phase already at RT) and the better the films, but at the cost of a larger D/A separation.

The most successful device was found for the pair of HBC-PhC<sub>12</sub>/PDI (4:6), which showed a maximum EQE of 34% at 490 nm, corresponding to an overall efficiency of 1.95%. The good performance is explained by the large interfacial area within the ‘bi-layer’ structure with PDI accumulating on the top and HBC at the bottom, which is formed during spin-coating procedure due to the different solubility and density of the two components. Devices based on HBCs are summarized in Table 4.1. For the other three HBCs, lower EQEs were observed. This can be attributed to their weaker intracolumnar organization because of the absence of additional phenyl units.<sup>63,140</sup>

**Table 4.1** Reported photovoltaic performance of HBC molecules

HBC:PDI (4:6)	EQE <sub>max</sub> (%)	I <sub>sc</sub> (μA/cm <sup>2</sup> )	V <sub>oc</sub> (V)	FF	η (%)	Literature
HBC-PhC <sub>12</sub>	34	33.5	0.69	0.40	1.95	43
HBC-C <sub>8</sub> *	19	3.4	0.46	0.33	0.10	62,138
HBC-C <sub>12</sub>	17	-	0.57	-	-	127**
HBC-C <sub>16</sub>	14	-	0.60	0.35	-	62,138

\*\* This device can reach EQE<sub>max</sub> = 30% with PDMS-annealing at 107 °C for 5 min.

Perylenediimide derivatives are known to support electron transport through the conduction band.<sup>141-144</sup> This feature, together with a strong absorptivity in the visible region of the spectrum and a high thermal and photochemistry stability, makes perylenediimide compounds promising candidates as *n*-type semiconductors in organic solar cells. Indeed,

since the successful introduction of the ‘Tang-cell’<sup>27</sup>, perylenediimide received extensive attention in photovoltaics,<sup>145-150</sup> especially as acceptor material for HBCs,<sup>43,62,138</sup> The structures of different substituted perylenediimide compounds are shown in Figure 4.2. Among these three compounds, only the device based on PDI showed high efficiency. The other two derivatives exhibited an EQE value lower than 5% while using HBC-PhC<sub>12</sub> as donor. This can be partly explained by the morphology. The crystallites in the films of *N*-(1-heptyloctyl)-perylene or tetraphenoxyperylene are much smaller than those in PDI films and cannot be seen in the blend devices anymore. It is supposed that either crystallization of the perylene is suppressed by the presence of HBC or the needles are covered by HBC.

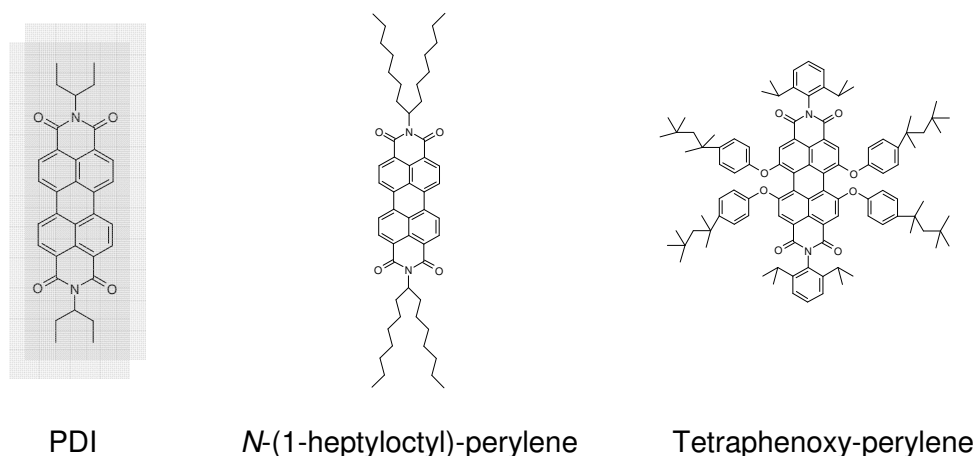


**Figure 4.2** Chemical structures of PDI molecules previously used in solar cells

To clarify this, a better knowledge on morphology is required, which is also instructive to understand how HBC and PDI perform in a solar cell. Based on the reported results, PDI is used as acceptor material for all the HBCs in the following study.

## 4.2 Photodiodes based on HBC-PhC<sub>12</sub>

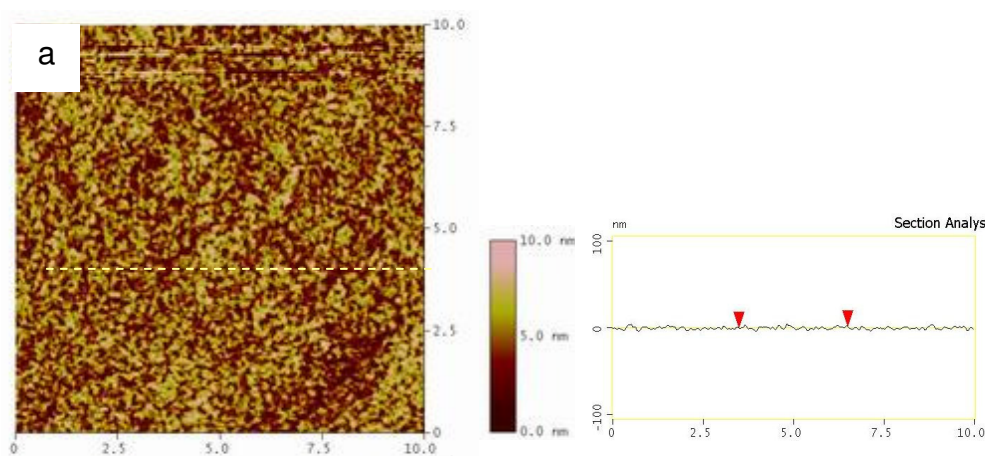
The devices based on HBC-PhC<sub>12</sub> have been shown to be the best donor material among the reported HBCs, and hence it was chosen as the model compound in this work

for further studies on morphology of the films and thermal treatment of the devices, which serve as a way to optimize the performance of solar cells. The investigation on morphology starts with the film forming ability of the two materials followed by an observation on PDI crystallites with and without the presence of HBC-PhC<sub>12</sub>.

#### 4.2.1 Film Forming

HBC-PhC<sub>12</sub> shows very good solubility in chloroform and forms homogeneous film with root mean square (RMS) roughness less than 10 nm by spin-coating. The films are continuous without apparent features (Figure 4.3a), which is characteristic of a room temperature LC. The thickness of the film can influence the RMS roughness values, which vary from 2 nm for a 30 nm thick film to 9 nm for a 140 nm thick film, as given in Table 4.2.

PDI was used as received from Syntec GmbH, Germany. It shows good solubility in chloroform. PDI differs from HBC-PhC<sub>12</sub> in that it crystallizes during the evaporation of the solvent. High crystallinity in spin-coated films of PDI has been observed by electron diffraction.<sup>43</sup> As observed by AFM, the films appeared to be much rougher and less homogeneous than those of HBC-PhC<sub>12</sub>. Cylindrical crystals could be clearly observed throughout the film, producing a RMS roughness greater than 25 nm (Figure 4.3b). Further investigation into the morphology of the crystals is discussed in the following section.



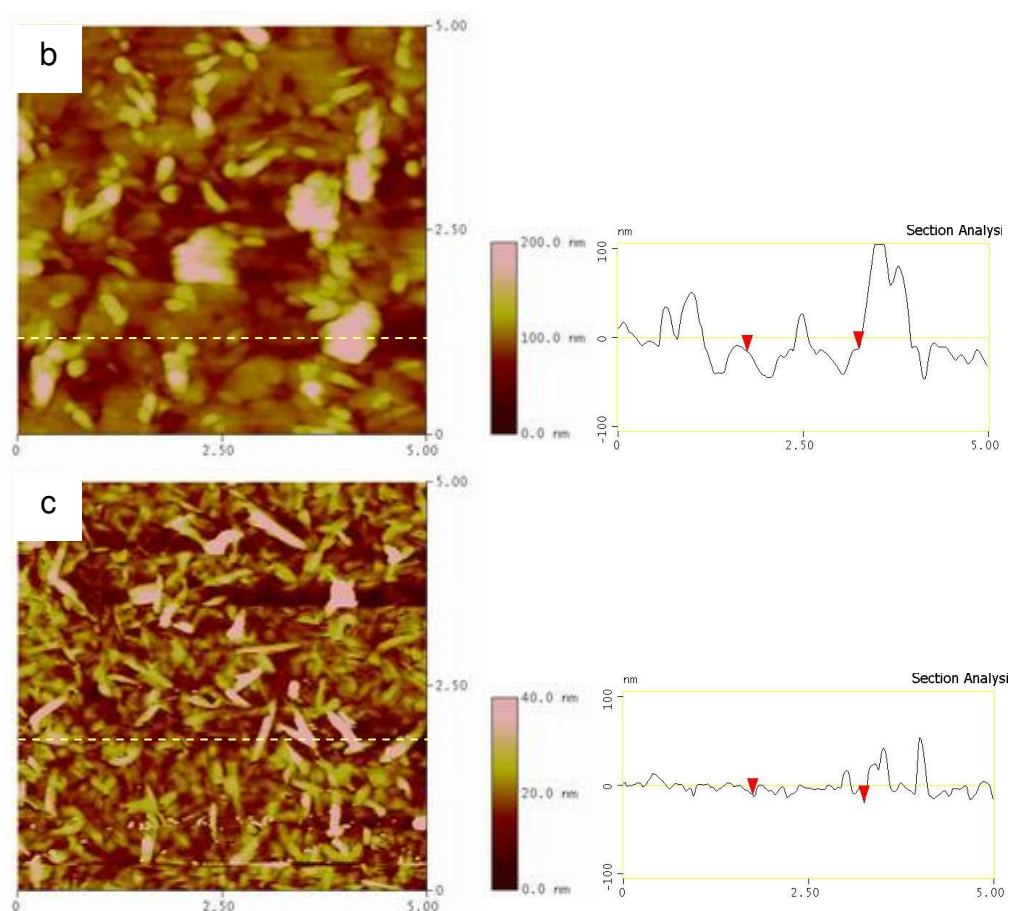


**Figure 4.3** Tapping mode AFM images of a) HBC-PhC<sub>12</sub>, b) PDI, and c) their blend at the weight ratio of HBC:PDI=4:6. The section analysis of the roughness is given on the right.

**Table 4.2** RMS roughness (nm) of the spin-coated film

Film thickness	30 nm	80/60 nm	140 nm
HBC-PhC <sub>12</sub>	1.9 nm	5.7	8.7
PDI	28.0	38.1	88.3
HBC:PDI (4:6)	-	5.9	9.3

Similar cylindrical crystals were observed in the films of a blend containing 40 wt% HBC-PhC<sub>12</sub> and 60 wt% PDI. The crystals dispersed more evenly on the surface, with a RMS roughness value in the range of 6-10 nm, which was much less than that of PDI films.

This indicates that the addition of HBC-PhC<sub>12</sub> improves the quality of the film, probably because they are miscible and the crystallization of PDI in large domains is hindered.

#### 4.2.2 Morphology Studies on PDI Crystals

Struijk et al. examined three N-alkyl-substituted perylene diimide derivatives, which showed multiple phase transitions indicating several crystalline and liquid crystalline phases.<sup>143</sup> The combination of the interdigitation of the linear alkyl chains, attractive  $\pi$ - $\pi$  interactions between the perylene moieties, and the strong dipolar interactions between the diimide moieties within one column and between adjacent columns results in a highly ordered structure. PR-TRMC measurements show the *N*-octadecyl derivative has a charge carrier mobility of 0.1 cm<sup>2</sup>V<sup>-1</sup>s<sup>-1</sup> in the liquid crystalline phase, and in the crystalline phase a charge carrier mobility as high as 0.2 cm<sup>2</sup>V<sup>-1</sup>s<sup>-1</sup>. The DSC curve (in the range between -50 °C to 150 °C) reveals only one phase transition peak at 67 °C indicating crystalline phase to columnar phase. This low temperature assures thermal processing applicable on the device.

It is known that the improvement of efficiency requires an increase in the exciton-diffusion length upon light absorption as well as in the transport of charge carriers after exciton dissociation. A well-ordered arrangement of the organic moieties in the conducting material has been shown to accomplish these conditions.<sup>43,100</sup> In fact, it has been demonstrated that increased ordering of PDI molecules leads to higher exciton-diffusion lengths,<sup>101-103</sup> stabilizes charge-separated states,<sup>151</sup> and enhances electron mobilities.<sup>43</sup> As such, the control of PDI crystals in the real devices, which presents in the morphology of the film, is an important way to improve the performance of the cells.

Thin films of PDI spin-coated from chloroform solution onto silicon wafer were prepared, and then observed by AFM and SEM. As shown in Figure 4.4, the films are inhomogeneous, and even discontinuous at some points. Crystals can be observed lying or standing tilted on the surface. The size of the crystals varies from hundreds of nanometers (nm) to a few micrometers ( $\mu$ m), resulting in different morphologies. The small cylindrical crystals organize in parallel to form foliage-like crystals (Figure 4.4c) lying on the substrate. This morphology often leads to homogeneous surfaces with low RMS roughness. Large cylindrical crystals (Figure 4.4b), especially those with dimensions in the

micrometer range, often stand at a tilt and partly protrude out of the surface because their size is much greater than the film thickness ( $\sim 100$  nm). As a result, such films exhibit high roughness.

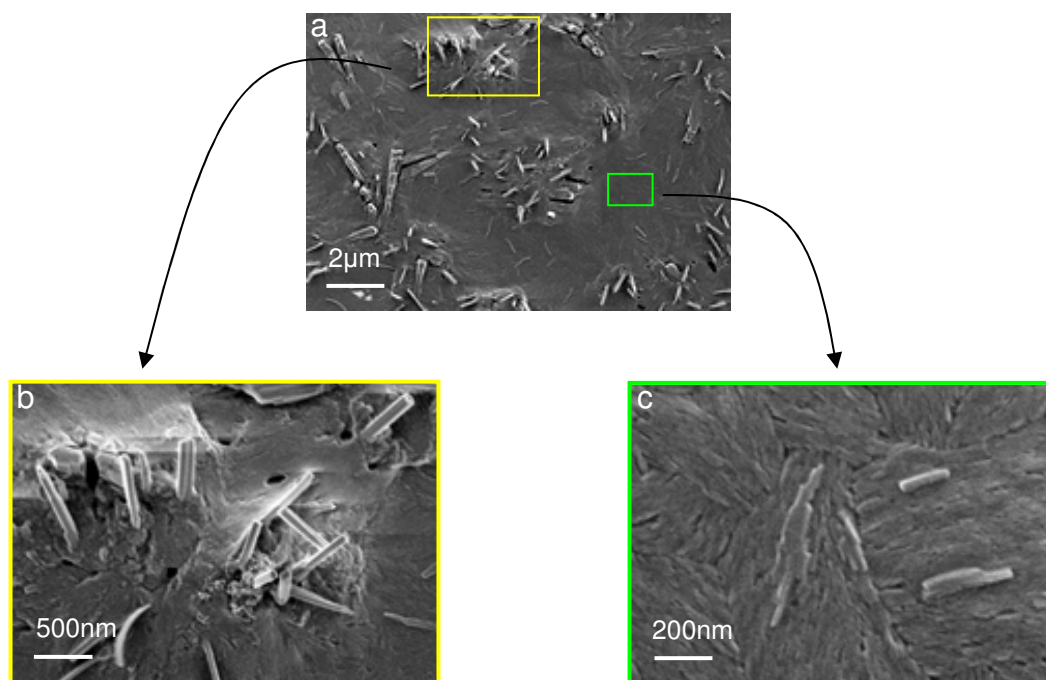


**Figure 4.4** SEM images of PDI films spin-coated onto a silica wafer.

Close-packing and ordering of PDI molecules at the nano- and micro-scale are usually attained by self-organization,<sup>152</sup> a process driven by  $\pi$ - $\pi$  stacking,<sup>43,153-157</sup> hydrogen bonding,<sup>158,159</sup> metal-ligand interactions,<sup>160-162</sup> electrostatic forces,<sup>163</sup> or even predefined structures by means of covalent links.<sup>164-170</sup> Among these, thermal treatment induced crystallization has the advantage of easy processibility even on fabricated devices, versatility for different D/A systems, and little requirement on circumstances. In this work, thermal treatment at 120 °C was performed on the films in inert atmosphere. It is shown in Figure 4.5 that the cylindrical crystals were greatly developed after the treatment. The



surface of the film became rougher and the crystals were more clearly observable, as concluded in table 4.3.

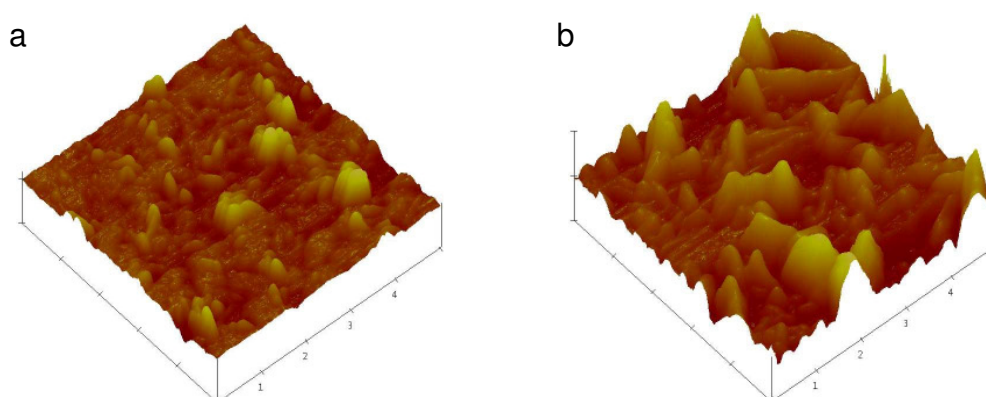


**Figure 4.5** AFM pictures of PDI film a) before and b) after annealing at 120 °C for 1 h.

**Table 4.3** RMS roughness (nm) of the film

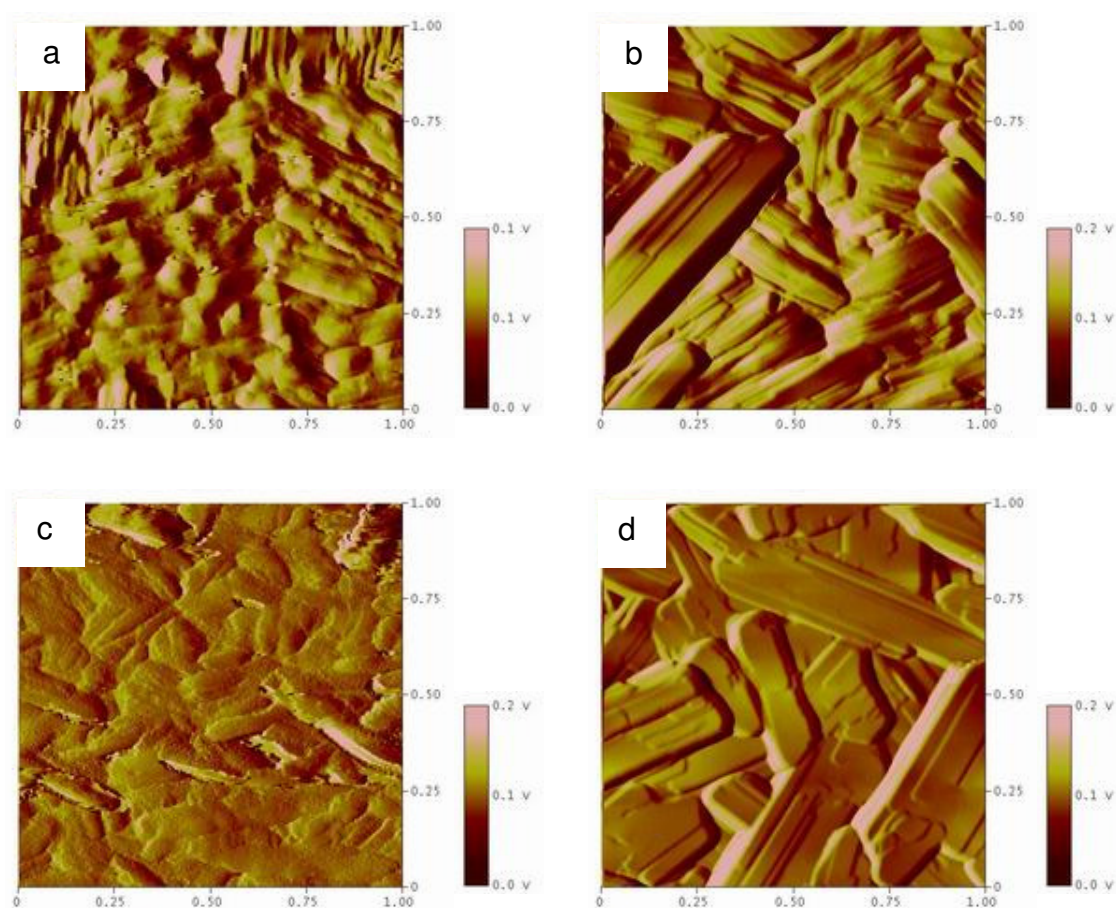
Film thickness		30 nm	80/60 nm	140 nm
HBC-PhC <sub>12</sub>	pristine	1.9	5.7	8.7
	annealed	1.2	4.2	8.4
PDI	pristine	28.0	38.1	88.3
	annealed	61.9	88.8	103.5
HBC:PDI (4:6)	pristine	-	5.9	9.3
	annealed	-	21.0	11.3

Table 4.3 gave the RMS roughness of the separate HBC-PhC<sub>12</sub> and PDI film, as well as the blend films before and after the thermal treatment. For HBC-PhC<sub>12</sub>, the roughness of the film did not vary by the treatment. This was understood as that the material maintained in the same columnar LC phase during the annealing procedure, therefore, no rearrangement of molecules could occur. However for PDI film, the roughness largely increased due to the development of PDI crystals, suggesting that the development of the crystals was accompanied by the depletion of the materials from the surroundings. The

same phenomena were observed for the blend films, although the roughness was much smaller than that of PDI films. This will be discussed below in relation with the thickness of the film.

### PDI Crystals in the Blend of HBC-PhC<sub>12</sub> and PDI

HBC-PhC<sub>12</sub> is in a liquid crystalline phase at RT, so no apparent features were found in its spin-coated films (Figure 4.3a). Thermal treatment did not change the morphology of the films. The RMS roughness remained less than 10 nm.



**Figure 4.6** Tapping mode AFM pictures of film of blend containing 40 wt% HBC and 60 wt% PDI. The thickness is 70 nm for a and b, 140 nm for c and d. Both b and d were annealed at 120 °C for 1 h.

Both thin films (~ 80 nm) and thick films (~ 140 nm) were prepared of the blend containing HBC-PhC<sub>12</sub> and PDI at the D/A = 4:6. Compared with the PDI films, the films of the blend are much more homogeneous. The corresponding RMS roughness shows values in between those of the films of the separate components. It has been shown that the thermal treatment can develop the crystallization of PDI in its pure films. The similar phenomenon was observed in the films of the blend. After annealing, the crystals became larger and were more clearly observed, which indicates depletion of the cover material or stratification within the film.

The section view of the film was observed to clarify the stratification. It was clearly seen that a ‘bi-layer’ like structure existed in the annealed film, which indicates that the phase separation of the components and crystallization of PDI developed further during annealing. This coincides with the reported ‘bi-layer’ structure in the blend of HBC-PhC<sub>12</sub> and PDI, which enhanced charge transport in the separate domains, thus leading to a highly efficient device.<sup>43</sup> In those films, PDI is enriched on the surface while HBC-PhC<sub>12</sub> accumulates at the bottom. This can be explained by the different solubility of HBC and PDI in chloroform, the lower surface tension of PDI, and/or the lower density of PDI.

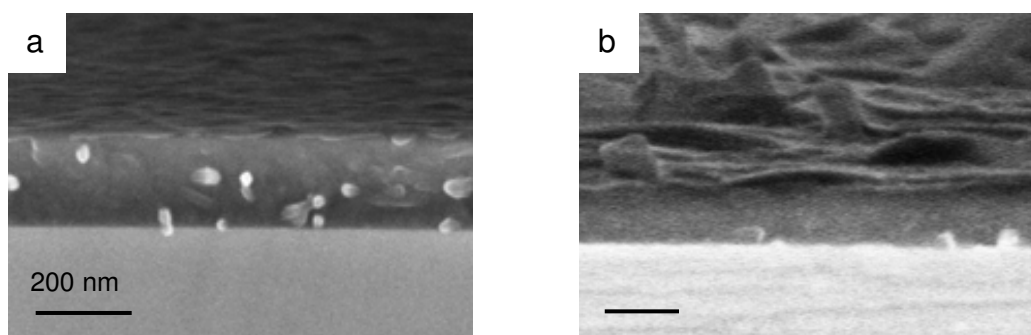


**Figure 4.7** SEM images of film of blend containing 40 wt% HBC and 60 wt% PDI a) before and b) after annealing at 120 °C for 1 h.

Except for the variation of the internal morphology after annealing, the development of PDI crystals was found to correlate with the thickness of the film. The crystals were larger in thin films (~ 80 nm) than in the thick films (~ 140 nm), as shown in Figure 4.8. This might occur for two reasons: 1, the crystals have smaller free space in which to grow

in thicker film; 2, the crystals may stand tilted on the surface and so show only a projection of the cylinder. Here, it is assumed that there are enough PDI molecules for the growth of crystals, as when the film thickness was decreased further, for example to 30 nm, the size of the crystals decreased again due to the incomplete crystallization resulting from deficiency of the material.

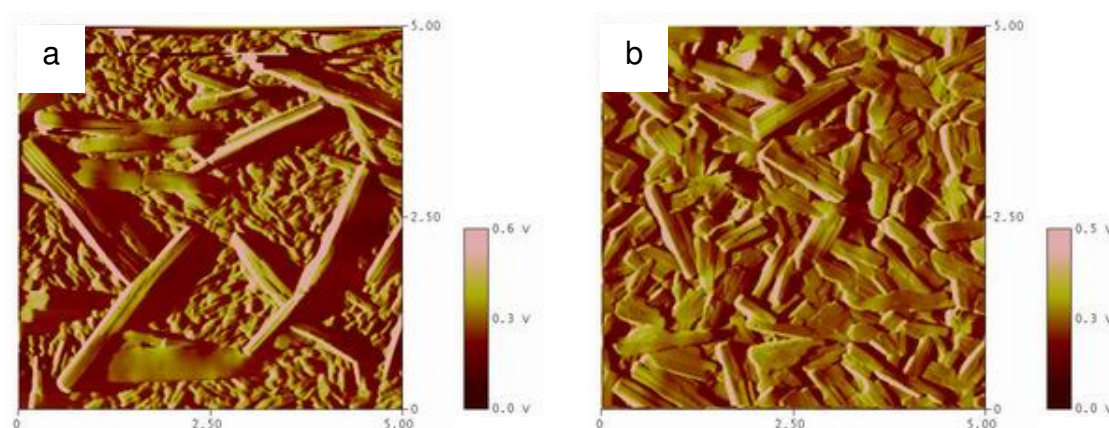


**Figure 4.8** AFM pictures of film of blend containing 40 wt% HBC and 60 wt% PDI. The thickness is a) 70 nm and b) 140 nm. Both are annealed at 120 °C for 1 h.

Although the crystals in the thin film appear to be larger than those in the thick film, their size is inhomogeneous with crystal dimensions varying from 300 nm to 3  $\mu\text{m}$ . By comparison, the thick film shows a uniform crystal size of about 1  $\mu\text{m}$ . This is in accordance with the RMS roughness listed in Table 4.3, which gave a value of 21 nm for the thin film and 11 nm for the thick film. Since a smooth and homogeneous film is preferred in solar cells, a thickness of 140 nm was adopted to fabricate devices containing HBC-PhC<sub>12</sub> and PDI.

## 4.2.3 Device

### 4.2.3.1 Thermal Treatment

Devices were fabricated and annealed at 120 °C to investigate the effect of thermal treatment upon the development of PDI crystals. The active layer was composed of 40 wt% HBC-PhC<sub>12</sub> and 60 wt% PDI. ITO was used as the anode and Ag as the cathode. The device was annealed in an inert atmosphere before the deposition of the top electrode. The EQE curves are shown in Figure 4.9. The morphology of the films is shown in Figures 4.6c-d.

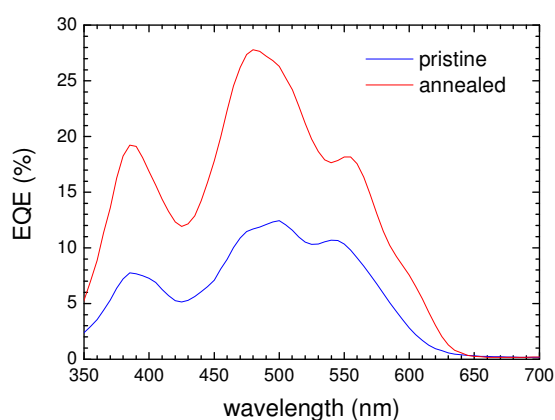


**Figure 4.9 a)** Photovoltaic performance of device ITO/HBC-PhC<sub>12</sub>:PDI(4:6)/Ag before (blue line) and after (red line) annealing at 120 °C for 1 h.

The EQE<sub>max</sub> increased for the annealed device, reaching 28% at 480 nm. Since during annealing, the dispersed small crystals were replaced by large separated domains, faster charge transport and less charge recombination due to the decreased D/A interface were expected. Further, the stratification within the film (SEM images in Figure 4.7 and illustration in Figure 4.10) supplied better percolation pathways, which improved charge transport and at the same time diminished charge recombination at trap sites. Besides, the enrichment of HBC-PhC<sub>12</sub> near the anode and PDI near the cathode facilitated charge/electron injection into the electrodes. This observation is in accordance with the reported device based on HBC-PhC<sub>12</sub>/PDI, where a high efficiency (EQE<sub>max</sub> ~ 34%) was achieved for the device with an ideal morphology of spontaneous stratification. The same morphology was obtained in this study, however, corresponding to a littler lower efficiency (EQE<sub>max</sub> ~ 28%). The difference in efficiencies might result from the different

batch of commercialized acceptor material (for example, impurities) and the possibly varied testing conditions in two different labs.

This result proves that annealing is an efficient way to develop crystals of PDI in films of pure material and of blends with HBC as well. At a certain D/A ratio, the thickness of the film plays an important role on phase separation and the size of the crystals, that is, small crystals with uniform size for thick film (~ 140 nm) and big crystals with varied size for thin film (~ 70 nm). This supplies a way to control the morphology of the active layer. Except for the higher electron mobility in the greatly developed PDI crystals, the de-mixing phases (Figure 4.10) form better percolation pathways to reduce the charge recombination in the fine D/A mixture before annealing. This work thus suggests that annealing is a successful strategy for optimizing the performance of HBC-PhC<sub>12</sub>/PDI devices, and even for other devices using PDI as acceptor.

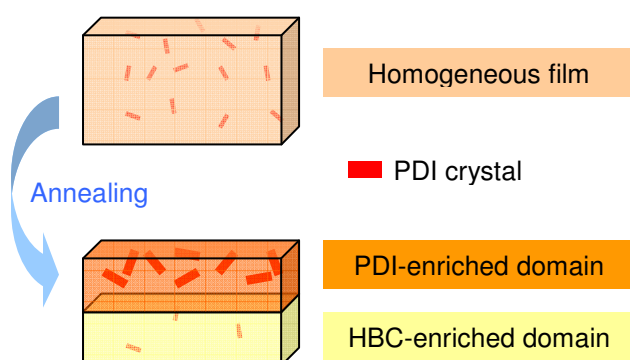


**Figure 4.10** *Illustration of stratification within the film.*

#### 4.2.3.2 HBC-PMI

It has been shown in the previously investigated HBCs that there is a compromise between the chain-length and intermolecular distance between the donor and the acceptor. The larger side chains always correspond to the lower phase transitions and the better film-forming ability. On the other hand, the larger side chains lead to a larger D/A separation scale, and so a smaller D/A interface for charge separation. One way to avoid this is the

use of a small amount of a compatilizer. This can minimize the phase separation scale by enhancing the intermolecular contact of the two components, and at the same time maintain the film quality since normally the amount of compatilizer is too small to influence the film-forming properties of the blends.

For the blend of HBC-PhC<sub>12</sub> and PDI, a suitable compatilizer would be a compound containing the two functional groups, i.e. an HBC core and a perylene dye, linked by either a conjugated band (benefiting charge transfer) or an un-conjugated band (preventing charge recombination). Accordingly, HBC-PMI was designed and synthesized by M. Kastler in our group. The molecule has an HBC unit on one side and a peryleneimide unit on the other side, linked by a triple band (Figure 4.11). This structure is designed to afford the intimate contact of the HBC side with HBC-PhC<sub>12</sub> and of the perylene side with PDI.

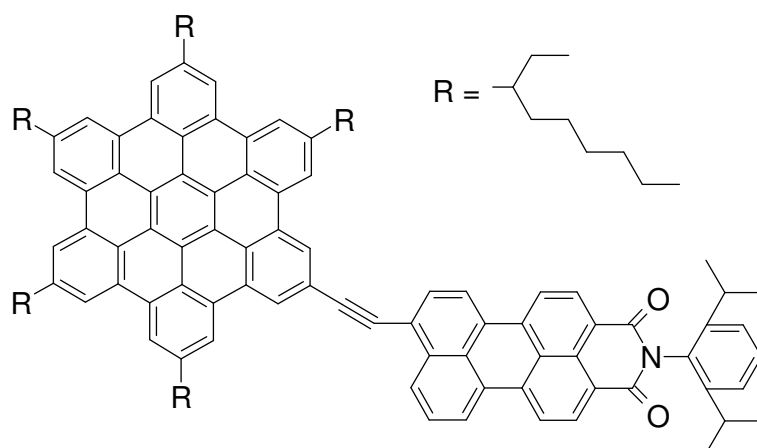


**Figure 4.11** Chemical structure of HBC-PMI

Devices containing HBC-PMI based on HBC-PhC<sub>12</sub>/PDI blend (4/6) were fabricated and the morphology of the films was studied. Two different contents (1% and 5%) of HBC-PMI in the HBC-PhC<sub>12</sub>/PDI (4:6) blend were tested. Thermal treatment was further performed to optimise the devices. The results were compared with the device without HBC-PMI. As shown in Figure 4.12, the device having 1% HBC-PMI shows lower efficiency than the device without HBC-PMI, and the efficiency is even lower for the device containing 5% HBC-PMI. This indicates that the presence of HBC-PMI deteriorates

the performance of the device. However, after the thermal treatment under the same condition as for the HBC-PhC<sub>12</sub>/PDI device above, the efficiency increases greatly, for devices with and without HBC-PMI. Similar efficiencies were observed for devices without and with 1% HBC-PMI, and a little lower for device having 5% HBC-PMI. It should also be noted that a shoulder peak near 600 nm appears for the device containing 5% HBC-PMI after the annealing procedure.

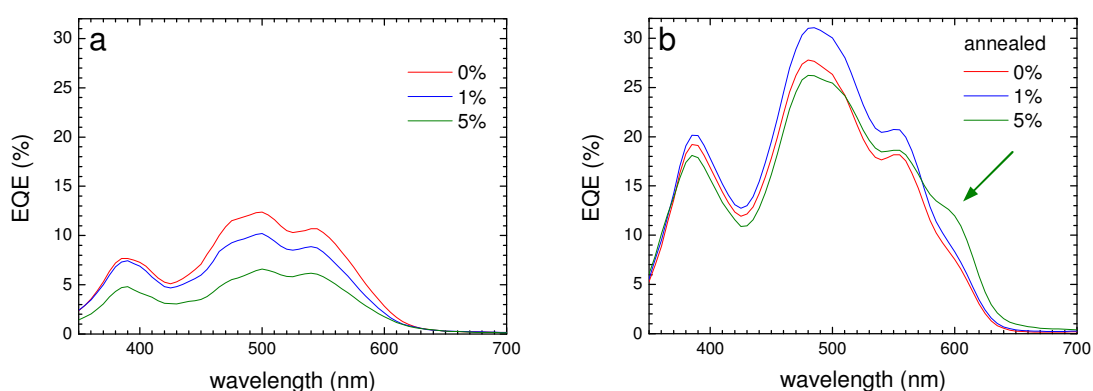


**Figure 4.12** Photovoltaics performance of device ITO/HBC-PhC<sub>12</sub>:PDI(4:6)/Ag doped with HBC-PMI a) before and b) after annealing at 120 °C for 1 h. The numbers in the figures indicate the percent content of HBC-PMI in the blend of HBC-PhC<sub>12</sub>:PDI (4:6).

The performance of the device was contrary to what was expected from addition of HBC-PMI, as it was anticipated that this would minimize phase separation scale to create a larger charge separation interface, thus leading to higher efficiency. Moreover, the thermal treatment, which is known to aid the development of PDI crystals, increases the performance of the devices to a similar level no matter how much HBC-PMI they contain. Both procedures should modulate directly the phase separation scale, which was expected to be observable.

The direct observation of phase separation was performed by SEM on the spin-coated film. Films with 1% and 5% HBC-PMI, before and after annealing, were observed.



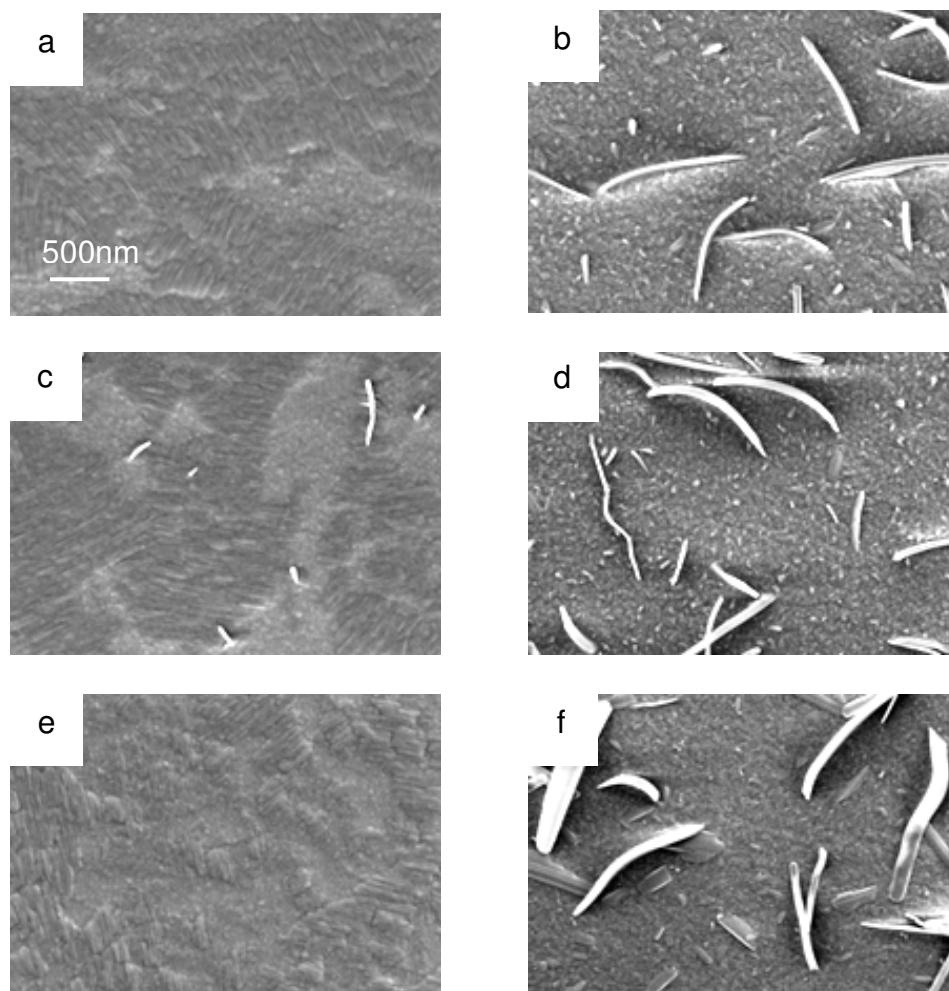


**Figure 4.13** SEM images for pristine (left) and annealed (right) HBC-PhC<sub>12</sub>/PDI thin films. From top to down, the films contain 0%, 1%, 5% HBC-PMI, respectively. The scale bar is 500 nm for all images.

As shown in Figure 4.13, two kinds of domains are observed in all films. One type of domain contains ordered crystals, and the other consists of amorphous areas without apparent features. Upon increasing the content of HBC-PMI, the two different domains decrease in size, proving a smaller phase separation scale is obtained by adding HBC-PMI. After annealing, the morphologies of the films containing different content of HBC-PMI become similar, with big cylindrical crystals dispersed on the surface. Less HBC-PMI or

developed PDI crystals correspond to the larger separation scale. This indicates better percolation pathways rather than a larger D/A interface is needed to improve performance in HBC-PhC<sub>12</sub>/PDI devices. Therefore, charge transport rather than charge separation is the dominant factor in determining efficiency for this system.

The shoulder peak at 600 nm, which is shown in the EQE- $\lambda$  spectrum of device containing 5% HBC-PMI, was assigned to absorption by HBC-PMI because of its strong absorption in this region (Figure 4.14). This result indicates that HBC-PMI contributes to photon-electron conversion after the thermal treatment. HBC-PMI absorbs light and forms excitons, which are then separated into holes and electrons within the molecules, and transported to adjacent domains of HBC and PDI. By comparison, in the device before annealing, a relatively small amount of HBC-PMI excitons are trapped by intimate contact between HBC and PDI molecules, as demonstrated in Figure 4.15. After annealing, the percolation pathways were better developed so that the charges separated on HBC-PMI molecules could more quickly find pathways for charge transport. The device with 1% HBC-PMI does not show the peak at 600 nm, which proves that a certain minimum amount of material is required for this effect to become apparent.

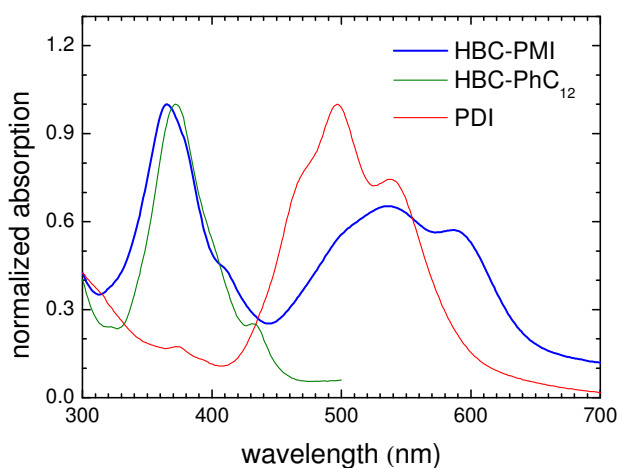


**Figure 4.14** Absorption spectrum of HBC-PMI, HBC and PDI as thin films.

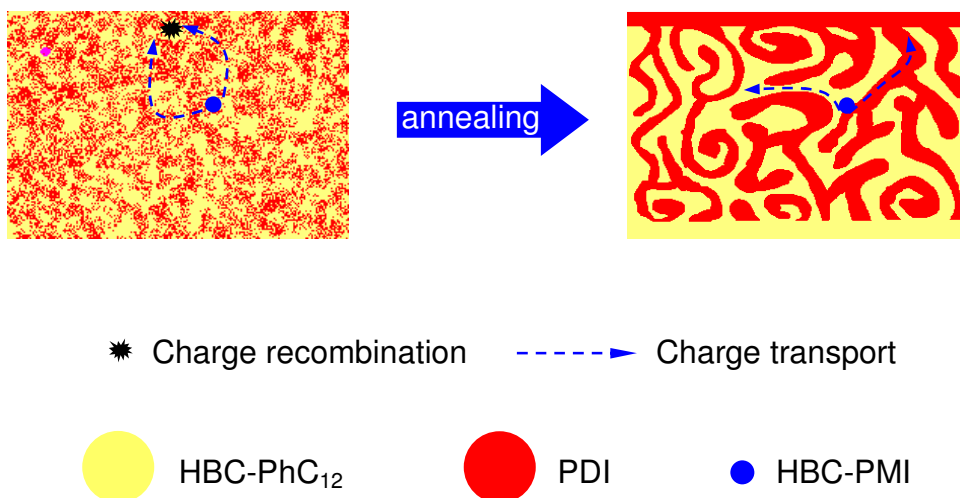


**Figure 4.15** *Rough schematic of HBC-PMI/HBC/PDI blends before and after annealing illustrating enhancement of charge transport pathways.*

The similar efficiencies for all annealed devices indicate that the effect of the compatilizer is overcome by the effects of annealing. The above experimental results also suggest that above a critical amount of HBC-PMI, phase separation cannot be recovered to the level without HBC-PMI just by annealing.

#### 4.2.4 Summary

The morphology of PDI film with and without the presence of HBC was systematically investigated. Two kinds of crystallites (foliage-like and cylindrical crystals) exist, while cylindrical crystals were the dominant morphology of PDI in the blend device. The size of the crystals depended on the thickness of the film, and could be developed by the annealing procedure. This was used as a strategy to control the morphology. The device was further studied to combine the influence of morphology which suggests thermal treatment as a way to optimize the charge transport and to inhibit charge recombination, thus improving the performance of the device. A new compound functioned as a compatilizer for HBC-PhC<sub>12</sub> and PDI was applied to modulate the morphology of the film.

The results of the corresponding devices indicated that charge transport was the decision feature in HBC-PhC<sub>12</sub>/PDI devices.

### 4.3 Photodiodes Based on Branched-alkyl Substituted HBCs

The previous work reveals the role of PDI crystals for charge transport in the device, and suggests the heat treatment as a way to improve the performance. As the donor for PDI, HBC will be discussed in this section to fulfill the overall understand on the D/A pair. Three HBC derivatives differing only in the length of the attached alkyl side chains (HBC-C<sub>6,2</sub>, 2-ethyl-hexyl; HBC-C<sub>10,6</sub>, 2-hexyl-decyl; and HBC-C<sub>14,10</sub>, 2-decyl-tetradecyl) were used as donors together with PDI as acceptor material in heterojunction photovoltaic devices. The photovoltaic behavior has been investigated with respect to the influence of the alkyl side chains. It was found upon increasing the side chain length, the HBC chromophore becomes diluted, thus decreasing the amount of light absorbed. The DSC and powder X-ray investigation reveal that the HBC with the 2-ethyl-hexyl side chain is in a crystalline state at room temperature, while the other two HBCs with 2-hexyl-decyl and 2-decyl-tetradecyl substituents in so-called plastic crystalline state. The HBC with the shortest side chain is proven to be the best donor for perylenediimide, showing a highest external quantum efficiency of 12%. Scanning Electron Microscopy suggested that further the thermal treatment of the device played an important role in determining the morphology.

#### 4.3.1 Introduction

The HBCs were synthesized by M. Kastler and D. Wasserfallen in our group.<sup>150</sup> The structures are shown in Figure 4.16. HBC-C<sub>10,6</sub> and HBC-C<sub>14,10</sub> exhibit excellent solubility in common organic solvents and form homogeneous films by spin-coating. The RMS roughness of the spin-coated films was characterized by AFM and the values were less than 5 nm. HBC-C<sub>6,2</sub> is less soluble, however, the necessary concentrations were obtained

by stirring and slight heating of the solution. The spin-coated films showed rougher surfaces (RMS roughness ~5-10 nm).

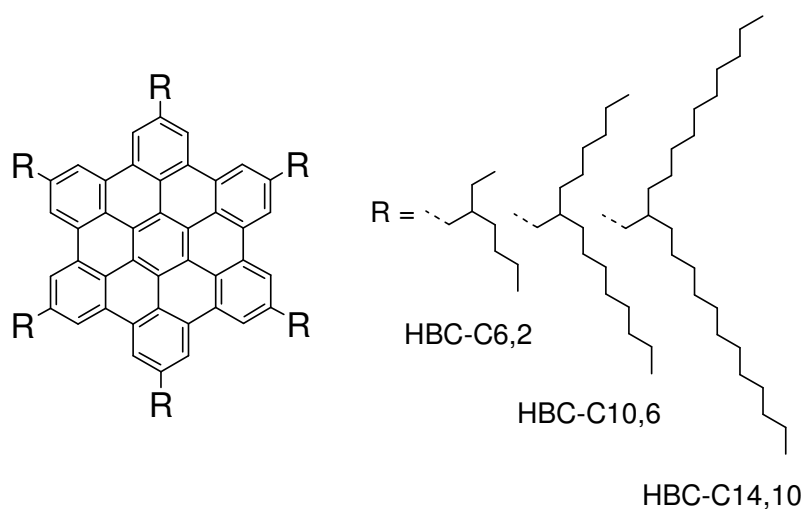


**Figure 4.16** Chemical structures of HBCs used.

To gain an insight into the thermotropic behavior of the three discotic donor compounds, W. Pisula investigated the thermal properties by means of differential scanning calorimetry (DSC) and the respective phases were characterized by X-ray diffractometry. The thermal behavior of all studied compounds is summarized in Table 4.4.

**Table 4.4** Thermal behavior determined by DSC for the investigated materials

Compound	Temperature (°C)	Phase transition*
HBC-C <sub>6,2</sub>	97	Cr - Col <sub>d</sub>
HBC-C <sub>10,6</sub>	24	Col <sub>p</sub> - Col <sub>d</sub>
	93	Col <sub>d</sub> - I
HBC-C <sub>14,10</sub>	46	Col <sub>p</sub> - I
PDI	67	Cr - I

\*Cr - crystalline phase; Col<sub>p</sub> - plastic crystalline phase; Col<sub>d</sub> - disordered columnar phase; I - isotropic melt.

Contrary to the other two HBCs, the HBC-C<sub>6,2</sub> is a microcrystalline powder below the first detected transition at 97 °C, where the material enters the mesophase. HBC-C<sub>10,6</sub> and HBC-C<sub>14,10</sub> reach the isotropic phase at temperatures of 93 and 46 °C, respectively, which is low compared to other HBCs. These two compounds are assigned as being in a plastic crystalline phase at room temperature, due to their soft and waxy natures. Typically, there are three important phases for HBC molecules, which are characterized by the order and the mobility of the molecules. The low temperature phases show higher intracolumnar organization, whereby the side chains are in a disordered state around the periphery of the core. Due to the packing conditions of the two nanophases and the reduced molecular mobility, the aromatic cores are tilted with respect to the columnar axis. In general this phase is assigned as crystalline, what might be not correct in the precise sense. Nevertheless, in order to follow the nomenclature used to assign the different phases for triphenylenes, this term will be used in this study to refer to this higher order phase. The designation ‘plastic crystalline’ distinguishes another low temperature phase also with high structural order, but points out the increase of molecular mobility. Also in the plastic crystalline the molecules reveal a tilted arrangement.

Powder X-ray diffraction indicates a high degree of crystallinity for all the three HBCs at room temperature (Figure 4.17). However, it is obvious that the reflections of HBC-C<sub>6,2</sub> in the wide-angle range are more distinct compared to the two materials with the longer chains. Since these reflections are assigned to intracolumnar correlations, the molecules of HBC-C<sub>6,2</sub> are obviously organized in a much more defined way in the supramolecular columns than HBC-C<sub>10,6</sub> and HBC-C<sub>14,10</sub>, which is important for an unperturbed charge carrier migration.<sup>171</sup> The distinct equatorial reflections in the 2D-WAXS patterns (Figure 4.18) of the extruded filaments also provide important evidence of this. The intracolumnar packing of HBC-C<sub>6,2</sub> is exceptionally well pronounced as indicated by the high number of higher-order, off-meridional reflections arising not only from the intracolumnar but also from strong intercolumnar correlations between the discs. This indicates the corresponding phases of HBC-C<sub>10,6</sub> and HBC-C<sub>14,10</sub>, due to the absence of long-range correlation, can be assigned as plastic-crystalline phases, whereas HBC-C<sub>6,2</sub> forms a crystalline phase at room temperature. Further, solid-state NMR experiments revealed a relatively high mobility of the flexible surrounding of HBC-C<sub>10,6</sub> and HBC-C<sub>14,10</sub> in the room temperature phase, supporting the above assignment.<sup>172</sup> The same experiments proved that the side chains in HBC-C<sub>6,2</sub> were rather crystalline, showing much lower dynamics.

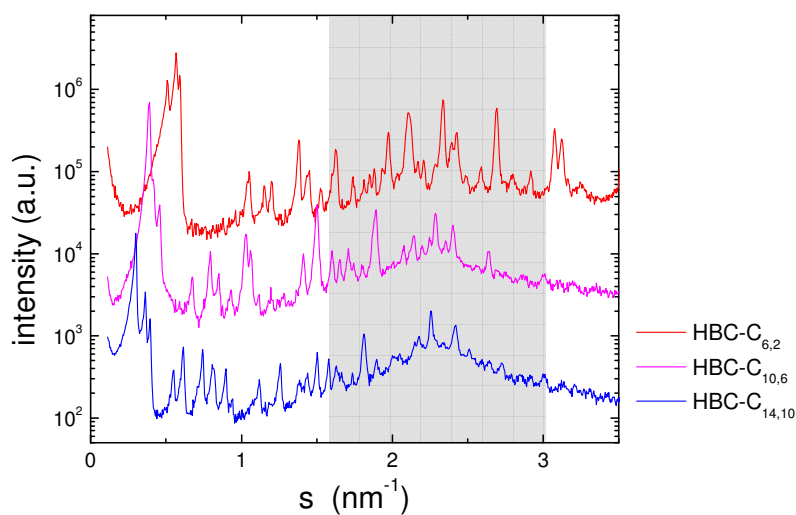


**Figure 4.17** Powder X-ray diffraction of the investigated HBCs (the wide-angle range corresponding to the intra-columnar correlations is represented in the grey field).

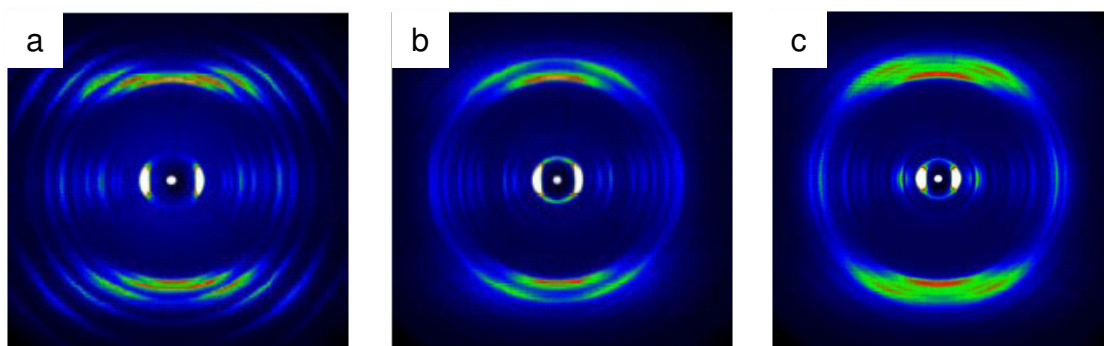


**Figure 4.18** 2D-WAXS pattern of filament extruded a) HBC-C<sub>6,2</sub> in crystalline phase, b) HBC-C<sub>10,6</sub> and c) HBC-C<sub>14,10</sub> in plastic crystalline phase.

### 4.3.2 Optical Properties

The optical properties of the three HBC derivatives were investigated both in solution (by M. Kastler) and as films (Figure 4.19). The films were prepared at the similar thickness of 100 nm to simulate the real light absorption in the device.

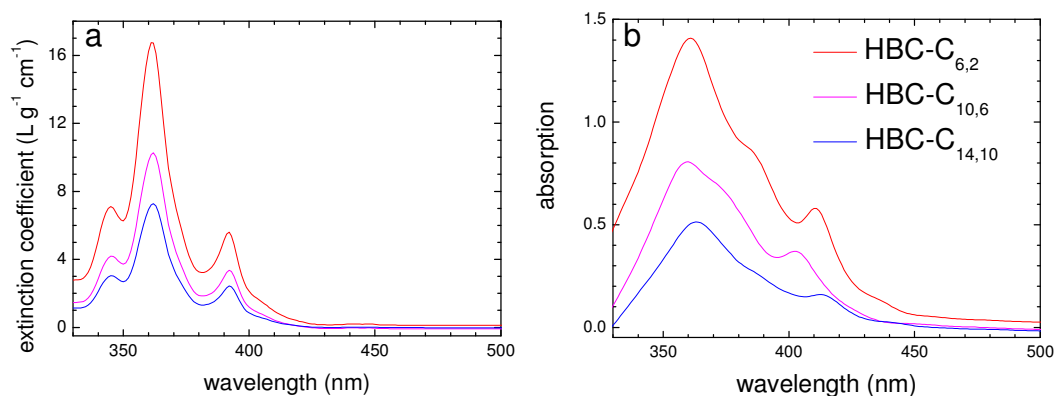


**Figure 4.19** UV/vis absorption spectra of HBCs a) in solution and b) as thin films (thickness of  $100 \pm 10$  nm).

The typical absorptions of the three HBCs occur with maxima at 362 nm, which is about 10 nm blue shifted when compared with HBC-PhC<sub>12</sub>. This arises from the weaker intracolumnar organization of the former because of the absence of the additional phenyl units.<sup>63</sup> It can be clearly seen that the extinction coefficients ( $\epsilon$ ) calculated from the spectra in solution decreased as the length of the alkyl substituents are increased. The corresponding values of  $\epsilon$  are  $16.75 \text{ L g}^{-1} \text{ cm}^{-1}$  for HBC-C<sub>6,2</sub>,  $10.27 \text{ L g}^{-1} \text{ cm}^{-1}$  for HBC-C<sub>10,6</sub>, and  $7.29 \text{ L g}^{-1} \text{ cm}^{-1}$  for HBC-C<sub>14,10</sub>. Assuming the same packing density, the HBC chromophore density in HBC-C<sub>6,2</sub> is 77 mol%, in HBC-C<sub>10,6</sub> 38 mol% and in HBC-C<sub>14,10</sub> 26 mol%, respectively, which correlates with the above extinction coefficients. The extension of the alkyl chains “dilutes” the “active” aromatic core, which is responsible for the absorption observed in the UV/vis spectra. As expected, thin films of the three HBC derivatives with the same thickness showed different light absorptions due to their different chromophore concentrations (Figure 4.19b). The higher absorption cross-section showed HBC-C<sub>6,2</sub> to be the most promising material, since a potential solar cell using it would collect 40% more photons than one using the same amount of HBC-C<sub>14,10</sub>. Analogous phenomena have been reported for polythiophene based solar cells.<sup>173</sup> PDI absorbs light between 450 and 600 nm, which ensures in the blend a photon absorption from 330 to 600 nm, covering the strongest emission of the solar light to fulfill one key requirement for efficient solar cells.



### 4.3.3 Characterisation of Energy Levels

The design of photovoltaic devices requires the knowledge of the potential energy levels of both donor and acceptor components. Cyclic voltammetry (CV) was carried out to obtain the electronic levels of the spin-coated HBC derivatives (Figure 4.20).

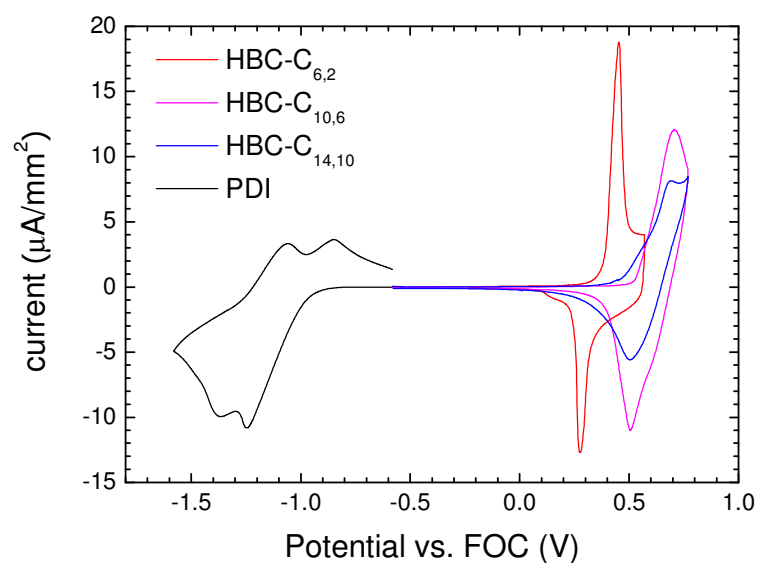


**Figure 4.20** Cyclic voltammetry curve of HBCs and PDI spin-coated on ITO glass, scanning rate of 25 mV/s.

**Table 4.5** Energy potential values determined by CV for the investigated materials.

Compound	$E_{\text{ox/red}}$ (Onset, V)	HOMO (eV)	LUMO (eV)	$E_g$ (Optical, eV)
HBC-C <sub>6,2</sub>	0.4	-5.2	-2.3	2.9
HBC-C <sub>10,6</sub>	0.5	-5.3	-2.4	2.9
HBC-C <sub>14,10</sub>	0.5	-5.3	-2.4	2.9
PDI	-1.0	-5.8	-3.8	2.0

Reversible oxidation peaks were observed in all positive scans, while no reduction peaks were detected in the scanned range. According to the calculation of the bandgap from the absorption spectra, the reduction was expected to happen above -2 V vs.  $\text{Fc}^+/\text{Fc}$ ,

which was out of the testing range and so not observable. The oxidation peak positions were used to estimate the HOMO energy levels. For HBC-C<sub>6,2</sub>, a HOMO level of -5.2 eV was calculated from the onset oxidation potential, while HBC-C<sub>10,6</sub> and HBC-C<sub>14,10</sub> showed a little lower energy level of -5.3 eV. This might arise from the stronger intermolecular interaction in HBC-C<sub>6,2</sub> in its crystalline phase than the other two HBCs in their plastic crystalline phase at RT, resulting in a hybrid orbital with higher HOMO. Meanwhile, the peak current decreased when the side chain changed from C<sub>6,2</sub> to C<sub>14,10</sub>. This result indicates that HBC with longer side chains need more potential to be oxidized, which can be explained by the shielding effect of the insulating alkyl substituents in HBC-C<sub>10,6</sub> and HBC-C<sub>14,10</sub> (Figure 4.21).

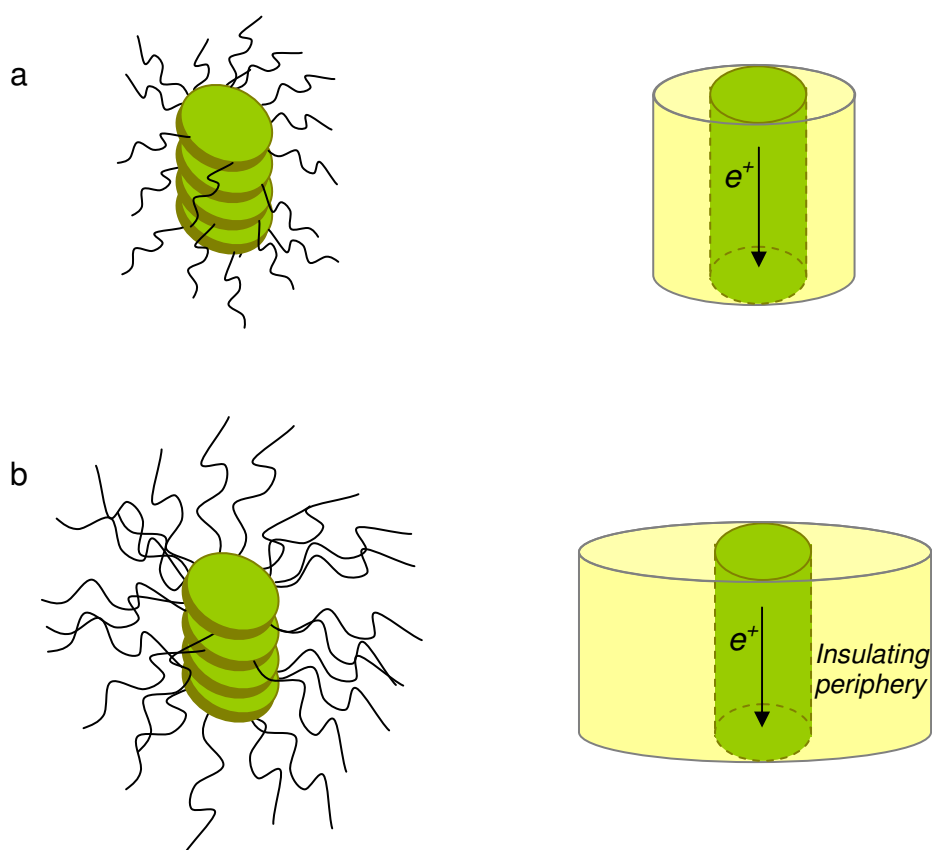


**Figure 4.21** Illustration for shielding effect of the alkyl substituents on the periphery of HBC cores: a) short alkyls and b) long alkyls.

The shielding effect arises from the insulating property of the alkyl substituents around the semi-conducting columns composed by stacked HBC cores. So the stacking of HBC molecules in the solid state can be described as a double cable with semi-conducting core surrounded by insulating peripheries. The inter-column charge hopping can occur only when the carrier overcomes the energy barrier of the insulating peripheries. The larger barrier is expected in the longer alkyl groups. Therefore, HBC-C<sub>6,2</sub> shows better reproducibility of CV scans and higher peak current than HBC-C<sub>14,10</sub>, implying that the chemical/electrical stability and charge injection and/or transporting ability for shorter side chain HBCs are better than those for longer ones. Similar phenomena have been reported for derivatives of poly(phenylene vinylene) and polynaphthalene, where the increase of the side chain length increased the energy barrier for the anodic reaction.<sup>174-176</sup>

The insulating effect in HBC was also observed by time-resolved pulse-radiolysis microwave conductivity measurements. Very long life-times of charges were observed for HBC-C<sub>10,6</sub> and HBC-C<sub>14,10</sub>, which was explained by a suppressed charge carrier recombination due to the shielding of the bulky alkyl mantle.<sup>177</sup> For the photovoltaic device, this would hamper an efficient exciton polarization at the interface between the donor and the acceptor moiety and thus reduce the efficiency of the solar cell.

Using the optical band gap of 2.9 eV (onset of the p-band in the solid-state UV/vis spectra), the LUMOs were calculated to be -2.3 for HBC-C<sub>6,2</sub>, -2.4 eV for HBC-C<sub>10,6</sub> and HBC-C<sub>14,10</sub>. These levels suggest that these HBC are suitable donor materials for PDI, which exhibits HOMO and LUMO energy levels of -5.8 and -3.8 eV respectively. The energy difference of >1 eV in the LUMO levels promotes electron transfer from HBC to PDI, and 0.4~0.5 eV difference in the HOMO energies allows transfer of holes from PDI to HBC.

#### 4.3.4 Photovoltaic Device

Photovoltaic devices were fabricated using the HBC derivatives as donor materials and PDI as acceptor material. The electrodes used were ITO as anode and aluminum as cathode, both with a thickness of 100 nm (The structure of the devices is written as

ITO/HBC:PDI/Al). Four different ratios of HBC:PDI (2:8, 4:6, 5:5, and 6:4) were tested to decide the best content of the donor in the working layer. All the films were prepared by spin-coating the solution in chloroform onto a pre-treated ITO substrate. The roughness of the films, as determined by AFM, increased slightly in comparison to the pure HBCs, owing to the existence of dispersed cylindrical PDI crystals.

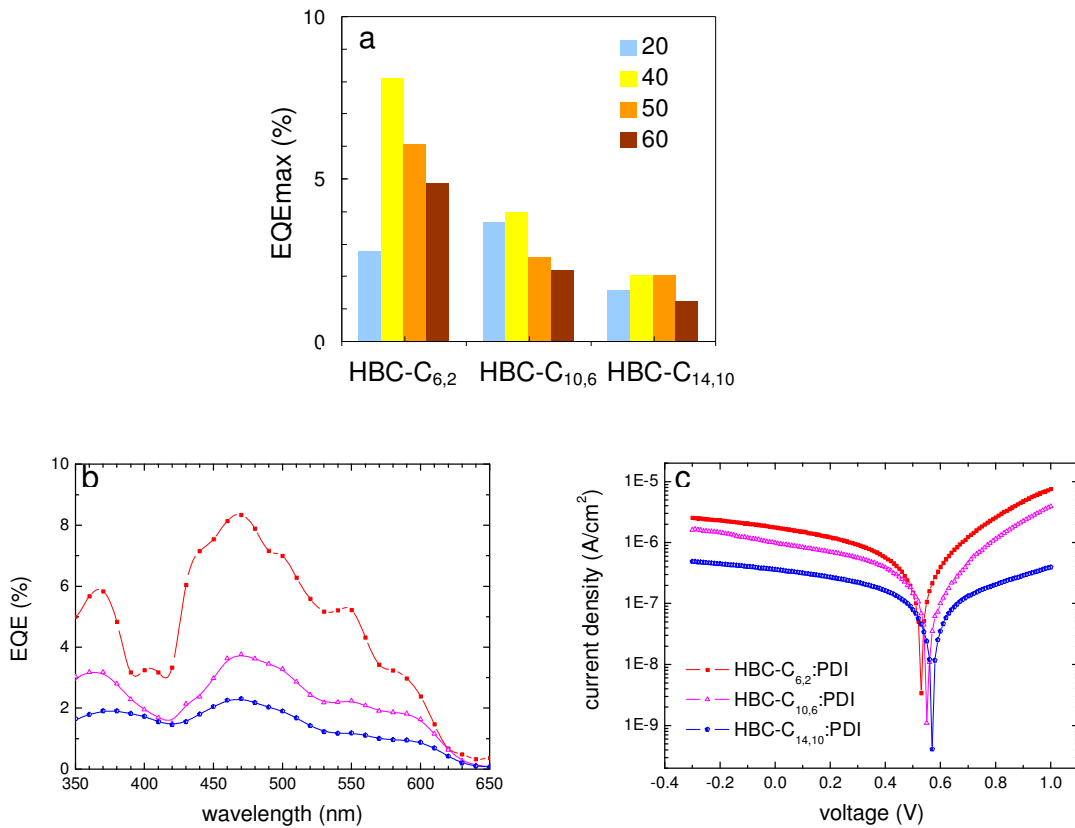


**Figure 4.22** ITO/HBC:PDI/Al device: a) performance at different D/A ratios, the legend number indicates the weight percent of HBC in active layer; b) EQE spectra at ratio of HBC:PDI=4:6 and c) corresponding I-V characteristics under monochromatic illumination at 490 nm (incident light intensity of  $0.24 \text{ W/m}^2$ ).

Independent of the donor used, an optimal weight ratio between HBC and PDI of 4:6 was determined (Figure 4.22a). Thermal treatment at  $120 \text{ }^\circ\text{C}$  for 1 h on the device was

immediately performed due to prior experience showing that annealing could greatly improve the photocurrent. It was noted that at the annealing temperature of 120 °C, only HBC-C<sub>6,2</sub> remained in the solid state while all other compounds melted. The results for the devices before and after annealing are given in Table 4.6.

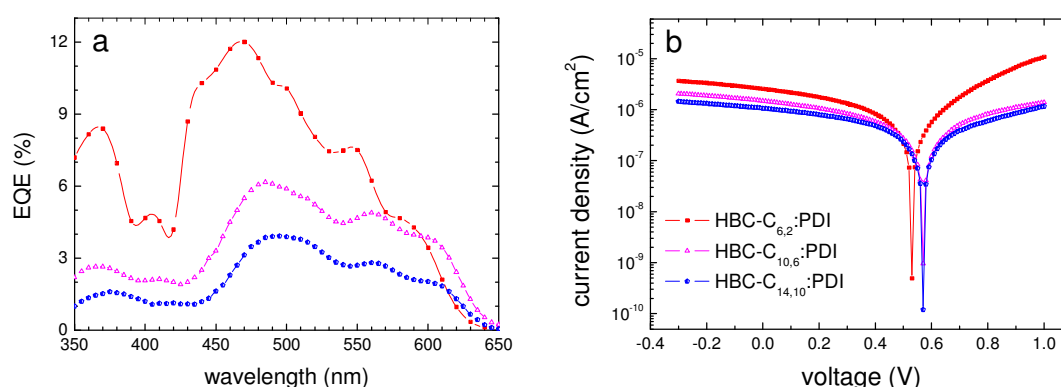


**Figure 4.23** ITO/ HBC:PDI /Al device: a) optimized EQE spectra at ratio of HBC:PDI=4:6 (film thickness 100 nm, annealed at 120 °C) and b) corresponding I-V characteristics under monochromatic illumination at 490 nm (incident light intensity of 0.24~0,25 W/m2).

**Table 4.6** Average photovoltaic performance

Donor material		I <sub>sc</sub> (μA/cm <sup>2</sup> )	V <sub>oc</sub> (V)	FF	η (%)	EQE <sub>max</sub> (%)
HBC-C <sub>6,2</sub>	pristine	1.8	0.53	0.29	1.09	8.3
	annealed	2.6	0.53	0.29	1.58	12.0
HBC-C <sub>10,6</sub>	pristine	1.0	0.55	0.31	0.72	3.8
	annealed	1.5	0.57	0.30	0.99	6.6
HBC-C <sub>14,10</sub>	pristine	0.4	0.57	0.33	0.28	2.3
	annealed	0.7	0.57	0.33	0.54	3.3

As expected, the annealing procedure improved the performance of the devices. The maximum EQE value for devices with HBC-C<sub>6,2</sub> increased from 8.3% to 12.0%, and corresponding overall efficiency from 1.09% to 1.58% upon annealing. Similar

improvements were also found for HBC-C<sub>10,6</sub> and HBC-C<sub>14,10</sub> containing device. The reason can be correlated with the development of the PDI crystals and corresponding better percolation pathways for charge transport, which will be discussed later as part of studies on the morphology of these films.

The performance of the devices was significantly influenced by the attached alkyl side chains. For the annealed solar cell with HBC-C<sub>6,2</sub>, an EQE<sub>max</sub> of 12 % was reached, which corresponded to a power efficiency of 1.5% at 490 nm (Figure 4.23). The HBC derivatives with the longer alkyl chains revealed lower performances, 6% EQE<sub>max</sub> for HBC-C<sub>10,6</sub> containing cell and 4% for HBC-C<sub>14,10</sub> (Figure 4.23a). The I-V curves showed similar behavior (Figure 4.23b). Both HBC-C<sub>10,6</sub> and HBC-C<sub>14,10</sub> exhibited an open circuit voltage of 0.56 V, while the one for HBC-C<sub>6,2</sub> was slightly lower (0.52 V). This can be explained by the higher HOMO level for the derivative with the shortest chain. Besides, the device with HBC-C<sub>6,2</sub> showed the highest short circuit current, which was in accordance with the CV result. This again indicated that the charge injection and/or transport were retarded due to the longer side chains.

Furthermore, the different behavior of devices based on the different HBCs can also be explained by their different supramolecular organizations. While HBC-C<sub>6,2</sub> formed spontaneous microcrystalline domains, the other two materials only self-organized into a plastic crystalline phase, where a lower columnar order was found. The higher self-association propensity of HBC-C<sub>6,2</sub> led to a better vertical segregation, which allowed the charge carriers to migrate along these percolation pathways.

#### 4.3.5 Morphology Investigation

Direct observation of the thin films by AFM and SEM was performed. Films were investigated both before and after annealing.

The films of the HBCs before and after annealing at 120 °C for 1 h are shown in Figure 4.24. The features became clearer for HBC-C<sub>6,2</sub> and HBC-C<sub>14,10</sub> after annealing, and larger for HBC-C<sub>10,6</sub>. As discussed before, the three HBC derivatives are in a crystalline

phase or plastic crystalline phase at RT. The different features observed by AFM indicate that the derivatives have different types of crystals. SEM was applied to observe the annealed films on a larger scale, and the images are shown in Figure 4.25.

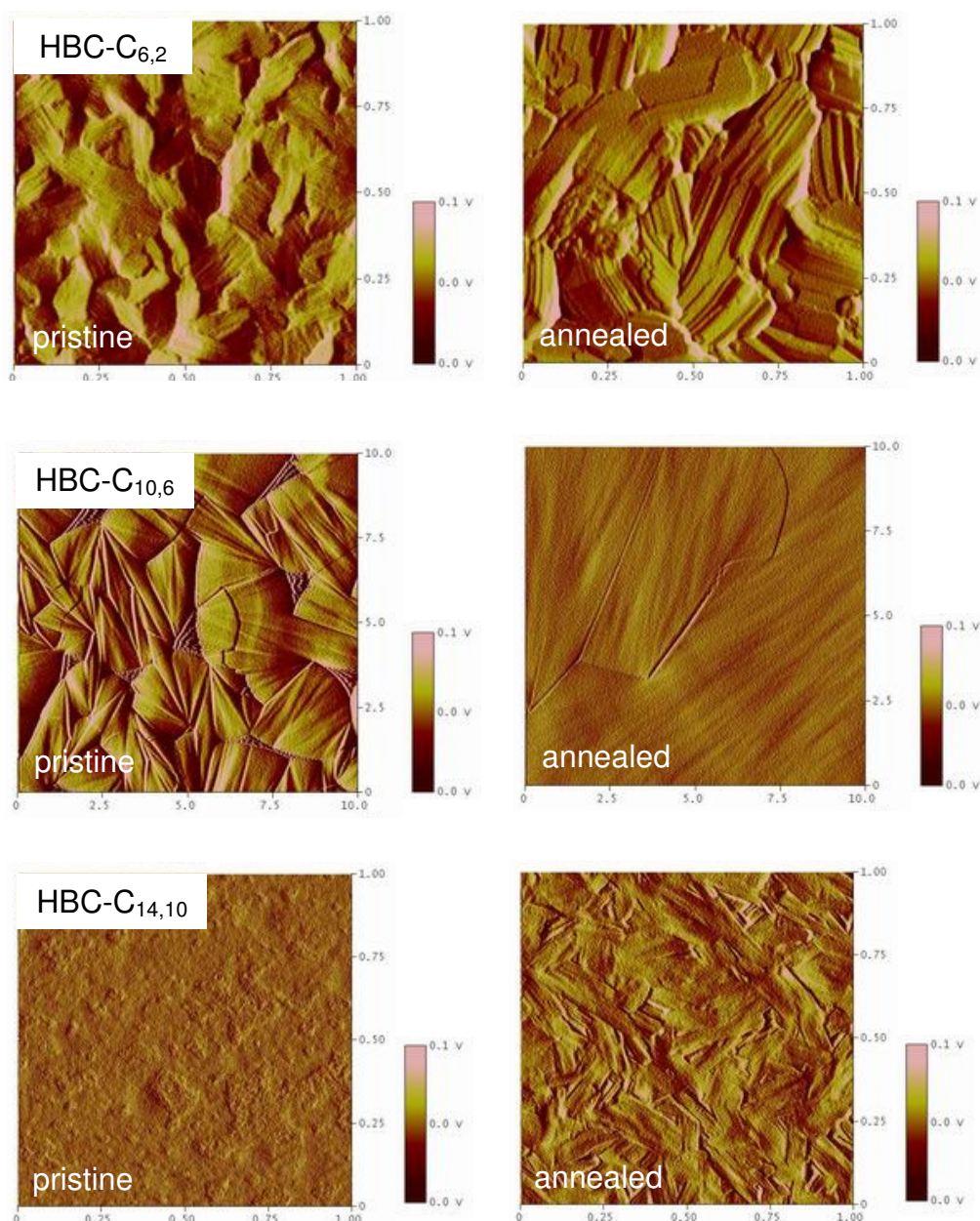




**Figure 4.24** AFM images of HBCs as thin films on silica wafer. Both pristine (left row) and annealed (right row) films are shown.

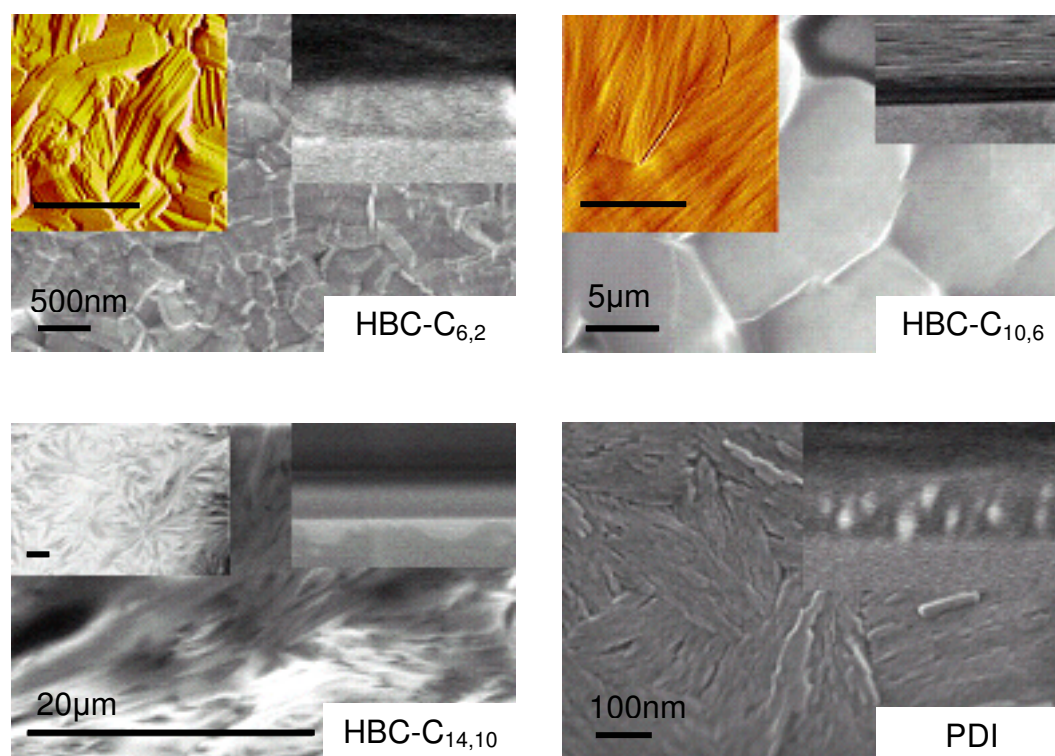


**Figure 4.25** SEM and AFM (insets on the left) images of HBCs and PDI as thin films on a silica wafer. The right insets show the section view, imaged with the substrate tilted  $15^\circ$  from normal to the incident electron beam. All the films were annealed at  $120^\circ\text{C}$  for 1 h in a nitrogen atmosphere.

In HBC- $\text{C}_{6,2}$ , a parallel arrangement of cylindrical crystals resulted in flake like domains with a thickness of about 5 nm, while HBC- $\text{C}_{10,6}$  showed only a blurred texture. HBC- $\text{C}_{14,10}$  formed typical spherulitic crystals with a diameter of ca.  $60\ \mu\text{m}$ . For PDI, foliage crystals composed of parallel cylindrical crystals were observed lying on the substrate. Cross-sectional SEM images were also taken to investigate the internal morphology of the thin film. As shown in the insets in Figure 4.25, no apparent morphology was observed for any of the HBCs, while for PDI, typical cylindrical crystals were seen.



### Morphology Study on the Blends

The morphologies of the films obtained upon blending the donor and acceptor together differed from those of the pure materials. Films of different D/A ratios (HBC:PDI=2:8, 4:6, 5:5, 6:4) were investigated (Figure 4.26).

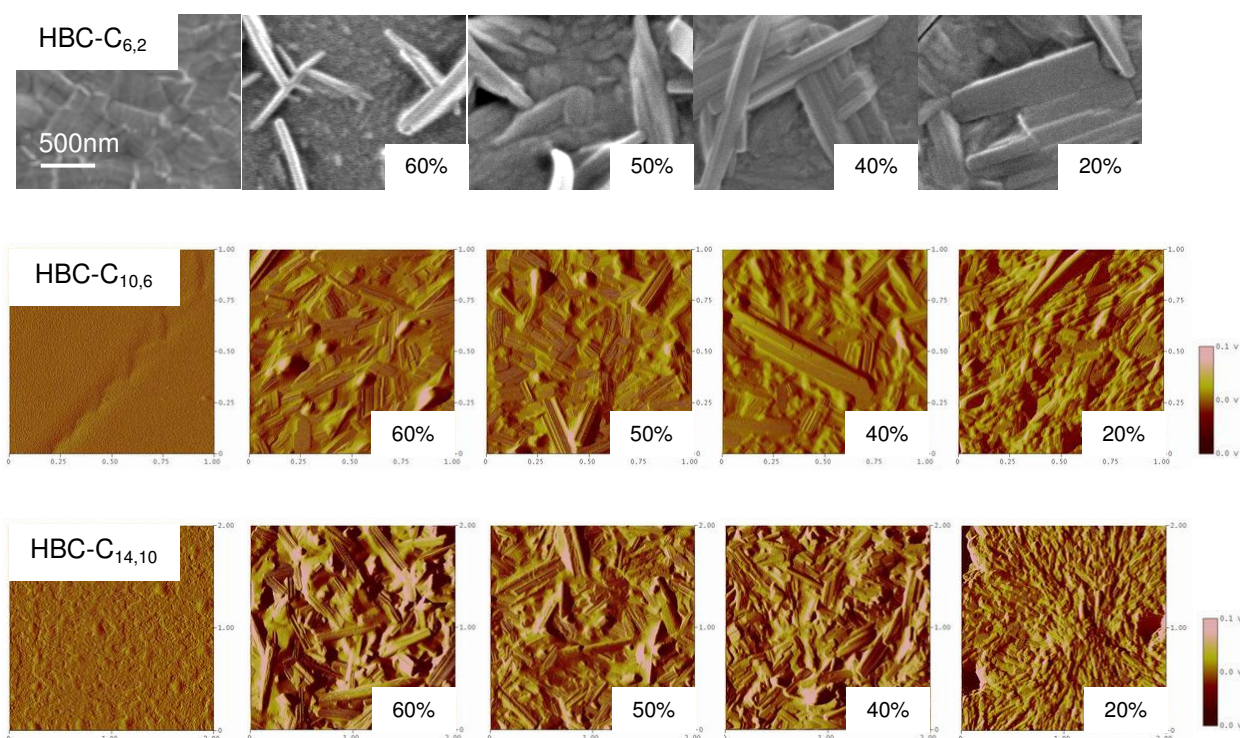
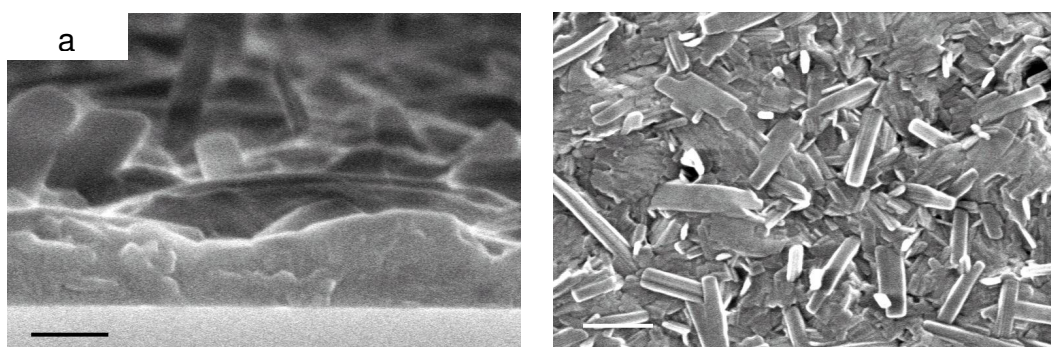


**Figure 4.26** SEM and AFM images ( $1 \times 1 \mu\text{m}^2$  for HBC-C<sub>10,6</sub> and  $2 \times 2 \mu\text{m}^2$  for HBC-C<sub>14,10</sub>) of the blend samples at different D/A ratios (by weight). The percent numbers indicate the content of HBC in the blend. The films of HBCs are also given for comparison.

For films containing 60 wt% HBC-C<sub>6,2</sub>, the relatively small crystals of PDI are surrounded by large areas without apparent features. When the content of HBC-C<sub>6,2</sub> is lower than 40%, the films are covered by big crystals with features similar to those in a PDI film. For the other two HBCs with longer alkyl substituents, more and more

cylindrical crystals are observed as the PDI content in the film increases. To conclude, as the content of PDI increases in the blend, the cylindrical crystals become the dominant feature for all films. This confirms that the cylindrical crystals belong to the PDI in the blend.

The films containing 40% HBC and 60% PDI were further investigated after the thermal treatment, which strongly influenced the film morphology, with the roughness increasing by a factor of 7~10. As shown in Figure 4.27, although similar columnar crystals were observed on the surface for all three blends, the bulk morphology appeared to be quite different in their cross-section images. Thin films of HBC-C<sub>10,6</sub>:PDI and HBC-C<sub>14,10</sub>:PDI were ‘homogeneous’ across the thickness with cylindrical crystals evenly dispersed from bottom to top. However, in the films of the HBC-C<sub>6,2</sub>:PDI, the bottom layer is rather featureless with some crystals protruding from the surface. This difference can be explained by the different thermal behavior of the introduced donor compounds. When cooled down from the annealing temperature of 120 °C, the PDI crystallized in a mobile, soft matrix of HBC-C<sub>10,6</sub> and HBC-C<sub>14,10</sub>, which were either isotropic or in the mesophase. By contrast, HBC-C<sub>6,2</sub> crystallized thermally before PDI and precipitated to the bottom, which led to the formation of smaller and more defined crystal domains of PDI. This crystallization resulted in concentration gradients of HBC-C<sub>6,2</sub> and PDI within the film. Therefore, more HBC was deposited close to the ITO while PDI was enriched at the aluminum electrode, thus offering good percolation pathways for the charges.



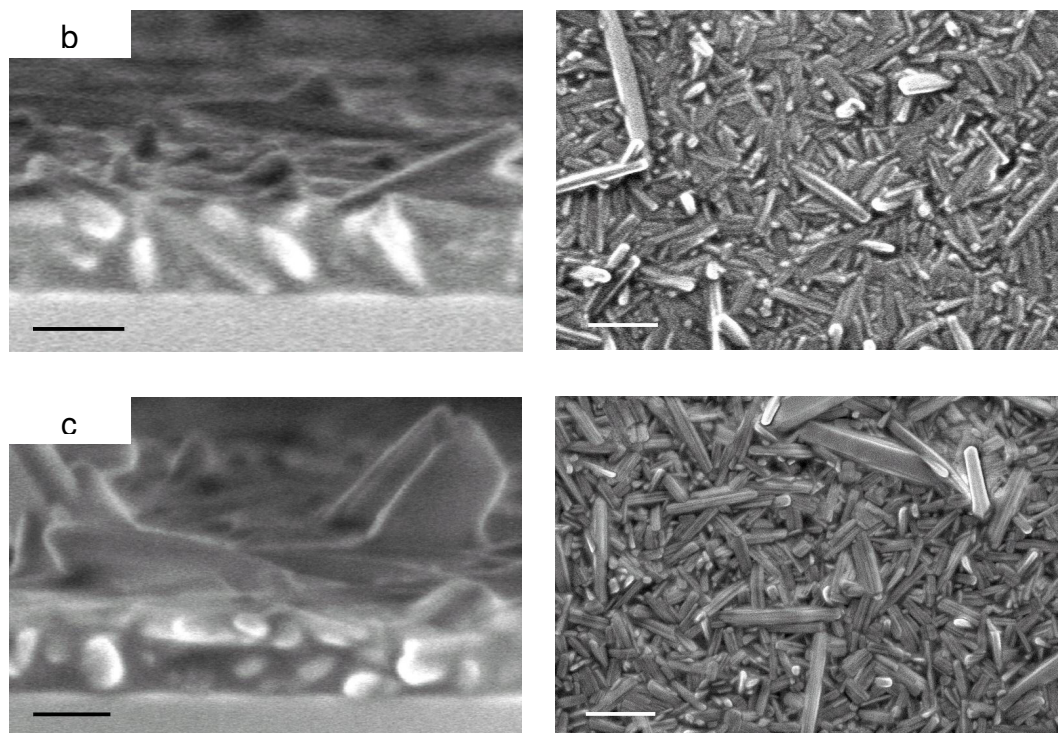


**Figure 4.27** SEM images of the cross-section view of the blend sample (scale bar for 100 nm): a) HBC-C<sub>6,2</sub>:PDI (4:6), b) HBC-C<sub>10,6</sub>:PDI (4:6), and c) HBC-C<sub>14,10</sub>:PDI (4:6). The top view images were also shown on the right (scale bar for 500nm). All the films were annealed at 120 °C for 1 h in a nitrogen atmosphere.

In general, phase segregation between the donor and the acceptor is required to establish separate percolation pathways. For the fusible derivatives (exhibiting isotropic state) with the longer branched alkyl chains, one can speculate that the two components did not segregate from the highly mobile phases and thus formed a mixed phase, leading to columnar structures containing both compounds. This has recently been observed for a PDI derivative and HBC-C<sub>10,6</sub> after melt-processing by Dr. W. Pisula.<sup>178</sup> The mixed phase thus resulted in an intimate contact between the donor and the acceptor on molecular level, which offered a large D/A interface for charge separation at the cost of a lack of separate percolation pathways.

#### 4.3.6 Summary

Blends of a series of HBCs bearing varied lengths of alkyl substituents with PDI have been tested as active layers in bulk heterojunction photovoltaic devices. The device efficiency has been found to decrease with increasing length of the substituents in the HBC. Thus, the derivative with the smallest alkyl mantle, being more crystalline compared to the HBCs with longer alkyl chains, gave the highest  $\text{EQE}_{\text{max}}$  of 12%. A large interfacial separation was found in the blend of HBC-C<sub>6,2</sub> and PDI, since the crystallization of the acceptor occurred in a solid matrix of HBC. This led to small dispersed organized domains and benefited the charge transport. In contrast, blends of HBC-C<sub>10,6</sub>/PDI or HBC-C<sub>14,10</sub>/PDI revealed a rather homogeneous film limiting the percolation pathways due to a mixed phase. The correlation between the film morphology and the device performance indicated that the ordered separate domains for both the donor and the acceptor were the dominant factor in this D/A system. The lower amount of insulating alkyl surroundings did not hinder the exciton polarization and separation, which stood in contrast to the highly shielded derivatives with the longer side chains. This was verified by the stronger oxidation peak of HBC-C<sub>6,2</sub> than HBC-C<sub>10,6</sub> and HBC-C<sub>14,10</sub> in the CV measurement, and further the biggest  $I_{\text{sc}}$  obtained by HBC-C<sub>6,2</sub> containing device. The higher concentration of the aromatic chromophore in this system led to a higher photon absorption and therefore to a more efficient exciton creation. This study has provided a deeper insight into the structure-performance relations in photovoltaic devices not only for discotic materials.

#### 4.4 HBC-C<sub>3</sub>OC<sub>10,6</sub> - A New Discotic Material for Solar Cells

Except for the HBCs with dove-tailed side alkyl chains branched at the  $\beta$ -position, the performance in a solar cell of an HBC with ether linkages on the side chain was also investigated. It has been reported that smaller discotic systems such as triphenylenes<sup>179</sup> and phthalocyanines<sup>180</sup> bearing alkoxy groups at or within their core periphery, revealed spontaneous face-on arrangement inducing macroscopic homeotropic alignment with the columnar axis perpendicular to the substrate. This alignment is desired in the active layer for photovoltaic devices, since it coincides with the direction of charge transport. The

heteroatoms in the molecules influenced strongly the supramolecular arrangement. Therefore, oxygen has been introduced into the side chains of HBC materials to enhance their ability to homeotropically align. HBC-C<sub>3</sub>OC<sub>10,6</sub> was synthesized by B. El Hamaoui.

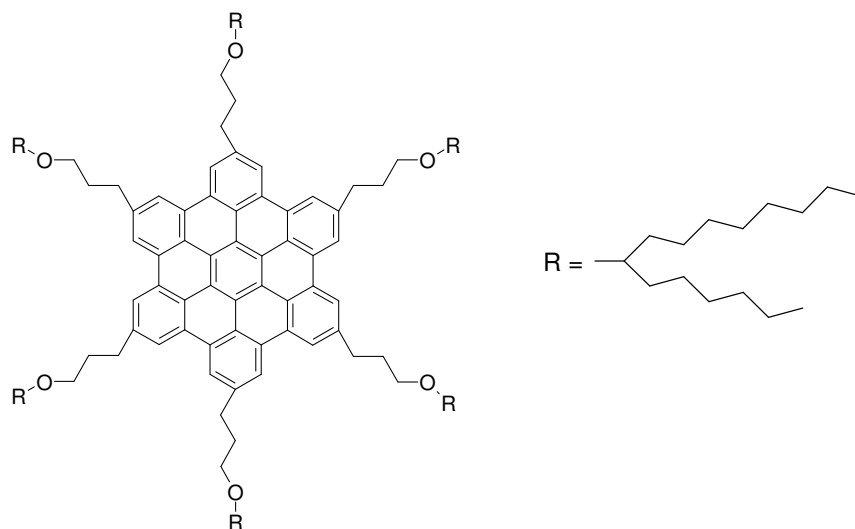


**Figure 4.28** Molecular structure of HBC-C<sub>3</sub>OC<sub>10,6</sub>

HBC-C<sub>3</sub>OC<sub>10,6</sub> is a room temperature liquid crystal, and goes into the isotropic melt at around 162 °C. The thermal properties are listed in Table 4.7.

**Table 4.7** Thermal behaviour determined by DSC for HBC-C<sub>3</sub>OC<sub>10,6</sub>. The re-crystallization temperatures and the enthalpies during cooling are given in brackets.

Temperature (°C)	Enthalpy (J.g <sup>-1</sup> )	Phase transition
-1 (-5)	13.8 (12.9)	Col <sub>p</sub> -Col <sub>d</sub>
162 (155)	2.9 (3.5)	Col <sub>d</sub> -I

No bathochromic shift was observed for HBC-C<sub>3</sub>OC<sub>10,6</sub> in comparison with alkyl substituted HBCs, which was ever reported for alkoxythiophene based polymers and copolymers<sup>181,182</sup> due to the electron-donating effect of the alkoxy group and the more



planar conformation of the polymers.<sup>183,184</sup> This indicates that the effect of alkoxy is suppressed by the strong  $\pi$ - $\pi$  interactions of the planar HBC cores.

During controlled cooling between two glass or aluminium surfaces, HBC-C<sub>3</sub>OC<sub>10,6</sub> aligned uniformly homeotropically, even at cooling rates as fast as 20 °C min<sup>-1</sup>, proving the high attraction of the polar groups to this kind of surface.<sup>185</sup> However, when the thickness decreased to 100 nm, the film forming became a problem for fabricating devices. The material tended to de-wet from the ITO substrate during cooling from the isotropic state (Figure 4.29). This limits the application of HBC-C<sub>3</sub>OC<sub>10,6</sub> directly as donor material for PDI, since the latter bears also a poor film forming ability. The same problem was reported for poly(3-decyloxythiophene), which did not have sufficiently high uniformity for fabricating devices due to poor film forming ability.<sup>186</sup>

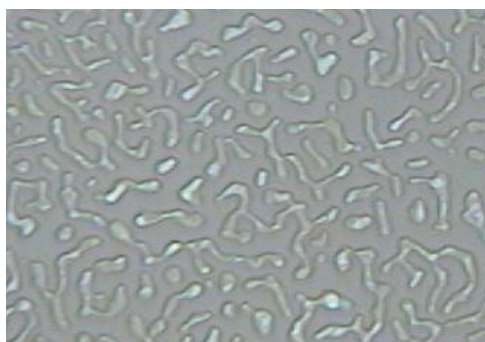


**Figure 4.29** Film of HBC-C<sub>3</sub>OC<sub>10,6</sub> spin-coated from chloroform solution onto glass.

In order to optimise the film forming property of HBC-C<sub>3</sub>OC<sub>10,6</sub>, HBC-PhC<sub>12</sub> was adopted as a second donor material in the HBC/PDI device. HBC-PhC<sub>12</sub> has a similar molecular structure, therefore it's expected to be well miscible with HBC-C<sub>3</sub>OC<sub>10,6</sub> and to form homogeneous domains of HBCs. The homeotropic arrangement of HBC-C<sub>3</sub>OC<sub>10,6</sub> can also possibly induce the organization of HBC-PhC<sub>12</sub> to form better percolation pathways for charge transport (Figure 4.30).

Devices were fabricated with active layers containing HBC-C<sub>3</sub>OC<sub>10,6</sub>/HBC-PhC<sub>12</sub>/PDI (2:2:6) or HBC-PhC<sub>12</sub>/PDI (4:6) doped with 5% HBC-C<sub>3</sub>OC<sub>10,6</sub>. Thermal treatment was performed on the devices to induce homeotropic arrangement. The results are shown in Figure 4.31.

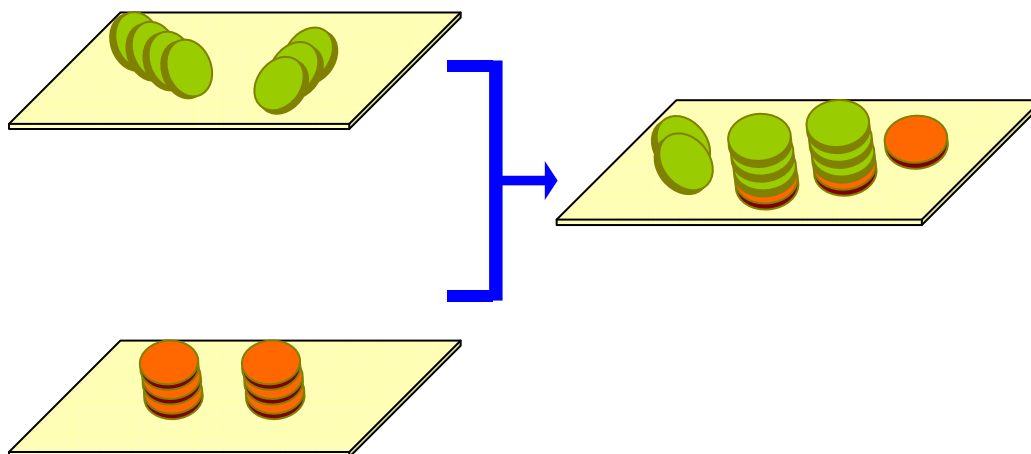


**Figure 4.30** Illustration of  $\text{HBC-C}_3\text{OC}_{10,6}$  (red disk) induced face-on arrangement of  $\text{HBC-PhC}_{12}$  (green disk).

The device having 5%  $\text{HBC-C}_3\text{OC}_{10,6}$  showed a maximum EQE value of 16% at 485 nm, which is markedly higher than that of the device containing 20%  $\text{HBC-C}_3\text{OC}_{10,6}$  ( $\text{EQE}_{\text{max}} = 6\%$ ). Both are notably less efficient than the  $\text{HBC-PhC}_{12}:\text{PDI}$  (4:6) device without  $\text{HBC-C}_3\text{OC}_{10,6}$ , however. After annealing in the isotropic state of  $\text{HBC-C}_3\text{OC}_{10,6}$  ( $170^\circ\text{C}$ ), short-circuit tended to occur in all devices. This resulted from the de-wetting effect of  $\text{HBC-C}_3\text{OC}_{10,6}$ , leading to inhomogeneous or even discontinuous films where charge flows through the pin holes.

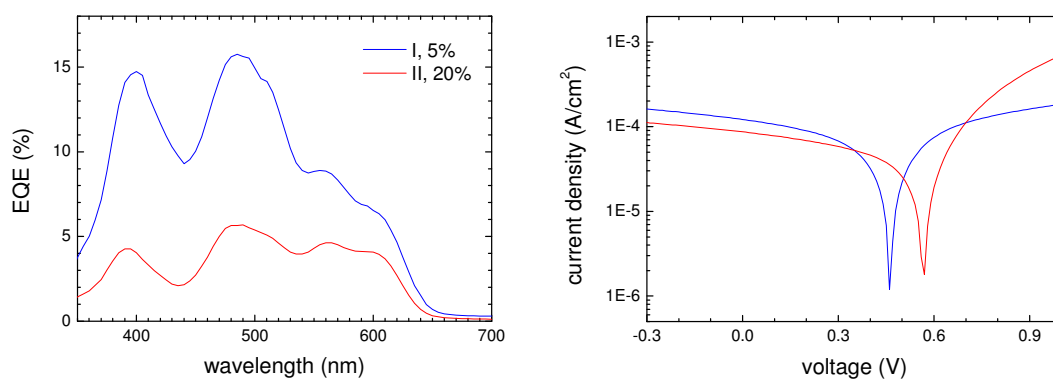


**Figure 4.31** Device **I** of ITO/HBC-PhC<sub>12</sub>:PDI (4:6)/Ag, doped with 5% HBC-C<sub>3</sub>OC<sub>10,6</sub> (blue line). The corresponding I-V curve was recorded under sunlight with light intensity of 99 W/m<sup>2</sup>; and device **II** of ITO/HBC-PhC<sub>12</sub>:HBC-C<sub>3</sub>OC<sub>10,6</sub>:PDI (2:2:6)/Ag (red line), with I-V curve recorded under sunlight ( $I_{inc} = 121 \text{ W/m}^2$ ).

**Table 4.8** Average photovoltaic performance

Device	$I_{sc}$ ( $\mu\text{A/cm}^2$ )	$V_{oc}$ (V)	FF	$\eta$ (%)	$\text{EQE}_{max}$ (%)
<b>I</b> (5% HBC- C <sub>3</sub> OC <sub>10,6</sub> )	0.12	0.46	0.36	0.21	16
<b>II</b> (20% HBC- C <sub>3</sub> OC <sub>10,6</sub> )	0.09	0.57	0.37	0.15	6

The device did not show the expected high efficiency, although HBC-C<sub>3</sub>OC<sub>10,6</sub> was introduced to induce the possibly realizable face-on self-organization of HBC-PhC<sub>12</sub>, which was observed in the film of HBC-C<sub>3</sub>OC<sub>10,6</sub>. This indicated that the homeotropic alignment was not realized, since otherwise a high  $I_{sc}$  could be achieved due to the better percolation pathways for charges. The occurrence of short-circuit for devices after the thermal treatment illustrated that the film forming ability of the blend was the reason for the poor performance because the de-mixing of the blends may happen during annealing. This also partly explained the lower efficiency for the device containing more HBC-C<sub>3</sub>OC<sub>10,6</sub>. Therefore, the improvement on film forming ability must be fulfilled in order to apply this kind of molecular design in thin film devices.

It has been shown that HBC without heteroatoms on the periphery has good film forming ability, especially for those with phase transition temperature (Cry-LC or Cry-I) near RT. This indicates that the introduction of the heteroatoms is the source of the problem, thus supplying the possibility of reducing the number of heteroatoms as one resolution. Therefore, a compromise between the homeotropic alignment and the film forming ability is required for the optimal performance of the device. The other way is to increase the solubilizing alkyl groups on the periphery. It has been reported that the branched and long alkyls can reduce the phase transition temperature for HBCs<sup>187</sup> and improve the film forming ability of the material. For copolymers of thiophene and benzothiadiazole and benzobis(thiadiazole), side chains of hexyl, dodecyl, and 2-ethylhexyl gave polymer products with low molecular weight and poor solubility, while



3,7,11-trimethyldodecyl side chains gave polymer products with higher molecular weight, good solubility, and film forming ability.<sup>188</sup>

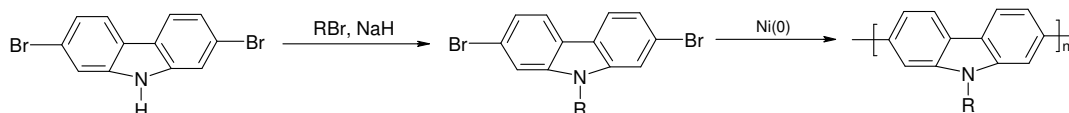
## Chapter 5 Poly(2,7-Carbazole)s as Donor Materials in Photovoltaics

It has been mentioned earlier that due to the electron-donating properties of the nitrogen atoms, poly(2,7-carbazole)s (PCz) are promising materials for solar cells. However, their application has not been explored so far. One reason is that due to their relatively low number of solubilizing groups they tend to have low molecular weights.<sup>189</sup> For conjugated polymers like P3HT, the molecular weight can control the microstructures in films, which is decisive for charge carrier mobility.<sup>190</sup> Low-molecular-weight P3HT (the number average molecular weight  $M_n < 4000$  g/mol) has a photoresponse limited by confinement of the conjugation length, generally accepted to be greater than, but not far from, 20 units.<sup>191</sup> This value is increased by solid-state effects. P3HT of ca. 10 000 g/mol, which forms crystalline nanorods, exhibits low charge mobilities due to poor long-range interconnectivity of polymer chains. P3HT of a higher molecular weight ( $M_n$  ca. 30 000 g/mol) displays a completely different structure, based on crystalline, interwoven fibrils connected over long distances (ca. 500 nm), which lead to improved values of charge mobility.<sup>190</sup> After blended with PCBM in the device, it is found that high power conversion efficiencies above 2.5% can only be achieved if  $M_n$  is greater than 10 000 g/mol.<sup>192</sup> Furthermore, the optimized performance of the device was related to the condition of thermal treatment at varied molecular weights.<sup>69,193-199</sup> Based on this, PCz with high molecular weight is required in order to apply the material in photovoltaics. Fortunately, this was realized by F. Dierschke in our group using Yamamoto type polymerisation.<sup>92</sup> Here, the use of various carbazole-based polymers as donor materials in photovoltaics is examined for the first time. All the devices were optimized to establish a correlation between the molecular structure and the device performance.

### 5.1 Introduction

#### 5.1.1 Synthesis of Poly(2,7-carbazole)

PCz was synthesized from 2,7-dibromocarbazole<sup>92</sup> by alkylation with 2-decyltetradecylbromide<sup>187</sup> followed by Ni(COD)<sub>2</sub> mediated Yamamoto polymerisation carried out in a DMF/toluene mixture under an argon atmosphere.<sup>200</sup>



**Scheme 5.1** Synthesis of PCz

The ‘long dove tail’ alkyl chains were introduced to improve the processibility of the material. It has been shown previously that this is an efficient way to increase the solubility of perylene based dyes<sup>201,202</sup> and two-dimensional polycyclic aromatic hydrocarbons.<sup>187</sup> The resulting PCz is highly soluble in common organic solvents such as chloroform, or toluene, and shows excellent film-forming properties.

The polymer has  $M_n$  of  $3.9 \times 10^4$  g/mol with  $D = 1.93$  (PS standard), which is higher than the required  $M_n$  of P3HT (10 000 g/mol) as reported for devices.<sup>192</sup> Therefore, PCz is explored in this work for its application as donor material in the organic bulk heterojunction devices. The DSC measurement was performed within a temperature range of  $-50$  °C ~  $250$  °C, and revealed one phase transition peak at  $232$  °C. It was reported for poly(2,7-(9-octadecylcarbazole)) that the phase transition at  $108$  °C was presumably as the melting point due to the crystallization of the side chains,<sup>203</sup> like what observed for some alkyl substituted polythiophenes.<sup>204</sup>

### 5.1.2 Optical Properties

The UV-vis absorption spectra of PCz were observed both in CHCl<sub>3</sub> solution (1 mg/50 ml) and in a thin film spin-coated from concentrated solution (15 mg/ml). As shown in Figure 5.1, the absorption maximum in solution is at 391 nm, with a 5 nm bathochromic shift in the thin film, which might be due to the  $\pi$ -stacking of the polymer chains in the solid state and will be further discussed in Chapter 5.3.3. Fluorescence of the film was

excited at 380 nm. The spectrum exhibits a peak at 429 nm, with finer characters than the absorption spectrum.

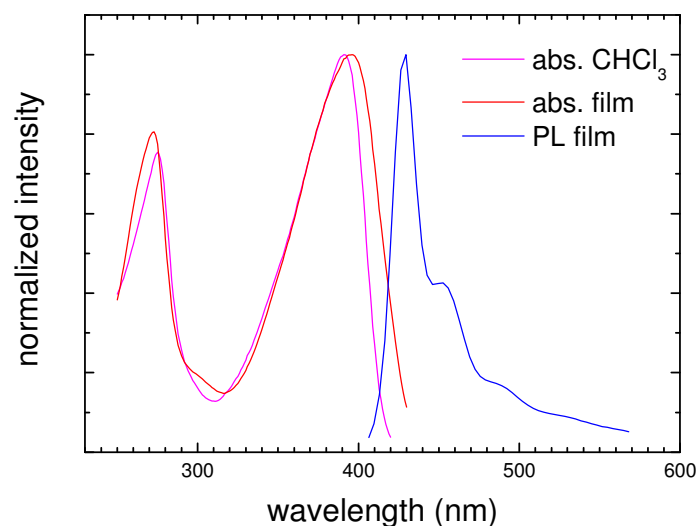


**Figure 5.1** Absorption and PL spectra of PCz in solution and as thin films on quartz glass.

The absorption of PCz is mainly in the violet or ultraviolet, which forms only a small proportion of solar light. In this case, a material with strong absorption in the ~2-3 eV range would be required as acceptor in order to enhance the ability of light absorption in the strongest emission part of the solar spectrum, to ensure that as many photons as possible contribute to the photon-electron conversion.

### 5.1.3 Characterization of Energy Levels

The potential applicability of PCz in solar cells was confirmed by determination of the frontier molecular orbital energy levels by CV measurements. A thin film on an ITO substrate was tested in a three-electrode system. An irreversible oxidation peak with an onset potential vs. ferrocene of 0.8 V was observed. The corresponding HOMO energy level was thus decided to be -5.6 eV. The bandgap calculated from the absorption spectrum of the thin film is 3.0 eV, so the LUMO is at -2.6 eV. The curve shown in Figure 5.2

revealed the clear irreversible oxidation of PCz, indicating unfavourable reduction for this material. This was explained by the formation of the dimer during the oxidation by cross linking the active 3- or 6- position.<sup>189,205-207</sup> It has also been found that if the 3- and 6-positions are substituted, reversible oxidation can be observed.<sup>208,209</sup>

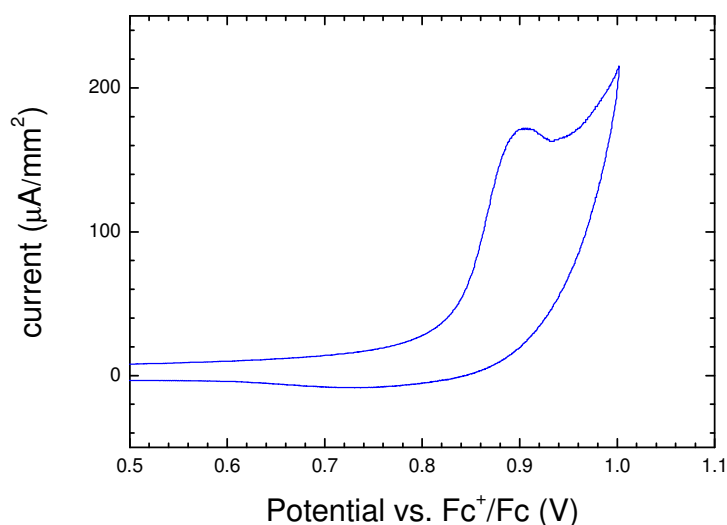


**Figure 5.2** CV curve of PCz in thin film at a scanning rate of 100 mV/s.

The HOMO level of PCz (-5.6 eV) is lower than polythiophene (-5.2 eV) and PPV (-5.1 eV), so it is in principle less easily oxidized and so more stable towards air. The HOMO level is relatively low, being comparable to that of some potential acceptor materials such as PDI (-5.8 eV) and derivatives of terrylene tetracarboxdiimide (TDI, -5.4 eV). When one considers the energy level matching of the two components in the solar cell, this means an acceptor with a lower HOMO energy level than -5.6 eV is required when using PCz as the donor material.

#### 5.1.4 Comparison of PCz and PF in Solar Cell

Poly(dialkylfluorene)s (PFs) are important conjugated semiconducting materials with potential for high-performance emissive and photo-responsive applications.<sup>210</sup> The

HOMO/LUMO energies for poly(dioctylfluorene) have been measured by CV as being -5.8/-2.3 eV.<sup>211</sup> An efficient charge generation has been observed by Cavendish Lab researchers in a blend of hole-accepting and electron-accepting fluorene copolymers.<sup>212-214</sup> The corresponding photovoltaic efficiency values depended strongly on the morphology of the films. PCz has a similar molecular structure to PF, in which the electron rich nitrogen might facilitate charge flow along the chain and make it a better electron donor than PF.

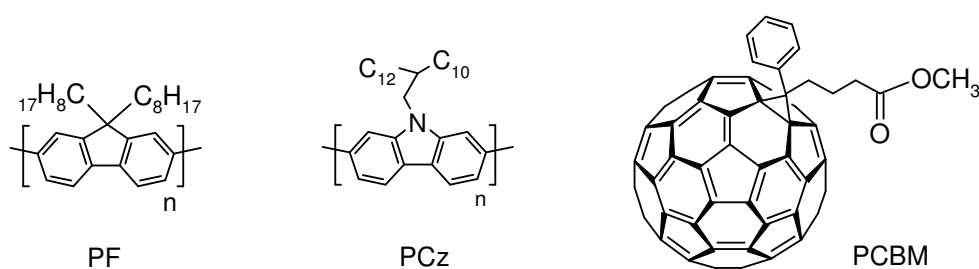


**Figure 5.3** Chemical structures of PF, PCz, and PCBM.

Motivated by these results, we fabricated solar cells using PF and PCz as donor materials to compare their capabilities as electron donors. PCBM was chosen as the acceptor material because of its successful application in polymer based solar cells. It satisfies the energy level requirement, with its HOMO/LUMO values being at -6.0/-4.1 – -4.3 eV.<sup>80,215</sup> The devices used ITO as the anode and silver as the cathode. The active layer was composed of PCz/PCBM or PF/PCBM at a ratio of 1:1 (weight), with a thickness of about 100 nm. The results are shown in Figure 5.4.

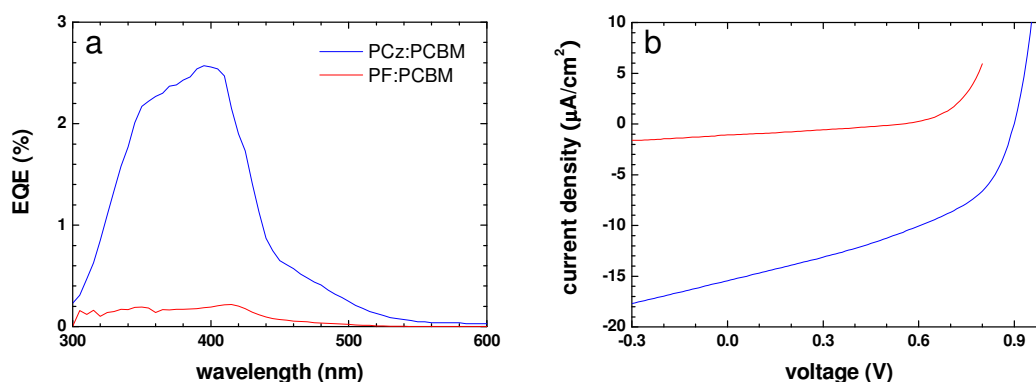


**Figure 5.4** Photovoltaic performance of devices ITO/PCz:PCBM(1:1)/Ag and ITO/PF:PCBM(1:1)/Ag: a) EQE- $\lambda$  curve, and b) I-V curve under solar light AM1.5 G with light intensity of 115 W/m<sup>2</sup>.

**Table 5.1** Average photovoltaic performance

Active layer	I <sub>sc</sub> ( $\mu\text{A}/\text{cm}^2$ )	V <sub>oc</sub> (V)	FF	Efficiency (%)	EQE <sub>max</sub> (%)
PCz/PCBM (1:1)	15	0.90	0.44	0.05	2.5
PF/PCBM (1:1)	1	0.55	0.29	0.001	0.2

The device containing PCz is clearly much more efficient than the device based on PF. The photocurrent of the PCz cell is much higher, which indicates a more efficient charge transport if one assumes comparable numbers of charges are produced from the similar light absorption. The charge transport properties are normally evaluated by charge carrier mobility of the material. The mobility depends on the chemical structure and chain length/aggregates, which is attributable at least in part to the existence of electron-rich N-atoms along the chain.

This result shows that PCz is a promising donor material in organic solar cells. The optimization of the device is discussed in the following section.

## 5.2 Photodiodes Based on PCz

### 5.2.1 Pairing PCz with PDI or PCBM

It has been shown that PDI is a good acceptor for HBCs,<sup>43,140</sup> as well as for conjugated polymers.<sup>145,146</sup> Besides, PCBM is the most successful acceptor material in

organic photovoltaics.<sup>29,38,39</sup> Therefore, both PDI and PCBM were chosen as potential acceptor materials for PCz. These two acceptors were compared with regard to:

- Light absorption
- Charge transfer (PL quenching of PCz)
- Matching of energy levels
- Device performance

### 5.2.1.1 Optical Properties of the Blends

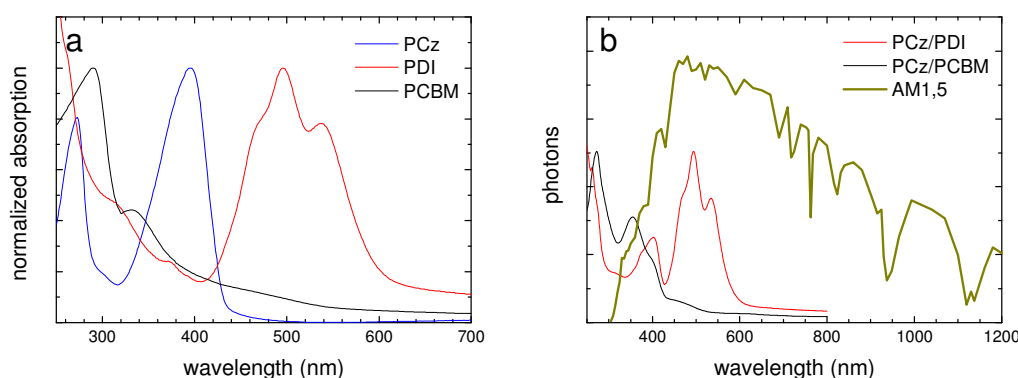


**Figure 5.5** UV absorption spectra of a) PCz, PDI, PCBM in thin films, and b) blend thin films at a D/A ratio of 1:4, the AM 1.5 G solar spectrum is shown for comparison.

The band-gap in PCz is not small ( $\sim 3$  eV), and hence a material with a strong absorption in the 2-3 eV range is required as acceptor in order to achieve a device with high efficiency. PDI has an absorption maximum at 524 nm in  $\text{CHCl}_3$  and at 537 nm in a thin film (Figure 5.5a). PCBM shows an absorption peak at 332 nm with an extended tail to 600 nm. When one compares blends of PCz with each of these two acceptors, one sees that the PCz/PDI film achieves a broad absorption from 300 nm to 600 nm, covering the strongest emission of the solar spectrum (Figure 5.5b), whereas the PCz/PCBM film only shows strong absorption below 400 nm, and so has a much smaller overlap with the solar



spectrum. Therefore, PDI compensates PCz more efficiently than PCBM does in terms of light absorption.

### 5.2.1.2 Matching Energy Levels of D/A

As part of the current work CV measurements were performed on PDI films on an ITO substrate (see Figure 4.19).<sup>216</sup> The HOMO and LUMO levels were estimated to be at -5.8 eV and -3.8 eV, respectively. The corresponding levels for PCBM have been reported to be at -6.0 eV and  $\sim$ -4.1 – -4.3 eV.<sup>80,215</sup> Both materials can potentially be used as an acceptor materials with PCz as donor, as illustrated in Figure 5.6.

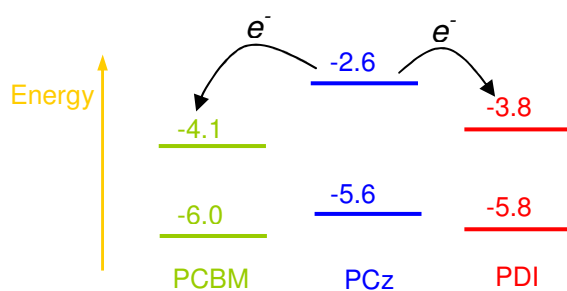


**Figure 5.6** Potential diagram for the materials used to fabricate the devices.

### 5.2.1.3 Charge Transfer from the Donor to the Acceptor

The fluorescence quenching of the donor material by adding acceptor material was used to verify the charge transfer from the donor to the acceptor. Fluorescence measurements on thin film blends of PCz with PDI or PCBM at a ratio of 1:1 were taken. As shown in Figure 5.7, the fluorescence peak of PCz at 429 nm is almost fully quenched by adding the same weight of PDI or PCBM. At the same time, no enhancement of fluorescence of PDI or PCBM is observed. This indicates an efficient charge transfer from PCz to PDI and PCBM.

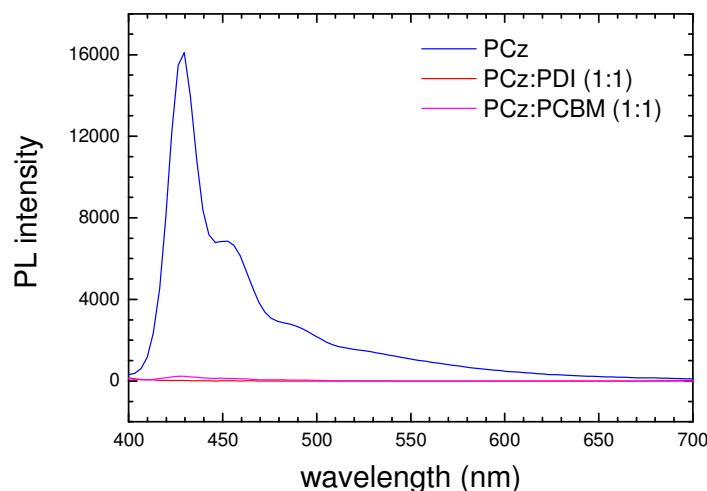


**Figure 5.7** The fluorescence spectra of PCz, and its blend with PDI or PCBM in thin films. The blue line is for PCz, red for PCz/PDI film, and purple for PCz/PCBM film.

This was further verified by calculating the energy variation in the two competing processes, that is, charge transfer (CT) and energy transfer (ET). The changes in free energy for CT ( $\Delta G_{CT}$ ) and ET ( $\Delta G_{ET}$ ) were used to evaluate the process. When  $\Delta G_{CT} < \Delta G_{ET}$ , charge transfer tends to occur. The data were listed in Table 5.2. The energy levels of the first singlet-excited state ( $E(S_1)$ ) was obtained from the thin film fluorescence spectra. PDI was used for calculation since PCBM was not easy for self-fluorescence. The onsets of oxidation ( $E_{ox}$ ) and reduction ( $E_{red}$ ) were tested by CV in the previous work in order to decide the HOMO/LUMO potential levels of the material.

**Table 5.2** Change in free energy for CT and ET for the blend of PCz/PDI, calculated from  $\Delta G_{CT} = (E_{ox}^D - E_{red}^A) - E(S_1)^D$  and  $\Delta G_{ET} = E(S_1)^A - E(S_1)^D$

Material	$\lambda_{emi}$ (nm)	$E(S_1)$ (eV)	$E_{ox}^*$ (V)	$E_{red}^*$ (V)	$E_{ox}^D - E_{red}^A$	$\Delta G_{CT}$	$\Delta G_{ET}$	$\Delta G_{CT} - \Delta G_{ET}$
PCz (D)	429	2.9	0.8	1.0				
PDI (A)	575	2.2	-2.2	-1.0				
D:A					1.8	-1.1	-0.7	-0.4

\*values vs. Fc/Fc<sup>+</sup>

The above calculation clearly showed  $\Delta G_{CT} - \Delta G_{ET} < 0$ , indicating that charge transfer would occur in the D/A pair of PCz/PDI. However, as shown by Friend et al. extra energy was required to separate the bulk exciton into two separate charges.<sup>217</sup> Further, the energy was decided to be in the range of 0.33 to 0.45 eV in the polymer-dye systems.<sup>218</sup> Based on these results, it can be concluded that charge transfer is energetically favourable than energy transfer.

#### 5.2.1.4 Photovoltaic Device

Photovoltaic devices were fabricated based on the blends of PCz/PDI and PCz/PCBM at a D/A ratio of 1:1. The results are summarized in Table 5.3. The EQE- $\lambda$  spectrum of the device using PCBM exhibits only one peak near 400 nm with a value of 2.5%. By contrast, the device using PDI has a broad EQE- $\lambda$  spectrum with two strong peaks showing EQE values of 3.4% at 420 nm and 3.8% at 500 nm, which corresponds to the absorption of PCz and PDI, respectively. The broader photo response of the latter leads to a higher  $I_{sc}$  ( $57 \mu\text{A}/\text{cm}^2$ ) for the device containing it, than for the device containing PCBM ( $15 \mu\text{A}/\text{cm}^2$ ). This results in a much higher overall efficiency for the device using PDI.

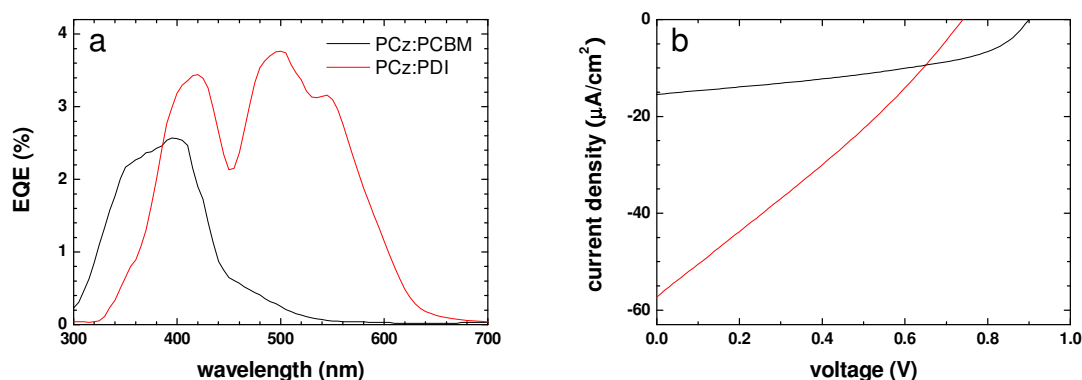


**Figure 5.8** Photovoltaic performance of devices ITO/PCz:PDI(1:1)/Ag (red curve) and ITO/PCz:PCBM(1:1)/Ag (black curve): a) EQE- $\lambda$  curve, and b) I-V curve under solar light AM1.5 G with light intensity of 100 W/m<sup>2</sup>.

**Table 5.3** Average photovoltaic performance

Active layer	$I_{sc}$ ( $\mu\text{A}/\text{cm}^2$ )	$V_{oc}$ (V)	FF	Efficiency (%)	$\text{EQE}_{max}$ (%)
PCz/PDI (1:1)	57	0.74	0.28	0.12	3.8
PCz/PCBM (1:1)	15	0.90	0.44	0.05	2.5

The higher photocurrent of the PDI device arises from more photons being absorbed by the active layer, as shown in the EQE- $\lambda$  spectrum. The relative area covered by the spectrum represents the relative number of photons which contribute to the photocurrent. For the PDI-containing device, this area is about two times of that for the device using PCBM, thus leading to a higher  $I_{sc}$ .

## 5.2.2 Optimization of Device PCz/PDI

The device using PCz as donor and PDI as acceptor was further optimized by varying the D/A ratio and the annealing procedure.

### 5.2.2.1 D/A Ratio

The ratio of donor/acceptor not only determines how large is the interface where the excitons can separate into electrons and holes, but that of the transport pathways as well. This is very important and can profoundly influence the device behavior. An optimized D/A ratio is necessary for achieving the best performance. Here, blends (PCz/PDI) with

varying weight ratios from 1:1 to 1:5 were tested. The results were summarized in Table 5.4.

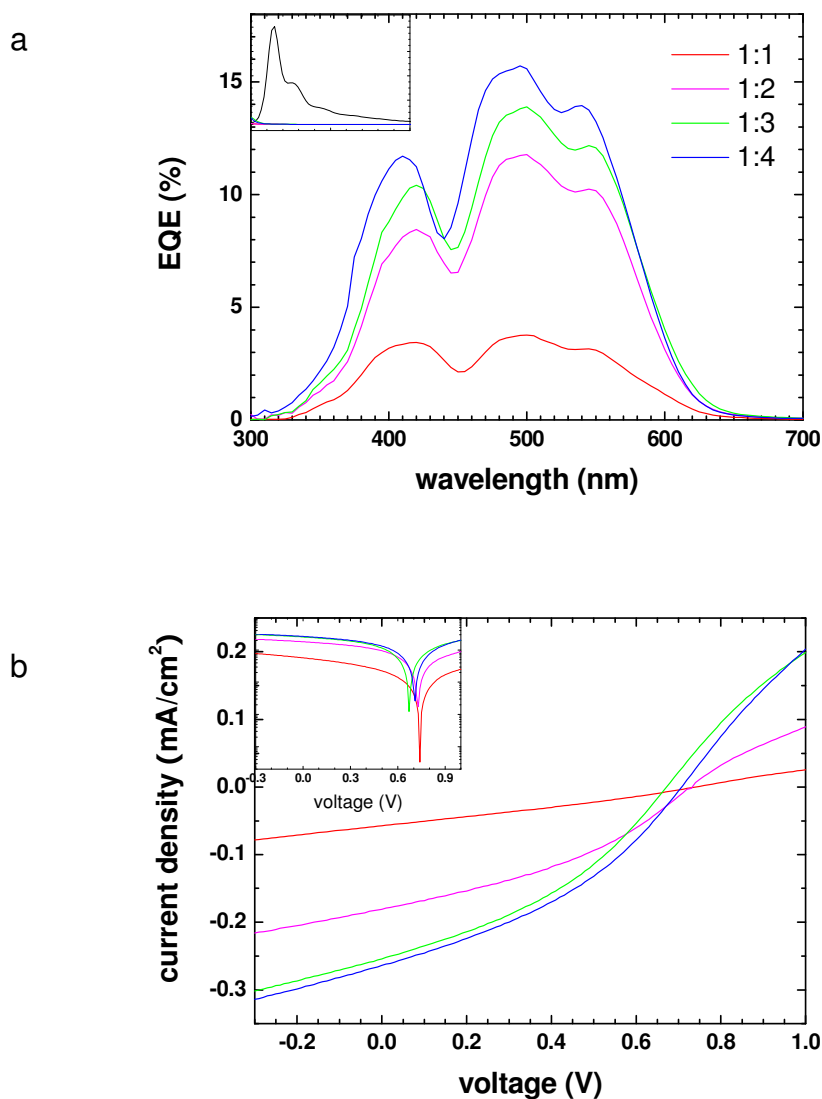


**Figure 5.9** Photovoltaic performance of devices ITO/PCz:PDI/Ag at different D/A ratios: a)  $EQE-\lambda$  curve, and b) I-V curve under solar light AM1.5 G with light intensity of  $100 \text{ W/m}^2$ . The insets are a) Fluorescence spectra of PCz and blends with PDI in thin film excited at 380 nm, b) I-V curve with logarithmic ordinate.

**Table 5.4** Average photovoltaic performance

PCz/PDI	$I_{sc}$ ( $\mu\text{A}/\text{cm}^2$ )	$V_{oc}$ (V)	FF	Efficiency (%)	$\text{EQE}_{max}$ (%)
1:1	57	0.74	0.28	0.12	3.8
1:2	180	0.73	0.37	0.48	11.8
1:3	254	0.67	0.37	0.63	13.9
1:4	264	0.71	0.37	0.67	15.7
1:5	456	0.32	0.30	0.44	19.9

It can be clearly seen that the PDI content strongly affects the photocurrent.  $I_{sc}$  increases from  $57 \mu\text{A}/\text{cm}^2$  at a 1:1 ratio to  $264 \mu\text{A}/\text{cm}^2$  at 1:4, i.e. about four times higher. The  $V_{oc}$  remains 0.7 V for different ratios, except for  $D/A = 1:5$ . The FF increases from 1:1 to 1:2, and then remains the same for ratios of 1:3 and 1:4. The best performance is achieved for the blend containing 20 wt% of PCz and 80 wt% of PDI (1:4), corresponding to an overall efficiency of 0.67%, and a maximum EQE of 15.7% at 495 nm. When the content of PDI increases further, the film quality becomes poor since PDI does not possess as good film-forming ability as PCz and tends to crystallize. The poor film leads to poor performance with a low  $V_{oc}$  of 0.32 V for the device containing 83% PDI ( $D/A = 1:5$ ).

The EQE spectra were further compared with the UV absorption spectra in Figure 5.10. The  $\pi-\pi^*$  transition of PDI at 540 nm was blue-shifted by 10 nm when PCz was introduced to the blend. This suggests that PCz disrupts the self-organization of PDI. On comparing the EQE spectra, it was found that although the absorption of PCz ( $\sim 400$  nm) is stronger than the absorption of PDI ( $\sim 500$  nm) at  $D/A = 1:1$ , the number of electrons detected at 500 nm is still greater than that produced at 400 nm. This indicates that the photons absorbed by PDI can contribute to the photocurrent more effectively than those absorbed by PCz.

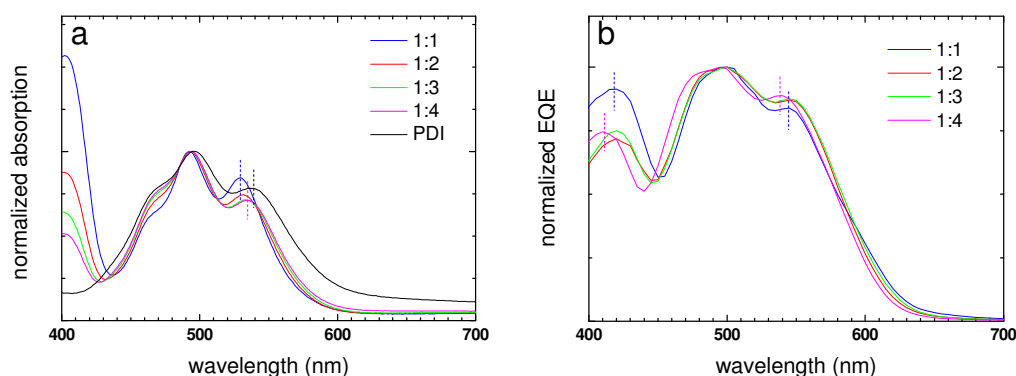
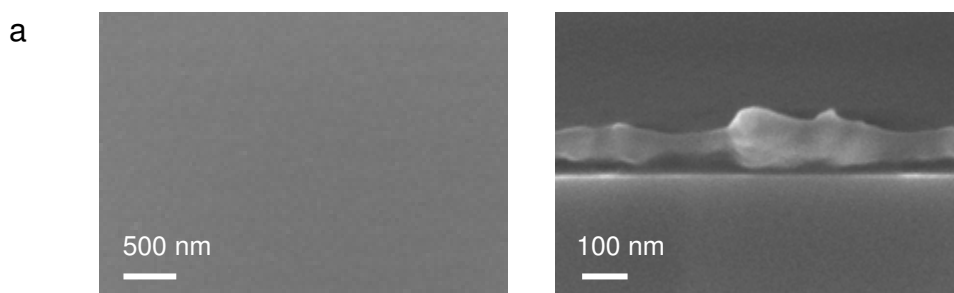


**Figure 5.10** a) UV-vis spectra of PCz/PDI blends at different ratios as thin films, normalized at about 500 nm (absorption of PDI is also given), and b) normalized EQE- $\lambda$  curve at the same D/A ratios as in Figure 5.9a.

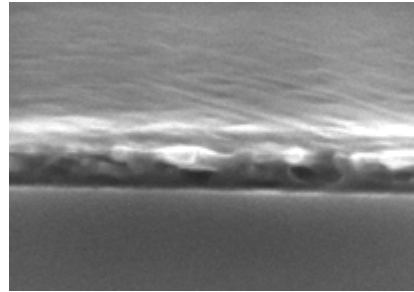
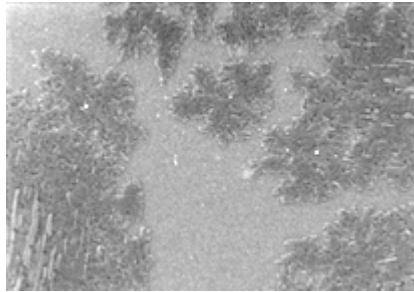
The peaks in the blend corresponding to the absorption of PDI (490 nm and 530 nm) undergo a bathochromic shift upon increasing the PDI content. However, the peaks in the EQE spectra remain at the same position at ratios from 1:1 to 1:3, and only undergo a 5 nm blue shift at 1:4 ratio. This can be attributed to a more intimate contact between PCz and PDI, which should also be observable on the morphology of the film.

A direct observation was made by SEM of both the top view and the section view, through which information can be obtained on the internal morphology of the films. The pure PCz film is homogeneous without any apparent texture (Figure 5.11a). By comparison, the PDI film is much rougher with foliage-shaped crystals all over the surface and some cylindrical crystals protruding out of the surface (Figure 5.11g). This kind of cylindrical crystals is also observed evenly dispersed within the film. Two kinds of morphology are typically seen for PDI: foliage-like crystals and cylindrical crystals. The former is composed of the latter which stack themselves parallel to each other on the substrate (yellow circle in Figure 5.11g). The observed morphology depends on the amount of material present and the free space it gets during crystallization. Foliage-type crystals are grown when there is enough PDI and relatively large free space.

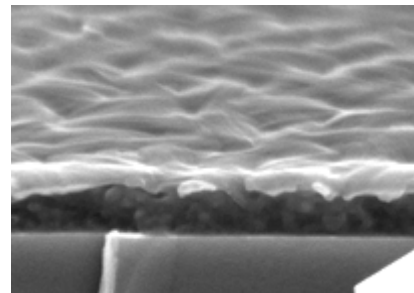
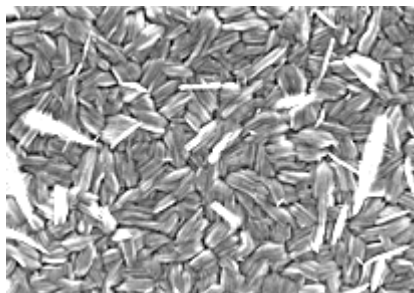
After PCz and PDI were blended, the films showed quite diverse morphology varying with D/A ratios. Both kinds of morphology of PDI were observed in the blend films.



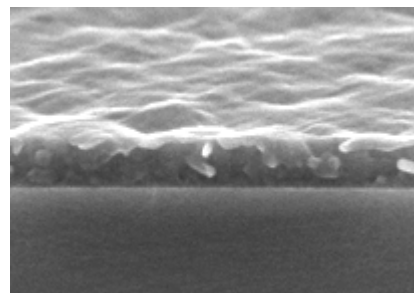
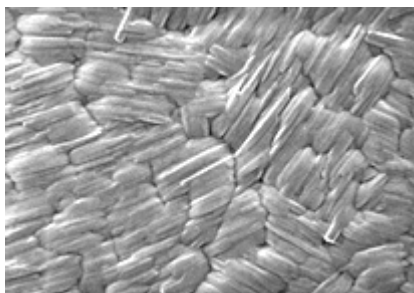
b



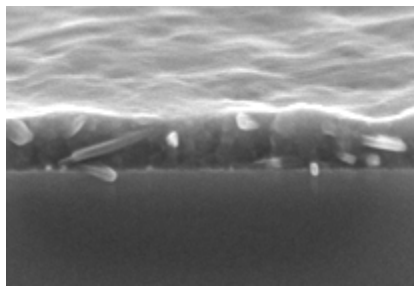
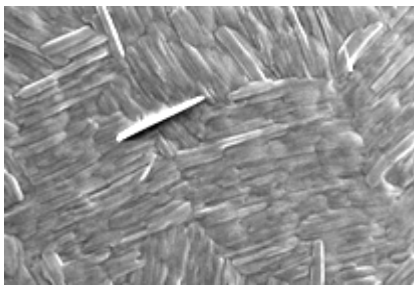
c



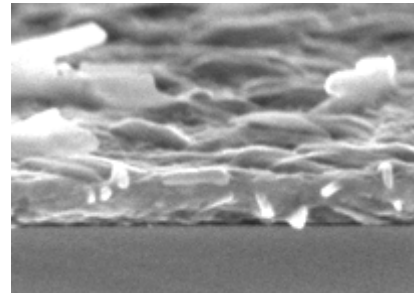
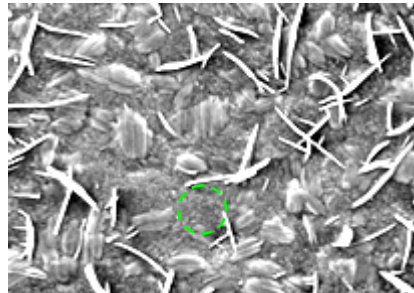
d



e



f





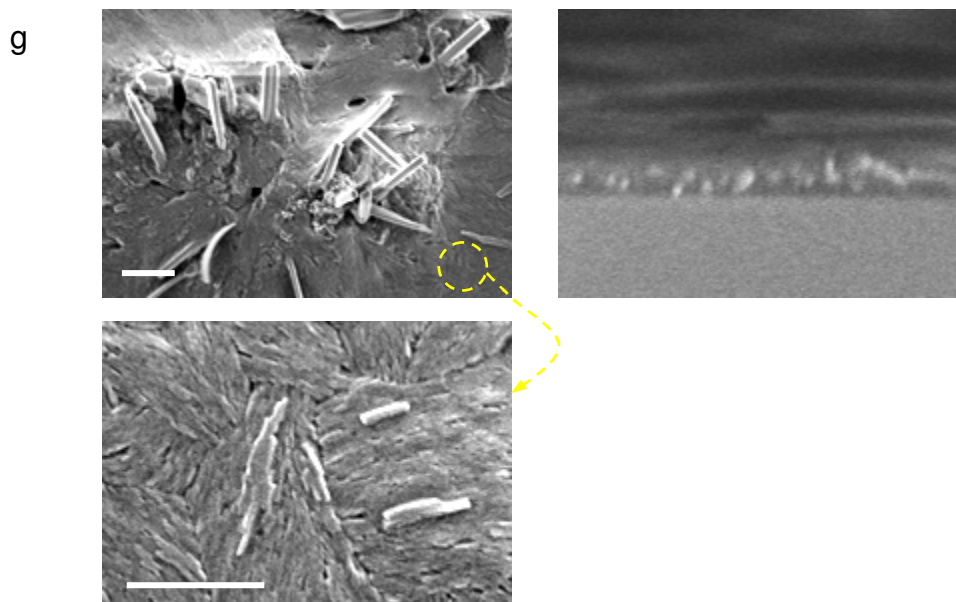


**Figure 5.11** SEM images of a) PCz, g) PDI, and their blends at different ratios: b) PCz:PDI = 1:1, c) 1:2, d)1:3, e)1:4, f)1:5. The films are spin-coated on Si wafer from chloroform solution. The scale bars in the top view images stands for 500 nm, and 100 nm in the section view images.

The section view images show the tendency of the morphology to change from ‘bi-layer’ to ‘homogeneous’ as the PDI content is increased. At the ratio of PCz to PDI = 1:1 (PDI content is 50 wt%), some discontinuous foliage-like crystals float on the featureless layer. In view of the volume ratio, there must be PDI present in this featureless layer, indicating the existence of a homogeneous blend of PCz and PDI. The discontinuous foliage-like crystals of PDI develop into a continuous layer when the content of PDI increases to 66 wt% (D/A = 1:2), thus forming a clear bi-layer structure composed of an upper layer characterized by closely packed foliage-like crystals, with a cross-sectional area of  $\sim 0.5\text{-}1\ \mu\text{m}^2$ , and a bottom layer of a homogeneous blend of PCz and PDI. When more PDI is contained within the blend, the size of the foliage crystals increase in size up to  $\sim 5\text{-}10\ \mu\text{m}^2$  at 75 wt% (1:3) and to  $\sim 10\text{-}20\ \mu\text{m}^2$  at 80 wt% (1:4). In the corresponding section images from 66 wt% to 80 wt% PDI, the upper layer gradually becomes blurred and merges into the bottom layer. The bi-layer structure develops into one ‘homogeneous’ layer for the film containing 83 wt% (1:5) PDI, where the surface is composed of both

crystalline domains (cylindrical and foliage-like crystals) and featureless domains (green circle in Figure 5.11 f). The cylindrical crystals on the surface which are similar to those in a pure PDI film can be observed in the bottom layer for all the D/A ratios, and are especially notable when the content of PDI is higher than 75%. There is a sudden change in surface morphology from D/A = 1:4 to 1:5, where the continuous PDI crystal layer disappears. So the top image at 1:5 is more representative of the morphology inside the film. In conclusion, the blend films contain two kinds of morphologies, a featureless region consisting of a miscible blend of PCz and PDI, and a crystalline domain of pure PDI.

The phase separation can be understood by the low entropy of mixing the donor material and the acceptor material, under which mixtures of D/A deposited from organic solvents tend to phase separate during the evaporation of the solvent. The length scale on which this phase separation occurs decides the morphology of the film. Bi-layer appears when the length scale is rather big ( $\sim\mu\text{m}$ ), and vice versa, small length scale ( $\sim\text{nm}$ ) leads to homogeneous film. The scale depends on a variety of parameters such as the individual solubility of the materials in the solvent, the layer thickness, the evaporation speed of the solvent, the annealing temperature, and the interaction with the substrate.<sup>30,219-221</sup> Here, the morphology of bi-layer was observed for film at low content of PDI (50 wt%), and homogeneous film was obtained for film at high content of PDI (75 wt%).

First of all, the formation of the bi-layer structure can be explained by the properties of PCz and PDI. The films are prepared from chloroform solution (10-20 mg/ml) spin-coated onto silicon wafer at 1000-2000 rpm. The solvent evaporates quickly (within seconds) during spinning and the solution rapidly becomes thicker and thicker until the concentration is greater than the solubility limit of the material, which will then start to crystallize on the substrate. PCz has a lower solubility than PDI, so it separates out from the solution first and accumulates on the substrate because of its higher density.

However, the solubility is not the only driving force for the separation of the two materials. Since this is a very rapid process, dynamics of molecular diffusion in the solution should also affect the phase separation. Just before the solidification of PCz, the PDI molecules which are miscible with PCz and so have not separated in this short time interval, start to come out of solution with PCz to form the bottom layer on the substrate. After this, the rest of the PDI-rich solution continues to lose solvent as PDI crystals develop on the surface. This explains the SEM images, where a top layer similar to a pure PDI film is observed.

Correlating the morphology with the device performance, one can conclude that with a decrease in the phase separation scale, the device behaves better and better. It has been reported that the main problem when using organic material in photovoltaics is that excitons travel at most few tens of nanometers before they decay radiatively or nonradiatively back to the ground state.<sup>98,99</sup> Thus, efficient charge generation requires that most excitons are generated within a short distance of the interface between the electron-donating and electron-accepting phase, which can be realized in a homogeneous film. On the other hand, the charge transport is determined by the percolation pathways for both holes and electrons, which lie on the volume ratio and the interpenetrating network formed by the separate materials, except for the consideration on charge carrier mobility. Both procedures (charge separation and transport) correlate with phase separation, therefore, the performance of the device is explained based on the observation of the morphology.

The excitons are separated at the D/A interface in the homogeneous blend of PCz/PDI and at the crystals/homogeneous blend interface. The separated charges are then transported to the anode (e.g. ITO) through the continuous domains of PCz and electrons are transported to the cathode (e.g. Ag) through the percolation pathways composed of neighboring crystals, which are evenly dispersed within the films. Given the known high charge carrier mobility within PDI crystals,<sup>43</sup> the charge transport in the devices is thus mainly decided by the hole transport within the PCz domains. The corresponding percolation pathways are more well-defined with a higher content of PCz. Based on the observation of the section view images, if one supposes that the top layers of foliage crystals are composed of 10%, 30%, 20%, 15% PDI for D/A = 1:1 to 1:4 respectively, then the bottom layers are composed of 50% PCz + 40% PDI, 33% PCz + 36% PDI, 25% PCz + 55% PDI, 20% PCz + 65% PDI, respectively. Although homogeneous blends can be formed at all these ratios, only in the film of 1:1, does PCz dominate the bottom layer, which leads to the formation of the desired percolation pathways. This is verified by the EQE spectrum. The peak at 420 nm is relatively stronger than in any of the devices containing more PDI. Besides, the highest content of PCz among all devices should also be taken into account for the relatively stronger EQE peak near the absorption of PCz.

Through the above discussion, it can be concluded that a homogeneous film rather than a bi-layer structure is preferred in the PCz/PDI system to maximize efficiency. This indicates that among the two competitive courses, that is, charge separation and charge transport, the former is decisive in this system. Therefore, a large D/A interface is required,

which can be achieved by realizing a homogeneous film. This is in accordance with the earlier reported MDMO-PPV/PCBM system, where a higher efficiency was obtained by modulating the morphology of the film using different solvents.<sup>30</sup> A good charge transport property was thus expected for PCz, making this kind of materials promising as donors for solar cells.

### 5.2.2.2 Thermal Treatment

It was shown above that for HBC based devices, annealing can assist the crystallization and reorganization of the two materials in the film, which produces better performance. Here, thermal treatment (120 °C, 1 h) was adopted as a way to optimize the PCz/PDI device. Four different ratios were tested, from 1:1 to 1:4. The results are shown in Figure 5.12.

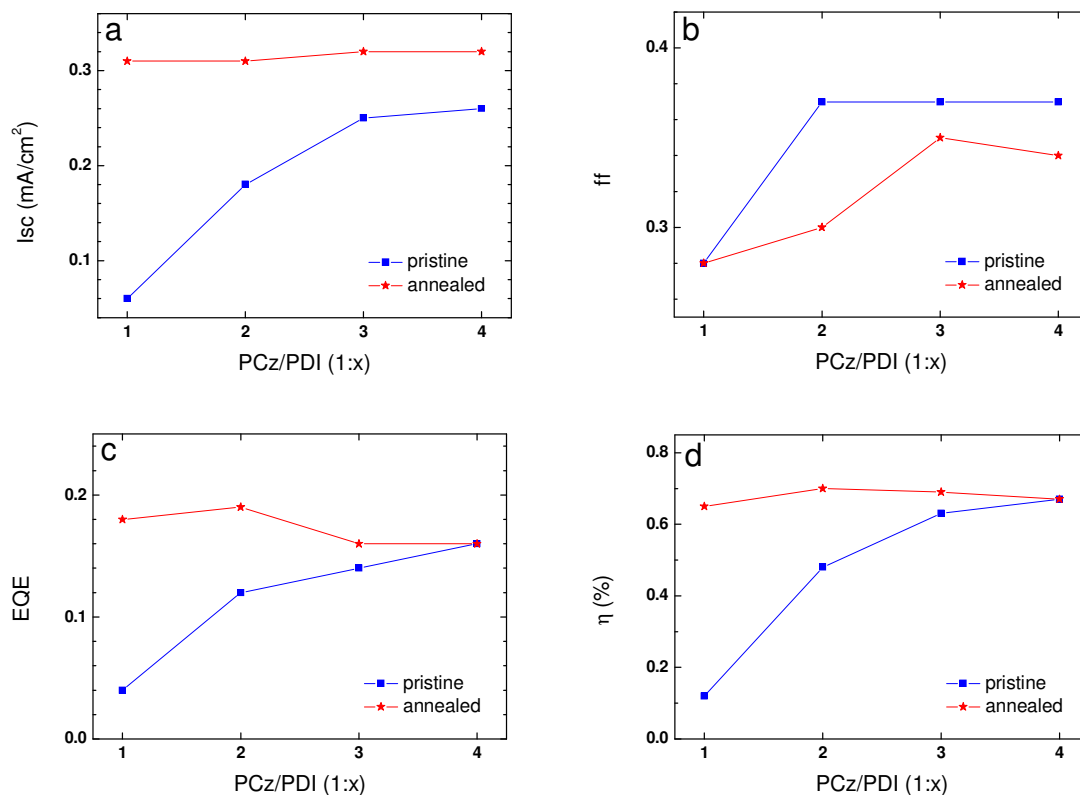
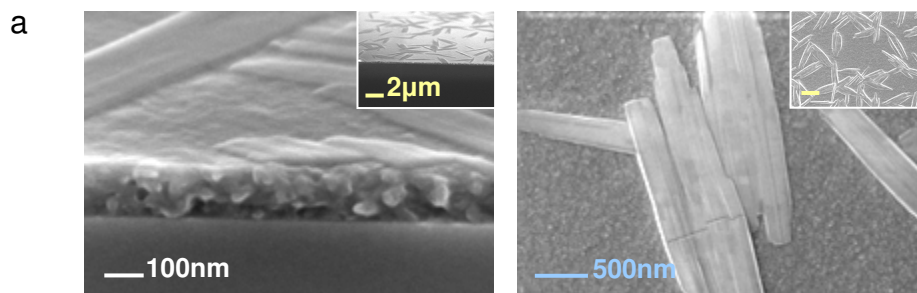


**Figure 5.12** Device performance of devices ITO/PCz:PDI/Ag before and after annealing at 120 °C for 1 h. The ratio of PCz/PDI varies from 1:1 to 1:4. Four parameters are compared here: a)  $I_{sc}$ , b) FF, c) EQE, and d) overall efficiency under solar light.

The annealing procedure improved the devices, with the degree of improvement being found to strongly depend upon the PDI content in the blend. As a rule, the  $V_{oc}$  remained unchanged, since the internal potential conditions were not changed by the annealing procedure. The photocurrent increased largely, but the fill factors decreased. The overall efficiency (under solar light) and  $EQE_{max}$  for the 1:1 device increased by a factor of six and three, respectively. For the 1:2 device, both efficiencies increased by 50%. The performance of device using the 1:3 blend showed only a small increase. No improvement was observed for the device with D/A = 1:4 after the thermal treatment. This variation of the annealing effect at different D/A ratios can be explained based on morphologies.

The morphologies of the films were investigated by SEM. The annealed film of PCz remains featureless, like the film prior to annealing (Figure 5.11a). By contrast, formation of crystals could be observed in the films of the blends after annealing.

However, the development of crystals varied with the content of PDI in the blend, as presented in Figure 5.13. At the D/A ratio of 1:1, thin foliage-like crystals float on the surface discontinuously, with a homogeneous bottom layer. The film of the 1:2 blend still shows the bi-layer structure after annealing, but the size of the foliage-like crystals is larger. In both cases, it is obvious that the crystallization of PDI is greatly enhanced by thermal annealing. The thickness of the crystals develops from several nm at 1:1 to about 100 nm at 1:2. This explains the great increase in the photocurrent and the overall efficiencies for devices using D/A ratios of 1:1 and 1:2, since more developed crystals can enhance charge transport.



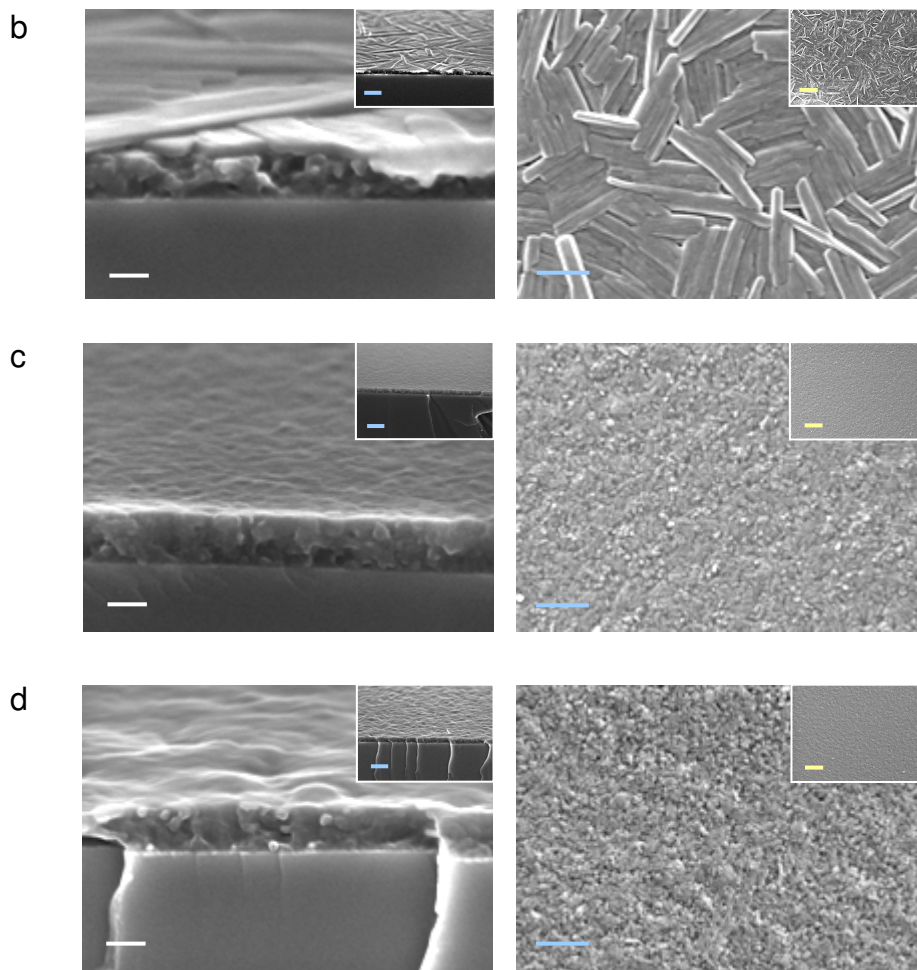


**Figure 5.13** SEM images of the PCz/PDI blend films after annealing at 120 °C for 1 h. The films possess ratios of PCz:PDI = a) 1:1, b) 1:2, c) 1:3, and d) 1:4. Both top view images and section view images are shown. The scale bars in section view images are 100 nm (white bar), and 500 nm (blue bar) for the insets except for the film of blend with ratio of 1:1 (the scale bar is 2  $\mu\text{m}$ ); in the top view images, the scale bars are 500 nm, and 2  $\mu\text{m}$  (yellow bar) for the insets.

The homogeneous characters of films of the blends with ratios of 1:3 and 1:4 are shown in their section view images. The top view images also display relatively homogeneous films with small crystalline domains and featureless domains, which are different from the layer of the cylindrical crystals observed before annealing. This

indicates that the thermal treatment makes PCz and PDI more miscible in the blend. This can also be observed in the section-view images, where the film is more homogeneous throughout the thickness, with several observable cylindrical crystals. This morphology is similar to that of the films before annealing, accounting for the similar performance of the device. To conclude, the thermal treatment improved greatly the crystallization of PDI in the films with D/A ratios of 1:1 and 1:2, thereby leading to much higher efficiencies; whereas the films with D/A ratios of 1:3 and 1:4 did not change much in morphology upon annealing and no apparent development of crystals were observed, resulting in similar performance before and after the thermal treatment.

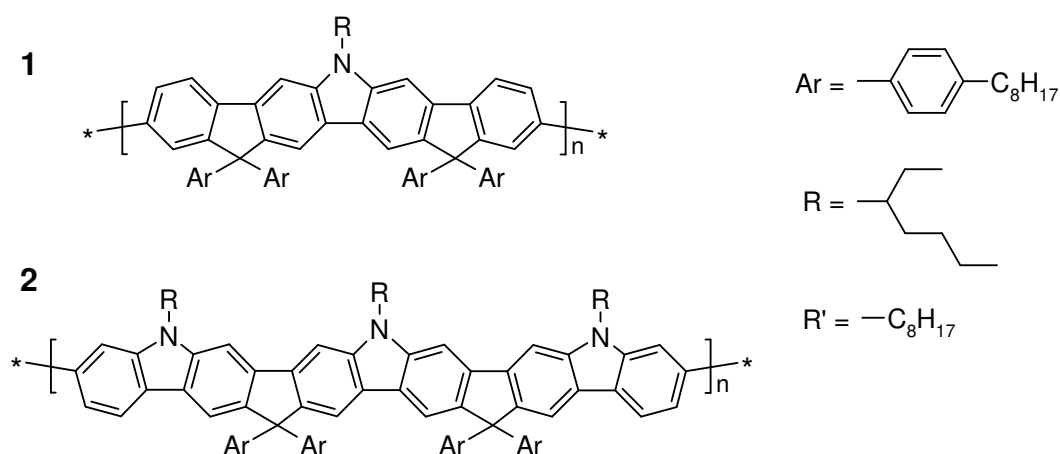
### 5.2.3 Summary

Poly(2,7-carbazole) was incorporated as a donor material in solar cells for the first time using PDI as an electron acceptor. The good fit in orbital energy levels and absorption spectra led to high efficiency (overall efficiency of 0.7% under solar light), which is a record value for non-fullerene containing systems. This result indicates that conjugated polymers with high band-gap, which is on the contrary to the low band-gap polymers whose band-gap is normally less than 2 eV, can also be applied as materials to build efficient solar cell if appropriate electron acceptors are chosen. The device was further optimized by thermal treatment at 120 °C. A big improvement in  $I_{sc}$  (and  $\eta$ ) was observed for devices containing less than 66 wt% PDI, which was correlated to the improvement in crystallization of PDI. For devices having more than 75 wt% PDI, the thermal treatment did not show any apparent effect on the performance of the device. This is in accordance with the observed morphologies of the film before and after annealing, where the development of crystals was suppressed by the more miscible blends. The results indicate that charge separation is decisive in these systems and a good charge transport property is expected for PCz, making this kind of materials promising as donors for solar cells.

## 5.3 Photodiodes based on Ladder Type Poly(2,7-Carbazole)s

PCz was shown to be a novel promising donor material in solar cells,<sup>222</sup> but it absorbs mainly in the violet or ultraviolet region, which limits its application as a good light-harvesting component in photovoltaic cells. The incorporation of a long, branched alkyl chain in polycarbazole on the one hand increases its solubility but on the other hand reduces the amount of light absorbing chromophore in the active layer. The large density of alkyl chains also increases the insulating effects<sup>174-176</sup>, which prevents the intermolecular contact of semiconducting material and hampers the facile photoinduced electron transfer from donor to acceptor material as well as the charge transport. It has been shown that the introduction of a ladder-type structure is an efficient way to red-shift the absorption spectra of carbazole-based polymers.<sup>223,224</sup> Due to their more extended conjugation ladder-type polycarbazoles absorb in the visible region where the solar spectrum is most prominent. Furthermore, poly(2,7-carbazole)s are known to be unstable towards electrochemical oxidation because of the ready oxidation of the electron-rich carbazole 3- and 6-positions.<sup>189</sup> One way to overcome this is to prepare ladder-type polycarbazoles in which all the 3- and 6-positions are substituted.<sup>223,224</sup> Based on this, the carbazole based ladder-type polymers **1-3** were designed and synthesized.

The synthesis of the nitrogen bridged ladder-type polytetraphenylene **1**<sup>225</sup>, and polyhexaphenylene **2-3**<sup>226</sup> have been reported recently. All three polymers were synthesized by A. K. Mishra in our group.





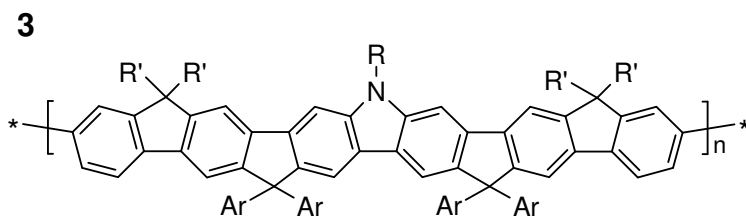


**Figure 5.14** Chemical structure of polymers **1-3**.

The polymers **1-3** are highly soluble in common organic solvents such as  $\text{CHCl}_3$  and THF. The molecular weights determined by GPC against PPP standard are recorded in the following table. The polymer **1** has much higher  $M_n$  than polymers **2** and **3**, which reduces its solubility, and so limits the film thickness achievable by spin-coating.

**Table 5.5** Molecular weight of polymers **1-3**(PPP standard)

Polymer	$M_n$ ( $\times 10^4$ g/mol)	$M_w$ ( $\times 10^4$ g/mol)	$D$	$n$
<b>1</b>	4.6	12.8	2.8	37
<b>2</b>	2.3	5.5	2.4	15
<b>3</b>	2.3	3.9	1.7	13

### 5.3.1 Optical Properties

The UV absorption spectra of the ladder-type polymers show at least a 40 nm bathochromic shift compared to PCz (Figure 5.15). Polymer **1** has an absorption maximum at 434 nm in thin film. The spectrum of polymer **2** exhibits the typical features of ladder-type polymers (small Stokes shift, sharp absorption onset etc.) with a  $\pi$ - $\pi^*$  transition at 456 nm. For polymer **3**, the absorption maximum of 445 nm is intermediate between that of the ladder-type polytetraphenylene **1** and polyhexaphenylene **2**.

Since the absorption of the polymers **1-3** is closer to the strongest emission part of solar light at 480 nm, they are capable of absorbing more solar photons than PCz. This reduction in band-gap also suggests that the relatively low band-gap fullerenes (bandgap of about 1.9 eV), such as PCBM, can be used as acceptor materials together with the polymers **1-3**.

The quenching of photoluminescence of a donor material by an acceptor material gives a first indication of an effective D/A charge transfer as described by Sariciftci for p-conducting polymers and fullerene derivatives. The fluorescence was checked for the ladder-type polymers **1-3** using PCBM and PDI as acceptor materials. Thin films with various D/A ratios were investigated, as illustrated in Figure 5.16. The fluorescence of the polymers was effectively quenched by adding PCBM or PDI, while no enhancement of fluorescence of PCBM or PDI is observed. This indicated efficient charge transfer from polymers to PDI. For PCBM, since it is not easy to self-fluorescence, the possibility of energy transfer could not be excluded.

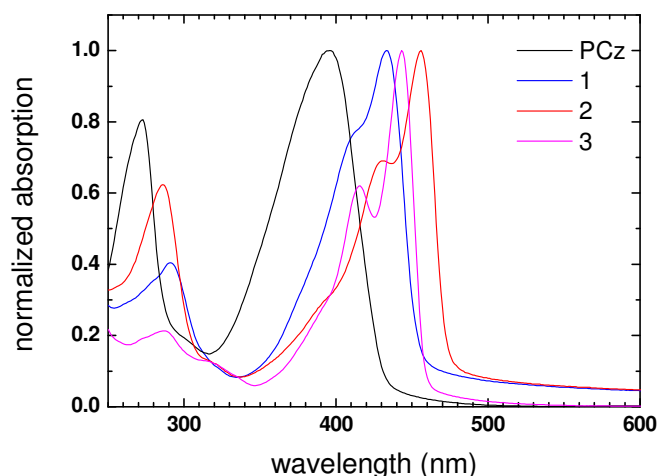


**Figure 5.15** UV-vis spectra of polymer **1-3** in thin films. The spectrum of PCz is also shown for comparison.

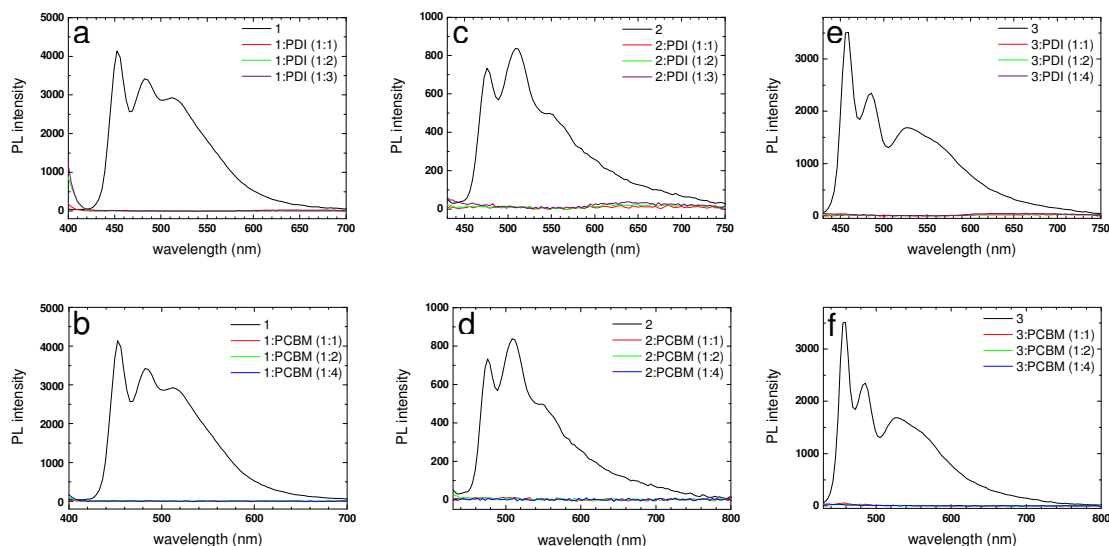


**Figure 5.16** PL spectra of the polymers **1** (a, b), **2** (c, d), **3** (e, f) and their blends with PDI (a, c, e) or PCBM (b, d, f) in thin films, excited at 380 nm.

### 5.3.2 Characterization of Energy Levels

The redox behavior of polymers **1-3** was investigated by cyclic voltammetry on thin films. Two oxidation peaks were observed, and no reduction peak was observed. The corresponding HOMO levels of polymer **1-3** are -5.54, -5.40, -5.46 eV, respectively. Polymer **2**, which has the largest density of electron-rich nitrogen on the backbone, shows the highest HOMO level and hence is the strongest electron donor among the three materials. Polymer **1** with the shortest conjugation unit shows the lowest HOMO level, and polymer **3** is intermediate between the polymers **1** and **2**. The bandgaps were calculated from the UV spectra to be 2.72, 2.62, 2.70 eV for polymers **1-3**. So the estimated LUMO levels are at -2.82, -2.78, -2.76 eV. These LUMO levels are higher than those of polythiophenes (-3.3 eV for P3HT) and PPVs (-3.0 for MEH-PPV). These values produce a larger potential difference in HOMO (D)-LUMO (A) than for PPV or P3HT. Since the difference between the HOMO of the donor and the LUMO of the acceptor decides the

open circuit voltage, a higher  $V_{oc}$  is thus expected for devices based on the ladder-type polymers **1-3** than for those based on P3HT and PPV.

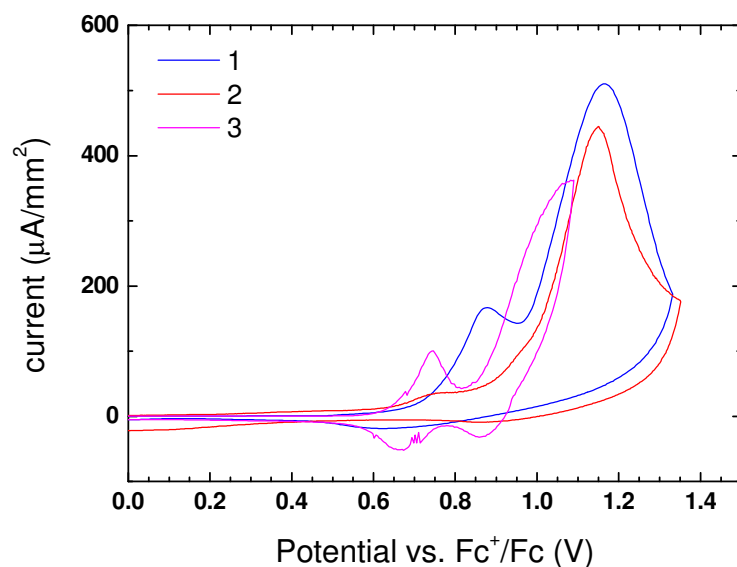


**Figure 5.17** CV curves of polymers **1-3** as thin film casted on Pt electrode.

**Table 5.6** Electrochemical Properties and Energy levels of polymers **1-3**

Polymer	$E_{ons}^{ox}$ (V)	HOMO (eV)	LUMO (eV)	$E_g$ (Optical, eV)
<b>1</b>	0.73	-5.54	-2.82	2.72
<b>2</b>	0.60	-5.40	-2.78	2.62
<b>3</b>	0.66	-5.46	-2.76	2.70

### 5.3.3 Self-organization Properties

Self-organization has an important bearing on the charge transport properties of the material. Control of polymer crystallinity, crystal orientation and morphology is necessary

to obtain high charge carrier mobility.<sup>100,190,227-232</sup> In principle, highly-organized chains provide better percolation pathways for efficient charge transport.

In this work, the UV spectra of polymers **1-3** were first examined in solution and as thin films. For comparison, PCz was also tested under the same condition. The self-organization of the polymers was further investigated by X-ray scattering experiments on extruded fibers. Although the packing of the chains is expected to be much more ordered in the fibers than in spin-coated films, the observation on the fibers supplies a way to look at possible different self-organization behaviors of these polymers.

A bathochromic shift from solution to film often indicates  $\pi$ -interactions between molecules in the solid state. For PCz, a bathochromic shift of 5 nm is observed, however no shift is seen for polymers **1-3**. This indicates that the more flexible side chains of PCz can potentially supply higher mobility to self-organize during the spin-coating procedure. The more planarized and conjugated chains of polymers **1-3** are too rigid to show observable ordered organization in films.

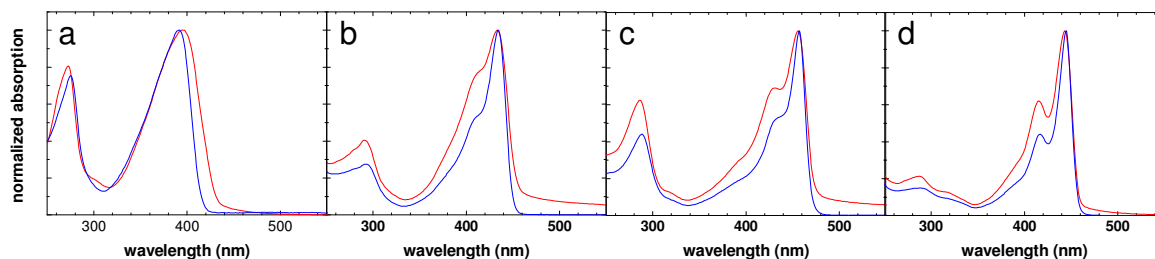


**Figure 5.18** UV-vis absorption spectra of a) PCz and b-d) polymer **1-3** in  $\text{CHCl}_3$  (blue line) and in thin film (red line).

The materials were further investigated by W. Pisula using X-ray scattering experiments on extruded fibers to relate their macromolecular architectures to their supramolecular organization. Since Differential Scanning Calorimetry (DSC) measurements did not reveal any phase transitions for the investigated polymers within a temperature range of  $-100\text{ }^\circ\text{C} \sim 220\text{ }^\circ\text{C}$ , the sample was prepared through a home-built mini-extruder at a temperature of  $200\text{ }^\circ\text{C}$ , at which the materials showed some plasticity.<sup>233</sup>

The X-ray scattering experiments were performed at room temperature. For all the investigated polymers, the organization did not change with temperature or after annealing. The extruded filament was positioned vertical toward the 2D-WAXS detector. The distribution of the reflections over the scattering pattern permits conclusions about the relative arrangement of the building units within the supramolecular organization.

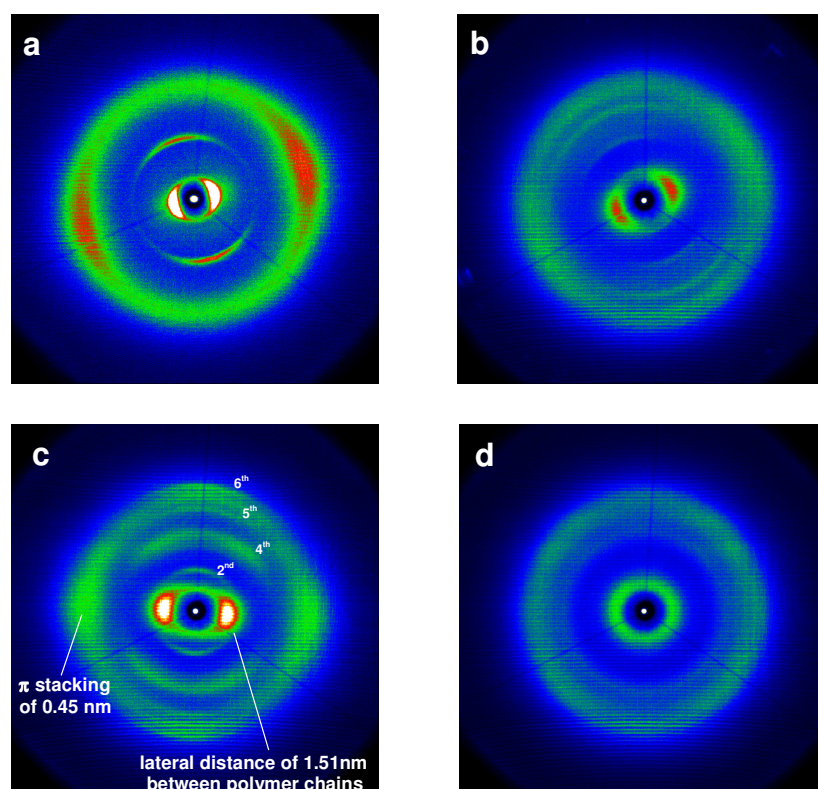


**Figure 5.19** 2D-WAXS of extruded filaments of a) PCz, b) **1**, c) **2**, and d) **3**.

Figure 5.19c shows a typical 2D-WAXS pattern of **2**. The high intensity and distinct reflections point toward a pronounced organization of polymer **2** in the extruded sample. The sharp equatorial small-angle reflections in Figure 5.19c, indicating the alignment of the macromolecules along the shearing direction and thus along the filament axis, correspond to a distance of 1.51 nm. This value was assigned to the lateral distance of the conjugated polymer chains from each other. On the other hand, the equatorial wide-angle

reflections at a correlation distance of 0.45 nm signified the  $\pi$ -stacking spacing between the polymer units. The meridional reflections correspond to the repeating distance between monomers along the polymer backbone. The theoretical distance between single units of 2.3 nm could not be derived in a straightforward way, since this reflection position was superimposed by the equatorial scattering intensity corresponding to 1.51 nm. However, multiple higher order reflections, which correlated with the distance between monomer units, appeared in the pattern. For instance, the second higher order reflection in the meridional relates to 1.15 nm, which is the half value of 2.3 nm. Reflections up to the sixth order were observed, confirming the high degree of order of the polymer chains towards each other. This was in good accordance with the strong  $\pi$ -stacking reflection, which suggested a pronounced interaction between the single building blocks. The organization of the conjugated polymer **2** is illustrated schematically in Figure 5.20.

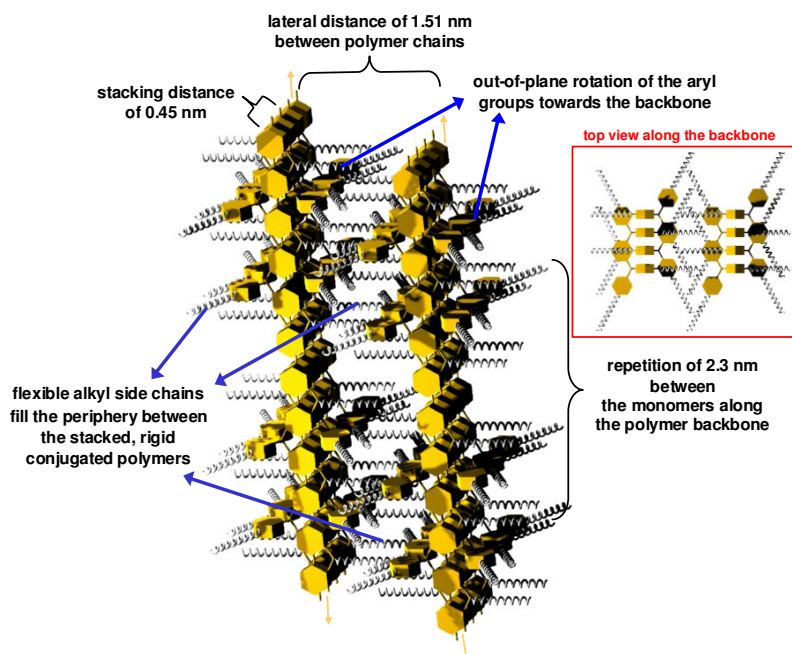


**Figure 5.20** Schematic illustration of the packing of **2**. The alkyl side chains are simplified. The inset shows the polymer packing along the alignment direction.

All essential periodicities are pointed out in the drawing. Due to simplifications, the alkyl side chains are shown as stiff. But in reality, the alkyl substituents are flexible and rather disordered, filling the periphery of the rigid conjugated macromolecules stacked on top of each other. The aryl groups play an important role not only in the solubility of the compound, but also influence the packing. Since these groups possess a rather high steric demand due to their out-of-plane position towards the polymer backbone of **2**, one can assume an alternate packing of the conjugated chain during self-assembly leading to the most favorable arrangement as illustrated in the inset to Figure 5.20. Therefore, the high steric requirements of the aryl groups do not necessarily decrease the  $\pi$ -orbital overlap, which is important for an unhindered interchain charge-carrier transport. On the other hand, the long and disordered alkyl chains will inhibit the interchain transport of charges.

Compound **1** revealed a similar X-ray pattern to **2**, but with somewhat weaker reflections, which corresponded to the same stacking distance and sequence repetition (Figure 5.19b). The packing parameters increased due to the difference in polymer architecture and the higher alkyl density between the rigid blocks. From the equatorial small-angle reflections, it was possible to derive a lateral polymer chain distance of 1.77 nm. An almost identical  $\pi$ -stacking distance of 0.48 nm was observed for **1** by the wide-angle reflections, which were much weaker in comparison to **2**, suggesting significantly less interaction between the polymer blocks. This assumption was verified by the low intensity of the 2<sup>nd</sup> order meridional reflection relating to a period of 0.79 nm between the monomer units along the conjugated chain. Nevertheless, an essentially identical organization of the polymer **1** was derived from the X-ray results as illustrated for **2** in Figure 5.20. A poor amorphous halo was also observed for **1**, which was typical for the disordered alkyl side chains filling the periphery of the conjugated polymers.

The influence on macroscopic order with the variation of the polymer structure was especially obvious for PCz and **3**. The 2D X-ray pattern of **3** revealed only isotropic reflections, indicating that there was no order in the extruded sample (Figure 5.19d). The small-angle reflection was correlated with a lateral interchain distance of 1.71 nm. This larger distance in comparison to **2** was also in very good agreement with the longer attached alkyl chains. As a result of the poor macroscopic order, no reflections related to the stacking and the intrachain correlation emerged. By contrast to polymer **3**, compound



PCz showed the highest supramolecular organization over long-range, as displayed by the intense and sharp reflections in Figure 5.19a. The equatorial small- and wide-angle reflections were correlated to a distance of 2.3 nm between polymer chains, and to a  $\pi$ -stacking distance of 0.46 nm. The C<sub>14,10</sub> (2-decyltetradecyl) alkyl side chains when attached to each carbazole monomer resulted in the largest lateral polymer distance determined in this study. Structural investigations of the polymer decorated with significantly shorter alkyl chains (2-ethylhexyl) revealed a distance of only 1.8 nm, emphasizing once again the strong influence of substituents on the packing parameters. The period of 0.81 nm between the carbazole units along the backbone of PCz was characterized by the meridional scattering intensities, which were also significantly stronger in comparison to the other polymers **1-3**.

### Relationship between the Polymer Structure and Supramolecular Order

To understand the relationship between polymer architecture and macroscopic order indicated by the structural results, one has to look into more details at the differences in the chemical structure between the investigated compounds. The most significant difference in the long-range organization was observed between **2** and **3**, where **2** revealed a higher degree of order and **3** showed only isotropic reflections in the X-ray pattern. This was especially interesting, since both polymers possessed an almost identical polymer design. Compound **2** has only carbazole units within the polymer backbone, which were substituted by short branched alkyl side chains. On the other hand, **3** contains only one carbazole and two fluorene units per monomer unit. Additionally, each of the two fluorene units was substituted by two n-octyl side chains which increased the steric requirements on the polymer backbone. It has been shown for low molecular weight species, such as discotic hexa-*peri*-hexabenzocoronenes, that longer alkyl side chains, which are branched close to the rigid conjugated building block, decrease the  $\pi$ -interaction between the individual molecules and thus increase the macroscopic disorder.<sup>171</sup> Therefore, the two octyl side chains on each of the two fluorene units decreased the interaction between the rigid polymer blocks of **3** and led to higher disorder in comparison to compound **2**.

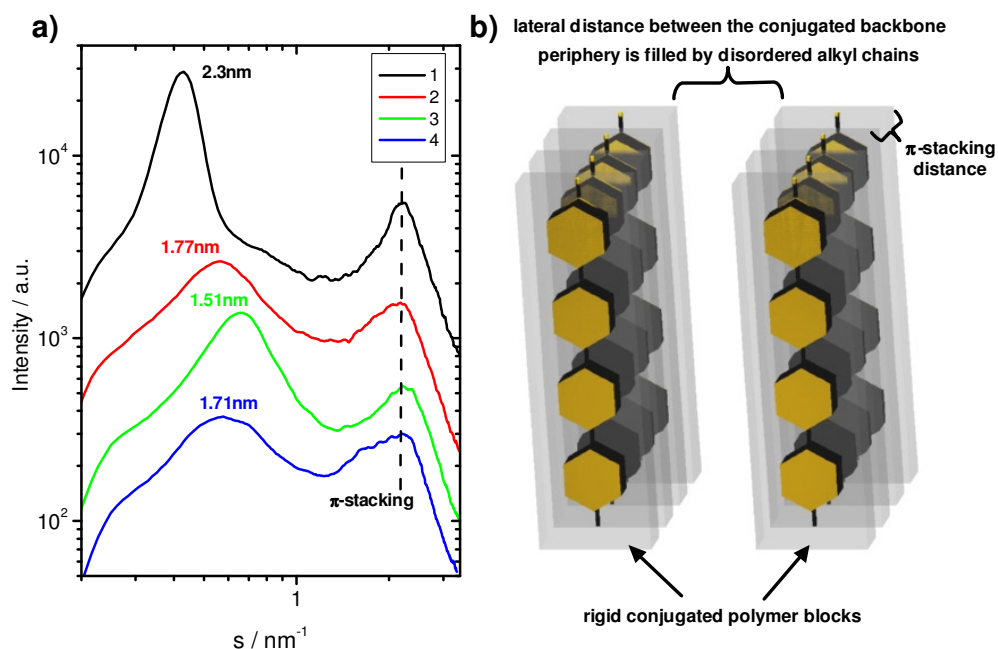


**Figure 5.21** The lateral distance of PCz and polymers **1-3** depending on the alkyl side chain length which also correlate with the photovoltaic performance: a) equatorial scattering intensity distribution as a function of the scattering vector, and b) schematic illustration of the periodicities observed in the plot.

Furthermore, the interaction between carbazole units was considered to be stronger than between fluorenes due to the heteroatoms. Since PCz and **2** consisted only of carbazoles, these compounds possessed the most pronounced macroscopic organization among the investigated polymers. On the other hand, the slight decrease in the order for **1** could be explained by its possessing the highest aryl fraction in relation to the molecular weight of each monomer unit and thus a larger “density” of aryl groups along the conjugated backbone. Since the aryl groups rotate out-of-plane with the polymer chain, they are sterically more demanding and decrease the degree of  $\pi$ -interaction. However, the X-ray results indicated a well-defined structure of **1** in the extruded filaments, since the polymer backbone was substituted by less flexible side chains than the other investigated compounds PCz and polymers **2** and **3**. It is important to note that the  $\pi$ -stacking distance

was almost identical for polymers PCz, **1** and **2** and was thus not affected by the polymer architecture.

The study by X-ray scattering experiments revealed a correlation between the molecular structure and the packing behavior of the polymer chains.

- The interaction between carbazole units is stronger than that between fluorene units through analysis on the packing behavior of the polymers;
- The long alkyl chains attached to the backbone correspond to a larger lateral distance between the polymer chains;
- A large density of substituted aryl group leads to a decrease in order;
- Branched alkyl chains close to the conjugated building block can decrease the  $\pi$ -interaction between the molecules.

### 5.3.4 Photovoltaic Device

The UV absorption of the polymers **1-3** shows at least a 40 nm bathochromic shift compared with PCz, which suggests that PCBM is a possible acceptor material in solar cells using these polymers, as the overlap with the solar spectrum will now be much better. The orbital energy values allow the pairing of these polymers with both PDI and PCBM. Photovoltaic devices based on these two acceptor materials are now introduced.

#### 5.3.4.1 PCBM based Device

Photovoltaic devices using PCBM as acceptor material and polymers **1-3** as donor materials were investigated. The polymer **1** was adopted as the model compound to optimize the D/A ratio in a ladder-type polymer/PCBM system. Four different ratios varying from 1:2 to 1:8 were studied, as shown in Figure 5.22. A thickness of 100 nm was used for the active layer.

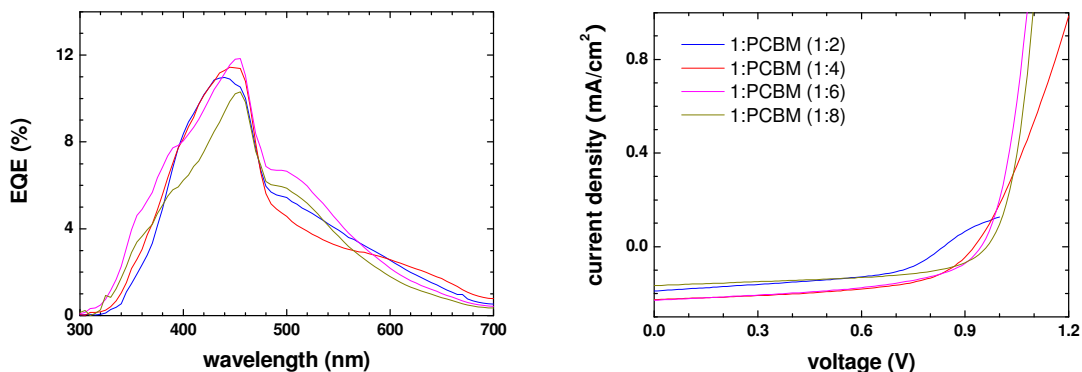


**Figure 5.22** Photovoltaic performance of devices ITO/polymer **1**:PCBM/Ag at different ratios. The I-V curves were tested under solar light AM1.5 G with light intensity of 150-160 W/m<sup>2</sup>.

**Table 5.7** Average photovoltaic performance

Polymer <b>1</b> /PCBM	I <sub>sc</sub> (mA/cm <sup>2</sup> )	V <sub>oc</sub> (V)	FF	Efficiency (%)	EQE <sub>max</sub> (%)
1:2	0.19	0.84	0.49	0.48	11
1:4	0.23	0.93	0.55	0.72	11
1:6	0.23	0.95	0.50	0.69	12
1:8	0.17	0.96	0.54	0.55	10

The highest efficiency was achieved for the device containing 20 wt% polymer and 80 wt% PCBM, corresponding to an overall efficiency of 0.72% under solar light and an EQE<sub>max</sub> of 12% at 450 nm. The EQE spectrum showed a strong peak near 440 nm, with a shoulder peak at 500 nm. The main peak corresponded to the  $\pi$ - $\pi^*$  transition of polymer **1**. The shoulder peak came partly from the absorption of PCBM at 500 nm, and partly from the expanded absorption of polymer **1** in thin films. The shape of the EQE spectrum indicated that both the donor and the acceptor contributed to the photocurrent as an efficient D/A pair. The V<sub>oc</sub> was 0.93V, greater than the V<sub>oc</sub> of 0.6 V obtained from a P3HT/PCBM device, which was the most successful organic solar cell reported so far.<sup>234</sup> An increase of ~ 0.1 V in V<sub>oc</sub> was observed for the device using a 1:4 blend compared to the device using a 1:2 blend and no further improvement was recorded on increasing the

PCBM content. The optimum D/A ratio was thus determined to be 1:4 for the polymer/PCBM device. Deviation from this ratio decreased the performance of the device, especially when the content of PCBM was lower than 66 wt% or higher than 88 wt% (Table 5.7).

Based on the above results, devices using polymers **2** and **3** as donor material and PCBM as acceptor material were fabricated at the same D/A ratio of 1:4 which is assumed to also be optimal for these polymers (Figure 5.23).

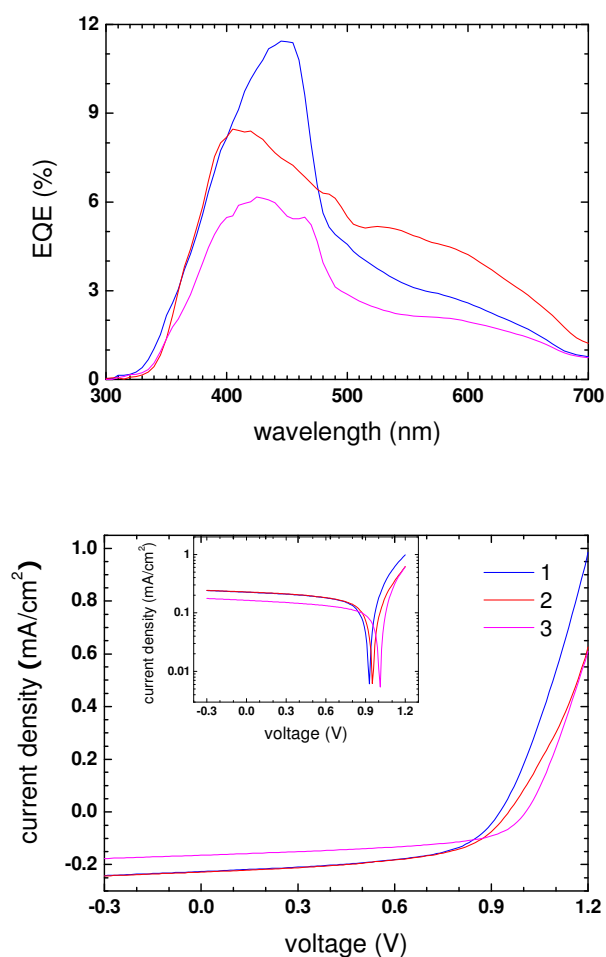


**Figure 5.23** Photovoltaic performance of devices ITO/polymer **1-3**:PCBM (1:4)/Ag. The I-V curves were tested under solar light AM1.5 G with light intensity of 150-160 W/m<sup>2</sup>. The inset shows the I-V curve with a logarithmic ordinate.

**Table 5.8** Average photovoltaic performance

Polymer/PCBM (1:4)	$I_{sc}$ (mA/cm <sup>2</sup> )	$V_{oc}$ (V)	FF	Efficiency (%)	$EQE_{max}$ (%)
<b>1</b>	0.23	0.93	0.55	0.72	11
<b>2</b>	0.23	0.95	0.54	0.74	9
<b>3</b>	0.16	1.01	0.55	0.56	6

The EQE curves show one main peak near the absorption maximum of the donor and a shoulder peak with an extended tail to 600 nm, arising from the absorption of PCBM. The device with polymer **1** shows the highest EQE, while the one with polymer **2** has the broadest spectrum, which result in comparable photocurrent and overall efficiency, as concluded in Table 5.8. For polymer **3**, a lower efficiency and EQE were observed, whereas it exhibits the highest  $V_{oc}$  among the three polymers.

To understand the variation in the device performance, one has to consider the chemical structures of the three polymers.

1. The highest efficiency is found for polymer **2**, and the lowest efficiency for polymer **3**. Both polymers are ladder-type polyhexaphenylenes, with a lot of structural similarity. However, polymer **2** has three nitrogen bridges as that in carbazole and two carbon bridges as that in fluorene per repeat unit, whereas polymer **3** has only one nitrogen bridge and four carbon bridges. It has been shown that the nitrogen bridge is more efficient than carbon bridge in facilitating charge migration along the chain. Therefore, better charge transport is expected for polymer **2** than **3**, which should lead to higher photocurrents. This agrees with the higher  $I_{sc}$  observed for the device containing **2** (0.23 mA/cm<sup>2</sup>) than **3** (0.16 mA/cm<sup>2</sup>).

2. The WAXD experiments reveal that polymer **2** possesses the most pronounced macroscopic organization. Although the packing behavior will be somewhat different in a thin film than in an extruded fiber, the tendency towards self-organization depends mainly upon the molecular structure. So, the small decrease in efficiency for the device based on polymer **1** can reasonably be attributed to its having reduced macroscopic order than **2** in a film. This is understood as that the exciton diffusion length can be improved by a well-

ordered arrangement of the molecules,<sup>100</sup> which on the other hand facilitates interchain charge transport.

3. It has been shown for HBC based devices that an insulating effect exists for alkyl chains, which can block charge hopping between the chains. Polymer **1** has only one octyl chain outside the backbone while polymer **2** has three. This will hamper the charge transport, leading to a lower efficiency.

4. Polymer **1** has the highest molecular weight, about two times that for polymers **2** and **3**. It has been reported for P3HT based devices that only polymers with  $M_n > 10\,000$  g/mol show high power conversion efficiencies ( $> 2.5\%$ ) since lower molecular weight corresponds to a reduced intermolecular ordering thus lowering the charge carrier mobility.<sup>38</sup>

The above device results on polymers **1-3** demonstrate the influence of structure on the device efficiency. The nitrogen bridges along the backbone, which facilitate charge migration, and fewer/shorter alkyl chains, which have less insulating effect, correspond to better performance in solar cell.

The typical  $V_{oc}$  of these ladder-type polymer/PCBM devices are in the range of 0.9 ~ 1.0 V, which is higher than that reported for P3HT/PCBM (0.6 V<sup>234</sup>) cell or PPV/PCBM cell (0.8 V<sup>192</sup>). This is in accordance with the HOMO of P3HT (-5.2 eV) or PPV (-5.1 eV) being higher than the HOMO of polymers **1-3** (-5.4~-5.5 eV). However, the photocurrent of the ladder-type polymers based device is much lower than that of P3HT or PPV based devices due to the better matching of light absorption for P3HT and PPV with solar spectrum and their strong ability for self-organization in thin films, which prolongs the diffusion length of excitons and induces a higher charge carrier mobility. For given donors, the optimization of photocurrent can be obtained by tuning of the transport property or tuning of cell geometry in dependence of the cell thickness.<sup>235</sup> This was done in the following section.

## Optimisation of Devices

In order to optimize the photocurrent in the polymer 1-3/PCBM device, the thickness was reduced to realize a thin device. This was expected to shorten the percolation pathways for charge transport, which would reduce the possibilities for charge recombination at the same time. A thickness of 70 nm was obtained for the device containing polymer 1, and 60 nm for that containing polymer 2 by spin coating a diluted solution. The results are shown in Figure 5.24.

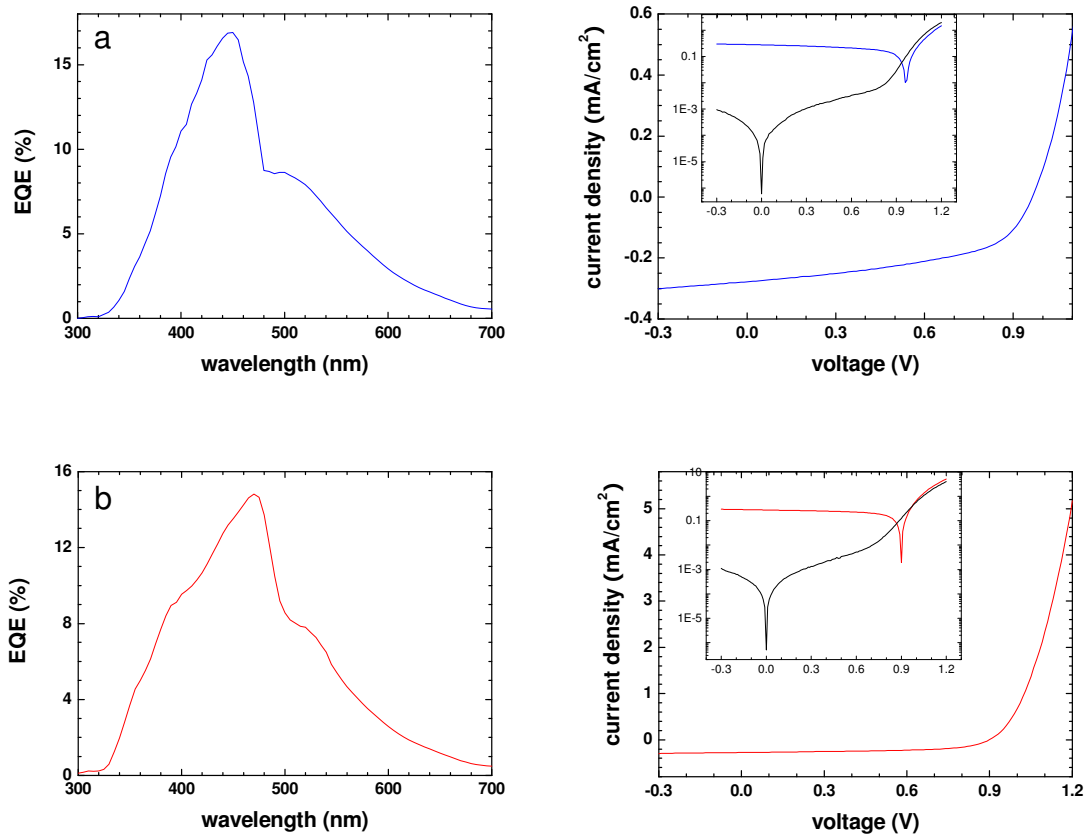


**Figure 5.24** Optimized devices ITO/polymer:PCBM (1:4)/Ag of a) 1:PCBM with a thickness of 70 nm, and b) 2:PCBM with a thickness of 60 nm. The I-V curves are tested under solar light AM1.5 G with light intensity of 150-160 W/m<sup>2</sup>.



**Table 5.9** Average photovoltaic performance

Polymer/PCBM (1:4)	$I_{sc}$ (mA/cm <sup>2</sup> )	$V_{oc}$ (V)	FF	Efficiency (%)	$EQE_{max}$ (%)
<b>1</b>	0.28	0.96	0.51	0.89	17
<b>2</b>	0.28	0.90	0.58	0.90	17

It can be seen that the thinner devices have higher photocurrent and EQE values than the ones with a thickness of 100 nm. An overall efficiency, as high as 0.9% under solar light, was achieved for both devices. Since more efficient charge transport is expected in the thinner device, the experimental result indicates that the charge carrier mobility of the ladder-type polymers might be one of the limiting factors for the low photocurrent. The reduced charge recombination in the thinner device has also to be taken into account, while the varied cell geometry depended on the thickness may also play a role. When comparing the difference in molecular structure between the polymers **1-3** and P3HT, which shows high charge carrier mobility among conjugated polymers, it could be noted that apart from the different conjugation units, the substituents for polymers **1-3** are much more bulky and larger than the hexyl substituent on P3HT. The large aryl/alkyl chains prohibit the efficient interchain transport of charges, which suggests a good material for solar cell should have as few and as small as possible solubilizing substituents consistent with the required processibility.

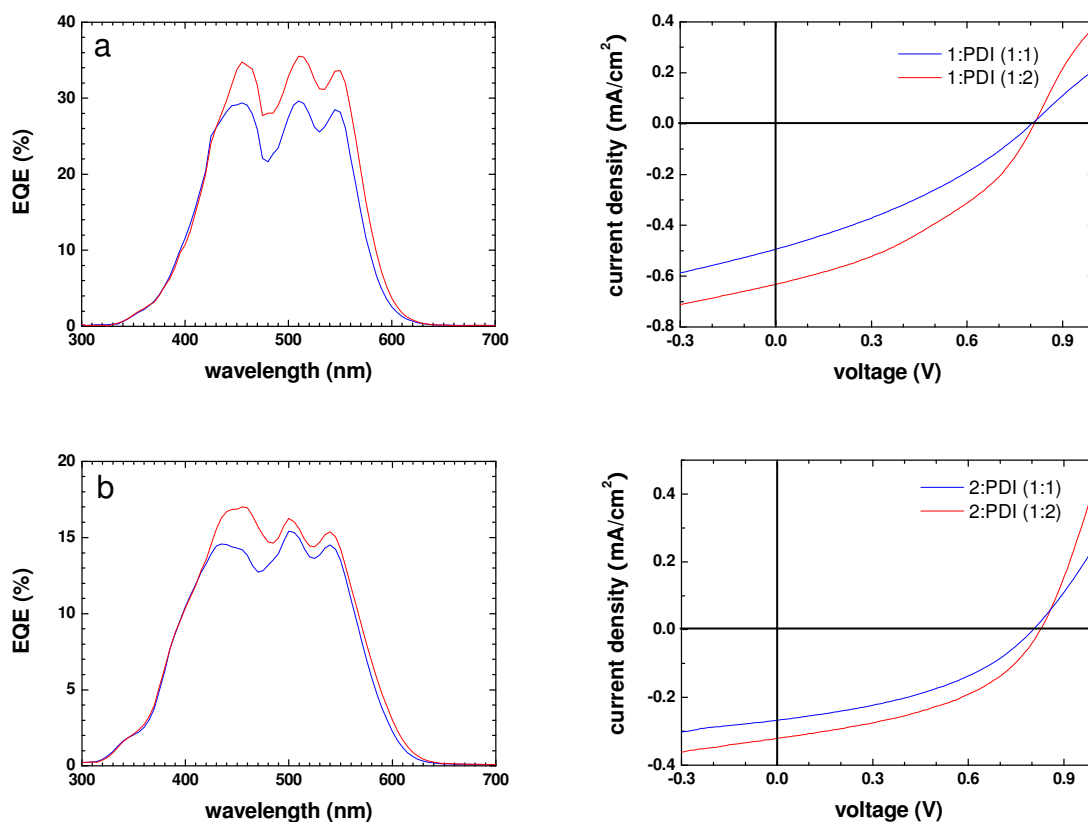
By comparison with the PCz/PCBM device, which showed an overall efficiency of 0.07% and an  $EQE_{max}$  of 4%, the efficiency values of **1-3** based devices are improved approximately ten fold. The above results clearly demonstrate that with minor alternations in monomer structure, it is possible to substantially improve the efficiency of polymer based solar cells. In the present study, it was shown that tuning of the absorption so as to absorb more of the solar energy without altering the HOMO level results in an enhanced efficiency.

#### 5.3.4.2 PDI based Device

Photovoltaic devices using PDI as acceptor material were also investigated. PDI absorbs photons near the strongest emission part of the solar light more efficiently than PCBM. So in devices containing polymers **1-3**/PDI, both of the components have the potential to absorb light and form excitons to contribute to the photon-electron conversion in the optimum part of the visible spectrum.

It has been shown for PCz/PDI devices that a higher efficiency is achieved with increasing PDI content; a ratio of 1:4 was found to be optimal. However, the content of PDI is limited by the film-forming ability of the blend, especially the donor. The polymers **1-3** do not show as good film-forming abilities as PCz, and therefore the highest content of PDI in a good film was found to be less than 66 wt% for polymers **1** and **2** and 50 wt% for polymer **3**. On addition of more PDI, the film becomes too poor to form stable devices.

Based on the results on PCBM containing devices, the performance can be optimized by realizing a thinner active layer. Therefore, a device containing polymer **1** was prepared with a thickness of 50 nm. The devices for polymers **2** and **3** were prepared at the default thickness of 100 nm. The results are shown in Figure 5.25.



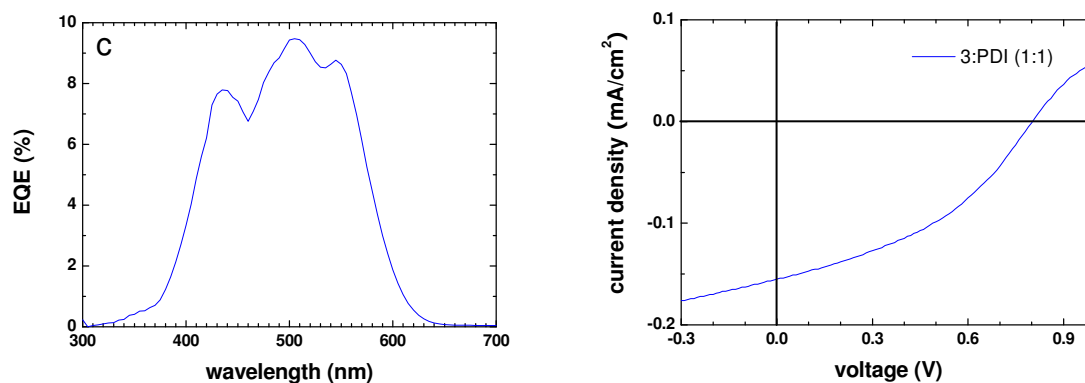


**Figure 5.25** Photovoltaic performance of devices ITO/polymer **1-3** (a-c):PDI/Ag at D/A ratios of 1:1 (blue line) and 1:2 (red line). The I-V curves are tested under solar light AM1.5 G with light intensity of 150-160 W/m<sup>2</sup>.

**Table 5.10** Average photovoltaic performance

Polymer/PDI	I <sub>sc</sub> (mA/cm <sup>2</sup> )	V <sub>oc</sub> (V)	FF	Efficiency (%)	EQE <sub>max</sub> (%)
<b>1</b> *	1:1	0.49	0.80	0.88	30
	1:2	0.63	0.81	1.32	35
<b>2</b>	1:1	0.27	0.80	0.54	16
	1:2	0.32	0.83	0.73	17
<b>3</b>	1:1	0.15	0.80	0.33	10

\* The thickness of the active layer is 50 nm. The thickness in the other devices is 100 nm.

An overall conversion efficiency as high as 1.32% was achieved for the device based on polymer **1**, which was the best for non-fullerene containing bulk-heterojunction cells. This could be attributed to the good light absorption compensation of the two components, which gave a broad EQE spectrum resulting in three strong peaks in the region of the solar emission, and the strong self-organization behaviour not only from PDI, but from polymer **1** as well. In comparison, the thick device based on polymer **2** showed lower efficiency (0.73%). This was in accordance with what was observed for the polymer**1-2**/PCBM devices, and again supported the notion that a thin device could

perform better than a thick device. Moreover, the device based on polymer **3** was the least efficient, which agreed with the proposition that more nitrogen bridges along the backbone and less bulky side chains were to be preferred in the molecular design of donor materials for solar cells.

The efficiencies increased with increasing PDI content in the device. For polymer **1**, the overall efficiency varied from 0.88% to 1.32%; and for polymer **2** based devices from 0.54% to 0.73%. This is in accordance with the monotonic increase of efficiency of PCz/PDI device with the content of PDI up to the D/A ratio of 1:4. Therefore, higher efficiencies are expected if more PDI can be incorporated into the ladder-type polymer based devices. Other perylene derivatives with better film forming ability should be tested to decide an optimum content of the acceptor.

In comparison with PCz (0.67~0.74 V)<sup>219</sup>, the polymer **1-3** showed the  $V_{oc}$  of about 0.8 V. The  $I_{sc}$  was in the range of 0.15~0.49 mA/cm<sup>2</sup> at D/A = 1:1, which was much higher than the corresponding value for PCz based device (0.06 mA/cm<sup>2</sup>). The combined effects of structure and device design have thus resulted in a great improvement in efficiency for the devices based on ladder-type polymers (0.33~0.88% for polymer **1-3**) compared with those based on PCz (0.12%), proving the introduction of ladder structure as a successful strategy to optimize the polymers.

### Morphology of the Films

Observation of films containing equal amounts of polymers **1-3** and PDI (Figure 5.26) shows homogeneous morphologies without featured cylindrical crystals of PDI, which are usually observed in the films of blends of PDI with PCz or HBC. This indicates that the ladder-type polymers inhibit the crystallization of PDI, so that the two components form homogeneous blends. The films appear rougher at a D/A ratio of 1:2 than at 1:1, suggesting the fine blends are becoming replaced by coarse phase separation. This on the one hand can be explained by the enlargement of the crystal domains, and on the other hand by the poor film forming ability of the polymers and PDI.

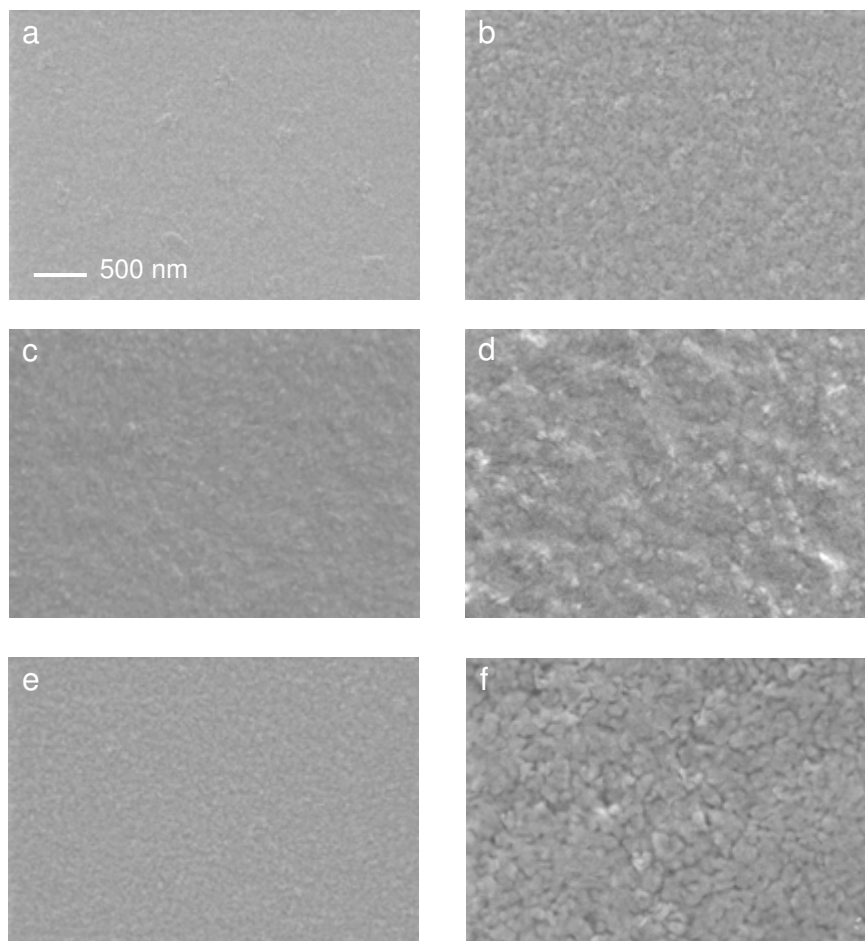


**Figure 5.26** SEM images of the blend films containing polymers **1-3** and PDI (a and b for **1**, c and d for **2**, e and f for **3**). The ratios of polymer:PDI = 1:1 (a, c, e) and 1:2 (b, d, f). The scale bar is 500 nm for all images.

### Mechanism of Charge Transfer

A typical EQE spectrum for the ladder-type polymer based device has three peaks. The first peak is around 450 nm, near the absorption maximum of the polymers. The second and the third peak come from the absorption of PDI, located at 500 and 550 nm. This verified that both components absorb light and contribute to the photocurrent. Therefore, two kinds of mechanism for charge transfer exist, that is, electrons transferring

from the LUMO of the excited donor to the LUMO of the acceptor, or electrons from the HOMO of the donor to the HOMO of the excited acceptor (Figure 5.28). In order to elucidate which mechanism dominates, EQE spectra of devices based on polymer **2** at three different D/A ratios (1:1, 1:2, and 1:3) were compared with the absorption spectra at the same ratios (Figure 5.27).

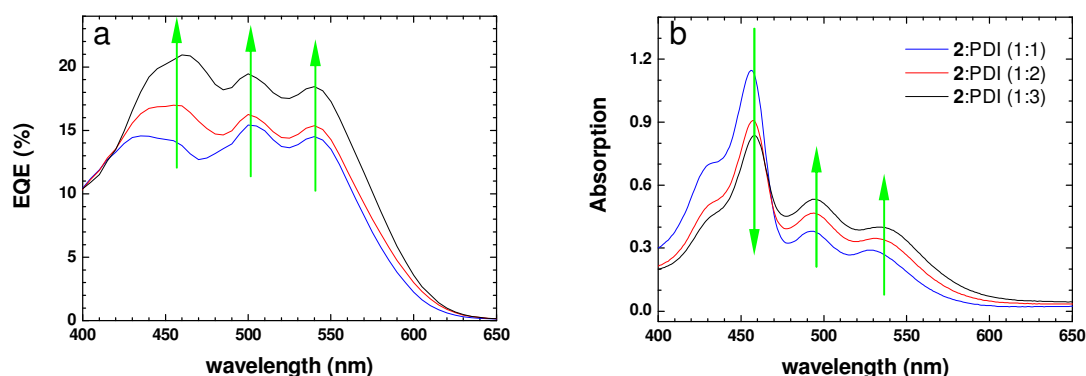


**Figure 5.27** a) EQE- $\lambda$  spectra of devices ITO/polymer **2**:PDI/Ag at D/A ratios from 1:1 to 1:3, and b) the corresponding UV-vis absorption spectra of the active layer.

The position of the peaks in the EQE- $\lambda$  curve is in accordance with the absorption spectra. In the absorption spectra, the peak at 450 nm is mainly from polymer **2**, with very little contribution from PDI. Therefore, the intensity of this peak becomes lower when the content of the polymer decreases in the blend. The other two peaks at 500 and 550 nm correspond to the absorption of PDI, which becomes stronger when more PDI is added. For the blend at the D/A ratio of 1:1, the relative intensity of the peak at 450 nm (abs. = 1.15) is much stronger than the other two peaks (abs. = 0.39 and 0.30) displayed in Figure 5.27b. However in the EQE spectra (Figure 5.27a), all the three peaks have similar values. This can only be explained by the higher conversion efficiency of photons absorbed by PDI than by polymer **2**, which also accounts for the trends in peak intensity at 450 nm in the EQE spectra and in the absorption spectra.

If the photons absorbed by PDI can contribute to the photocurrent more efficiently than the polymer, the charge transfer between the donor and the acceptor must prefer to

happen by path *II* rather than by path *I* as illustrated in Figure 5.28. Therefore, in the polymer/PDI system, most of the excitons form on the PDI because of greater absorption by the PDI and/or energy transfer from the polymer to the PDI. Electrons are excited to the conduction band, followed by the transfer of an electron from the HOMO of the donor material.

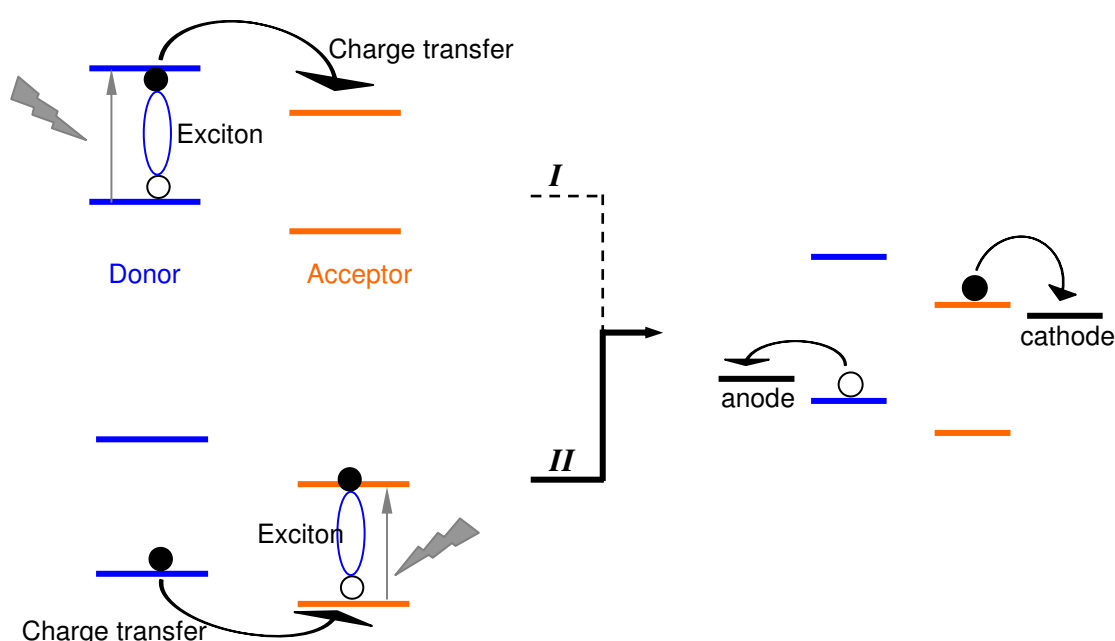


**Figure 5.28** Mechanism illustration of charge transfer from donor to the acceptor.

### Thermal Treatment

It has been shown that annealing at 120 °C for PDI containing devices can greatly improve their performance, since crystallization of PDI during the thermal treatment assists charge transport in the crystalline domains. Therefore, the devices based on polymers **1-3**/PDI were treated at 120 °C for 1 h for optimisation. The results are shown in Figure 5.29.

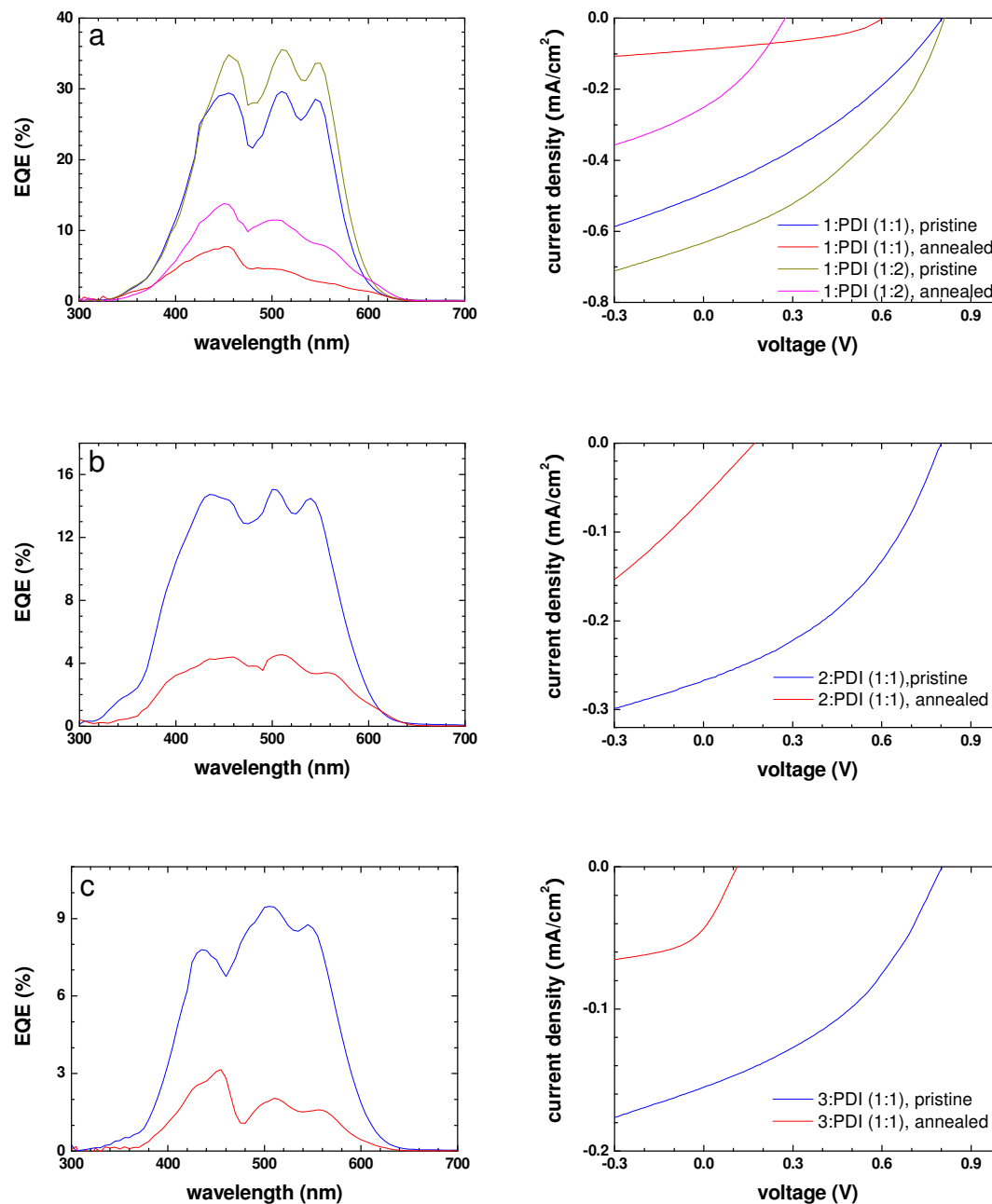


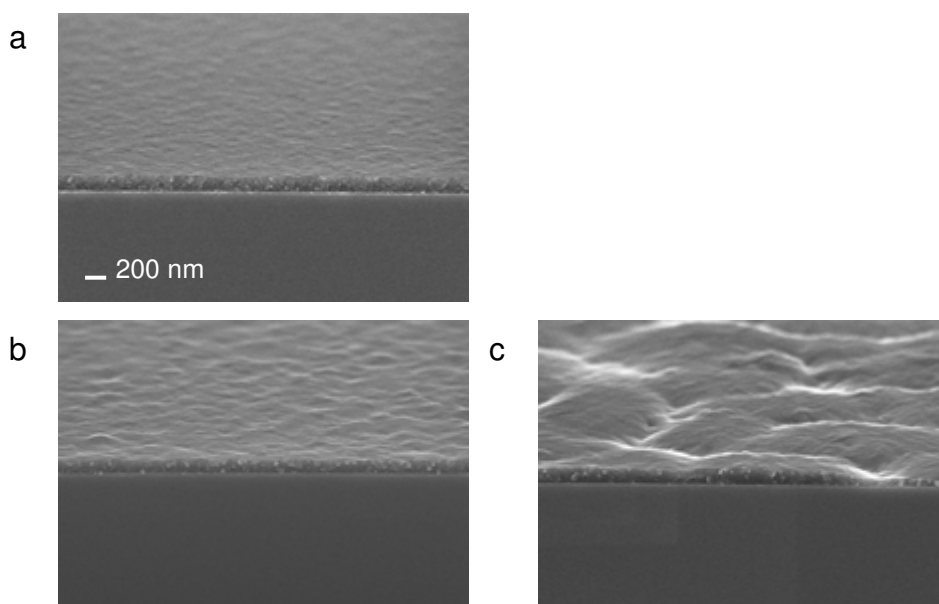
**Figure 5.29** Photovoltaic performance of devices ITO/polymer **1-3** (a-c):PDI/Ag after annealing at 120 °C for 1 h. The I-V curves were measured under solar light AM1.5 G with light intensity of 150-160 W/m<sup>2</sup>.



**Table 5.11** Average photovoltaic performance

Active layer		$I_{sc}$ (mA/cm <sup>2</sup> )	$V_{oc}$ (V)	FF	Efficiency (%)	$EQE_{max}$ (%)
<b>1:PDI (1:1)</b>	pristine	0.49	0.80	0.33	0.88	30
	annealed	0.09	0.60	0.41	0.10	8
<b>1:PDI (1:2)</b>	pristine	0.63	0.81	0.38	1.32	35
	annealed	0.25	0.27	0.33	0.14	14
<b>2:PDI (1:1)</b>	pristine	0.27	0.80	0.41	0.54	16
	annealed	0.06	0.17	0.26	0.02	5
<b>3:PDI (1:1)</b>	pristine	0.15	0.80	0.40	0.33	10
	annealed	0.04	0.11	0.29	0.01	3

Contrary to expectations, the thermal treatment did not induce any improvement in the device performance. Instead, both  $I_{sc}$  and  $V_{oc}$  decreased markedly, indicating both diminishing charge transport and weaker charge transfer from the donor to the acceptor. This can be explained by the limited film forming ability of polymers **1-3** and PDI. During annealing, the development of the crystals occurs by depletion of PDI from surrounding areas, thus producing a film with uneven thickness. The area covered by too little material has a higher electron field, resulting in an invalidation of the D/A junction and a deviation of  $V_{oc}$  determined by the HOMO of the donor and the LUMO of the acceptor. This is proved by the direct observation on the annealed films.



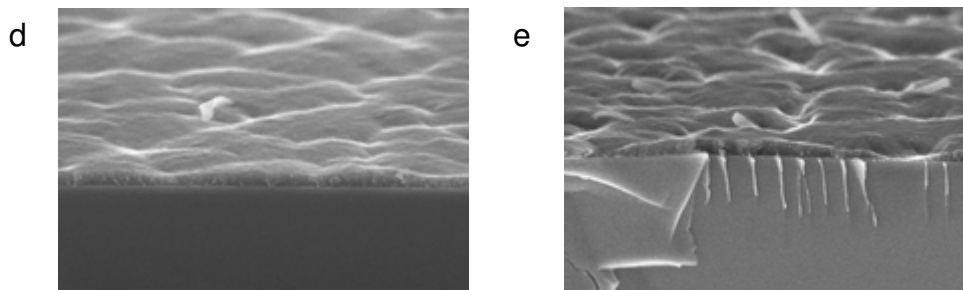


**Figure 5.30** Section view images of films containing blends of polymer **2** and PDI at D/A ratios of: a) 1:1, b) 1:2, c) 1:2 annealed at 120 °C for 1 h, d) 1:4, e) 1:4 annealed, photographed by SEM. The scale bar is 200 nm for all images.

The images in Figure 5.30 clearly show the change in film morphology upon annealing. At the D/A ratio of 1:1, the annealed film is still relatively homogeneous, similar to the unannealed film at the ratio of 1:2, with the latter being a little bit rougher. After annealing, the film of D/A = 1:2 looked like the pristine film of D/A = 1:4, which in turn became even more uneven after the thermal treatment. Some parts of the film became so thin that the substrate was uncovered. These observations explain the much lower efficiencies of the annealed devices.

### 5.3.5 Summary

The solid state packing of new ladder-type polyhexaphenylenes with one and three nitrogen bridges per repeat unit has been investigated. The polymer **2** with three nitrogen bridges showed more red-shifted absorbance and emission and better packing in the solid-state than the analogous polymer **3** with only one nitrogen bridge per monomer unit. The more ordered packing of **2** is expected to possess longer exciton diffusion length and faster charge transport, which function together to give a higher overall efficiency for **2**-based device (0.54% with PDI as acceptor) than **3**-based device (0.33%). The performance of these new materials as electron donating components in photovoltaic devices using PCBM and PDI as electron acceptor was investigated. An overall efficiency as high as 1.3% under

solar light was obtained for the device based on **1** and PDI, compared with 0.7% for a PCz based device. The device performance correlates to a large extent with the solar light absorption ability and the lateral distance between conjugated polymer chains. Since the lateral distance is determined by the length and the number of attached alkyl side chains, it is possible to assume that these substituents insulate the charge carrier pathways and decrease the device performance. As an additional consequence, the active semiconductor is diluted in the insulating matrix leading to a lower light absorption.

The mechanism of charge transfer was further investigated to show a dominant process of  $D + A^* \Rightarrow D^+ + A^-$ . Although the thermal treatment has been proved to be a successful strategy to optimise other PDI contained devices, this method is not effective for the new polymers, due to the poor film forming ability of the ladder-type polymers and PDI.

This work demonstrated the successful application of the new ladder-type carbazole based polymers as donor materials in photovoltaic devices, and suggested ways to improve device performance by molecular design, *viz.* maintaining the HOMO level while bathochromically shifting the absorption by adopting a more rigid ladder-type structure. Also, a high ratio of nitrogen bridges with small alkyl substituents was a desirable feature both in terms of adjusting the absorption and of maintaining a low lateral inter-chain separation, which was necessary for obtaining high current and efficiency values.

## 5.4 Low Band-gap Materials containing 2,7-linked Carbazole

The incorporation of alternating electron donating and electron accepting moieties along the polymer backbone (D-A structure) has been shown to generate low band-gap conjugated polymers.<sup>74,236</sup> The low band-gap in these materials derive from a partial charge transfer in the polymer main chain, induced by the donor-acceptor system when they are linked by conjugated bridge or short saturated spacer (shown in Figure 5.31). Most of the reported low band-gap polymers based on D-A structure are linked by conjugated bridge.

(see Figure 1.10) Here, several D-A structured polymers and small molecules containing 2,7-linked carbazole were investigated for application in solar cells.

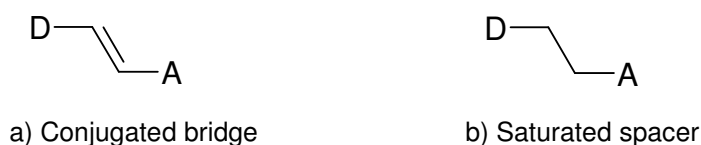


**Figure 5.31** Illustration for the conjugated bridge and saturated spacer in D-A type molecules

#### 5.4.1 Copolymer of PCz and PDI

It has been shown that PDI is a good acceptor material for PCz. But the performance of the device is limited by a low photocurrent. One way to improve this is to enlarge the D/A interface for charge generation, which requires phase separation much finer than the spontaneous morphology achieved by spin-coating the blend (PCz and PDI) solution. One way to achieve this is to covalently link the donor and acceptor in a single polymer chain. The covalent bond enables a predefined control over the characteristic distance between the donor and the acceptor and thereby the extent of phase separation. Two types of covalently linked donor-acceptor polymers have recently been reported. The first consists of a semiconducting polymer as a donor with pendant acceptor groups,<sup>237-241</sup> while the second has extended donor and acceptor units arranged in a diblock copolymer.<sup>242,243</sup> The latter strategy may have important advantages because the intrinsic tendency of each segment in block copolymers to aggregate in an individual phase provides a means to create a well-ordered nanoscale morphology (*e.g.*, spheres, cylinders, lamellae). While this principle has been utilized in engineering various materials to create fascinating architectures, the use of block copolymers in functional, conjugated polymers has received limited attention,<sup>244-248</sup> and even less for the combination of PCz and PDI.

A new class of copolymer based on PCz and PDI, presented as **P4** in Figure 5.32, was synthesized by C. Yang. **P4** is obtained by the polycondensation of diol derivatives of

PCz and PDI at a weight ratio of 1:1 and sebacoyl chloride as a saturated spacer, followed by the addition of an excess of sebacoyl chloride to remove any unreacted terminal alcohol functionality. followed by the addition of an excess of sebacoyl chloride to remove any unreacted terminal alcohol functionality. However, the ratio of the structural composition between PCz, PDI and sebacate units can not be determined from the integration of the NMR peaks since the benzyl signals from the end groups of the PCz-diol can not be assigned in the NMR spectrum. The resulting copolymer shows excellent solubility in common organic solvents. GPC analysis of this polymer exhibits a  $M_n$  value of  $1.26 \times 10^4$  g/mol and  $M_w$  of  $3.34 \times 10^4$  g/mol with a polydispersity of 2.66 (THF, PPP standard).

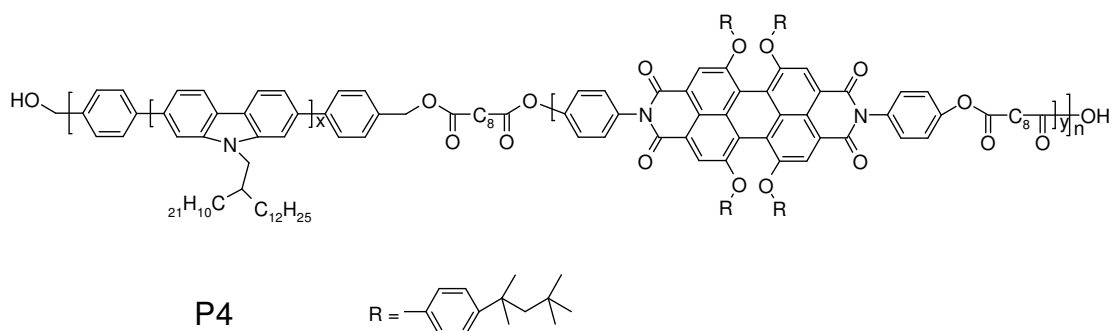


**Figure 5.32** chemical structure of copolymer **P4** based on carbazole and perylene

### Optical Properties

The absorption and PL properties of the polymer **P4** were investigated in THF solution. As shown in Figure 5.33, **P4** exhibits three dominant absorption bands with 392, 537 and 575 nm. The band at 392 nm can be assigned to the absorption from PCz block, whereas the lower-energy peak is clearly attributed to the PDI block. The PL spectrum of **P4** in solution has a large blue emission peak ( $\lambda_{max} = 420$  nm) due to the PCz unit and a PDI emission ( $\lambda_{max} = 600$  nm) when excited at 392 nm. The absorption and PL spectra of **P4** in solution demonstrate predominantly absorption and emission from the PCz block. It is postulated that inefficient intramolecular energy transfer to the chromophores in solution

occurs so that the emission is predominantly from the PCz backbone, though emission is seen from PDI units.

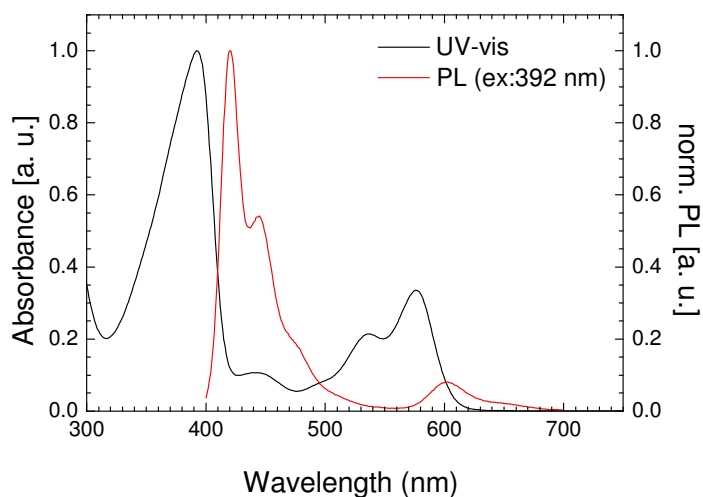
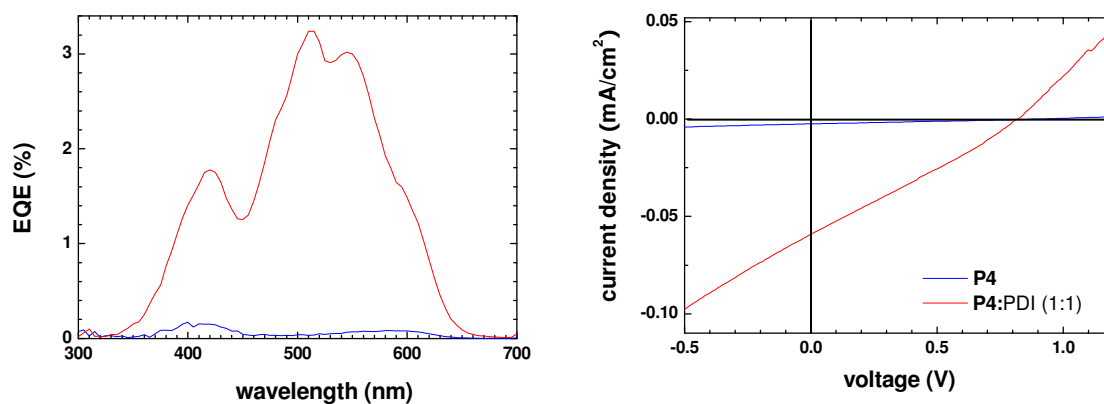


Figure 5.33 UV-vis and PL spectra of polymer **P4** ( $\lambda_{exc} = 392$  nm) in THF solution.

### Photovoltaic Device

Single layer photovoltaic devices were fabricated to investigate the properties of polymer **P4**. The blend of **P4** and PDI at a weight ratio of 1:1 was also tested to see the effect of enhanced acceptor content in the active layer. The result is shown in Figure 5.34.



**Figure 5.34** Photovoltaic performance of devices ITO/active layer/Ag with active layer of polymer **P4** (blue line) or polymer **P4:PDI (1:1)** (red line). The I-V curves are measured under solar light AM1.5 G with light intensity of 164 W/m<sup>2</sup>.

**Table 5.12** Average photovoltaic performance

Active layer	I <sub>sc</sub> (μA/cm <sup>2</sup> )	V <sub>oc</sub> (V)	FF	Efficiency (%)	EQE <sub>max</sub> (%)
<b>P4</b>	2.5	0.90	0.26	0.004	0.2
<b>P4/PDI (1:1)</b>	59	0.82	0.27	0.08	3.2

The photovoltaic device data are summarized in Table 5.12. The V<sub>oc</sub> for **P4** was comparable to or even higher than the V<sub>oc</sub> of PCz/PDI blends. It should be noted that the former is not a bulk heterojunction device, so the upper limit of V<sub>oc</sub> is not decided by the potential difference between the HOMO of the donor and the LUMO of the acceptor any more. The higher V<sub>oc</sub> of **P4** indicates a lower voltage loss at all kinds of interface than in the blend device. However, the I<sub>sc</sub> (2.5 μA/cm<sup>2</sup>) was much lower than that of PCz/PDI (1:1) devices (57 μA/cm<sup>2</sup>), so that the overall efficiency for **P4** was much lower. When illuminated with simulated solar light, efficiencies of 0.004% for **P4** and 0.08% for **P4/PDI (1:1)** were obtained. On the other hand, when the blend (**P4/PDI = 1:1**) is compared with the device PCz/PDI (1:3), the I<sub>sc</sub> was lower than that of the latter (254 μA/cm<sup>2</sup>).

The poor performance of the devices based on **P4** is contrary to the notion that the inherent tendency of each segment in the block copolymer **P4** to aggregate in an individual phase is a means to achieve a well-ordered morphology. The lower efficiency of devices based on **P4** is understood as indicating that there are no efficient percolation pathways for charge transport. It was observed in the study on morphology of thin films composed of PCz and PDI that the formation of PDI crystals results in an enhanced photocurrent and charge transport. An increase in domain size of the PDI crystals corresponds to a higher photocurrent. However in **P4**, a poorer percolation path for charge transport might occur because of the random arrangement of D/A blocks on the polymer chain. As a result, the two moieties cannot set up an efficient percolation path by packing in the solid state.

To confirm this hypothesis, the devices based on the copolymer **P4** and the blend of **P4** and PDI were annealed at 120 °C to facilitate the crystallization of PDI. The comparison of the devices with and without thermal treatment is depicted in Figure 5.35. The EQE of the device using **P4**/PDI increased by a factor of two after annealing, while the EQE of the the **P4** device remained the same. This is consistent with the crystallization of PDI becoming more developed in the blend device which benefits charge transport, but remaining suppressed in the copolymer.

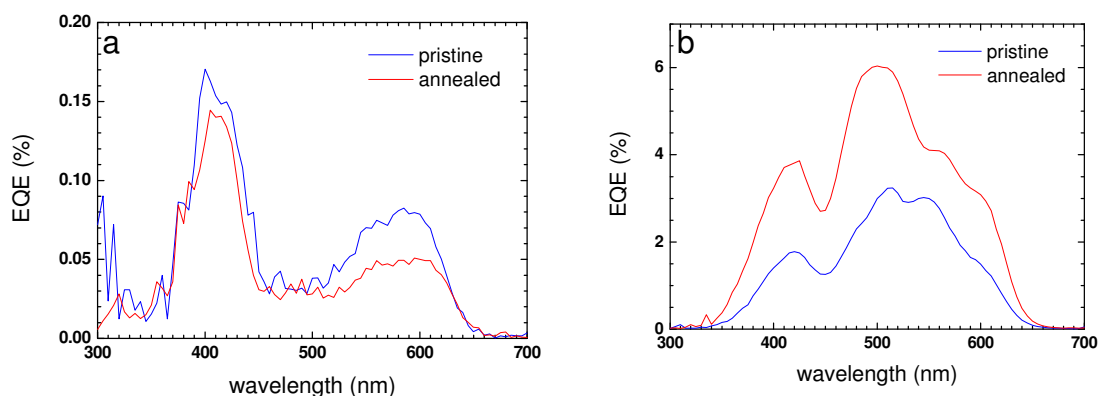


**Figure 5.35** Photovoltaic performance of devices ITO/active layer/Ag annealed at 120 °C for 1 h, with active layer of a) **P4** and b) **P4:PDI (1:1)**.

## Summary

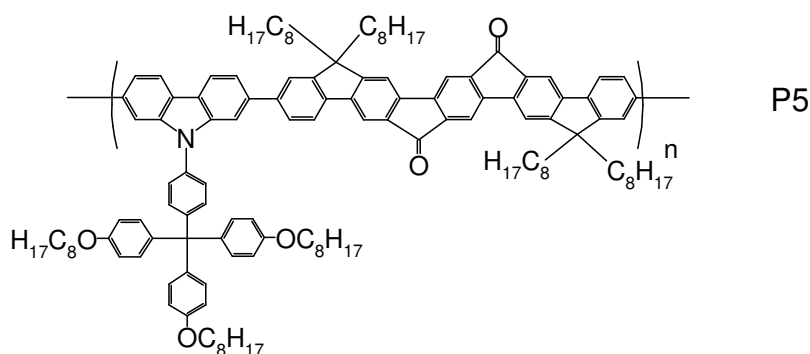
The donor-bridge-acceptor type block copolymer (**P4**) has been synthesized by random condensation of functionalized PCz donor and PDI acceptor units with sebacate saturated spacer units. **P4** and blend (**P4**: PDI, 1:1 wt%) has been tested in photovoltaic devices. While the PDI in **P4** is effective as an acceptor in charge generation, it is less effective in charge transport, due to the donor-acceptor domains occurring in a random fashion along the main chain. This is in contrast to the desired morphology involving donor-donor/acceptor-acceptor stacking. In this case, charges generated in the solar cell have inefficient pathways to travel to the electrodes, which in part accounts for the observed results. The device results on **P4** can provide an important guideline for



design of new block copolymers that could be more effective in polymer photovoltaic cells. To overcome this tendency of donor and acceptor segments to give alternating stacks, stronger antagonistic interactions such as hydrogen-bonding<sup>249</sup> that direct the microscopic morphology should be introduced. This can also be accomplished by introducing anchoring points on the polymer chains (*e.g.*, via interchain hydrogen bonds) that secure the relative positions of donor and acceptor, or by a more regular arrangement of donor and acceptor units along the chain.

#### 5.4.2 Conjugated Copolymers of 2,7-linked Carbazole and Ladderized Pentaphenylene with Diketone Bridge (LPPK)

The direct conjugated link of a donor unit and an acceptor unit has important advantages because the built-in intramolecular charge transfer can facilitate ready manipulation of the electronic structure, so as to lower the band-gap of the material. We have previously reported that a ladder-type pentaphenylene with two ketone groups at the bridges as an excellent electron accepting material.<sup>250</sup> Based on this, the alternating copolymers **P5** and **P6** consisting of carbazole as electron donating moiety and LPPK as electron withdrawing moiety have been synthesized by Dr. M. Zhang.<sup>251</sup> **P5** comprises carbazole and LPPK chromophores in a 1:1 ratio whereas **P6** contains a 2:1 ratio in backbone. Both copolymers show excellent solubility in common organic solvents. GPC analysis exhibits a  $M_n$  value of  $1.01 \times 10^4$  g/mol and  $M_w$  of  $1.31 \times 10^4$  g/mol with a polydispersity of 1.38 for **P5**, and a  $M_n$  value of  $4.41 \times 10^4$  g/mol and  $M_w$  of  $8.41 \times 10^4$  g/mol with a polydispersity of 1.91 for **P6** (THF, PPP as reference).



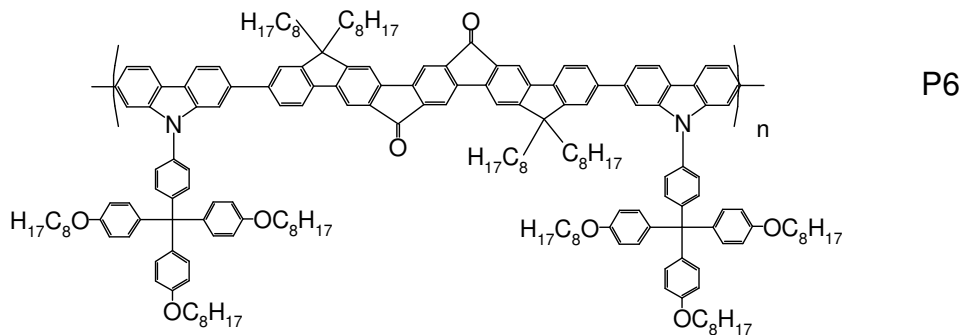


**Figure 5.36** chemical structures of copolymer **P5** and **P6** based on 2,7-linked carbazole and LPPK

### Optical Properties

The UV spectra show the maximum absorption at 408 nm for both polymers and a shoulder peak at 345 nm for **P5** and 347 nm for **P6**. In comparison with aryl PCz, whose  $\lambda_{\text{max}} = 387$  nm, the introduction of LPPK units bathochromic shifts the absorption by 20 nm. The PL spectra in solution are very weak, only one maximum at 696 nm is observed, which is attributed to LPPK units in these copolymers.

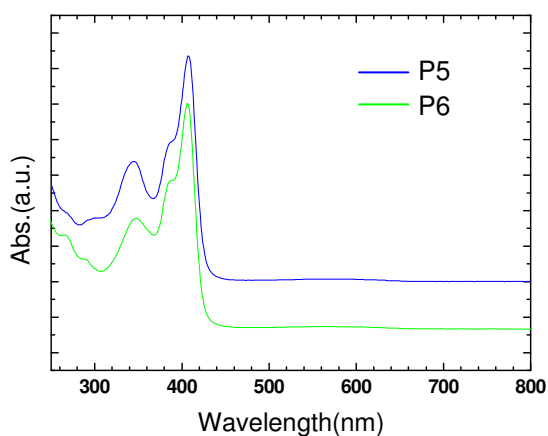


**Figure 5.37** UV-vis spectra of polymer **P5** and **P6** in  $\text{CHCl}_3$  solution.

### Photovoltaic Device

PDI was chosen as acceptor material for the polymers as its absorption spectrum and theirs are complementary. The D/A ratio was set as 1:4, based on the earlier results with PCz/PDI devices.

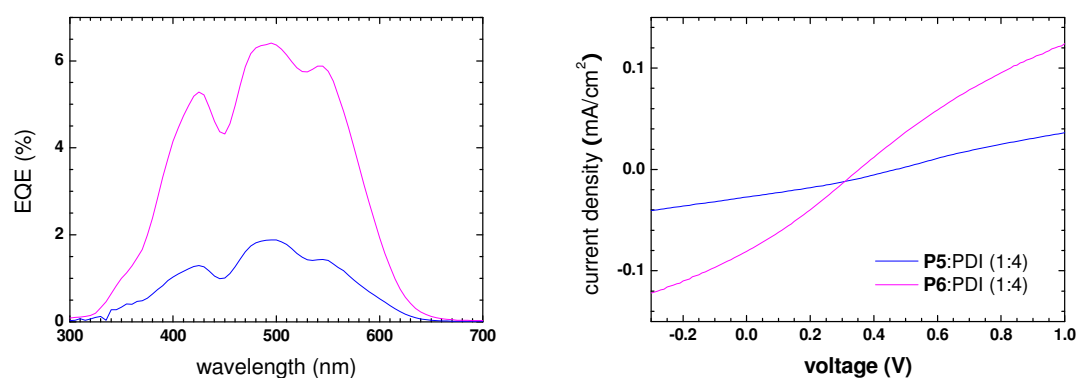


**Figure 5.38** Photovoltaic performance of devices ITO/polymer:PDI(1:4)/Ag with **P5** (blue line) or **P6**:PDI (1:1) (peach line). The I-V curves are measured under solar light AM1.5 G with light intensity of 159 W/m<sup>2</sup>.

**Table 5.13** Average photovoltaic performance

Polymer:PDI (1:4)	I <sub>sc</sub> (μA/cm <sup>2</sup> )	V <sub>oc</sub> (V)	FF	Efficiency (%)	EQE <sub>max</sub> (%)
<b>P5</b>	27	0.47	0.30	0.024	1.9
<b>P6</b>	81	0.35	0.28	0.050	6.4

The device based on **P6** with one more carbazole moiety in the repeat unit than **P5** shows higher efficiency, corresponding to an overall efficiency of 0.05% under solar light and a maximum EQE value of 6.4% at 490 nm. This result suggests that a higher content of the electron donating carbazole unit as in **P6** is preferable in donor materials for solar cells, as it can assist charge transport, resulting in a three fold increase in I<sub>sc</sub> for **P5**.

## Summary

Although the absorption of the copolymers **P5** and **P6** is bathochromically shifted in comparison to PCz, the anticipated low band-gap was not realized. This might arise from the existence of the intermediate fluorene bridges, which undergoes internal energy transfer within the LPPK units<sup>250</sup> so as to inhibit the charge transfer induced light absorption more than would be seen in a D/A system with a directly linked carbazole unit and ketone unit. Besides, the bulk side chains attached to 'N' might prohibit the charge hopping between the chains and also the charge transfer from the donor to the acceptor. It has been reported that the side chain architecture of a series of PPV derivatives has a considerable impact on the performance of the solar cell.<sup>176</sup> The long/bulky branched side chains can not perform as well as the short chains. Upon pairing with PDI in the device to function as donor material, a lower density of carbazole units in the polymer chain leads to a lower efficiency than in the PCz based devices.

### 5.4.3 Small Molecule Based on Carbazole and Ketone

A direct conjugation link between the carbazole and the diketone units was realized in the ladder-type pentaphenylene **M1**, which was synthesized by Dr. S. H. Jung, shown in Figure 5.39. This compound shows good solubility in common organic solvent such as CHCl<sub>3</sub>, THF, etc.

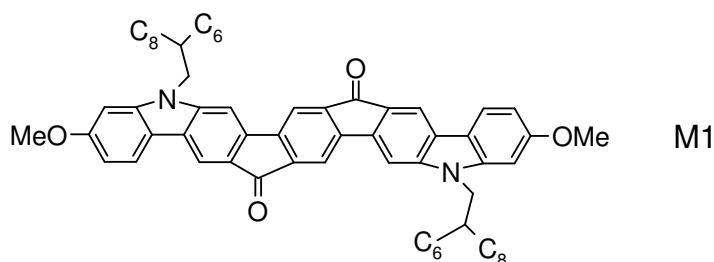


**Figure 5.39** chemical structure of molecule **M1**

## Optical Properties

Two prominent absorption bands are observed in Figure 5.40, the maximum at 376 nm with a second absorption band at 445 nm.

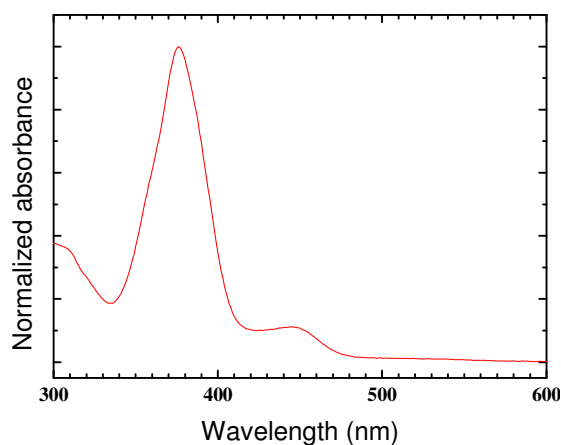


**Figure 5.40** UV-vis spectrum of **M1** in THF solution ( $1 \times 10^{-5} M$ ).

The high-energy absorption band is associated with a  $\pi\text{-}\pi^*$  transition of the donor-acceptor molecule, whereas, the absorption of the low energy band can be unambiguously assigned to strong intramolecular charge transfer (ICT) transition between the carbazole moiety and the aryldiketone system. Comparing with the maximum absorption at 407 nm for **P5-P6**, this observation indicates stronger D/A interaction existing in **M1** having directly linked carbazole unit and diketone unit, than in **P5** and **P6**, where the donor and acceptor units are linked by a fluorene bridge.

## Electrochemical Properties

The electrochemical redox behavior of the compound **M1** was investigated by CV against  $\text{Fc}/\text{Fc}^+$ . As shown in Figure 5.41, the material exhibits both oxidation and reduction peaks, arising from the carbazole and ketone units, respectively. The peaks are reversible with oxidation onset at 0.42 V and reduction onset at -1.99 V, corresponding to the HOMO value of -5.22 eV and the LUMO value of -2.81 eV. The electrochemical HOMO-LUMO gap is 2.41 eV, which is comparable to the optical bandgap value (2.58 eV) from the UV spectrum. These values suggest **M1** as an energetically allowed low band-gap donor material for PDI, whose HOMO/LUMO are -5.8/-3.8 eV.

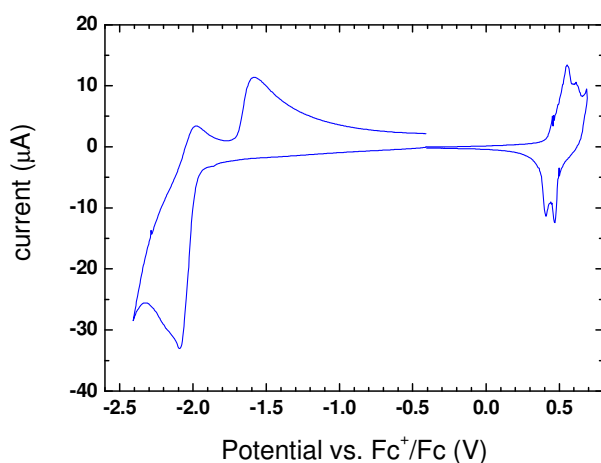


**Figure 5.41** CV curve of **M1** as thin film casted on gold electrode in the three-electrode cell.  $\text{TBAClO}_4$  and acetonitrile were used as electrolyte and solvent, scanning speed was 100 mV/s.

### Photovoltaic Device

To test this idea, photovoltaic devices were fabricated using **M1** as donor and PDI as acceptor at a weight ratio of 1:1. As shown in Figure 5.42, the device exhibits an open circuit voltage of 0.62 V, and a short circuit current of  $1 \mu\text{A}/\text{cm}^2$  when illuminated under solar light. The highest EQE of 0.2% was observed at 480 nm. This preliminary result suggests that **M1** could potentially be used as a donor material in solar cells, but considerable more work must be done to improve efficiencies.

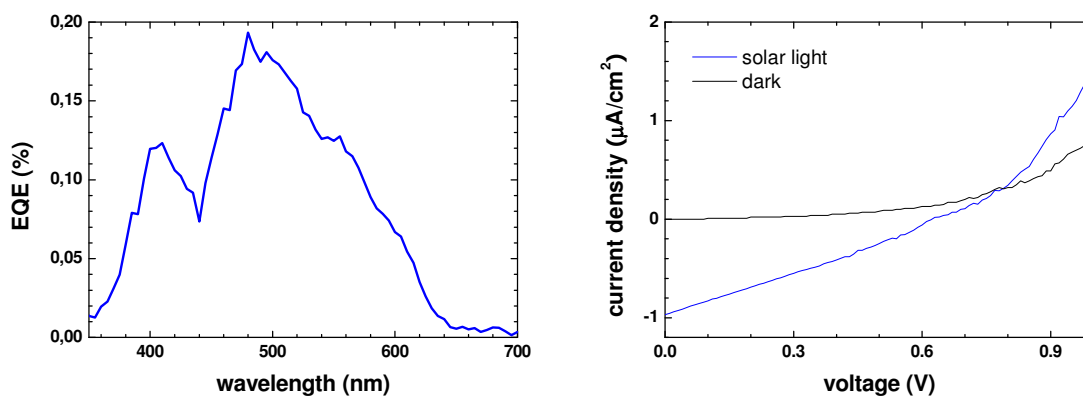


**Figure 5.42** Photovoltaic performance of device ITO/M1:PDI(1:1)/Ag. The I-V curve is measured under solar light AM1.5 G with incident light intensity of 162 W/m<sup>2</sup>.

**Table 5.14** Average photovoltaic performance

Active layer	I <sub>sc</sub> (μA/cm <sup>2</sup> )	V <sub>oc</sub> (V)	FF	Efficiency (%)	EQE <sub>max</sub> (%)
M1:PDI (1:1)	0.97	0.62	0.28	0.001	0.20

## Summary

A novel push-pull type small molecule based on 2,7-linked carbazole was synthesized, which possesses a high LUMO energy level and a lower band-gap than PCz. The design proves a more efficient D/A interaction for charge transfer from the carbazole unit to the ketone unit, compared to the D/A system in **P5-6**. Interest arises if a polymer can be realized based on **M1** since it's previously reported the molecular weight can strongly influence the behaviour of the cell.<sup>192</sup>

## Chapter 6 Guidelines for Solar Cell Design

A good D/A pair is the basis for fabricating efficient devices. There are several aspects one has to consider when pairing the donor material with an acceptor material. In this chapter, the matching of D/A pairs will be discussed in terms of the following:

- Absorption of solar light
- Energy level considerations
- Charge separation and transport
- Film forming

### 6.1 Absorption of Solar Light

It has been known that the strongest emission part of the solar light is in the range of 450-1100 nm. Therefore, a material (donor or acceptor) with absorption in this region is desired. Some possible approaches to adjust maximum absorption of materials are discussed below.

#### 1. Introduction of ladder-type structure

PCz was discussed in Chapter 5 as a novel donor material. However, its absorption deviates from the strongest emission part of solar light, which is the motivation for the synthesis of the ladder-type polymers **P1-3**. The introduction of ladder-type structure is proved to be an efficient way to enhance light absorption due to extended conjugation.<sup>222-</sup>  
<sup>225</sup> In comparison with **P1**, which shows  $\pi$ - $\pi^*$  transition peak at 433 nm (Figure 6.1a), PCz is less efficient for light absorption. Devices using PCz or **P1** as donor and PCBM as acceptor were fabricated to perform a direct observation. As shown in Figure 6.1b, the overall efficiency of 0.48% was achieved for **P1** based device, much higher than 0.07% for



PCz based device. This result clearly indicates the importance of enhancing light absorption.

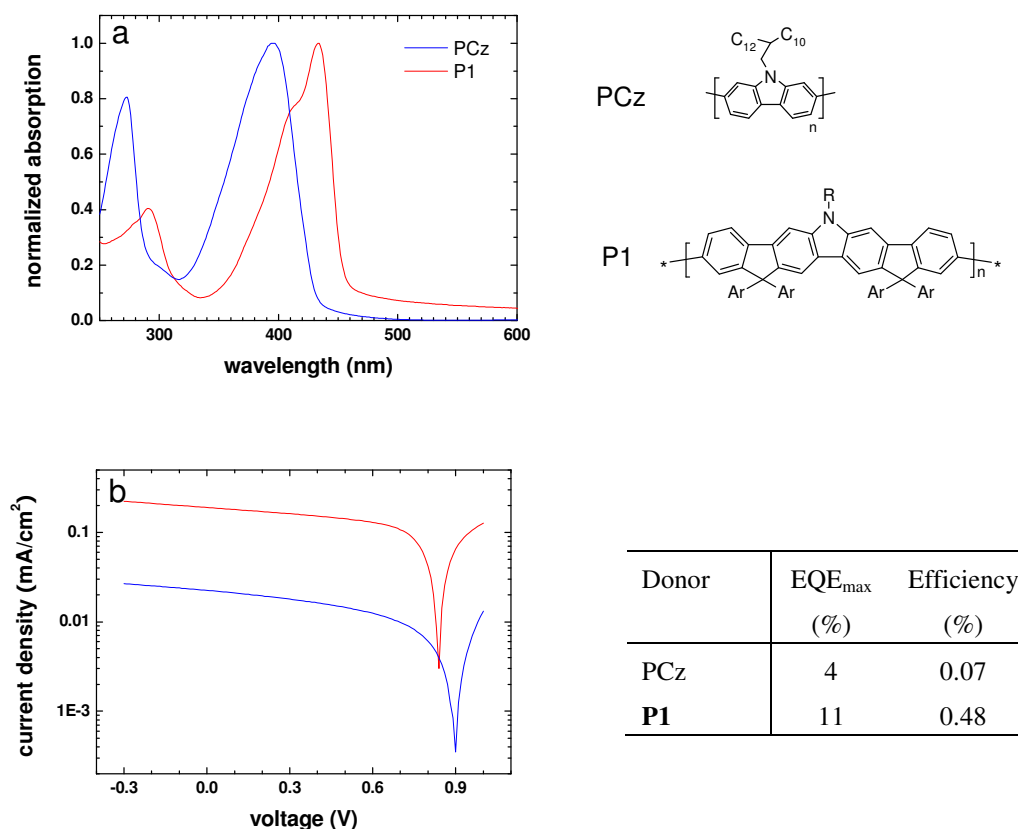


**Figure 6.1** a) UV-absorption spectra of PCz and P1 as thin film and b) I-V curves for device ITO/donor:PCBM(1:2)/Ag recorded under simulated AM 1.5G solar light with incident light intensity of  $105 \text{ W/m}^2$  for PCz device and  $150 \text{ W/m}^2$  for P1 device. The chemical structures are illustrated on the top right.

## 2. Chromophore density

The chromophore density is another important factor, as higher density with less solubilizing substituents provides stronger light absorption. This was observed in a series of HBCs varying in the length of the attached alkyl side chains from 2-ethyl-hexyl of

HBC-C<sub>6,2</sub>, and 2-hexyl-decyl of HBC-C<sub>10,6</sub>, to 2-decyl-tetradecyl of HBC-C<sub>14,10</sub> (Figure 4.18), where the absorption in a 100 nm thick film decreased from 1.4, to 0.8 to 0.5.

### 3. Linking donor unit and acceptor unit

The third option is to link the donor and the acceptor units in one compound. As discussed in Chapter 5, two kinds of links are possible, conjugated bridge (such as **P5-6** and **M1**) and saturated spacer (such as **P4**). The conjugated bridge has an important advantage in that intramolecular charge transfer induced light absorption can occur leading to a bathochromic shift in optical spectrum. For example, **M1** has a 50 nm bathochromic shift in comparison with PCz.

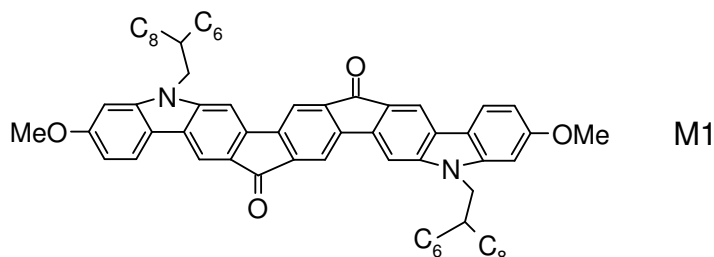


**Figure 6.2** The molecular structure of **M1**.

Because of the covalent bond and close proximity of the electroactive units, these molecular donor-acceptor systems generally provide a high efficiency for photoinduced charge generation and can be tailored to exhibit long radical ion state pair lifetimes.<sup>252</sup> Furthermore, the special D/A intermolecular interaction induced self-organization either in solution or in film can be applied in fabricating devices, which will be further discussed in section 6.3.

However, this is not always true that the material with stronger light absorption corresponds to better performance. For example, the dye quaterrylene tetracarboxydiimide (QDI), which has longer conjugated unit, can absorb double the amount of photons than PDI with an extended tail to 1000 nm. But the low band gap of QDI is achieved by increasing the HOMO level to -4.9 eV (corresponding LUMO is -3.7 eV), which is higher

than most donor materials (for example, -5.2 eV for P3HT and HBC, -5.6 eV for PCz). A lower efficiency was observed when doping 5% QDI in the PCz/PDI (1:4) device, shown in Figure 6.3. This might result from the mismatch of the potential levels of the donor (PCz) and the acceptor (QDI), leading to charge recombination (green star) at the QDI sites. The energetic requirements on pairing a donor and an acceptor are further discussed in section 6.2.

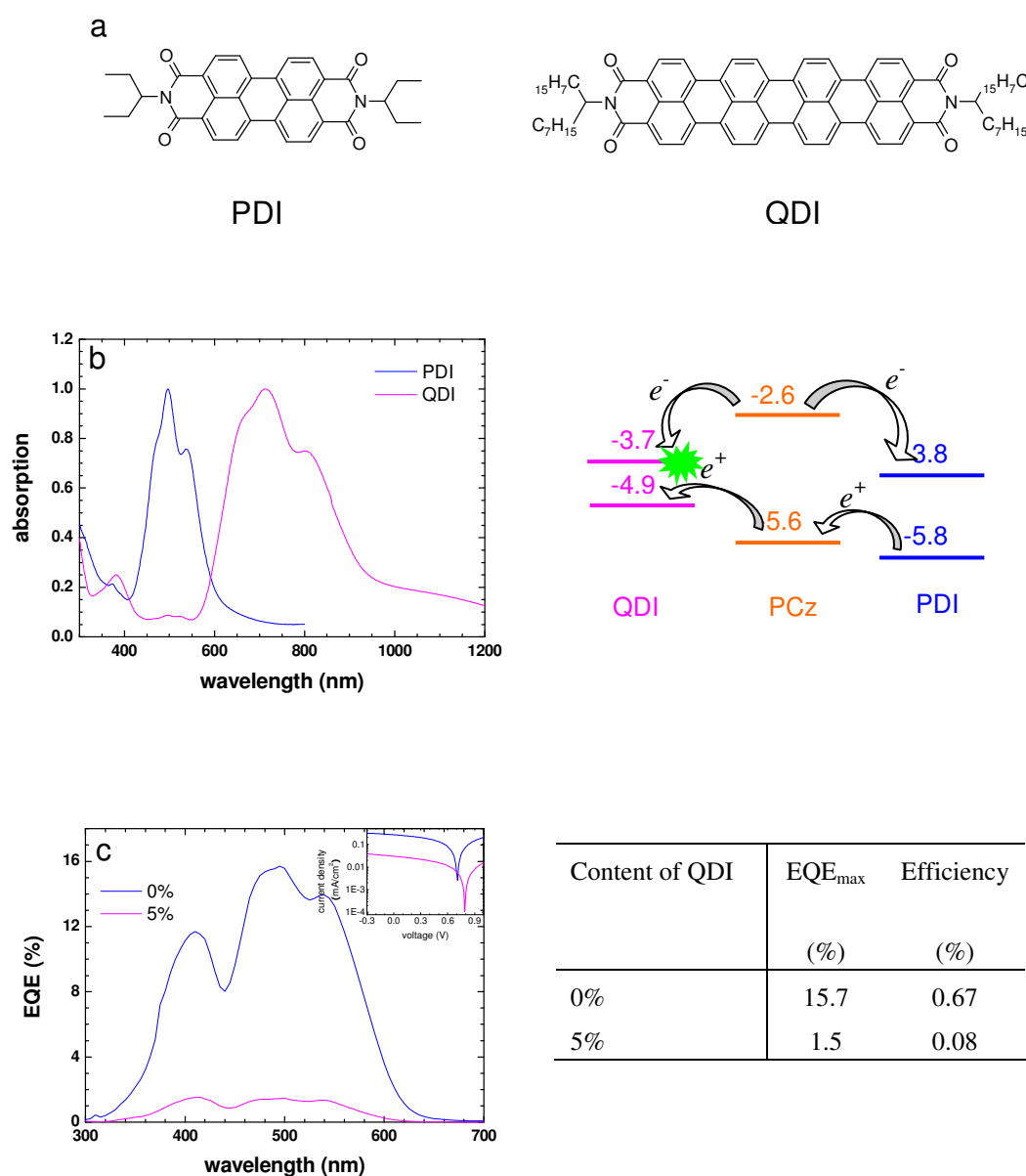


**Figure 6.3** a) The chemical structure of QDI in comparison with PDI. b) The UV absorption spectrum of QDI in thin film, with potential diagram in the D/A system of PCz/PDI/QDI on the right. c) Photovoltaic performance of the device ITO/PCz:PDI(1:4)/Ag upon doping with QDI. The percent number indicates the content of QDI in the blend. The inset I-V curve was recorded under solar light AM1.5 G with light intensity of  $100 \text{ W/m}^2$ . The parameters of the device are included in the table on the right.

## 6.2 Relative Energy Levels

The two-level system was introduced in Figure 2.5. This defines the energetic requirements for matching a donor and an acceptor. That is, the HOMO of the acceptor must lie beneath the HOMO of the donor for realizing a hole transfer, and at the same time, the acceptor must bear a lower LUMO than the donor allowing electron transfer. Since ITO is normally used as transparent anode and in most cases Al/Ag as cathode, the HOMO of the donor is required to be lower than  $-4.8 \text{ eV}$  (work function of ITO) and the LUMO of the acceptor should be higher than  $-4.2 \text{ eV}$  (work function of Al/Ag).

It has been discussed in Chapter 4 and 5 that the energy difference between the HOMO level of the donor and the LUMO level of the acceptor decides the maximum  $V_{oc}$  in a device. The higher the potential difference, the larger the value of  $V_{oc}$ .

This was observed in PCz/PDI and P3HT/PDI device. Both were prepared at the D/A ratio of 1:4 as shown in Figure 6.4. The  $\text{EQE}_{\text{max}}$  of 16 % was achieved at 490 nm for a PCz based device, corresponding to an efficiency of 3.2 % with incident light intensity of  $0.6 \text{ W/m}^2$ . At 470 nm, the cell showed a  $V_{oc}$  of 0.7 V, a short circuit current ( $I_{sc}$ ) of  $6.7 \mu\text{A/cm}^2$ , and a FF of 0.43. The P3HT based device displayed the  $\text{EQE}_{\text{max}}$  of 6.6 % and an efficiency of 0.39 %, under identical irradiation conditions compared to the PCz-based device. These values are comparable to those reported by Dittmer *et al.* for P3HT:PDI (1:4) device<sup>253</sup>, which produced a maximum EQE of 7 % and an efficiency of 0.4 % at 540 nm with light intensity of  $1.6 \text{ W/m}^2$ .

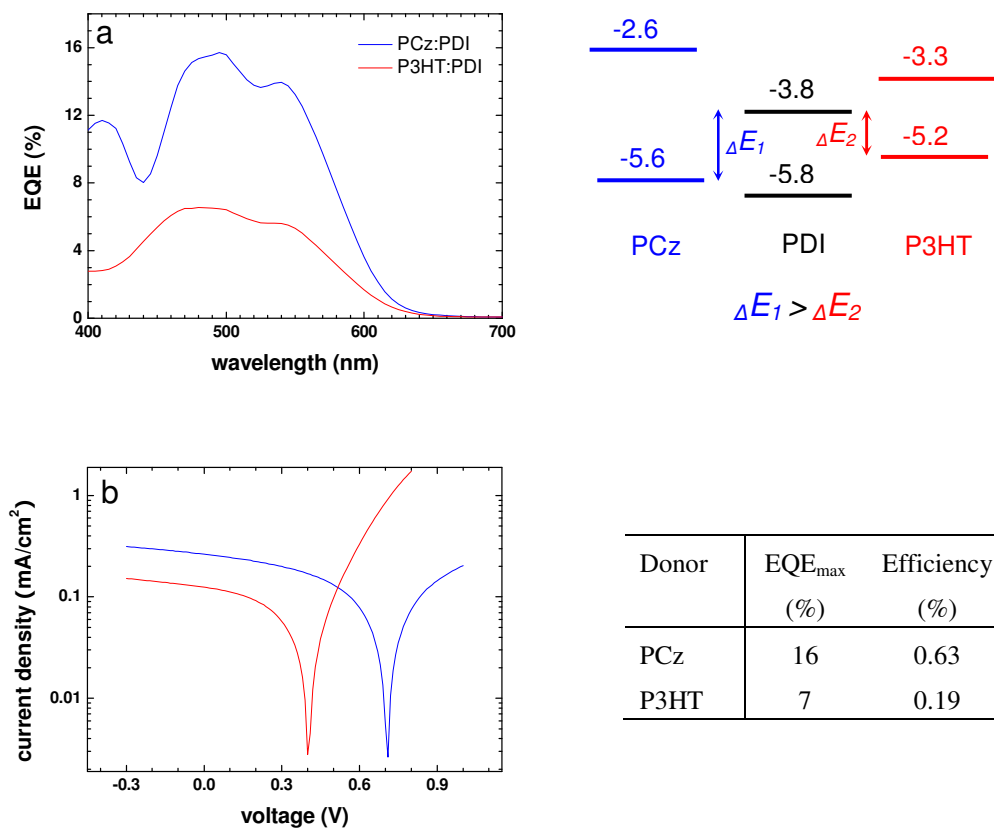


**Figure 6.4** a) EQE- $\lambda$  spectrum of ITO/donor:PDI(1:4)/Ag device. The potential diagram of the materials used is given on the right. b) I-V curve recorded under solar light at light intensity of 100 W/m<sup>2</sup>.

When illuminated with simulated solar light, the PCz:PDI (1:4) cell displayed an I<sub>sc</sub> of 0.26 mA/cm<sup>2</sup>, a V<sub>oc</sub> of 0.71 V, a FF of 0.37, and an efficiency of 0.63 %, which to the best of our knowledge is the highest efficiency yet reported for a polymer-based solar cell not incorporating PCBM. By contrast the P3HT:PDI (1:4) device showed an I<sub>sc</sub> of 0.12 mA/cm<sup>2</sup>, a V<sub>oc</sub> of 0.40 V, a FF of 0.39, and an efficiency of 0.19 %. It is clear that the PCz device has almost twice the I<sub>sc</sub> and V<sub>oc</sub> in comparison with the P3HT device, which in turn triples the efficiency of the PCz device. The higher efficiency of PCz based device is explained by the lower HOMO level of PCz (5.6 eV) than that of P3HT (-5.2 eV), as illustrated in Figure 6.4. The larger energy difference in the PCz based device is thus

consistent with the experimental results showing an increase in  $V_{oc}$  by 0.3 V despite voltage losses at all interfaces.

The results clearly prove the larger potential difference in the PCz/PDI system leads to higher  $V_{oc}$ , and so higher efficiency. However, this has to be carefully designed. There are two ways to increase the potential difference. One way is to reduce the HOMO level of the donor, which is limited by the HOMO of the acceptor and the requirement of approaching low band gap material. The other way is to increase the LUMO level of the acceptor, which will influence the charge transfer as discussed in Chapter 2.2.2. Therefore, for a target acceptor, for example PCBM (-6.0/-4.1 eV), the optimized donor should have LUMO in the range of  $\sim$ -3.1 – -3.5 eV, and a HOMO of  $\sim$ -4.9 – -5.3 eV from the view of energetic matching and light absorption.

A recently published paper showed a novel way to improve  $V_{oc}$  by introducing intermolecular hydrogen bonding between  $-\text{CH}=\text{CH}_2$  group with carboxylic dianhydride group in a bilayer device (Figure 6.5).<sup>254</sup> The intermolecular interaction promotes forward interfacial electron transfer and eliminates the subconducting band trap sites, resulting in a high  $V_{oc}$  of 2.07 V. This hypothesis is being explored in further studies.

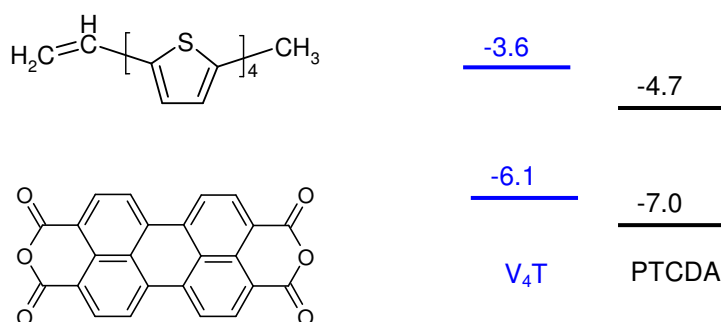


**Figure 6.5** Intermolecular hydrogen bonding used in the literature. The energy potential levels were given as reference.

### 6.3 Charge Transport and D/A Interfacial Area

Charge transport is another important process involved in a solar cell. After charge separation, the charges have to be transferred to electrodes to generate an electric current. Large D/A interface area favors charge separation. Minimizing phase separation scale in the D/A blend could theoretically magnify D/A interface area. However this might increase charge hopping between domain boundaries, which are not favorable for fast charge transport.

### 1. Influence of structure

For organic semiconductors, different types of conjugated units are desirable for charge migration, namely, electron-rich groups in the donor and electron-deficient groups for the acceptor. A comparison of PCz and PF as donor material for PCBM provides a clear illustration of the influence of molecular structure on the efficiency. The electron-rich carbazole unit facilitates charge migration along the polymer chain and thus leads to a much more efficient device than PF based device (Figure 6.6).

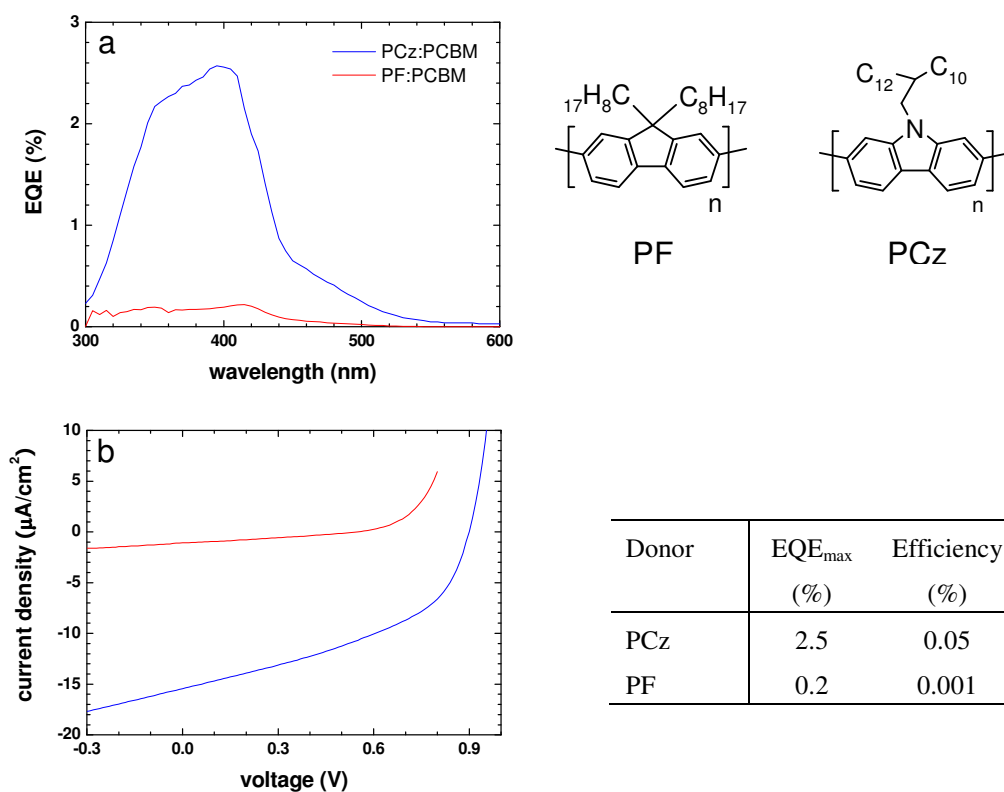


**Figure 6.6** Photovoltaic performance of devices ITO/PCz:PCBM(1:1)/Ag and ITO/PF:PCBM(1:1)/Ag: a) EQE- $\lambda$  curve, and b) I-V curve under solar light AM1.5 G with light intensity of  $115 \text{ W/m}^2$ .

## 2. Self-organization

As intermolecular charge hopping through disordered domains is not as efficient as within ordered domains,<sup>255</sup> the self-organization behavior of the material strongly influences the charge transport properties. In the investigation of the ladder-type poly(2,7-carbazole)s **P1-3**, the important elements in the polymer architecture, which affect the organization, were identified. Long alkyl side chains, especially which are branched close to the rigid conjugated building block, and a high ‘concentration’ of aryl groups along the backbone diminish the macroscopic order, which are not desired for efficient charge transport and will lead to lower efficiency. To be noted, the carbazole unit is found to enhance the packing of the conjugated polymers without compromising on its processibility. This is a highly desirable feature for materials to be useful in devices.

**The solubilizing substituents** attached to the conjugated backbones not only show important effects on the self-organization of the molecules, but also influence the energetic levels of the material as well. It was observed that an insulating effect existed in the alkyl chains, so as to reduce the HOMO level of the HBCs (Figure 6.7).

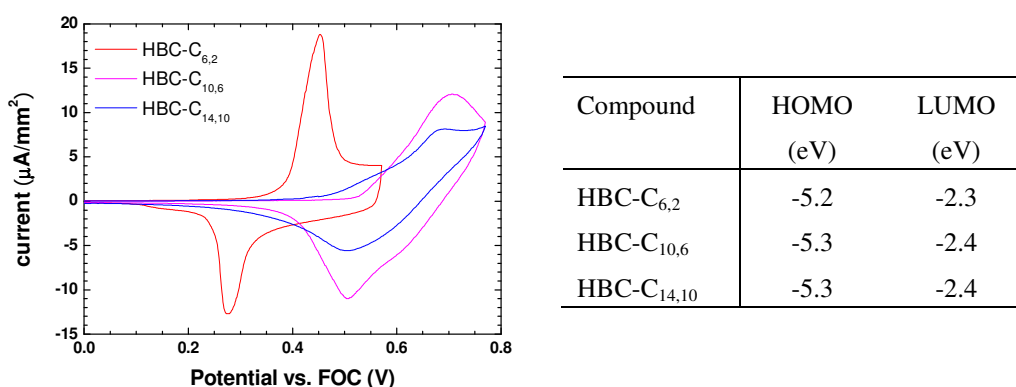


**Figure 6.7** CV curve of HBCs spin-coated on ITO glass, scanning rate of  $25 \text{ mV/s}$ . The table on the right gives the calculated values of the HOMO and the LUMO.



The long alkyl chains slows down the intermolecular charge hopping, as well as charge separation at the D/A interface, both undesirable for solar cells. Therefore, shorter substituents, sufficient to induce processibility, are preferable for device fabrication.

Except for the consideration on the capability of self-organization, the question how the molecules pack themselves are also quite important. It was recently reported that a short donor-acceptor distance created by aggregation in a slipped, *J*-type model can accelerate charge transfer and separation (Figure 6.8), in comparison with a fixed intramolecular distance in the aggregation of *H*-type model.<sup>256,257</sup> Although charge recombination becomes faster inevitably at the same time, this is expected to be a method to control the self-organization of the materials to optimize photovoltaic devices. Supramolecular interactions such as hydrogen-bonding, charge-transfer interactions, and  $\pi$ - $\pi$  stacking of functional  $\pi$ -conjugated systems may be used to create this kind of pre-defined systems.<sup>152,258-260</sup>

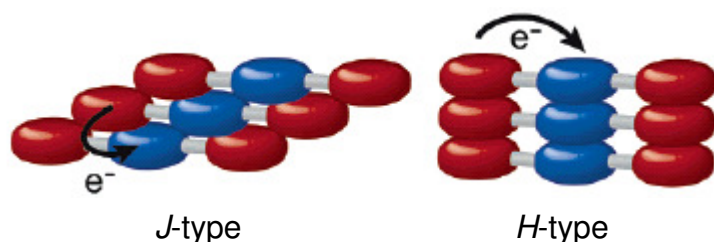
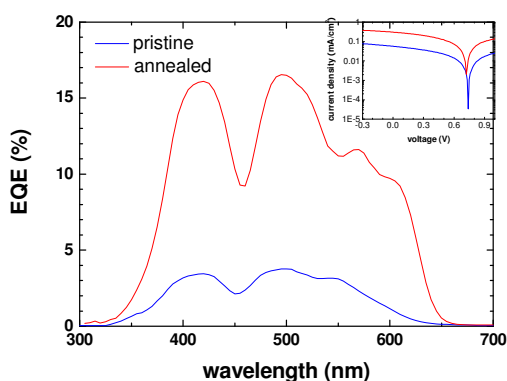


**Figure 6.8** Cartoon of one dimensional packing of *J*-type and *H*-type. The red and blue balls indicate two different units such as donor and acceptor.

### 3. Crystallization

Crystallization leads to highly ordered self-organization, which in turn results in faster charge transport. For example, like PDI, a charge carrier mobility of  $0.1 \text{ cm}^2\text{V}^{-1}\text{s}^{-1}$  is observed in the liquid crystalline phase, and in the crystalline phase it increases to as high as  $0.2 \text{ cm}^2\text{V}^{-1}\text{s}^{-1}$ . The formation of crystal phases and the crystalline organization is not only determined by the chemical architecture of the material itself, but also by the applied processing conditions.<sup>261-263</sup> In principle, materials with regular and symmetric structure tend to crystallize easily.

Thermal treatment is often used to develop crystallization in a film.<sup>264</sup> The increase of crystallinity results in an improvement of the optical absorption in the low photon energy region and in a bathochromic shift of the absorption spectrum.<sup>69</sup> Therefore, the overall efficiency can be greatly improved by appropriate thermal treatment.<sup>35</sup> Similar phenomena was observed for PDI based devices in this work. For PCz/PDI (1:1) device, the EQEmax increased from 3.8% to 17% after the device was annealed at 120 °C for 1 h, corresponding to an overall efficiency from 0.12% to 0.64% (Figure 6.9).



Thermal treatment?	EQE <sub>max</sub> (%)	Efficiency (%)
No	4	0.12
Yes	17	0.64

**Figure 6.9** Photovoltaics performance of devices ITO/PCz:PDI(1:1)/Ag with (red line) and without (blue line) annealing at 120 °C for 1 h. The I-V curve was recorded under solar light AM1.5 G of light intensity of 100 W/m<sup>2</sup>.

#### 4. Phase separation / Morphology

Since the crystallization is normally accompanied by the development of phase separation in the blend, which will influence the quality of the film, the film-forming ability of the components has to be considered before applying thermal treatment on devices. In comparison with PCz, the more rigid ladder-type polymers **P1-3** are less able to form good film. Therefore, the thermal treatment induces the discontinuous film, and no optimisation can be realized (Figure 5.34&5.35).

Except for the properties of the separate materials, the morphology of the blend films plays an important role on device performance, and has been found in some cases to influence the efficiency by a factor of more than two.<sup>233,235,265</sup> Normally, the concept of bulk-heterojunction is applied in organic solar cells. This requires the two components to

be soluble in the same solvent, so that a homogeneous solution can be formed and solidified in the film by spin coating. If the two components are soluble in the same solvent, they are miscible in principle. Therefore, a homogeneous morphology is expected in the blended film. However, phase separation can occur due to the different conditions during the evaporation of the solvent, the different phases (LC, Crystalline, or amorphous solid) of the components at RT, and the intermolecular action in the solid state. The scale of the phase separation (scale of the domains) is used to describe this and can be controlled by using solvents in which the two components show different solubility or whose boiling point is varied. The annealing procedure can also enlarge the size of the scale due to further development of phase separation and crystallization. If the two components are in different phases, for example in the blend of HBC-PhC<sub>12</sub> and PDI, the former is in LC state and the latter is in crystalline state at RT, a large phase separation scale is often observed. The ultimate phenomenon is the formation of bi-layer, which will benefit charge transport but at a cost of decreased D/A interface for charge separation. For materials with high charge carrier mobility, charge separation is more emphasized comparing with charge transport, thus a homogeneous film with small phase separation scale is required.

Another emerging concept to control the morphology relies on self-assembly in solution by kinds of intermolecular interaction, which is in principle applicable to all kinds of  $\pi$ -conjugated oligomers. The quadruple hydrogen-bonded oligo(*p*-phenylenevinylene) was successfully applied in solar cell, exhibiting a better performance than those without hydrogen-bond.<sup>249</sup> However, the homogeneous alignment of the supramolecular organized domains in the micrometer regime is still needed, appeared to be an appealing challenge in the field of supramolecular chemistry and also in the area of materials science.

## 6.4 Film Forming

A good film is a prerequisite to fabricate a device. Normally, a long, flexible alkyl chain can improve the film forming ability. The method of film forming is the second important factor to decide the quality of the film. The solvent-based film-deposition techniques can be classified into two groups based on the dynamics of solvent evaporation:

fast solvent evaporation, such as spin-coating, or slow solvent evaporation, such as doctor blade<sup>266</sup> and inkjet printing.<sup>71</sup> Among these, spin-coating is most widely used for fabricating the organic photovoltaic devices. In a word, the film is influenced by the following factors in the fabrication of devices:

- Compatibility of the two polymers
- Viscosity of the solution
- Wetting ability of the blend solution
- Film forming parameters

The compatibility of the two materials was discussed in the morphology part. Either large scale or micro scale phase separation is generally observed. Large-scale separation is not desirable for good film forming. The substrate for spin coating has to adopt ITO because of its high conductivity and transparency. The viscosity of the solution is mostly decided by the concentration, which can only be varied in a small range limited by the thickness of the film and the solubility of the material. In comparison, the choice of solvent and other parameters in spin coating are more easily modulated.

Variation of the casting solvent can have a profound influence on the quality of the film. For example, PCz and PDI dissolve in both  $\text{CHCl}_3$  and CB and form clear solution at a concentration of 15 mg/ml. But only the  $\text{CHCl}_3$ -solution casted film is homogeneous. The CB-casted film is discontinuous, as shown in Figure 6.10. This can be explained by the high boiling point of CB (131 °C), which takes longer time for evaporation during spin coating thus too little solution is left on the substrate to form the film.

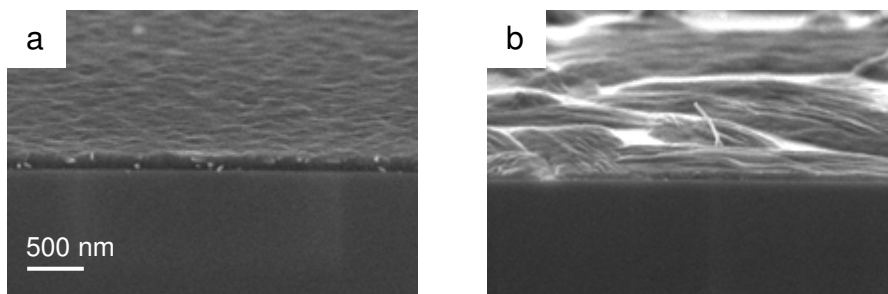


**Figure 6.10** section view SEM images of PCz/PDI (1:4) spin-coated from 15 mg/ml solution in a)  $\text{CHCl}_3$  and b) CB. The spin speed is 1500 rpm.

The speed for spin coating can influence the film thickness and the morphology in the film. A suitable spin speed has to be decided individually for different solutions. For example, for the blend solution of **P2**/PCBM (1:4), a good film was obtained at a spinning rate of 1000 rpm, and the film became discontinuous at higher speed (2000-4000 rpm), as illustrated in Figure 6.10. This can be understood considering the same phenomena as with high boiling point solvents. At higher spin speed, the stronger centrifugal force makes larger amount of solution off the substrate before the solvent is evaporated, leading to a discontinuous film with less material.

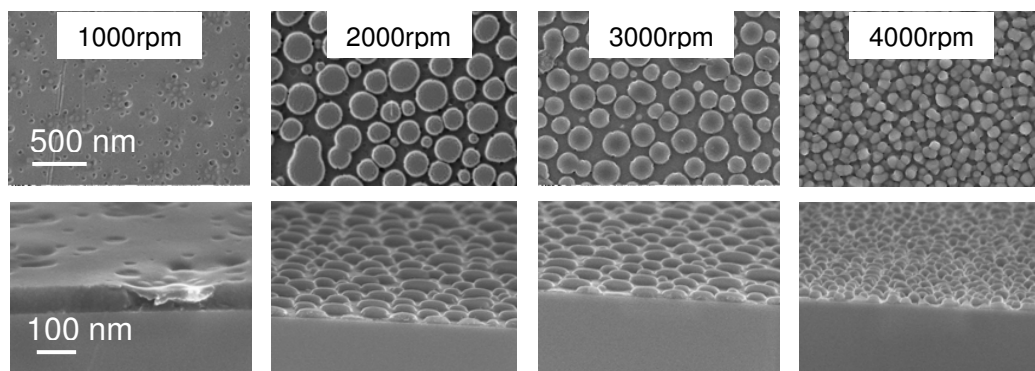


**Figure 6.10** SEM images of **P2**/PCBM (1:4) blends spin-coated from 15 mg/ml  $\text{CHCl}_3$  solution at different spinning rates, which are indicated by the inset numbers.

The discontinuous or inhomogeneous film can lead to uneven electric field in the device, resulting in an invalid D/A junction and a deviation of  $V_{oc}$  decided by the energy difference between the HOMO level of the donor and the LUMO level of the acceptor. Therefore, it is important to identify the best conditions suitable for film forming before fabrication of devices.

The factors described above are based on experiences gained in this study, which hopefully could give some guidelines on designing improved solar cells in the future.

## Conclusions and Outlook

### Conclusions

In this study, the use of the discotic liquid crystalline HBCs and conjugated polymers based on 2,7-carbazole were investigated in detail as donor materials in organic bulk-heterojunction solar cells. It has been shown that they perform efficiently in photovoltaic devices in combination with suitable acceptors. The efficiency was found to depend strongly dependent on the morphology of the film. By investigation of a series of donor materials with similar molecular structures based on both discotic molecules and conjugated polymers, a structure-performance relation was established, which is not only instructive for these materials but also serves as a guideline for improved molecular design.

For the series of HBCs used in this study, it is found that the device efficiency decreases with increasing length of the alkyl substituents in the HBC. Thus, the derivative with the smallest alkyl mantle, being more crystalline compared to the HBCs with longer alkyl chains, gave the highest EQE of 12%. A large interfacial separation was found in the blend of HBC-C<sub>6,2</sub> and PDI, since the crystallization of the acceptor occurred in a solid matrix of HBC. This led to small dispersed organized domains and benefited the charge transport. In contrast, blends of HBC-C<sub>10,6</sub>/PDI or HBC-C<sub>14,10</sub>/PDI revealed a rather homogeneous film limiting the percolation pathways due to a mixed phase.

For the first time, poly(2,7-carbazole) was incorporated as a donor material in solar cells using PDI as an electron acceptor. The good fit in orbital energy levels and absorption spectra led to high efficiency. This result indicates that conjugated polymers with high band-gap can also be applied as materials to build efficient solar cells if appropriate electron acceptors are chosen. In order to enhance the light absorption ability, new ladder-type polymers based on pentaphenylene and hexaphenylene with one and three nitrogen bridges per repeat unit have been synthesized and characterized. The polymer **2** with three nitrogen bridges showed more red-shifted absorbance and emission and better packing in the solid-state than the analogous polymer **3** with only one nitrogen bridge per monomer unit. An overall efficiency as high as 1.3% under solar light was obtained for the device based on **1** and PDI, compared with 0.7% for the PCz based device. Therefore, the device performance correlates to a large extent with the solar light absorption ability and the lateral distance between conjugated polymer chains. Since the lateral distance is determined by the length and number of attached alkyl side chains, it is possible to assume

that these substituents insulate the charge carrier pathways and decrease the device performance. As an additional consequence, the active semiconductor is diluted in the insulating matrix leading to a lower light absorption.

This work suggests ways to improve device performance by molecular design, *viz.* maintaining the HOMO level while bathochromically shifting the absorption by adopting a more rigid ladder-type structure. Also, a high ratio of nitrogen bridges with small alkyl substituents was a desirable feature both in terms of adjusting the absorption and maintaining a low lateral inter-chain separation, which was necessary for obtaining high current and efficiency values.

## **Outlook**

The efficiency of organic bulk-heterojunction solar cells is not high in comparison with the already commercialized inorganic solar cells, and the question on stability has to be resolved before commercializing them for clean energy. There are a lot of strategies to improve the device. In my opinion, any further work in this area should address the following issues with high priority:

### 1. Control of morphology

The morphology of the thin film can strongly influence the performance of the device. In order to realize the balance of charge separation and charge transport, a suitable scale of phase separation must be obtained by means of modulating film forming conditions, applied solvent, and realizable techniques for self-organization. A bi-continuous morphology of the nanometer scale (tens to hundreds) is expected to be the best to realize charge separation at the large D/A interfaces and at the same time charge transport in separate continuous pathways of donor and acceptor. Except for the physical techniques, the design of compounds with pre-defined D/A structure is also an important strategy.

### 2. Design of new materials



Any new molecular design should emphasize on extending light absorption and enhancing self-organization. The strategies, discussed earlier in this work, are summarized below:

- Introduction of ladder-type structures
- Introduction of D-A linked structures
- Increasing the chromophore density
- Minimizing solubilizing substituents
- Enhancing electron-donating unit in donor and electron-accepting unit in acceptor
- Approaching regular and symmetric structure as a whole

## References

- [1] [http://ren21wiki.syynx.de/index.php?title=Note\\_19](http://ren21wiki.syynx.de/index.php?title=Note_19)
- [2] J. H. Burroughes, D. D. C. Bradley, A. R. Brown, R. N. Marks, K. Mackay, R. H. Friend, P. L. Burns, A. B. Holmes, *Nature*, **1990**, 347, 539.
- [3] D. Braun, A. J. Heeger, *Appl. Phys. Lett.* **1991**, 58, 1982.
- [4] N. C. Greenham, M. C. Moratti, D. D. C. Bradley, R. H. Friend, A. B. Holmes, *Nature* **1993**, 365, 628.
- [5] Y. Yang, Q. Pei, A. J. Heeger, *J. Appl. Phys.*, **1996**, 79, 934.
- [6] N. Tessler, N. T. Harrison, R. H. Friend, *Adv. Mater.* **1998**, 10, 64.
- [7] F. Garnier, R. Hajlaoui, A. Yassar, P. Srivastava, *Science* **1994**, 265, 1684.
- [8] Y. Yang, A. J. Heeger *Nature* **1994**, 372, 344.
- [9] A. R. Brown, A. Pomp, C. M. Hart, D. M. Deleeuw, *Science* **1995**, 270, 972.
- [10] G. Horowitz, *Adv. Mater.* **1998**, 10, 365.
- [11] A. Dodabalapur, Z. Bao, A. Makhija, J. G. Laquindanum, V. R. Raju, Y. Feng, H. E. Katz, J. Rogers, *Appl. Phys. Lett.* **1998**, 73, 142.
- [12] H. Sirringhaus, H. N. Tessler, R. H. Friend, *Science* **1998**, 280, 1741.
- [13] T. Kawase, H. Sirringhaus, R. H. Friend, T. Shimoda, *Adv. Mater.* **2001**, 13, 1602.
- [14] A. Kraft, *Chem. Phys. Chem.* **2001**, 2, 163.
- [15] W. Pisula, A. Menon, M. Stepputat, I. Lieberwirth, U. Kolb, A. Tracz, H. Sirringhaus, T. Pakula, K. Müllen, *Adv. Mater.* **2005**, 17, 684.
- [16] D. Wöhrle, D. Meissner, *Adv. Mater.* **1991**, 3, 129.
- [17] J. J. M. Halls, C. A. Walsh, N. C. Greenham, E. A. Marseglia, R. H. Friend, S. C. Moratti, A. B. Holmes, *Nature* **1995**, 376, 498.
- [18] G. Yu, J. Gao, J. C. Hummelen, F. Wudl, A. J. Heeger, *Science* **1995**, 270, 1789.
- [19] L. S. Roman, M. R. Anderson, T. Yohannes, O. Inganäs, *Adv. Mater.* **1997**, 9, 1164.
- [20] L. S. Roman, L. Mammo, A. A. Pettersson, M. R. Anderson, O. Inganäs, *Adv. Mater.* **1998**, 10, 774.

- [21] M. Granström, K. Petrisch, A. C. Arias, A. Lux, M. R. Anderson, R. H. Friend, *Nature* **1998**, *395*, 257.
- [22] C. J. Brabec, N. S. Sariciftci: *Semiconducting Polymers*, G. Hadziioannou & P. F. van Hutten (Eds.), Wiley-VCH, Weinheim, **2000**.
- [23] C. J. Brabec, N. S. Sariciftci, J. C. Hummelen, *Adv. Funct. Mater.* **2001**, *11*, 15.
- [24] J. J. M. Halls, R. H. Friend: *Clean Electricity from Photovoltaics*, M. D. Archer & R. Hill (Eds.), Imperial College Press, London, **2001**, 844.
- [25] B. Maennig, J. Drechsel, D. Gebeyehu, P. Simon, F. Kozlowski, *Appl. Phys. A* **2004**, *79*, 1.
- [26] G. A. Chamberlain: *Organic solar cells: A review*. *Solar Cells* **1983**, *8*, 47.
- [27] C. W. Tang, *Appl. Phys. Lett.* **1986**, *48*, 183.
- [28] N. S. Sariciftci, L. Smilowitz, A. J. Heeger, F. Wudl, *Science* **1992**, *258*, 1474.
- [29] C. J. Brabec, G. Zerza, G. Cerullo, S. De Silvestri, S. Luzzati, J. C. Hummelen, N. S. Sariciftci, *Chem. Phys. Lett.* **2001**, *340*, 232.
- [30] S. E. Shaheen, C. J. Brabec, N. S. Sariciftci, F. Padinger, T. Fromherz, J. C. Hummelen, *Appl. Phys. Lett.* **2001**, *78*, 841.
- [31] J. M. Kroon, M. M. Wienk, W. J. H. Verhees, J. C. Hummelen, *Thin Solid Films* **2002**, *403-404*, 223.
- [32] T. Munters, T. Martens, L. Goris, V. Vrindts, J. Manca, L. Lutsen, W. D. Ceunick, D. Vanderzande, L. D. Schepper, J. Gelan, N. S. Sariciftci, C. J. Brabec, *Thin Solid Films* **2002**, *403-404*, 247.
- [33] T. Aernouts, W. Geens, J. Portmans, P. Heremans, S. Borghs, R. Mertens, *Thin Solid Films* **2002**, *403*, 297.
- [34] P. Schilinsky, C. Waldauf, C. J. Brabec, *Appl. Phys. Lett.* **2002**, *81*, 3885.
- [35] F. Padinger, R. S. Rittberger, N. S. Sariciftci, *Adv. Funct. Mater.* **2003**, *13*, 85.
- [36] M. Svensson, F. Zhang, S. C. Veenstra, W. J. H. Verhees, J. C. Hummelen, J. M. Kroon, O. Inganäs, M. R. Andersson, *Adv. Mater.* **2003**, *15*, 988.
- [37] M. M. Wienk, J. M. Kroon, W. J. H. Verhees, J. Knol, J. C. Hummelen, P. A. van Hall, R. A. J. Janssen, *Angew. Chem. Int. Ed.* **2003**, *42*, 3371.
- [38] Y. Kim, S. Cook, S. M. Tuladhar, S. A. Choulis, J. Nelson, J. R. Durrant, D. D. C. Bradley, M. Giles, I. McCulloch, C. Ha, M. Ree. *Nature Materials* **2006**, *5*, 197.
- [39] W. Ma, C. Yang, X. Gong, K. Lee, A. J. Heeger. *Adv. Funct. Mater.* **2005**, *15*, 1617.
- [40] V. Lemaire, D. A. da Silva Filho, V. Coropceanu, M. Lehmann, Y. Geerts, J. Piris, M. G. Debije, A. M. van de Craats, K. Senthilkumar, L. D. A. Siebbeles, J. M. Warman, J. L. Brédas, J. Cornil, *J. Am. Chem. Soc.*, **2004**, *126*, 3271.

- [41] A. Bayer, S. Zimmermann, J. H. Wendorff, *Mol. Cryst. Liq. Cryst.* **2003**, 396, 1.
- [42] J. M. Warman, A. van de Craats, *Mol. Cryst. Liq. Cryst.* **2003**, 396, 41.
- [43] L. Schmidt-Mende, A. Fechtenkötter, K. Müllen, E. Moons, R. H. Friend, J. D. MacKenzie, *Science* **2001**, 293, 1119.
- [44] S. Chandrasekhar, B. K. Sadashiva, K. A. Suresh, *Pramana* **1977**, 9, 471.
- [45] S. Chandrasekhar, *Liq. Cryst.* **1993**, 14, 3.
- [46] S. Chandrasekhar, S. Kumar *Sci. Spect.* **1997**, 8, 66.
- [47] S. Chandrasekhar, S. K. Prasad *Contemp. Phys.* **1999**, 40, 237.
- [48] M. L. Bushey, T. Q. Nguyen, W. Zhang, D. Horoszewski, C. Nuckolls *Angew. Chem. Int. Ed.* **2004**, 43, 5446.
- [49] C. D. Simpson *Ph. D. thesis* **2003**, Johannes Gutenberg University, Mainz.
- [50] A. M. Levelut, *J. Chem. Phys.* **1983**, 80, 149.
- [51] L. J. Prins, D. N. Reinhoudt, P. Timmermann, *Angew. Chem. Int. Ed.* **2001**, 40, 2382.
- [52] D. C. Sherrington, K. A. Taskinen, *Chem. Soc. Rev.* **2001**, 30, 83.
- [53] J. H. K. Ky Hirschberg, L. Brunsfeld, A. Ramzi, J. A. J. M. Vekemans, R. P. Sijbesma, E. W. Meier, *Nature* **2000**, 407, 167
- [54] J. J. van Gorp, J. Vekemans, E. W. Meijer, *J. Am. Chem. Soc.* **2002**, 124, 14759.
- [55] R. I. Gearba, M. Lehmann, J. Levin, D. A. Ivanov, M. H. J. Koch, J. Barbera, M. G. Debije, J. Piris, Y. H. Geerts, *Adv. Mater.* **2003**, 15, 1614.
- [56] T. Q. Nguyen, R. Martel, P. Avouris, M. L. Bushey, L. Brus, C. Nuckolls, *J. Am. Chem. Soc.* **2004**, 126, 5234.
- [57] F. Würthner, C. Thalacker, A. Sautter, *Adv. Mater.* **1999**, 11, 754.
- [58] T. Christ, B. Glüsen, A. J. Greiner, A. Kettner, R. Sander, V. Stümpflen, V. Tsukruk, J. H. Wendorff, *Adv. Mater.* **1997**, 9, 48.
- [59] L. Schmidt-Mende, M. Watson, K. Müllen, R. H. Friend, *Mol. Cryst. Liq. Cryst.*, **2003**, 396, 73.
- [60] A. M. van de Craats, N. Stutzmann, O. Bunk, M. M. Nielsen, M. Watson, K. Müllen, H. D. Chanzy, H. Sirringhaus, R. H. Friend, *Adv. Mater.* **2003**, 15, 495.
- [61] A. Tracz, J. K. Jeszka, M. D. Watson, W. Pisula, K. Müllen, T. Pakula, *J. Am. Chem. Soc.* **2003**, 125, 1682.

- [62] O. Bunk, M. M. Nielsen, T. I. Solling, A. M. Van de Craats, N. Stutzmann, *J. Am. Chem. Soc.* **2003**, *125*, 2252.
- [63] A. M. van de Craats, J. M. Warman, *Adv. Mater.* **2001**, *13*, 130.
- [64] D. Wasserfallen, *Ph.D. thesis*, **2006**, MaxPlanck Institute for Polymerresearch, Germany.
- [65] J. S. Wu, *Ph.D. thesis*, **2004**, MaxPlanck Institute for Polymerresearch, Germany.
- [66] A. Fechtenkötter, *Ph.D. thesis*, **2001**, MaxPlanck Institute for Polymerresearch, Germany.
- [67] T. L. Benanti, D. Venkataraman, *Photosynthesis Research* **2006**, *87*, 73.
- [68] G. Li, V. Shrotriya, Y. Yao, Y. Yang, *J. Appl. Phys.* **2005**, *98*, 43704.
- [69] D. Chirvase, J. Parisi, J. C. Hummelen, V. Dyakonov, *Nanotechnology* **2004**, *15*, 1317.
- [70] C. J. Brabec, F. Padinger, N. S. Sariciftci, J. C. Hummelen, *J. Appl. Phys.* **1999**, *85*, 6866.
- [71] S. E. Shaheen, R. Radspinner, N. Peyghambarian, G. E. Jabbour, *Appl. Phys. Lett.* **2001**, *79*, 2996.
- [72] G. Yu, A. J. Heeger, *J. Appl. Phys.* **1995**, *78*, 4510.
- [73] J. G. Xue, S. Uchida, B. P. Rand, S. R. Forrest, *Appl. Phys. Lett.* **2004**, *85*, 5757.
- [74] A. Hadipour, B. de Boer, J. Wildeman, F. B. Kooistra, J. C. Hummelen, M. G. R. Turbiez, M. M. Wienk, R. A. J. Janssen, P. W. M. Blom, *Adv. Funct. Mater.* **2006**, *16*, 1897.
- [75] H. A. M. van Mullekom, J. A. J. M. Vekemans, E. E. Havinga, E. W. Meijer, *Materials Science and Engineering: R: Reports* **2001**, *32*, 1.
- [76] O. Inganäs, M. Svensson, F. Zhang, A. Gadisa, N. K. Persson, X. Wang, M. R. Andersson, *Appl. Phys. A* **2004**, *79*, 31.
- [77] C. J. Brabec, C. Winder, N. S. Sariciftci, J. C. Hummelen, A. Dhanabalan, P. A. van Hal, R. A. J. Janssen, *Adv. Funct. Mater.* **2002**, *12*, 709.
- [78] S. K. Lee, N. S. Cho, J. H. Kwak, K. S. Lim, H. Shim, D. Hwang, C. J. Brabec, *Thin Solid Films* **2006**, *511-512*, 157.
- [79] J. Luo, Q. Hou, J. Chen, Y. Cao, *Synth. Met.* **2006**, *156*, 470.
- [80] M. M. Wienk, M. P. Struijk, R. A. J. Janssen, *Chem. Phys. Lett.* **2006**, *422*, 488.
- [81] M. M. Wienk, M. G. R. Turbiez, M. P. Struijk, M. Fonrodona, R. A. J. Janssen, *Appl. Phys. Lett.* **2006**, *88*, 153511.
- [82] M. Al-Ibrahim, H. K. Roth, U. Zhokhavets, G. Gobsch, S. Sensfuss, *Solar Energy Mater. & Solar Cells* **2005**, *85*, 13.

- [83] M. Al-Ibrahim, A. Konkin, H. K. Roth, D. A. M. Egbe, E. Klemm, U. Zhokhavets, G. Gobsch, S. Sensfuss, *Thin Solid Films* **2005**, *474*, 201.
- [84] J. V. Grazulevicius, P. Stroehriegl, J. Pieliowski, K. Pieliowski, *Prog. Polym. Sci.* **2003**, *28*, 1297.
- [85] J. F. Ambrose, R. F. Nelson, *J. Electrochem. Soc. Electrochem. Sci.* **1967**, *115*, 1159.
- [86] A. Siove, D. Adès, *Polymer* **2004**, *45*, 4045.
- [87] O. Brihaye, C. Legrand, A. Chapoton, C. Chevrot, A. Siove, *Synth. Met.* **1993**, *55*, 5075.
- [88] D. B. Romero, M. Schaer, M. Leclerc, D. Adès, A. Siove, L. Zuppiroli, *Synth. Met.* **1996**, *80*, 271.
- [89] M. Belletête, M. Bédard, M. Leclerc, M. Durocher, *J. Mol. Struct.* **2004**, *679*, 9.
- [90] M. Belletête, M. Bédard, J. Bouchard, M. Leclerc, M. Durocher, *Can. J. Chem.* **2004**, *82*, 1280.
- [91] J. F. Brière, M. Côté, *J. Phys. Chem. B* **2004**, *108*, 3123.
- [92] F. Dierschke, A. C. Grimsdale, K. Müllen, *Synthesis* **2003**, 2470.
- [93] T. Yamato, C. Hideshima, K. Suehiro, M. Tashiro, G. K. S. Prakash, G. A. Olah, *J. Org. Chem.* **1991**, *56*, 6248.
- [94] J. F. Morin, S. Beaupré, M. Leclerc, I. Lévesque, M. D'Iorio, *Appl. Phys. Lett.* **2002**, *80*, 341.
- [95] B. A. Gregg, M. A. Fox, A. J. Bard, *J. Phys. Chem.* **1990**, *94*, 1586.
- [96] B. A. Gregg, *Chem. Phys. Lett.* **1996**, *258*, 376
- [97] M. A. Fox, M. Chanon (Eds.): *Photoinduced electron transfer* (Elsevier, Amsterdam), **1988**
- [98] J. J. M. Halls, K. Pichler, R. H. Friend, S. C. Moratti, A. B. Holmes, *Appl. Phys. Lett.* **1996**, *68*, 3120.
- [99] K. Yamashita, Y. Harima, H. Iwashima, *J. Phys. Chem.* **1987**, *91*, 3055.
- [100] H. Sirringhaus, P. J. Brown, R. H. Friend, M. M. Nielsen, K. Bechgaard, B. M. W. Langeveld-Voss, A. J. H. Spiering, R. A. J. Janssen, E. W. Meijer, P. Herwig, D. M. De Leeuw, *Nature* **1999**, *401*, 685.
- [101] B. A. Gregg, *J. Phys. Chem.* **1996**, *100*, 852.
- [102] B. A. Gregg, J. Sprague, M. W. Peterson, *J. Phys. Chem. B* **1997**, *101*, 5362.
- [103] D. M. Adams, J. Kerimo, E. J. C. Olson, A. Zaban, B. A. Gregg, P. F. Barbara, *J. Am. Chem. Soc.* **1997**, *119*, 10608.
- [104] S. Yoo, B. Domdercq, B. Kippelen, *Appl. Phys. Lett.* **2004**, *85*, 5427.

- [105] J. C. Hummelen, B. W. Knight, F. Lepec, F. Wudl, *J. Org. Chem.* **1995**, *60*, 532.
- [106] C. J. Brabec, A. Cravino, D. Meissner, N. S. Sariciftci, T. Fromherz, M. T. Rispen, L. Sanchez, J. C. Hummelen, *Adv. Funct. Mater.* **2001**, *11*, 374
- [107] W. Hu, M. Matsumura, *J. Phys. D: Appl. Phys.* **2004**, *37*, 1434.
- [108] R. C. Haddon, A. S. Perel, R. C. Morris, T. T. M. Palstra, A. F. Hebard, R. M. Fleming, *Appl. Phys. Lett.* **1995**, *67*, 121
- [109] Z. Bao, A. J. Lovinger, A. Dodabalapur, *Appl. Phys. Lett.* **1996**, *69*, 3066
- [110] A. M. van de Craats, *PhD thesis: Charge transport in self-assembling discotic liquid crystalline materials* **2000**, Delft University Press: ISBN 90-407-2040-1
- [111] P. G. Schouten, *PhD thesis: Charge carrier dynamics in pulse-irradiated columnar aggregates of mesomorphic porphyrins and phthalocyanines* **1994**, Delft University of Technology: ISBN 90-73861-22-5
- [112] P. G. Schouten, J. M. Warman, M. P. de Haas, C. F. van Nostrum, G. H. Gelinck, R. J. M. Nolte, M. J. Copyn, J. W. Zwikker, M. K. Engel, M. Hanack, Y. H. Chang, W. T. Ford, *J. Am. Chem. Soc.* **1994**, *116*, 6880
- [113] A. M. van de Craats, J. M. Warman, *Synth. Met.* **2001**, *121*, 1287.
- [114] A. M. van de Craats, J. M. Warman, A. Fechtenkötter, J. D. Brand, M. A. Harbison, K. Müllen, *Adv. Mater.* **1999**, *11*, 1469.
- [115] J. Nelson, *Phys. Review B* **2003**, *67*
- [116] I. Riedel, J. Parisi, V. Dyakonov, L. Lutsen, D. Vanderzande, J. C. Hummelen, *Adv. Funct. Mater.* **2004**, *14*, 38.
- [117] I. Riedel, V. Dyakonov, *Physica Status Solidi A – Applied Research* **2004**, *201*, 1332
- [118] G. I. A. Rikken, D. Braun, E. G. L. Staring, R. Demand, *Appl. Phys. Lett.* **1994**, *65*, 219
- [119] M. Glatthaar, *Diploma thesis: Experimentelle Untersuchung und Modellierung organischer Solarzellen auf der Basis interpenetrierender Donator/Akzeptor Netzwerke* **2003**, Fraunhofer Institut für Solare Energiesysteme (ISE), Freiburg
- [120] T. Martens, J. D'Haen, J. V. Manca, M. D'Olielaeager, D. Vanderzande, L. de Schepper, *Physicalia Magazine* **2003**, *25*, 199.
- [121] T. Martens, J. D'Haen, T. Munters, Z. Beelen, L. Goris, J. Manca, M. D'Olielaeager, D. Vanderzande, L. de Schepper, R. Andriessen, *Synth. Met.* **2003**, *138*, 243.
- [122] T. Martens, T. Munters, L. Goris, J. D'Haen, K. Schouteden, M. D'Olielaeager, L. Lutsen, D. Vanderzande, W. Geens, J. Poortmans, L. de Schepper, J. V. Manca, *Appl. Phys. A* **2004**, *79*, 27.

- [123] T. J. Savenije, J. E. Kroeze, X. N. Yang, J. Loos, *Adv. Funct. Mater.* **2005**, *15*, 1260.
- [124] T. Erb, U. Zhokhavets, G. Gobsch, S. Raleva, B. Stühn, P. Schilinsky, C. Waldauf, C. J. Brabec, *Adv. Funct. Mater.* **2005**, *15*, 1193.
- [125] H. F. Zhong, X. N. Yang, B. deWith, J. Loos, *Macromolecules* **2006**, *39*, 218.
- [126] J. P. Schmidtke, R. H. Friend, M. Kastler, K. Müllen, *J. Chem. Phys.* **2006**, *124*, 174704.
- [127] T. Kietzke, D. Neher, M. Kumke, R. Montenegro, K. Landfester, U. Scherf, *Macromolecules* **2004**, *37*, 4882.
- [128] H. M. Koepp, H. Wendt, H. Strehlow, *Z. Electrochem.* **1960**, *64*, 483.
- [129] J. Pommerehne, H. Vestweber, W. Guss, R. F. Mahrt, H. Bassler, M. Porsch, J. Daub, *Adv. Mater.* **1995**, *7*, 551.
- [130] J. Piris, *Ph.D. thesis*, Delft University of Technology, *the Netherlands* **2004**.
- [131] G. Horowitz, *J. Mater. Chem.* **1999**, *9*, 2021.
- [132] A. M. van de Craats, J. M. Warman, M. P. deHaas, D. Adam, J. Simmerer, D. Haarer, P. Schuhmacher, *Adv. Mater.* **1996**, *8*, 823.
- [133] A. M. van de Craats, M. P. deHaas, J. M. Warman, *Synth. Met.* **1997**, *86*, 2125.
- [134] J. M. Warman, J. E. Kroeze, P. G. Schouten, A. M. van de Craats, *J. Porphyrins Phthalocyanines* **2003**, *7*, 342.
- [135] K. Ohta, K. Hatsusaka, M. Sugibayashi, M. Ariyoshi, K. Ban, F. Maeda, R. Naito, K. Nishizawa, A. M. van de Craats, J. M. Warman, *Mol. Cryst. Liq. Cryst.* **2003**, *397*, 325.
- [136] P. G. Schouten, W. M. Chen, J. M. Warman, M. P. Dehaas, J. F. Vanderpol, J. W. Zwikker, *Synth. Met.* **1991**, *42*, 2665.
- [137] A. van de Craats, J. M. Warman, K. Müllen, Y. Geerts, J. D. Brand, *Adv. Mater.* **1998**, *10*, 36.
- [138] L. Schmidt-Mende, *Ph.D. thesis*, **2002**, University of Cambridge, England.
- [139] P. G. Schouten, J. M. Warman, M. P. de Haas, M. A. Fox, H. L. Pan, *Nature* **1991**, *353*, 736.
- [140] I. Fischbach, T. Pakula, P. Minkin, A. Fechtenkötter, K. Müllen, *J. Phys. Chem. B* **2002**, *106*, 6408.
- [141] J. P. Meyer, D. Schlettwein, D. Wöhrle, N. I. Jaeger, *Thin Solid Films* **1995**, *258*, 317.
- [142] G. Horowitz, F. Kouki, P. Spearman, D. Fichou, C. Nogues, X. Pan, F. Garnier, *Adv. Mater.* **1996**, *8*, 242.



- [143] C. W. Struijk, A. B. Sieval, J. E. J. Dakhorst, M. van Dijk, P. Kimkes, R. B. M. Koehorst, H. Donker, T. J. Schaafsma, S. J. Picken, A. M. Van de Craats, J. M. Warman, H. Zuilhof, E. J. R. Sudhölter, *J. Am. Chem. Soc.* **2000**, *122*, 11057.
- [144] C. D. Dimitrakopoulos, P. R. L. Malenfant, *Adv. Mater.* **2002**, *14*, 99.
- [145] J. J. Dittmer, R. Lazzaroni, Ph. Leclère, P. Moretti, M. Granström, K. Petritsch, E. A. Marseglia, R. H. Friend, J. L. Brédas, H. Rost, A. B. Holmes, *Solar Energy Materials & Solar Cells* **2000**, *61*, 53.
- [146] A. J. Breeze, A. Salomon, D. S. Ginley, B. A. Gree, H. Tillmann, H. H. Hörhold, *Appl. Phys. Lett.* **2002**, *81*, 3085.
- [147] T. Tshimitsu, N. Hirota, N. Noma, Y. Shirota, *Thin Solid Films* **1996**, *273*, 177.
- [148] P. Peumans, S. Uchida, S. R. Forrest, *Nature* **2003**, *425*, 158.
- [149] D. Wöhrle, L. Kreienhoop, G. Schnurpfeil, J. Elbe, B. Tennigkeit, S. Hiller, D. Schlettwein, *J. Mater. Chem.* **1995**, *5*, 1819.
- [150] S. Günster, S. Siebentritt, D. Meissner, *Mol. Cryst. Liq. Cryst.* **1993**, *229*, 111.
- [151] P. M. Kazmaier, R. Hoffman, *J. Am. Chem. Soc.* **1994**, *116*, 9684.
- [152] F. Würthner, *Chem. Commun.* **2004**, *14*, 1564.
- [153] F. Würthner, C. Thalacker, S. Diele, C. Tschierske, *Chem. Eur. J.* **2001**, *7*, 2245.
- [154] L. H. Gade, C. H. Galka, R. M. Williams, L. De Cola, M. McPartlin, B. Dong, L. Chi, *Angew. Chem. Int. Ed.* **2003**, *42*, 2677.
- [155] M. J. Ahrens, L. E. Sinks, B. Rybtchinski, W. H. Liu, B. A. Jones, J. M. Giaimo, A. V. Gusev, A. J. Goshe, D. M. Tiede, M. R. Wasielewski, *J. Am. Chem. Soc.* **2004**, *126*, 8284.
- [156] F. Würthner, Z. Chen, F. J. M. Hoeben, P. Osswald, C. C. You, P. Jonkheijm, J. V. Herrikhuyzen, A. P. H. J. Schenning, P. P. A. M. Van der Schoot, E. W. Meijer, E. H. A. Beckers, S. C. J. Meskers, R. A. J. Janssen, *J. Am. Chem. Soc.* **2004**, *126*, 10611.
- [157] P. Yan, A. Chowhury, M. W. Holman, D. M. Adams, *J. Phys. Chem. B* **2005**, *109*, 724.
- [158] A. Sautter, C. Thalacker, B. Heise, F. Würthner, *Proc. Natl. Acad. Sci. U.S.A.* **2002**, *99*, 4993.
- [159] C. Thalacker, F. Würthner, *Adv. Funct. Mater.* **2002**, *12*, 209.
- [160] F. Würthner, A. Sautter, D. Schmid, P. J. A. Weber, *Chem. Eur. J.* **2001**, *7*, 894.
- [161] C. C. You, F. Würthner, *J. Am. Chem. Soc.* **2003**, *125*, 9716.
- [162] R. Dobrawa, M. Lysetska, P. Ballester, M. Gru, F. Würthner, *Macromolecules* **2005**, *38*, 1315.

- [163] Y. Guan, Y. Zakrevsky, J. Stumpe, M. Antonietti, C. F. J. Faul, *Chem. Commun.* **2003**, 7, 894.
- [164] T. Gensch, J. Hofkens, A. Heirmann, K. Tsuda, W. Verheijen, T. Vosch, T. Christ, T. Basché, K. Müllen, F. C. De Schryver, *Angew. Chem. Int. Ed.* **1999**, 38, 3752.
- [165] H. Langhals, M. Speckbacher, *Eur. J. Org. Chem.* **2001**, 13, 2481.
- [166] T. Weil, E. Reuther, K. Müllen, *Angew. Chem. Int. Ed.* **2002**, 41, 1900.
- [167] D. Dotcheva, M. Klapper, K. Müllen, *Macromol. Chem. Phys.* **1994**, 195, 1905.
- [168] H. Langhals, W. Jona, *Angew. Chem. Int. Ed.* **1998**, 37, 952.
- [169] E. E. Neuteboom, R. A. J. Janssen, E. W. Meijer, *Synth. Met.* **2001**, 121, 1283.
- [170] W. Wang, W. Wan, H. H. Zhou, S. Q. Niu, A. Li, *J. Am. Chem. Soc.* **2003**, 125, 5248.
- [171] W. Pisula, M. Kastler, D. Wasserfallen, M. Mondeshki, J. Piris, I. Schnell, K. Müllen, *Chem. Mater.* **2006**, 18, 3634.
- [172] S. Sensfuss, M. Al-Ibrahim, A. Konkin, G. Nazmutdinova, U. Zhokhavets, G. Gobsch, D. A. M. Egbe, E. Klemm, H. K. Roth, *Proc. SPIE* **2004**, 5215, 129.
- [173] R. Valaski, L. M. Moreira, L. Micaroni, I. A. Hümmelgen, *Brazilian J. Phys.* **2003**, 33, 392.
- [174] Z. K. Chen, W. Huang, L. H. Wang, E. T. Kang, B. J. Chen, C. S. Lee, S. T. Lee, *Macromolecules* **2000**, 33, 9015.
- [175] T. Yamamoto, B. L. Lee, *Macromolecules* **2002**, 35, 2993.
- [176] D. A. M. Egbe, L. H. Nguyen, H. Hoppe, D. Mühlbacher, N. S. Sariciftci, *Macromol. Rapid Commun.* **2005**, 26, 1389.
- [177] J. M. Warman, J. Piris, W. Pisula, M. Kastler, D. Wasserfallen, K. Müllen, *J. Am. Chem. Soc.* **2005**, 127, 14257.
- [178] W. Pisula, M. Kastler, D. Wasserfallen, F. Nolde, C. Kohl, K. Müllen, *Angew. Chem. Int. Ed.* **2006**, 45, 819.
- [179] N. Terasawa, H. Monobe, K. Kiyohara, Y. Shimizu, *Chem. Comm.* **2003**, 1678.
- [180] A. N. Cammidge, H. Gopee, *J. Mater. Chem.* **2001**, 11, 2773.
- [181] R. D. McCullough, R. D. Lowe, M. Jayaraman, D. L. Anderson, *J. Org. Chem.* **1993**, 58, 904.
- [182] T. A. Chen, X. Wu, R. D. Rieke, *J. Am. Chem. Soc.* **1995**, 117, 233.
- [183] X. Hu, L. Xu, *Polymer* **2000**, 4, 9147.

- [184] G. Daouet, M. Leclerc, *Macromolecules* **1991**, *24*, 455.
- [185] W. Pisula, Z. Tomović, B. El Hamaoui, M. D. Watson, T. Pakula, K. Müllen, *Adv. Funct. Mater.* **2005**, *15*, 893.
- [186] C. J. Shi, Y. Yao, Y. Yang, Q. B. Pei, *J. Am. Chem. Soc.* **2006**, *128*, 8980.
- [187] W. Pisula, M. Kastler, D. Wasserfallen, T. Pakula, K. Müllen, *J. Am. Chem. Soc.* **2004**, *126*, 8074.
- [188] E. Bundgaard, F. C. Krebs, *Macromolecules* **2006**, *39*, 2823.
- [189] A. Iraqi, I. Wataru, *Chem. Mater.* **2004**, *16*, 442.
- [190] R. J. Kline, M. D. McGehee, E. N. Kadnikova, J. Liu, J. M. J. Fréchet, M. F. Toney, *Macromolecules* **2005**, *38*, 3312.
- [191] T. Otsubo, Y. Aso, K. Takimiya, H. Nakanishi, N. Sumi, *Synth. Met.* **2003**, *133*, 325.
- [192] P. Schilinsky, U. Asawapirom, U. Scherf, M. Biele, C. J. Brabec, *Chem. Mater.* **2005**, *17*, 2175.
- [193] R. C. Hiorns, R. de Bettignies, J. Leroy, S. Bailly, M. Firon, C. Sentein, A. Khoukh, H. Preud'homme, C. Dagron-Lartigau, *Adv. Funct. Mater.* **2006**, *16*, 2263.
- [194] M. Al-Ibrahim, H. K. Roth, M. Schroedner, A. Konkin, U. Zhokhavets, G. Gobsch, P. Scharff, S. Sensfuss, *Org. Electron.* **2005**, *6*, 65.
- [195] M. Reyes-Reyes, K. Kim, D. L. Carroll, *Appl. Phys. Lett.* **2005**, *87*, 83506.
- [196] W. Ma, C. Yang, X. Gong, K. Lee, A. J. Heeger, *Adv. Funct. Mater.* **2005**, *15*, 1617.
- [197] X. Yang, J. Loos, S. C. Veenstra, W. J. H. Verhees, M. M. Wienk, J. M. Kroon, M. A. J. Michels, R. A. J. Jassen, *Nano Lett.* **2005**, *5*, 579.
- [198] Y. Kim, S. A. Choulis, J. Nelson, D. D. C. Bradley, S. Cook, J. R. Durrant, *Appl. Phys. Lett.* **2005**, *86*, 63502.
- [199] Y. Kim, S. A. Choulis, J. Nelson, D. D. C. Bradley, S. Cook, J. R. Durrant, *J. Mater. Sci.* **2005**, *40*, 1371.
- [200] T. Yamamoto, *Prog. Polym. Sci.* **1992**, *17*, 1153.
- [201] H. Langhals, S. Demming, T. Potrawa, *J. Prakt. Chem.* **1991**, *333*, 733.
- [202] H. Langhals, R. Ishmael, O. Yuruk, *Tetr.* **2000**, *56*, 5435.
- [203] J. F. Morin, M. Leclerc, *Macromolecules* **2002**, *35*, 8413.
- [204] Y. Zhao, D. Keroack, G. Yuan, A. Massicotte, R. Hanna, M. Leclerc, *Macromol. Chem. Phys.* **1997**, *198*, 1035.

- [205] J. F. Morin, M. Leclerc, D. Ades, A. Siove, *Macromolecular Rapid Communications* **2005**, *26*, 761.
- [206] M. Sonntag, P. Strohhriegl, *Chem. Mater.* **2004**, *16*, 4736.
- [207] G. Zotti, G. Schiavon, S. Zecchin, J. F. Morin, M. Leclerc, *Macromolecules* **2002**, *35*, 2122.
- [208] S. Janietz, D. D. C. Bradley, M. Grell, C. Giebeler, M. Inbasekaran, E. P. Woo, *Appl. Phys. Lett.* **1998**, *73*, 2453.
- [209] K. Brunner, A. Van Dijken, H. Borner, J. Bastiaansen, N. M. M. Kiggen, B. M. W. Langeveld, *J. Am. Chem. Soc.* **2004**, *126*, 6035.
- [210] R. H. Friend, R. W. Gymer, A. B. Holmes, J. H. Burroughes, R. N. Marks, C. Taliani, D. D. C. Bradley, D. A. D. Santos, J. L. Brédas, M. Lögdlund, W. R. Salaneck, *Nature* **1999**, *397*, 121.
- [211] G. F. He, J. Liu, Y. F. Li, Y. Yang, *Appl. Phys. Lett.* **2002**, *80*, 1891.
- [212] A. C. Arias, J. D. MacKenzie, R. Stevenson, J. J. M. Halls, M. Inbasekaran, E. P. Woo, D. Richards, R. H. Friend, *Macromolecules* **2001**, *34*, 6005.
- [213] H. J. Snaith, A. C. Arias, A. C. Morteani, C. Silva, R. H. Friend, *Nano Letters* **2002**, *2*, 1353.
- [214] H. J. Snaith, R. H. Friend, *Thin Solid Films* **2004**, *451*, 567.
- [215] M. C. Scharber, D. Mühlbacher, M. Koppe, P. Denk, C. Waldauf, A. J. Heeger, C. J. Brabec, *Adv. Mater.* **2006**, *18*, 789.
- [216] J. Li, M. Kastler, W. Pisula, J. W. F. Robertson, D. Wasserfallen, A. C. Grimsdale, J. Wu, K. Müllen, *Adv. Funct. Mater.* **accepted**, 10.1002/adfm.200600679.
- [217] J. J. M. Halls, J. Cornil, D. A. dos Santos, R. Silbey, D. H. Hwang, A. B. Holmes, J. L. Brédas, R. H. Friend, *Phys. Rev. B* **1999**, *60*, 5721.
- [218] D. Veldman, J. J. A. M. Bastiaansen, B. M. W. Langeveld-Voss, J. Sweelssen, M. M. Koetse, S. C. J. Meskers, R. A. J. Janssen, *Thin Solid Films* **2006**, *511-512*, 581.
- [219] S. Walheim, M. Böltau, J. Mlynek, G. Krausch, U. Steiner, *Macromolecules* **1997**, *30*, 4995.
- [220] P. Müller-Buschbaum, J. S. Gutmann, M. Stamm, *Macromolecules* **2000**, *33*, 4886.
- [221] J. J. M. Halls, A. C. Arias, J. D. MacKenzie, W. S. Wu, M. Inbasekaran, E. P. Woo, R. H. Friend, *Adv. Mater.* **2000**, *12*, 498.
- [222] J. Li, F. Dierschke, J. Wu, A. C. Grimsdale, K. Müllen, *J. Mater. Chem.* **2006**, *16*, 96.
- [223] F. Dierschke, A. C. Grimsdale, K. Müllen, *Macromol. Chem. Phys.* **2004**, *205*, 1147.
- [224] S. A. Patil, U. Scherf, A. Kadashchuk, *Adv. Funct. Mater.* **2003**, *13*, 609.

- [225] A. K. Mishra, M. Graf, F. Grasse, J. Jacob, E. J. W. Emil, K. Müllen, *Chem. Mater.* **2006**, in press
- [226] A. K. Mishra, J. L. Li, W. Pisula, F. Dierschke, J. Jacob, A. C. Grimsdale, K. Müllen, *submitted to Adv. Funct. Mater.*
- [227] H. Sirringhaus, R. J. Wilson, R. H. Friend, M. Inbasekaran, W. Wu, E. P. Woo, M. Grell, D. D. C. Bradley, *Appl. Phys. Lett.* **2000**, *77*, 406.
- [228] J. F. Chang, B. Sun, D. W. Breiby, M. M. Nielsen, T. I. Solling, M. Giles, I. McCulloch, H. Sirringhaus, *Chem. Mater.* **2004**, *16*, 4772.
- [229] D. H. Kim, Y. D. Park, Y. Jang, H. Yang, Y. H. Kim, J. Han, D. G. Moon, S. Park, T. Chang, C. Chang, M. Joo, C. Y. Ryu, K. Cho, *Adv. Funct. Mater.* **2005**, *15*, 77.
- [230] R. J. Kline, M. D. McGehee, M. F. Toney, *Nature Materials* **2006**, *5*, 222.
- [231] J. Veres, S. Ogier, G. Lloyd, D. De Leeuw, *Chem. Mater.* **2004**, *16*, 4543.
- [232] A. Salleo, M. Chabinyc, M. Yang, R. Street, *Phys. Rev. B* **2004**, *70*, 115311.
- [233] W. Pisula, Z. Tomovic, C. Simpson, M. Kastler, T. Pakula, K. Müllen, *Chem. Mater.* **2005**, *17*, 4296.
- [234] J. K. J. van Duren, X. Yang, J. Loos, C. W. T. Bulle-Lieuwma, A. B. Sieval, J. C. Hummelen, R. A. J. Janssen, *Adv. Funct. Mater.* **2004**, *14*, 425.
- [235] H. Hoppe, M. Niggemann, C. Winder, J. Kraut, R. Hiesgen, A. Hirsch, D. Meissner, N. S. Sariciftci, *Adv. Funct. Mater.* **2004**, *14*, 1005.
- [236] C. Winder, N. S. Sariciftci, *J. Mater. Chem.* **2004**, *14*, 1077.
- [237] F. L. Zhang, M. Svensson, M. R. Andersson, M. Maggini, S. Bucella, E. Menna, O. Inganäs, *Adv. Mater.* **2001**, *13*, 1871.
- [238] G. Zerza, A. Cravino, H. Neugebauer, N. S. Sariciftci, R. Gomez, J. L. Segura, N. Martin, M. Svensson, M. R. Andersson, *J. Phys. Chem. A* **2001**, *105*, 4172.
- [239] A. Cravino, G. Zerza, M. Maggini, S. Bucella, M. Svensson, M. R. Andersson, H. Neugebauer, N. S. Sariciftci, *Chem. Commun.* **2000**, 2487.
- [240] S. Wang, J. L. Yang, Y. L. Li, H. Z. Lin, Z. X. Guo, S. X. Xiao, Z. Q. Shi, D. B. Zhu, H. S. Woo, D. L. Carroll, I. S. Kee, J. H. Lee, *Appl. Phys. Lett.* **2002**, *80*, 3847.
- [241] D. M. Russell, A. C. Arias, R. H. Friend, C. Silva, C. Ego, A. C. Grimsdale, K. Müllen, *Appl. Phys. Lett.* **2002**, *80*, 2204.
- [242] B. de Boer, U. Stalmach, P. F. van Hutten, C. Melzer, V. V. Krasnikov, G. Hadziioannou, *Polymer* **2001**, *42*, 9097.
- [243] U. Stalmach, B. de Boer, C. Vidolot, P. F. van Hutten, G. Hadziioannou, *J. Am. Chem. Soc.* **2000**, *122*, 5464.

- [244] J. S. Liu, E. Sheina, T. Kowalewski, R. D. McCullough, *Angew. Chem., Int. Ed. Engl.* **2002**, *41*, 329.
- [245] H. B. Wang, H. H. Wang, V. S. Urban, K. C. Littrell, P. Thiyagarajan, L. P. Yu, *J. Am. Chem. Soc.* **2000**, *122*, 6855.
- [246] P. R. L. Malenfant, L. Groenendaal, J. M. J. Frechet, *J. Am. Chem. Soc.* **1998**, *120*, 10990.
- [247] M. A. Hempenius, B. M. W. Langeveld-Voss, J. van Haare, R. A. J. Janssen, S. S. Sheiko, J. P. Spatz, M. Moller, E. W. Meijer, *J. Am. Chem. Soc.* **1998**, *120*, 2798.
- [248] H. B. Wang, M. K. Ng, L. M. Wang, L. P. Yu, B. H. Lin, M. Meron, Y. N. Xiao, *Chem. Eur. J.* **2002**, *8*, 3246.
- [249] P. Jonkheijm, J. K. J. Van Duren, M. Kemerink, R. A. J. Janssen, A. P. H. J. Schenning, E. W. Meijer, *Macromolecules* **2006**, *39*, 784.
- [250] J. Jacob, S. Sax, T. Piok, E. J. W. List, A. C. Grimsdale, K. Müllen, *J. Am. Chem. Soc.*, **2004**, *126*, 6987.
- [251] M. Zhang, C. Yang, A. K. Mishra, W. Pisula, G. Zhou, B. Schmaltz, M. Baumgarten, K. Müllen, *Chem. Commun.*, **accepted**.
- [252] C. M. Atienza, G. Fernández, L. Sánchez, N. Matfín, I. S. Dantas, M. M. Wienk, R. A. J. Janssen, G. M. A. Rahman, D. M. Guldi, *Chem. Commun.* **2006**, 514.
- [253] J. J. Dittmer, E. A. Marseglia, R. H. Friend, *Adv. Mater.* **2000**, *12*, 1270.
- [254] P. Liu, Q. Li, M. Huang, W. Pan, W. Deng, *Appl. Phys. Lett.* **2006**, *89*, 213501.
- [255] R. A. Street, J. E. Northrup, A. Salleo, *Phys. Rev. B* **2005**, *71*, 165202.
- [256] E. H. A. Beckers, S. C. J. Meskers, A. P. H. J. Schenning, Z. Chen, F. Würthner, P. Marsal, D. Beljonne, J. Cornil, R. A. J. Janssen, *J. Am. Chem. Soc.* **2006**, *128*, 649.
- [257] E. H. A. Beckers, Z. Chen, S. C. J. Meskers, P. Jonkheijm, A. P. H. J. Schenning, X. Li, P. Osswald, F. Würthner, R. A. J. Janssen, *J. Phys. Chem.* **2006**, *110*, 16967.
- [258] E. E. Neuteboom, S. C. J. Meskers, E. H. A. Beckers, S. Chopin, R. A. J. Janssen, *J. Phys. Chem. A* **2006**, *110*, 12363.
- [259] F. J. M. Hoeben, P. Jonkheijm, E. W. Meijer, A. P. H. J. Schenning, *Chem. Rev.* **2005**, *105*, 1491.
- [260] P. Piotrowiak, *Chem. Soc. Rev.* **1999**, *28*, 143. e) A. P. H. J. Schenning, P. Jonkheijm, E. Peeters, E. W. Meijer, *J. Am. Chem. Soc.* **2001**, *123*, 409.
- [261] H. E. Katz, Z. Bao, *J. Phys. Chem. B* **2000**, *104*, 671.
- [262] H. Meng, J. Zheng, A. J. Lovinger, B. C. Wang, P. G. Van Patten, Z. Bao, *Chem. Mater.* **2003**, *15*, 1778.

- [263] X. Yang, J. K. J. van Duren, M. T. Rispens, J. C. Hummelen, R. A. J. Janssen, M. A. J. Michels, J. Loos, *Adv. Mater.* **2004**, *16*, 802.
- [264] T. Erb, U. Zhokhavets, H. Hoppe, G. Gobsch, M. Al-Ibrahim, O. Ambacher, *Thin Solid Films* **2006**, *511-512*, 483.
- [265] X. N. Yang, J. K. J. van Duren, R. A. J. Janssen, M. A. J. Michels, J. Loos, *Macromolecules* **2004**, *37*, 2151.
- [266] F. Padinger, C. J. Brabec, T. Fromherz, J. C. Hummelen, N. S. Sariciftci, *Opto-Electron. Rev.* **2000**, *8*, 280.

## List of Publications

- [1] **Jiaoli Li**, Marcel Kastler, Wojciech Pisula, Joseph William F. Robertson, Daniel Wasserfallen, Andrew Clive Grimsdale, Jishan Wu, Klaus Müllen, *Adv. Funct. Mater.*, **accepted** 10.1002/adfm.200600679: *Organic Bulk-heterojunction Photovoltaics Based on Alkyl Substituted Discotics*
- [2] **Jiaoli Li**, Frank Dierschke, Jishan Wu, Andrew C. Grimsdale, Klaus Müllen, *J. Mater. Chem.*, **2006**, *16*, 96-100: Poly(2,7-carbazole) and perylene tetracarboxydiimide: a promising donor/acceptor pair for polymer solar cells
- [3] Ashok K. Mishra, **Jiaoli Li**, Wojciech Pisula, Frank Dierschke, Josemon Jacob, Andrew C. Grimsdale, and Klaus Müllen, *Adv. Funct. Mater.*, **submitted**: *Relation between molecular structure, supramolecular order and solar cell efficiency of nitrogen-bridged ladder-type polymers*
- [4] Yajun Cheng, **Jiaoli Li**, Zaicheng Sun, Jochen S. Gutmann, *Phys. J. Appl. Phys.*, **submitted**: *TiO<sub>2</sub> nanogranular structures in solid-state dye sensitized solar cells*
- [5] Xuan Wang, Linjie Zhi, Nok Tsao, Željko Tomović, **Jiaoli Li**, and Klaus Müllen, *Science*, **submitted**: *Transparent Conductive Carbon Films as Electrodes in Organic Solar Cells*
- [6] **Jiaoli Li**, Xinghe Fan, Yongfeng Zhao, Xiaofang Chen, Qifeng Zhou, *Chinese Journal of Polymer Science*, **2004**, *22*, 289-293: Synthesis and Characterization of Copolymer



of 2,5-bis[(4-methoxyphenyl)-oxycarbonyl]- styrene and Styrene with High Molecular Weight

- [7] **Li, Jiaoli**; Fan, Xinghe; Chen, Xiaofang; Wan, Xinhua; Zhou, Qifeng, *Advances in Liquid Crystalline Polymers and Supramolecules*, **2002**, ISBN 7-5609-2807-2, 314-317: *Liquid Crystallinity and Mechanical Properties of MPCSt-St Copolymer*
- [8] **Li, Jiaoli**; Xi, Xifeng; Li, Xuxiang; Ni, Binghua; *Membrane Science and Technology*, **2002**, 22, 32-35: *Polysulfone/Polyacrylamide alloy membrane and its application in organic solvent recovery*
- [9] **Li, Jiaoli**; Li, Xuxiang; Ni, Binghua, *Petrochemical Technology and Application*, **2000**, 18, 295-297: *Development of ultrafiltration and its application in recovery of dewaxing solvent*

# Curriculum Vitae

## Li, Jiaoli

### PERSONAL DETAILS

---

Date of Birth: 04 December 1977  
Place of Birth: Shaanxi Province, China  
Nationality: Chinese  
Marital Status: Married

### UNIVERSITY EDUCATION

---

#### June 2003 - December 2006

*PhD studies, Max-Planck-Institute für Polymerforschung, Germany*  
*Prof. Dr. Klaus Müllen*  
*Topic: Organic Solar Cells based on Discotic Liquid Crystalline Material*  
*and Conjugated Polymers*

#### September 2001 - April 2003

*PhD studies, Peking University, China*  
*Prof. Zhou, Qi-Feng*  
*Topic: Synthesis and Characterization of Mesogen-Jacketed Liquid*  
*Crystalline Material*

#### September 1998 - July 2001

*Master studies, Xi'an Jiaotong University, China*  
*Prof. Li, Xu-Xiang*  
*Topic: Ultrafiltration Films for Recovery of de-waxed solvent in Petrol*  
*Industry*

#### September 1994 - July 1998

*Bachelor studies, Xi'an Jiaotong University, China*  
*Department of Applied Chemistry and Fine Chemical Engineering*

### SCHOOL EDUCATION

---

#### September 1988 - July 1994

*Si-Ling-Wu Middle School, Hanzhong*

#### September 1983 - July 1988

*Si-Ling-Wu Primary School, Hanzhong*